UNIVERSITÁ DEGLI STUDI DI TRIESTE

XXVII CICLO DEL DOTTORATO DI RICERCA IN FISICA

Neutrino constraints from clusters of galaxies and other probes

SETTORE SCIENTIFICO-DISCIPLINARE: FIS/05

Coordinatore:
PROF. PAOLO CAMERINI

Dottorando:
MATTEO COSTANZI
ALUNNO CERBOLINI

Supervisore:
PROF. STEFANO BORGANI

Co-Supervisore:
DR. MATTEO VIEL

Anno Accademico 2013/14

.

.

Contents

Introduction

In the last two decades the ever increasing quality of images from Cosmic Microwave Background (CMB) surveys (e.g. COBE, WMAP, Planck), provided us a clear picture of the $\sim 400,000$ years old Universe. These images reveal a homogeneous and isotropic Universe with small temperature fluctuations of the order of $\Delta T/T = 10^{-5}$, which correspond to density perturbations present at the time when the Universe became transparent to photons (recombination era). According to our current understanding the isotropy observed in the CMB sky is the result of an early period of exponential expansion (inflation) driven by the vacuum energy of one or more quantum fields, occurred right after the Big Bang. As a consequence of the exponential expansion any possible spatial curvature of the Universe is stretched, so that a generic prediction of the inflation scenario is that today's Universe should look flat on observable scales. The same mechanism is thought to be responsible for the production of the initial density perturbations through the amplification of quantum fluctuations present in the inflaton field. These density fluctuations, evolved under the action of gravity, produced the temperature fluctuations observed in the CMB and, eventually, the cosmic structures we observe nowadays in the Universe.

By the early 80's, observations of the low redshift Large Scale Structure (LSS) and strengthening upper limits on temperature anisotropies in the CMB made clear that purely baryonic models cannot account for structure formation: there is not enough time for the perturbations observed in the photon-baryon plasma at the recombination epoch to grow to form the structures observed in the nearby Universe. This favoured a scenario in which the matter component is dominated by non-baryonic, highly-massive particles, referred to as cold dark matter (CDM); such particles decouple from the radiation field with small thermal velocities long before recombination, so that their density perturbations can start to grow at early times and down to adequately small scales, preparing the potential wells where baryons,

after decoupling from photons, will quickly fall to form structures at a sufficiently high rate to reproduce the observed Universe.

In the early 90's, measurements of the large scale galaxy clustering (Maddox et al., 1990; Efstathiou et al., 1990), cluster abundance (e.g. White et al., 1993a), and cluster baryon fraction (White et al., 1993b), provided evidences against the "standard" CDM model, in which the dark matter component provides the critical density to close the Universe. Among the several alternatives proposed to overcome these observational issues, the so called ΛCDM model, in which $\sim$ 30% of the critical density is accounted for CDM and the remaining $\sim$ 70% for a cosmological constant, seemed to match all the observed properties of the CMB and LSS.

In 1998 two teams independently (Riess et al., 1998; Perlmutter et al., 1999) used the luminosity-distance relation of Type Ia supernovae (SN Ia) to show that the expansion of the Universe is accelerating at the present time. The simplest theoretical explanation for these results was the introduction of an additional energy component with properties very similar to those of Einstein's cosmological constant Λ. Subsequent observations of the SN Ia luminosity-distance relation, along with independent evidences from the study of the LSS and CMB anisotropies, confirmed that the Universe is undergoing a phase of accelerated expansion, whose characteristics are compatible with those predicted for a ΛCDM cosmology.

The wealth and accuracy of current cosmological data from measurements of the CMB, LSS and related probes allowed to determine with sub-percent precision the parameters of the ΛCDM model, which has been adopted as the concordance cosmological model. According to this, the Universe is flat and made of radiation, baryons, CDM, and a constant dark energy component with negative pressure, i.e. cosmological constant Λ.

Despite this encouraging result there is still a lot to be understood: the nature of the two dominant components of the Universe, cold dark matter and dark energy, is still unknown; whereas, several modifications of the Einstein's General Relativity still represent viable alternative explanations to the effects thought to be induced by one or both of these dark components. Moreover, tensions between the latest CMB results and constraints from low redshift probes, such as galaxy clusters and cosmic shear, suggest either the need for new physics, or systematics in the measurements, or a combination thereof. The lack of a comprehensive theoretical framework and the current instrumental limitations make the combination of datasets from different cosmological probes mandatory to tackle these issues. This is especially true for the measurement of those parameters which affect the late-time evolution of the Universe, and thus are poorly constrained by CMB data alone, such as the dark energy equation of state or the total neutrino mass.

This Thesis focuses on the study of the only component of dark matter which is currently known, i.e. neutrinos. Although in the Standard Model of particle physics (SM) neutrinos are described as elementary massless particles, oscillation experiments using solar and atmospheric neutrinos have provided compelling evidence for their non-vanishing mass. Moreover, several anomalous results from accelerator, gallium and reactor neutrino experiments suggest the existence of one or two extra light sterile neutrino species, not predicted by the SM. Unfortunately, neutrino oscillation experiments are only sensitive to mass squared differences between neutrino mass eigenstates – i.e. they cannot be used to determine their absolute mass scale – while current high-energy physics experiments provide only loose constraints on the total neutrino mass. On the other hand, cosmology provides powerful means to constrain the neutrino properties. Produced in the early Universe by frequent weak interactions, cosmic neutrinos, when still relativistic, contribute to the radiation energy content affecting the background evolution; at lower redshift, when they become non relativistic, neutrinos suppress the matter fluctuations at small scales due to their high thermal velocity. These effects leave a characteristic imprint on several cosmological observables that have been used to put constraints on the total neutrino mass. Massive neutrinos have also been advocated as a possible means to relieve the tension between Planck measurements of the CMB temperature anisotropies and measurements of the low redshift growth of structure from various probes of the LSS.

Among the different probes of the LSS, the population of galaxy clusters is particularly suited to study the late-time evolution of cosmic structures. Arising from the high density peaks of the initial matter distribution, galaxy clusters are the most massive bound objects in the Universe, whose population bears the imprints of the statistical distribution of the initial perturbations and their subsequent growth. In particular, the number density of galaxy clusters is sensitive to the amplitude of the density perturbations, whereas its evolution is directly related to their growth rate. Additionally, the spatial distribution of clusters provides complementary information on the shape and amplitude of the matter power spectrum of density fluctuations and the evolution of the clustering properties is sensitive to their growth as well. Despite this potential, the actual constraining power of galaxy cluster catalogues depends on our capability to recover cluster masses from proxies and to have reliable theoretical predictions for their spatial number density (the halo mass function, HMF) and bias. The accuracy with which the cluster mass is estimated is related to the proxy used to infer the mass – e.g. richness, optical or X-ray luminosity, lensing or X-ray temperature – the availability of follow-up data to calibrate the mass-proxy relation, and the theoretical assumptions made

about the morphology and dynamical state of the clusters used to calibrate this relation. As for the HMF and bias, by the end of 90's N-body simulations became the standard tool for their calibration. However, despite the accuracy of the numerical results has improved considerably over the past decade, systematic errors e.g. related to baryonic feedback processes or massive neutrino effects, still need to be understood in detail. Nevertheless, current clusters datasets – based on relatively small sample of ~ 100 objects detected at redshift below ~ 1 – provide competitive cosmological constraints to that inferred from other probes such as cosmic shear or Baryonic Acoustic Oscillations (BAO).

Furthermore, in few years the number of clusters available for cosmology is expected to increase by orders of magnitude with the advent of the next generation of X-ray (e.g. eROSITA[1]), Sunyaev-Zeldovich (SZ) (e.g. CCAT[2], SPT-3G) and optical (e.g. LSST[3], Euclid[4]) surveys. Such large amount of data will significantly improve cosmological constraints from cluster data, provided that robust mass proxies and accurate theoretical predictions for the cluster abundance will be available. In this respect, it is crucial to quantify the constraining power of such surveys and investigate possible limiting factors in their cosmological exploitation.

This Thesis is devoted to the derivation of cosmological constraints by using different probes of the large scale structure, with focus on massive neutrinos constraints from galaxy clusters surveys. In particular, we deal with three different issues among those mentioned above: *i*) we explore the cosmological information carried by the cluster catalogue that will be provided by the photometric redshift survey of ESA's Euclid mission, focusing on neutrino constraints from cluster counts and clustering of clusters; *ii*) we discuss the effects that massive neutrinos have on the statistic of the halo population providing a recipe to recover a well-calibrated HMF to be used in cosmology with non-zero neutrino mass along with its effects on parameter inference; *iii*) we perform a joint analysis of various low redshift probes with CMB data to assess to what extent massive neutrinos provide a means to alleviate the recently highlighted tension between Planck CMB measurements and constraints from observations of the LSS.

The structure of this Thesis is organised as follows:

[1] http://www.mpe.mpg.de/eROSITA
[2] http://www.ccatobservatory.org/index.cfm
[3] http://www.lsst.org/lsst/
[4] http://www.euclid-ec.org/

To facilitate the understanding of the analysis carried out in this Thesis we provide in Chapter 1 a concise review on cosmic structure formation. We start outlining the general framework of the standard ΛCDM model and the linear perturbation theory. We move then to the statistics of the matter density field, introducing the statistical tools used in the analyses presented in this Thesis – the matter power spectrum, HMF and halo bias – and lingering on their dependence on cosmological parameters. The last part of this Chapter is devoted to the neutrino physics; after having illustrated the origin and characteristics of the cosmic neutrino background, we explain the effects that massive neutrinos induce on the evolution of cosmic structures and how these are reflected on the statistic of the matter density fluctuations (i.e. the matter power spectrum). The Chapter concludes with a summary of the most recent constraints on active and sterile neutrino properties inferred from cosmological data.

Chapter 2 presents an overview of the cosmological probes that have been considered to derive the cosmological constraints presented in this Thesis: CMB, galaxy clusters, BAO, cosmic shear and Ly-α forest. For each of these we illustrate their properties, observational techniques and cosmological relevance, also briefly reviewing some recent results. Particular emphasis is given to galaxy clusters surveys, being the probe mostly used for the results of this Thesis. The methodology used to build cluster samples from optical/near-IR, X-ray and microwave data is reviewed, along with the respective techniques and proxies used to estimate the cluster mass.

The original work of my Ph.D. project constitutes the topic of the last three Chapters of the Thesis.

In Chapter 3 we present a forecast analysis on the capability of the Euclid photometric cluster survey in constraining the neutrino properties. Firstly, we illustrate the procedure used to build the mock data and the likelihood functions employed for the parameter inference. The forecast errors are derived by means of the Monte Carlo Markov Chain technique exploiting the cosmological information carried by the cluster number counts and the cluster power spectrum in combination with Planck-like CMB data. The analysis is performed for various extension of the ΛCDM : we start considering massive neutrino and a non-standard effective number of neutrino species. The analysis is then extended to wCDM and curved models in order to explore possible degeneracies between parameters. We also take into account the impact on neutrino constraints due to an uncertain knowledge of

the relation between the observable on which cluster selection is based and cluster mass, assuming different levels of prior knowledge on the parameters which define this relation. The results of this analysis have been published in Costanzi Alunno Cerbolini et al. (2013), JCAP:06(2013)020.

In Chapter 4 we present a study of the accuracy of the HMF in reproducing the halo abundance in the presence of massive neutrinos. By means of a set of N-body simulations we show that an improved fit to the simulations results on the HMF is obtained once the suppression of the total dark matter density fluctuations on scales smaller than the neutrino free-streaming length is neglected, confirming the results of Ichiki and Takada (2012). As a quantitative application of our findings we consider a Planck-like SZ-clusters survey and we compare the number of clusters expected to be detected within such survey computed using the standard or the improved calibration of the HMF. We thus analyse how the difference in the predicted number of clusters affects the determination of cosmological parameters from clusters data, using as case study a sample of 188 SZ-selected clusters with measured redshift observed by the Planck satellite. The constraints obtained assuming one or three degenerate massive neutrino species for the two HMF prescriptions are presented and the biases introduced by an inaccurate HMF calibration quantified. The results presented in this Chapter have been published in Costanzi et al. (2013), JCAP:1312(2013)012.

Motivated by the recent claims of neutrino mass detection from the combination of CMB and LSS data we discuss in Chapter 5 the reliability of neutrino mass constraints, either active or sterile, from the joint analysis of different low redshift Universe probes with measurements of CMB anisotropies. For this analysis we consider WMAP 9-year or Planck CMB data in combination with recent BAO and cosmic shear measurements, Ly-α forest constraints and galaxy cluster mass function. As for the cluster data analysis we rely on the results of Chapter 4 for the calibration of the HMF in cosmology with massive neutrino; moreover, we explore the impact of the uncertainty in the mass bias and re-calibration of the HMF due to baryonic feedback processes on cosmological parameters. In order to avoid misleading results due to model dependence of the constraints we perform a full likelihood analysis for all the datasets employed. The results are firstly presented for single data combinations of one of the two CMB datasets with one low redshift probe, to assess if the extension to massive neutrinos, either active or sterile, provides agreement between datasets. We start then to combine CMB data with different probes of the LSS simultaneously, to determine which datasets combina-

tion, if any, provides evidence for non-zero neutrino mass, and recover constraints on their total mass. The results presented in this Chapter have been published in Costanzi et al. (2014), JCAP:10(2014)081.

Chapter 6 summarizes the results presented in this Thesis, emphasizing the critical points which are worth to be further investigated and discusses possible future directions of investigation.

1

Cosmic structure formation

According to the standard picture of cosmic structure formation the astronomical objects that we observe nowadays in our Universe are the results of the evolution of small primordial perturbations in the density field present at the end of the inflationary epoch. Depending on the scale considered different physical processes dominate the evolution of these objects. On sufficient large scale ($\gtrsim$ 10Mpc) the evolution of the cosmic structures is dominated by gravitational dynamics, which makes the description of their formation relatively simple. On smaller scales, instead, different astrophysical processes related to galaxy formation and evolution – e.g. gas cooling, star formation and feedback from supernovae (SN) or active galactic nuclei feedback – become relevant, affecting the observational properties of the structures. In this chapter I will review the general framework of the standard cosmological model (1.1) and briefly describe the linear perturbations theory (§ 1.2) which allows to describe the evolution of density perturbations as long as their density contrast relative to the background remain much smaller than unity. Furthermore, the statistical tool used for cosmological parameter inference exploited in this Thesis will be presented in § 1.3. Finally, I will review the physics of massive neutrinos and their effects on cosmic structure formation § 1.5. For a comprehensive treatment of these topics the reader can refer to classical textbooks as Peebles (1993), Peacock (1999) and Mo et al. (2010).

1.1 Evolution of the uniform background

Modern cosmology is based, among the others, upon the cosmological principle – the hypothesis that the Universe is spatially homogeneous and isotropic on scales larger than ~ 100 Mpc – and Einstein' s theory of general relativity, according to which the structure of space-time is determined by the mass distribution in the Universe. From the cosmological principle it follows that the space-time metric is described by the Robertson-Walker one:

$$\mathrm{d}s^2 = c^2\mathrm{d}t^2 - a^2(t)\left[\frac{\mathrm{d}r^2}{1-Kr^2} + r^2(\mathrm{d}\vartheta^2 + \sin^2\vartheta\mathrm{d}\varphi^2)\right] \tag{1.1}$$

where r, ϑ and φ are the comoving spatial coordinates and t the proper time. The parameter K is related to the spatial curvature and can take the values: $K = 0$ for a spatially flat geometry, $K = 1$ for a positive curvature and $K = -1$ for a negative curvature. Finally, the cosmic scale factor $a(t)$ describes the expansion history of the Universe. This is related to redshift through the relation: $a = a_0/(1+z)$.

The time evolution of the scale factor can be determined exploiting the Einstein' s field equations which describe the relation between the 4-dimensional space-time metric and its matter-energy content through:

$$G_{\alpha\beta} = R_{\alpha\beta} - \frac{1}{2}Rg_{\alpha\beta} = \frac{8\pi G}{c^4}T_{\alpha\beta} + \Lambda g_{\alpha\beta}\,. \tag{1.2}$$

In this equation, the indices α and β run from 0 to 3, $G_{\alpha\beta}$ is the Einstein tensor, $g_{\alpha\beta}$ is the metric tensor, and R and $R_{\alpha\beta}$ are the Ricci' s scalar and tensor, respectively. The constant Λ, originally introduced by Einstein to achieve a stationary Universe, is the cosmological constant. Finally, the term $T_{\alpha\beta}$ is the energy-momentum tensor, which describes the physical properties of the different matter-energy components of the Universe. By including in Eq. (1.2) the Robertson-Walker metric, and considering $T_{\alpha\beta}$ for a perfect fluid, one obtains the Friedmann equation:

$$\left(\frac{\dot{a}}{a}\right)^2 = H^2(t) = \frac{8\pi G}{3}\left[\rho_{\mathrm{m},0}\left(\frac{a_0}{a}\right)^3 + \rho_{\mathrm{r},0}\left(\frac{a_0}{a}\right)^4 + \rho_{\Lambda,0}\right] - \frac{Kc^2}{a^2} \tag{1.3}$$

where the subscript '0 'stands for quantities evaluated at the present time t_0, and the dot denotes time derivatives. The Hubble parameter $H(t)$, defined as the ratio of the expansion velocity and the scale factor, represents the rate of change of the proper distance between two fundamental observers at time t. Quantities that depend on the value of H_0 are usually expressed in terms of $h \equiv H_0/100\,\mathrm{km\,s^{-1}Mpc^{-1}}$

to parametrize the uncertainty on its measurement. The quantities $\rho_{\mathrm{i},0}$ represent the present matter-energy densities of the various components of the Universe: m for the non-relativistic matter component (DM and baryons), r for the relativistic component (radiation and relativistic matter) and Λ for the dark energy component (cosmological constant). Note that in this equation the cosmological constant Λ of Eq. (1.2) is expressed as an energy density defined as: $\rho_\Lambda = \Lambda c^2/8\pi G$. To get dimensionless quantities these energy densities are often recasted in units of the critical density $\rho_{\mathrm{cr}} = 3H^2/8\pi G$ as:

$$\Omega_i \equiv \frac{\rho_i}{\rho_{\mathrm{cr}}}, \qquad \text{with } i = r, m, \Lambda\,,$$

such that, for a flat Universe ($K = 0$), from Eq. (1.3) one gets $\Omega_0 \equiv \sum_i \Omega_i = 1$.

Since the different components of the total energy density scale differently with time (see Eq. (1.3)) it is possible to define three cosmic epochs depending on which component dominates the dynamics of the Universe. The radiation dominated era lasts until the so-called equivalence redshift:

$$1 + z_{\mathrm{eq}} \approx 2.4 \times 10^4 \Omega_{\mathrm{m},0} h^2 \approx 3250\,, \tag{1.4}$$

after which the evolution of the Universe is driven by the matter component. The second transition from a matter dominated Universe to a dark energy one occurs at:

$$1 + z_\Lambda = \left(\frac{\Omega_\Lambda}{\Omega_{\mathrm{m}}}\right)^{1/3}, \tag{1.5}$$

which for $\Omega_\Lambda \simeq 0.7$ and $\Omega_{\mathrm{m}} \simeq 0.3$ gives $z_\Lambda \simeq 0.33$. Depending on the precise values of the energy density parameters the transition epochs occur at different redshifts and the Universe expands at different rates; this in turn influence the structure formation history and consequently the statistical properties of the observable used to infer cosmological parameters as will be shown in the next sessions.

1.2 Linear perturbation theory

In the previous section I introduced the equations that describe the evolution of a uniform background and its components. However, to explain the formation and evolution of the cosmic structure we need some deviation from a perfectly homogeneous Universe. These inhomogeneities in the density field arise during the inflationary era from quantum fluctuations of the inflaton field. In this section I

intriduce basic concepts of the linear perturbation theory which allows to follow the evolution of these density perturbations as long as their overdensities with respect to the background are small. Furthermore, I will report some specific solutions for the evolution of the density fluctuations on sub-horizon scales, in the framework of the ΛCDM model, that will be useful for the treatment of this Thesis.

1.2.1 Newtonian approximation

For small density fluctuations with sizes much smaller than the Hubble radius[1] – so that causality can be assumed to be instantaneous – it is sufficient to consider the Newtonian perturbation theory in the linear regime. If we model the Universe as a non-relativistic multi-component fluid, the time evolution of each component under the action of the gravitational potential ϕ is given by the continuity equation (which describes mass conservation), the Euler equations (the equations of motion) and the Poisson equation (which describes the gravitational field):

$$\frac{\partial \delta}{\partial t} + \frac{1}{a}\nabla \cdot [(1+\delta)\mathbf{v}] = 0 \quad \text{(continuity)}, \tag{1.6}$$

$$\frac{\partial \mathbf{v}}{\partial t} + \frac{\dot{a}}{a}\mathbf{v} + \frac{1}{a}(\mathbf{v}\cdot\nabla)\mathbf{v} = -\frac{\nabla\Phi}{a} - \frac{\nabla P}{a\bar{\rho}(1+\delta)} \quad \text{(Euler)}, \tag{1.7}$$

$$\nabla^2\Phi = 4\pi G\bar{\rho}a^2\delta \quad \text{(Poisson)}, \quad \Phi \equiv \phi + a\ddot{a}x^2/2\,, \tag{1.8}$$

where P is the fluid pressure, $\nabla \equiv \nabla_{\mathbf{x}}$ is the Laplacian operator and $\mathbf{x} = \mathbf{r}/a(t)$, $\mathbf{v} = a\dot{\mathbf{x}}$ the comoving coordinates and peculiar velocities, respectively. The equations are expressed as functions of the dimensionless density contrast δ defined as:

$$\delta(\mathbf{x}, t) = \frac{\rho(\mathbf{x}, t) - \bar{\rho}(t)}{\bar{\rho}(t)}, \tag{1.9}$$

with ρ being the density field of the fluid and $\bar{\rho}$ the average density of the Universe computed over a sufficient large volume. The above description, based on the assumption that the matter content of the Universe is a non-relativistic fluid, can be extended to the ΛCDM case i.e. a Universe which include also a smooth background of relativistic particle (photons and neutrinos) and dark energy (the cosmological constant). Indeed, one can easily prove that Eqs. (1.6)–(1.8) hold if the density contrast δ is defined with respect to the mean non-relativistic matter

[1]The Hubble radius is the proper distance that correspond to speed of light c: $R_H = c/H(z)$. This radius represents the region within which it is possible to exchange information.

density rather than the total one. The net effect of adding a smooth component is only to change the expansion rate of the background, that is to change the form of the scale factor $a(t)$.

To study the evolution of the different modes k independently it is useful to solve the above system of equations in the Fourier space. For isentropic perturbations in a barotropic fluid, $P = P(\rho)$, after linearising Eqs. (1.6) and (1.7) the solution of the system (in Fourier space) reads:

$$\frac{\mathrm{d}^2\delta_{\mathbf{k}}}{\mathrm{d}t^2} + 2\frac{\dot{a}}{a}\frac{\mathrm{d}\delta_{\mathbf{k}}}{\mathrm{d}t} = \left[4\pi G\bar{\rho} - \frac{k^2 c_s^2}{a^2}\right]\delta_{\mathbf{k}}, \tag{1.10}$$

with $c_s = (\partial P/\partial\rho)^{1/2}$ the adiabatic sound speed in the fluid. This equation has the form of damped harmonic oscillator. The second term on the left-hand side is the Hubble drag term, which tends to suppress the growth of perturbations due to the expansion of the Universe. The first term on the right-hand side is the gravitational term and drives the growth of the density contrast via gravitational instability, while the latter is the pressure term which acts against the gravitational collapse. The competition between these two terms determines the evolution of the perturbation. Defining the characteristic proper length (Jeans length) as:

$$\lambda_J \equiv \frac{2\pi a}{k_J} = c_S\sqrt{\frac{\pi}{G\bar{\rho}}}, \qquad k_J = \left(\frac{4\pi G\bar{\rho}a^2}{c_s^2}\right)^{1/2}, \tag{1.11}$$

and neglecting Hubble expansions, one gets that for $\lambda > \lambda_J$ ($k < k_J$) the pressure can no longer support the gravity and the growing mode solution of Eq. (1.10) is that of a non-propagating wave with an amplitude that increases with time, i.e. a gravitational (or Jeans) instability as it will be shown explicitly in § 1.2.2.

1.2.2 Specific solutions

Pressureless fluid

The generic solution of Eq. (1.10) can be cast in the form:

$$\delta(\mathbf{k}, t) = \delta_+(\mathbf{k}, t_\mathrm{i})D_+(t) + \delta_-(\mathbf{k}, t_\mathrm{i})D_-(t)\,, \tag{1.12}$$

where D_+ and D_- are the growing and decaying modes, respectively. For a non-relativistic pressureless fluid (e.g. CDM), or when $k \ll k_j$, the pressure term

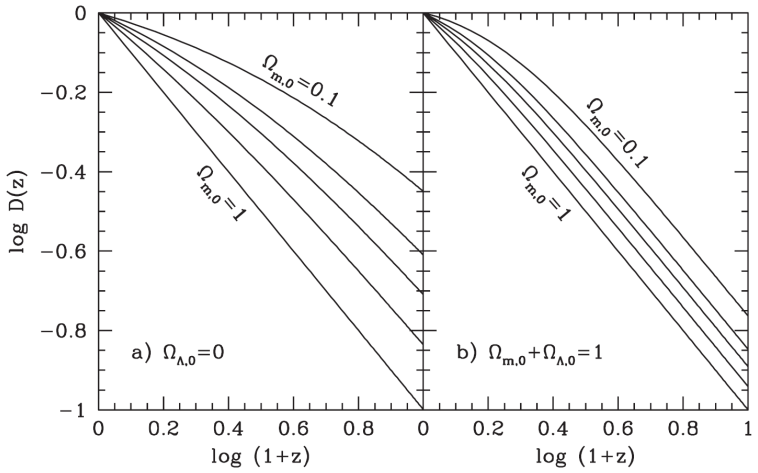

Figure 1.1: Evolution of the linear growth factor (normalized at $z = 0$) as a function of redshift for different combination of the parameters $\Omega_{m,0}$ and $\Omega_{\Lambda,0}$. The left panel assumes $\Omega_{\Lambda,0} = 0$ while the right panel assumes $\Omega_{\Lambda,0} = 1 - \Omega_{m,0}$. From top to bottom the curves correspond to $\Omega_{m,0} = 0.1$, 0.2, 0.3, 0.5 and 1. Figure from Mo et al. (2010).

$4\pi G\bar{\rho}a^2/c_s^2$ can be set to zero, and the expression for the growing mode takes the form:

$$D_+(z) = \frac{5}{2}\Omega_{m,0}E(z)\int_z^\infty \frac{1+z'}{E^3(z')}dz', \tag{1.13}$$

with (see Eq. (1.3)):

$$E(z) = \frac{H(z)}{H_0} = [\Omega_{\Lambda,0} + \Omega_{k,0}(1+z)^2 + \Omega_{m,0}(1+z)^3 + \Omega_{r,0}(1+z)^4]^{1/2}, \tag{1.14}$$

where the curvature parameter is defined as: $\Omega_{k,0} \equiv -Kc^2/(H_0a_0)^2 = 1 - \Omega_0$. In Figure 1.1 is shown the evolution with redshift of the growth factor $D \equiv D_+$ for different cosmological models. The growth of perturbations is faster in an Einstein-de Sitter model ($\Omega_m = 1$) and becomes slower as Ω_m decreases. The different behaviour is due to an enhancement of the Hubble drag (i.e. larger expansion rate) in open universes ($\Omega_0 < 1$) or universes with a dark energy component ($\Omega_\Lambda \neq 0$). From this example it is clear that any probe capable of sampling the growth of structures at various redshifts is a valuable tool to constrain cosmological parameters.

Acoustic waves

Let us now consider isentropic perturbations in a fluid consisting of baryons and CDM in the matter dominated era ($\Omega_{\rm m} = \Omega_{\rm cdm} + \Omega_{\rm b} \simeq 1$). According to the standard ΛCDM model the CDM is the dominant component in mass in the Universe: $\rho_{\rm cdm} \gg \rho_{\rm b}$ and $\bar{\rho}_0 \simeq \bar{\rho}_{\rm cdm}$. The equation for the evolution of the density perturbations in baryons, $\delta_{\rm b}$, can be thus approximated to:

$$\frac{{\rm d}^2\delta_{\rm b}}{{\rm d}t^2} + 2\frac{\dot{a}}{a}\frac{{\rm d}\delta_{\rm b}}{{\rm d}t} + \frac{k^2c_s^2}{a^2}\delta_{\rm b} = 4\pi G\frac{\bar{\rho}_{\rm cdm}a_0^3}{a^3}\delta_{\rm cdm}\,, \tag{1.15}$$

where the CDM perturbations, $\delta_{\rm cdm}$, evolves as in Eq. (1.13). A solution of this equation valid for $k \ll k_J$, and assuming a polytropic fluid with $P \propto \rho^{4/3}$, for which $c_s^2 a =$ constant is:

$$\delta_b(\mathbf{k},t) = \frac{\delta_{\rm cdm}(\mathbf{k},t)}{1+k^2/k_J^2}, \quad \text{with} \quad k_J^2 = \frac{3a^2H^2}{2c_s^2}. \tag{1.16}$$

At large scales, where the pressure can be neglected ($k \ll k_J$), the baryonic perturbations closely follow those of CDM. On small scales ($k \gg k_J$), however, the pressure cannot be neglected and the baryonic component starts to oscillate (acoustic waves) with a frequency $\omega \simeq kc_s$ that slowly damps due to the expansion of the Universe. Acoustic waves play a role during the pre-recombination era, when baryons and photons are tightly coupled and can be considered as a single fluid with sound speed:

$$c_s = \frac{c}{\sqrt{3(1+\mathscr{R})}}\,, \quad \mathscr{R} \equiv \frac{3}{4}\frac{\bar{\rho}_b(z)}{\bar{\rho}_\gamma(z)} \approx 27\Omega_{{\rm b},0}h^2\frac{1}{1+z}. \tag{1.17}$$

In this case the acoustic waves are driven by the photon pressure, and for a given mode the properties of the waves depend on the density ratio between baryon and photons through the sound speed c_s. The acoustic waves in the photon-baryon plasma give rise to the so-called acoustic peaks in the power spectrum of the CMB temperature anisotropy; the relative amplitudes and positions of the various peaks thus provide us strong cosmological information (see §2.1). Moreover, the acoustic waves also perturbed the baryons, which couple gravitationally to the CDM. Therefore, the characteristic length scale travelled by the sound waves from inflation to the baryon-photon decoupling – the so-called acoustic horizon - is imprinted in the clustering of matter on large scale. The acoustic horizon shows up as a series of peaks – the baryonic acoustic oscillations (BAO) – in matter power spectrum (see §1.3.1), whose positions can be used as a standard ruler to estimate cosmological parameters (see §2.3).

Silk damping

The coupling between baryons and photons in the pre-recombination era is not perfect, in the sense that the photon mean-free path between two Thomson scattering is not zero. Therefore, photons tend to diffuse from high-density to low-densities regions, dragging with them the tightly coupled baryonic fluid. This mechanism, known as Silk damping (Silk, 1967), causes the exponential suppression of perturbations in the baryon-photon plasma during the pre-recombination era. The scale on which the Silk damping is relevant depends on the mean distance that a photon can diffuse in a Hubble time, which exploiting the random walk approximation is:

$$\lambda_{\rm Silk} \simeq (R_H/\sigma_{\rm T} n_{\rm e})^{1/2}\,, \tag{1.18}$$

where R_H is the Hubble radius, $\sigma_{\rm T}$ the Thomson cross section and $n_{\rm e}$ the electron density.

Meszaros effect

In the presence of a smooth relativistic component along with the baryonic and CDM ones the scale factor is given by:

$$\left(\frac{\dot{a}}{a}\right)^2 = \frac{8\pi G}{3}\left[\rho_{\rm m,0}\left(\frac{a_0}{a}\right)^3 + \rho_{\rm r,0}\left(\frac{a_0}{a}\right)^4\right] \tag{1.19}$$

Neglecting the baryon component the growing mode solution of Eq. (1.10) for the CDM density contrast is:

$$D_+(z) \propto 1 + \frac{3}{2}\zeta \qquad \text{with} \quad \zeta \equiv \frac{\bar{\rho}_{\rm m}}{\bar{\rho}_{\rm r}} = \frac{(1+z_{\rm eq})}{(1+z)}\,. \tag{1.20}$$

Therefore, in the epoch dominated by the relativistic component ($z \gg z_{\rm eq}$), within R_H, the Hubble drag causes a stagnation of the perturbation growth in the non-relativistic component ($D_+ \simeq$ constant), known as Mészáros effect (Meszaros, 1974). Actually, since matter perturbations enter the horizon (at $\zeta = \zeta_{\rm enter}$) with non-zero "velocities" ($\dot{\delta} \neq 0$) , δ is not frozen quite at the horizon-entry value, but continues to grow until this initial "velocity" is redshifted away, which gives a total boost factor of roughly $\ln(\zeta_{\rm enter})$. After the matter-radiation equivalence, the growing mode solution of Eq. (1.10) approaches asymptotically that of an Einstein-de Sitter universe ($\Omega_{\rm m} = 1$) with $D_+ \propto a$.

1.3 Statistical properties of the density field

In order to be able to relate theory to observations we need to characterize the statistical properties of the cosmological perturbations. To this end, in the following section I will introduce the matter power spectrum and the halo mass function – two statistical tools that will be extensively used throughout this Thesis – lingering on their dependence on cosmological parameters.

1.3.1 The linear matter power spectrum

If the initial density field is a Gaussian random field, as predicted for a large class of standard inflation models, all its statistical information is encoded in its mean and variance. It follows from the definition of the density contrast, Eq. (1.9), that its spatial average at a given redshift is null, $\langle \delta(\mathbf{x}, z) \rangle = 0$. Instead, taking the Fourier transform of $\delta(\mathbf{x}, z)$, and calculating its variance, one gets:

$$\sigma^2(z) = \langle \delta^*(\mathbf{k}, z) \delta(\mathbf{k}, z) \rangle = \frac{1}{2\pi^2} \int_0^\infty P(k, z) k^2 \mathrm{d}k \,, \tag{1.21}$$

where $P(k, z)$ is the power spectrum of the density fluctuations as a function of redshift. Note that in Eq. (1.21) the assumption of an isotropic Universe allows us to express the power spectrum as only function of the modulus of the wavenumber $k = |\mathbf{k}|$. Another useful quality to study the statistics of collapsed objects, which arise from initial perturbations of size R, is the variance of the density field smoothed on a sphere of comoving radius R, defined as:

$$\sigma^2(R, z) = \frac{1}{2\pi^2} \int_0^\infty P(k, z) \tilde{W}_R^2(k) k^2 \mathrm{d}k \,, \tag{1.22}$$

where the convolution kernel $\tilde{W}_R(k)$ is the Fourier transform of a spherical top-hat filter of radius R.

In the linear regime different modes of the perturbation field evolve independently of each other, hence if the initial field were Gaussian, so is the linearly evolved one. Moreover, for each mode $\delta(\mathbf{k}, z)$, its evolution can be described as a linear function of the initial condition. From these considerations, it follows, that the power spectrum at different redshifts can be factorized as:

$$P(k, z) = T^2(k) D^2(z) P_{\mathrm{in}}(k) \,, \tag{1.23}$$

where $T(k)$ is the linear transfer function, $D(z)$ the growing mode of Eq. (1.13)[2] and $P_{\rm in}(k)$ the primordial power spectrum, usually parametrized with a power law: $P_{\rm in}(k) = A_s k^{n_s}$. While given an inflationary model it is possible to make theoretical predictions for the spectral index n_s (typically $n_s \simeq 1$), the current theory has no predictive power regarding the amplitude A_s, which has to be determined from observations of the CMB or the LSS. For historical reasons, a common parametrization of the power spectrum normalization involves the variance of the matter density field smoothed over a sphere with a comoving radius of $8h^{-1}$Mpc : $\sigma_8 \equiv \sigma(R = 8h^{-1}\text{Mpc}, 0)$ (see Eq. (1.22)). The choice of $R = 8h^{-1}$Mpc derives from the results of early galaxy surveys (e.g. Davis and Peebles, 1983) which found the variance of the galaxy number counts to be about unity inside spheres of that radius. A top-hat sphere of such radius contains a mass $M \sim 5 \times 10^{14} \Omega_{\rm m} {\rm M}_\odot$, typical of a moderately rich galaxy cluster. Therefore, as we shall see later, the abundance of galaxy clusters provides a direct measurement of σ_8.

The linear transfer function $T(k)$ introduced in Eq. (1.23) relates the amplitudes of sub-horizon Fourier modes in the post-recombination era to the initial conditions. In other words, it bears the (scale-dependent) imprints of the evolutionary effects described in Section 1.2.2 According to the ΛCDM model, the dominant matter component of the Universe is the CDM. Such particles decouple from the primaeval plasma when they are already non-relativistic, thus their free-streaming length[3] is too small ($\ll$ 1Mpc) to be of any cosmological relevance. The first characteristic wavenumber imprinted in the transfer function is that corresponding to the horizon size at the matter-radiation equality, $k_{\rm eq}$: during the radiation-dominated era, density perturbation inside the horizon are suppressed due to the Mészáros effect, and the structures growth can only proceed on scale larger than the equivalence one ($k < k_{\rm eq}$), beyond the causal influence of the radiation pressure. From the definition of $k_{\rm eq}$ it follows that:

$$k_{\rm eq} = \frac{2\pi a_{\rm eq}}{R_H(a_{eq})} \propto \Omega_{\rm m,0} h^2 \,. \tag{1.24}$$

Hence, increasing the matter content $\Omega_{\rm m,0}$ increases $z_{\rm eq}$ which in turn reduces the horizon size at equivalence shifting the knee of the matter power spectrum

[2]Strictly speaking the factorization $T(k,z) = T(k)D(z)$ is only possible in restricted models, such as a matter or Λ dominated Universe assuming $\delta_{\rm b} = \delta_{\rm cdm}$. More in general – e.g. in model with massive neutrinos; § 1.5.3 – the evolution of sub-horizon perturbations depends also on the wavenumber k and the transfer function $T(k,z)$ cannot be split in a scale- and time-dependent factor.

[3]The free-streaming length is the scale below which collisionless particles cannot cluster due to their high thermal velocity; see § 1.5.3.

to higher k.

On smaller scales, in the pre-recombination era, the shape of the transfer function is affected by the acoustic oscillations of the baryon-photon fluid and Silk damping. The former introduce oscillatory features in the transfer function (BAO), on k larger than that of the sound horizon at decoupling, which is about $k_{\rm s} = 2\pi(\Omega_{\rm b,0}h^2/0.02)/150\,{\rm Mpc}^{-1}$. Thus increasing the baryon content $\Omega_{\rm b,0}$ (but keeping $\Omega_{\rm m,0}$ constant) shifts the first peak to larger k and increases the amplitude of the wiggles due to the larger baryon fraction. The wavenumber at which the Silk damping is effective is related to the mean distance covered by a photon in an Hubble time , and it can be approximated by the fitting formula:

$$k_{\rm Silk} \simeq 1.6(\Omega_{\rm b,0}h^2)^{0.52}(\Omega_{\rm m,0}h^2)^{0.73}\left[1+(10.4\Omega_{\rm m,0}h^2)^{0.95}\right]{\rm Mpc}^{-1} \tag{1.25}$$

The effects of the various evolutionary processes on the transfer function and matter power spectrum along with their dependence on cosmological parameters are shown in Figure 1.2 in the *upper* and *lower* panel, respectively.

1.3.2 The halo mass function

The halo mass function (HMF), $n(M,z)$, gives the comoving number density of virialized halos with masses in the range $[M, M+{\rm d}M]$, found at redshift z. To derive this function we need to go beyond the linear regime since collapsed objects, such galaxies and clusters of galaxies, have densities orders of magnitude higher than the average density of the Universe ($\delta \gg 1$). In general, non-linear gravitational dynamics cannot be solved analytically, and computer simulations have to be used to follow the evolution in detail. However, as we will see shortly, if simple assumptions about the symmetry of the system are made it is possible to find an analytical solution, which nevertheless provides valuable insights to understand the formation process of virialized DM halos.

The top-hat spherical collapse

Let us consider a spherical perturbation of radius R at time t_i during the matter-dominated era ($\Omega_{\rm m} \simeq 1$), with constant density ρ_p inside it, such that $\delta(t_i) > 0$ and $\delta(t_i) \ll 1$. The perturbation is taken to be expanding with the background Universe, in such a way that the peculiar velocity at the edge is zero. According to the Birkhoff's theorem, given the symmetry of the system, the over-dense region can be treated as a stand-alone Universe which evolve under the local density

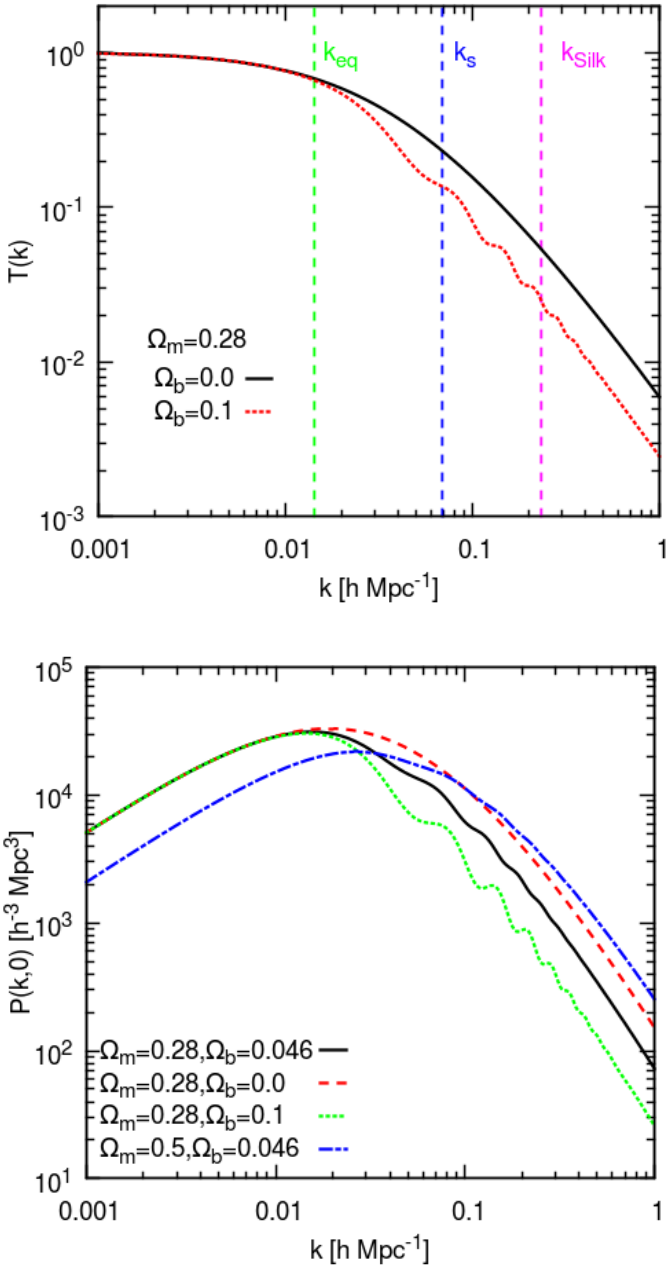

Figure 1.2: *Upper* panel: Transfer function for a model with only CDM ($\Omega_{cdm,0} = \Omega_{m,0} = 0.28$, $\Omega_{b,0} = 0$) and a model with a large amount of baryons ($\Omega_{m,0} = 0.28$, $\Omega_{b,0} = 0.1$). Also shown in the plot with vertical lines are the characteristic wavenumbers (k_{eq}, k_{Silk} and k_s) described in the text for the model with $\Omega_b = 0.1$. *Lower* panel: Dependencies of the matter power spectrum on cosmological parameters Ω_m and Ω_b, within a flat ΛCDM model. On both panels, all the unspecified cosmological parameters are set to the reference ΛCDM values provided by WMAP 9-years (Hinshaw et al., 2013). All the curves are computed using the publicly available Boltzmann code `CAMB` (Lewis et al., 2000).

parameter ρ_p. The condition for the perturbation to detach from the Hubble flow, and eventually collapse, is to have an initial density parameter $\Omega_p(t_i) = \Omega(t_i)(1 + \delta(t_i))$ larger than unity (closed Universe). In this case, the region will expand up to a maximum radius R_m at turn-around time t_m, before starting to collapse and reach thermal equilibrium supported by the velocity dispersion of DM particles. The time at which this occurs, the virialization time t_vir, is set by the virial equilibrium condition $E = K + U = -K$, with E, K and U being the total, the kinetic and the potential energy, respectively. Assuming a dissipationless collapse the energy conservation gives the relation $R_\mathrm{vir} = R_\mathrm{m}/2$ for the radius at virial equilibrium, which allows us to compute the overdensity of the perturbation at t_vir (see e.g. Borgani, 2006, for details):

$$\Delta_\mathrm{vir} = \frac{\rho_p(t_\mathrm{vir})}{\rho(t_\mathrm{vir})} \simeq 178\,. \tag{1.26}$$

This result explains why an overdensity of about 200 with respect to the background density is taken as typical value for a DM halo which has reached virial equilibrium.

On the other hand, linearly extrapolating the density contrast at t_vir, according to Eq. (1.13) yields:

$$\delta_c \equiv \delta_+(t_\mathrm{vir}) = \delta_+(t_i) D_+(t_\mathrm{vir}) \simeq 1.69\,. \tag{1.27}$$

Clearly the linear theory extrapolation significantly underestimates the overdensity at virialization, however it provides the threshold value for the density contrast within a region of the density field for it to end up in a virialized object. As will be shown in the next section, the value of δ_c characterizes the HMF as it gives the overdensity that a perturbation in the initial density field must have to end up in a virialized structure. The above derivation can be generalized to models with $\Omega_\mathrm{m} \neq 1$, for which, for a reasonable range of Ω_m values, the quantity δ_c remains almost unvaried.

The Press & Schechter approach

Now I will derive an analytical expression for the HMF following the approach originally devised by Press and Schechter (1974). Consider the overdensity field linearly extrapolated to the present time t_0: $\delta_0(\boldsymbol{x}) \equiv \delta(x, t_0) = \delta(\mathbf{x}, t)/D(t)$, where $\delta(\mathbf{x}, t)$ is the overdensity field at an arbitrary $t < t_0$ and $D(t)$ is the linear growth rate normalized to unity at present time. According to the spherical collapse model

described earlier, regions of the density field with $\delta_0(\mathbf{x})$ larger than $\delta_c(t) = \delta_c/D(t)$, or equivalently with $\delta(\boldsymbol{x}, t) > \delta_c \sim 1.69$, will have collapsed to form virialized objects. In order to assign a mass to the collapsed regions let us consider the density field smoothed on mass scale M:

$$\delta_S(\mathbf{x}; M) \equiv \int \delta_0(\mathbf{x}')W(\mathbf{x} + \mathbf{x}'; R)\mathrm{d}\mathbf{x}, \tag{1.28}$$

where the relation between smoothing radius R and mass M depends on the shape of the window function $W(\mathbf{X}, R)$ (e.g. for a spherical top-hat filter, $M = 4\pi/3\bar{\rho}R^3$). The ansatz of the Press & Schechter (PS) formalism states that the fraction of mass elements that at time t will form halos with mass larger than M, $F(> M)$, is equal to the probability that $\delta_S(\mathbf{x}; M) > \delta_c(t)$. In other words, the fraction of matter ending up in collapsed objects with mass above M, by time t, is equal to the fraction of the initial density field smoothed on the mass–scale M, $\delta_S(\mathbf{x}; M)$, lying at an overdensity exceeding the critical threshold $\delta_c(t)$. Assuming $\delta_0(\mathbf{x})$ to be a Gaussian random field, the probability for the linearly-evolved smoothed filed $\delta_S(\mathbf{x}; M)$ to exceed the threshold $\delta_c(t)$ reads:

$$\begin{aligned} \mathscr{P}[\delta_S(M) > \delta_c(t)] = F(> M) &= \frac{1}{\sqrt{2\pi}\sigma(M)} \int_{\delta_c(t)}^{\infty} \exp\left[-\frac{\delta_S^2}{2\sigma^2(M)}\right] \mathrm{d}\delta_s \\ &= \frac{1}{2}\mathtt{erfc}\left[\frac{\delta_c(t)}{\sqrt{2}\sigma(M)}\right], \end{aligned} \tag{1.29}$$

with $\sigma(M)^2 = \langle\delta_S^2(\mathbf{x}; M)\rangle = \sigma^2(R = (M/\bar{\rho})^{1/3})$ (see Eq. (1.22)), and $\mathtt{erfc}$ the complementary error function. In principle, taking the limit of $M \to 0$ – that is, considering objects of arbitrary small mass – one would expect to recover the whole mass content of the Universe. However, computing this limit one gets $\mathscr{P}[\delta_S(M \to 0) > \delta_c(t)] \to 1/2$, which means that only half of the mass of the Universe is contained in collapsed objects of any mass. This result shows a fundamental limit of the PS approach. Basically this is due to fact that, in this derivation, one gives a null probability for a point with $\delta_S(\mathbf{x}; M) < \delta_c(t)$ to overcome δ_c for some larger filtering scale $M' > M$. However, underdense regions can be enclosed within larger overdense regions, giving them a finite probability to end up in collapsed objects of larger mass. Bond et al. (1991) provided a more rigorous derivation of the HMF, which correctly accounts for the missing factor 2, at least for the particular choice of a sharp-k filter. Including ad hoc in the PS ansatz the "fudge factor" 2,

$F(>M) = 2\mathscr{P}[\delta_S(M) > \delta_c(t)]$, the HMF reads:

$$\begin{aligned} n(M,t)\mathrm{d}M &= \frac{\bar{\rho}}{M}\frac{\partial F(>M)}{\partial M}\mathrm{d}M = 2\frac{\bar{\rho}}{M}\frac{\partial \mathscr{P}[\delta_S(M) > \delta_c(t)]}{\partial \sigma_M}\left|\frac{\mathrm{d}\sigma_M}{\mathrm{d}M}\right|\mathrm{d}M \\ &= \sqrt{\frac{2}{\pi}}\frac{\bar{\rho}}{M^2}\frac{\delta_c(t)}{\sigma_M}\exp\left[-\frac{\delta_c(t)^2}{2\sigma_M^2}\right]\left|\frac{\mathrm{d}\ln\sigma_M}{\mathrm{d}\ln M}\right|\mathrm{d}M, \end{aligned} \tag{1.30}$$

where the fraction of volume in objects with mass in the range $[M : M + \mathrm{d}M]$, $[\partial F(>M)/\partial M]\mathrm{d}M$, has been divided by the volume occupied by each halo, $V_M = M/\bar{\rho}$, in order to get the number density of such objects.

From Eq. (1.30) one can get insight on the non-linear structure formation in a hierarchical model. Indeed, from the exponential term in Eq. (1.30) it follows that only halos with $M \lesssim M^*(t)$, with $M^*(t)$ defined such that $\sigma_{M^*} = \delta_c(t) = \delta_c/D(t)$, can have formed in significant number at time t. Hence, given that $D(t)$ increases with time and σ_M decreases with mass, as time goes by $M^*(t)$ increases, and more and more massive halos can start to form. Taking Eq. (1.30) in the limit of massive objects (i.e. rich galaxy clusters) the exponential term dominates the shape of the HMF. This explain the exponential sensitivity of HMF to the cosmological parameters mentioned throughout this Chapter (Ω_m, Ω_Λ, σ_8, H_0, n_s) which enter through σ_M and its dependence on the power spectrum (Eq. (1.22)), through the linear growth factor $D(t)$ (Eq. (1.13)), and, to a lesser extent, through δ_c. In particular, the power spectrum normalization σ_8 and the matter density Ω_m – due to their influence on the amplitude of the power spectrum at cluster scale and linear grow factor – are the two parameters which mainly affect the amplitude and the shape of the HMF. This is displayed in Figure 1.3, which shows the sensitivity of the cumulative HMF, $n(M > 5\times10^{14}\mathrm{M}_\odot, \mathrm{z})$, to the two parameters. A larger value of σ_8 increases the amplitude of the mass fluctuations at a given scale causing the structures to start to form at earlier time (compare *orange*, *black* and *red* curves). While, increasing Ω_m reduces the time during which $\Omega_\mathrm{m} \ll 1$ and the perturbations cannot grow, boosting the overall mass function to higher values (compare *cyan*, *black* and *blue* curves).

Numerical calibration of the HMF

After the pioneering work of PS, many authors attempted to improve and refine their analysis. In particular in the last decades, thanks to the ever increasing computational power available, N-body simulations became the standard tool to study the structure formation in non-linear regime, and thus the HMF. The functional

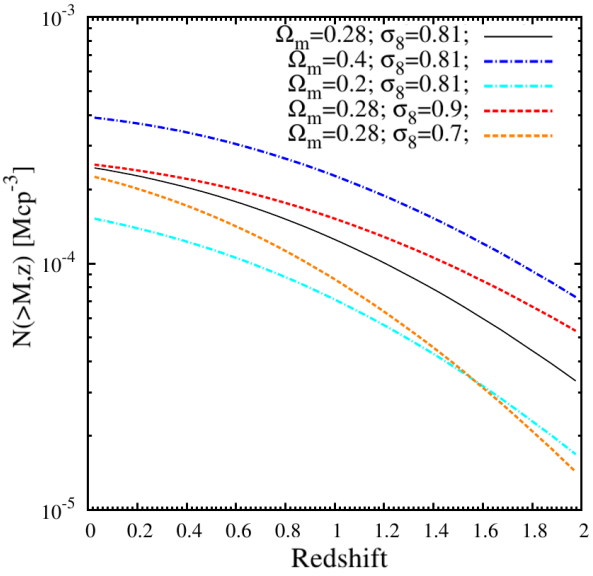

Figure 1.3: Cumulative HMF mass function for halos with $M > 5 \times 10^{14} M_\odot$ between redshift 0 and 2, for different combination of the parameters σ_8 and Ω_m within a ΛCDM model . Figure from Sartoris (2012).

form usually adopted to describe the HMF calibrated against N-body simulation is:

$$n(M,z) = \frac{\rho}{M} f(\sigma_M, z) \frac{\mathrm{d} \ln \sigma_M^{-1}}{\mathrm{d}M} . \tag{1.31}$$

Using this definition, it follows from Eq. (1.30) that the PS expression is recovered by setting:

$$f_{\mathrm{PS}}(\sigma_M, z) = \frac{2}{\pi} \frac{\delta_c(t)}{\sigma_M} \exp\left[-\frac{\delta_c(t)^2}{2\sigma_M^2} \right] \tag{1.32}$$

A crucial aspect in the calibration of the HMF is related to the algorithm used to identify the halos, the two most widely used being the "Friend of Friend" (FoF)[4] and the "Spherical Overdensity" (SO)[5] one. In the latter case the mass of the halo

[4]The FoF algorithm considers two particles in the simulation to be members of the same group (i.e., "friends"), if they are separated by a distance that is less than a given linking length. Friends of friends are considered to be members of a single group – the condition that gives the algorithm its name.

[5]The SO algorithm defines the boundary of a halo as a sphere of radius enclosing a given density contrast Δ with respect to a reference background density. To be defined an SO halo also requires a

is given by:

$$M_{\Delta_{c/m}} = \frac{4}{3}\pi R^3_{\Delta_{c/m}} \Delta_{c/m} \rho_{c/m}(z)\,, \tag{1.33}$$

the mass contained in a sphere of radius $R_{\Delta_{c/m}}$ encompassing an average density equal to $\Delta_{c/m}$ times the critical (subscript c) or mean (subscript m) density at a given redshift.

Incorporating the effect of non-spherical collapse, Sheth and Tormen (1999) generalized the PS expression to:

$$f(\sigma_m, z) = \sqrt{\frac{2 \cdot 0.707}{\pi}} 0.3222 \left[1 + \left(\frac{\sigma_M^2}{a\delta_c^2}\right)^{0.3}\right] \frac{\delta_c}{\sigma_M} \exp\left[-\frac{a\delta_c^2}{2\sigma_M^2}\right] \tag{1.34}$$

where the best-fitting values (0.707, 0.3) have been obtained using the results of N-body simulations, in which the halos were identified using a SO algorithm, and their masses computed within a radius encompassing a mean overdensity equal to the virial one, $\Delta_{\rm vir}$. Jenkins et al. (2001), looking for an universal form of the HMF – universal in the sense that the same functional form and parameters hold for different cosmologies and redshifts – proposed a different expression for $f(\sigma_M, z)$:

$$f(\sigma_M, z) = 0.315 \exp(-|\ln \sigma_M^{-1} + 0.61|^{3.8}), \tag{1.35}$$

obtained as the best-fit to the results of a set of simulations covering a wide dynamical range. Subsequent works analysed the accuracy of Eq. (1.35) (e.g. Evrard et al., 2002; White, 2002; Springel et al., 2005; Warren et al., 2006) in reproducing numerical results, also discussing its universality for generic cosmologies, and stressing the role of different algorithms used to identify the halos and to compute their mass. More recently, many authors turned their attention on the evolution of the HMF with redshift (e.g Reed et al., 2003, 2007; Lukić et al., 2007; Cohn and White, 2008) or on the effects of baryonic feedback processes (e.g. Rudd et al., 2008; Stanek et al., 2009). In particular, Tinker et al. (2008) studying the limits of universality of the HMF provided the following formula:

$$f(\sigma) = A \left[\left(\frac{\sigma}{b}\right)^{-a} + 1\right] e^{-c/\sigma^2} \tag{1.36}$$

where the values of fitting parameters (A, a, b, c) depend on the density threshold used to define the mass, Δ_m (see Table 2 in Tinker et al., 2008)). Also, to keep

definition of the halo centre. The common choices for the centre in theoretical analyses are the peak of density, the minimum of the potential, the position of the most bound particle, or, more rarely, the centre of mass.

a statistical precision of 5% up to redshift 2.5, the authors introduced a redshift dependence into the fitting parameters of Eq. (1.36). Figure 1.4 shown the accuracy of the Tinker fitting function (1.36) in reproducing the simulations results between redshift $z = 0$ and $z = 2.5$

Still today, the large number of ongoing (Planck, SPT, DES) and upcoming (eROSITA, LSST, Euclid) cluster surveys prompts the research in this field. In particular, in the last few years, many works have been presented on the dependencies of the HMF on cosmological parameters beyond the ΛCDM ones – e.g. massive neutrino (Brandbyge et al., 2010b; Marulli et al., 2011; Ichiki and Takada, 2012; Villaescusa-Navarro et al., 2013), dark energy equation of state, non-Gaussianity (Grossi et al., 2007; Dalal et al., 2008) – and on the effects of baryonic feedback processes on the halo mass distribution, and thus, on the HMF itself (e.g. Cusworth et al., 2014; Velliscig et al., 2014; Vogelsberger et al., 2014; Martizzi et al., 2014; Cui et al., 2014). Forecast analyses for next future cluster surveys indicate that an accuracy of $\lesssim 5\%$ in the HMF calibration will be needed to fully exploit the cosmological information carried by such surveys.

1.4 Halo-mass bias

Dark matter halos, arising from the high-density peaks of the initial matter distribution, are expected to be biased tracer of the underlying matter fluctuations. This means that the fluctuations in number density of DM halos in a given volume of the Universe, $\delta_h = n(M)/\bar{n}(M) - 1$, and that of the underlying matter density in the same volume, $\delta_s(M)$, are different. The relationship between δ_h and δ_m is called the halo-mass bias, and can be defined as:

$$b^2 = \frac{P_h(k)}{P_{\rm lin}(k)}\,, \tag{1.37}$$

i.e. as the ratio of the halo power spectrum to the linear matter power spectrum.

A first attempt to model analytically the halo-mass bias has been made by Mo and White (1996). Using the spherical collapse model (PS formalism) and the pick-background split approximation (Bond et al., 1991) the authors derived the equation:

$$b(\nu) = 1 + \frac{\nu^2 - 1}{\delta_c} \tag{1.38}$$

with $\nu = \delta_c/\sigma_M$. Recalling the characteristic mass M^* defined above, one can see that halos whit $M > M^*$ are biased ($\delta_h > \delta_s(M)$), while halos with $M < M^*$ are

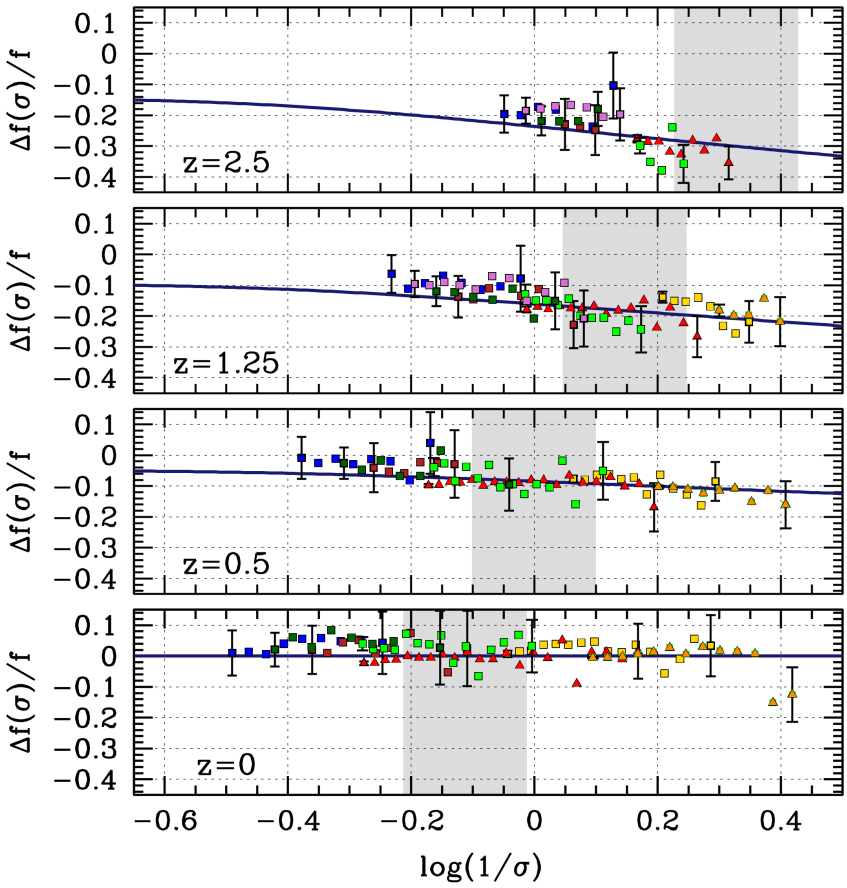

Figure 1.4: Residuals of the $z = 0$ Tinker mass function for $\Delta = 200$ with respect to the HMF measured from simulations at $z = 0$, $z = 0.5$, $z = 1.25$ and $z = 2.5$. The *solid* lines have been obtained using Eq.(1.36) and considering the redshift evolution of the fitting parameters. Error bars are shown only for the first and last points of each simulation. The shaded regions bracket the mass range $10^{13}h^{-1}M_{\odot} - 10^{14}h^{-1}M_{\odot}$. Figure from Tinker et al. (2008).

anti-biased ($\delta_h < \delta_s(M)$), relative to the mass density field. Moreover, since M^* increases with time the halo-mass bias increases with redshift at fixed mass (see Figure 1.5).

However, this equation in not able to reproduce the relation found in simulations, in particular in the low-mass end (e.g. Jing, 1998; Sheth and Tormen, 1999);

as in the PS formalism the Mo and White (1996) derivation assumes an unrealistic spherical collapse model. More rigorous (and physically-motivated) derivations of the halo-mass bias have been proposed, for instance, assuming an ellipsoidal collapse model (Sheth et al., 2001)), or fitting the relation against N-body simulations, as the one suggested by Tinker et al. (2010):

$$b(\nu) = 1 - A\frac{\nu^a}{\nu^a + \delta_c^a} + B\nu^b + C\nu^c\,, \tag{1.39}$$

where the value of the six parameters (A, a, B, b, C, c) depends on the value of the overdensity Δ_m chosen to measure the mass. In the *left* panel of Figure 1.5 are shown the bias functions proposed by Mo and White (1996), Sheth et al. (2001) and Tinker et al. (2010) as a function of ν, in comparison with the results of N-body simulations (coloured points), along with their residual with respect to the fitting function of Tinker (*lower* panel). In the *right* panel of Figure 1.5 the Tinker et al. (2010) halo-mass bias is shown as a function of mass for different redshifts. In the mass range typical of clusters, $\sim 10^{13} - 10^{15} h^{-1} M_\odot$, the overdensity of halos is always larger than that of the underlying matter ($b > 1$).

1.5 Massive neutrinos

In the previous sections, the evolution of the Universe and the structure formation history in the framework of the ΛCDM model have been described. However, nowadays there exist compelling evidences from neutrino oscillation experiments that neutrinos are massive particles. Depending on their masses cosmic neutrinos make up a different fraction of the dark matter of the Universe, affecting both the background evolution and growth of structure. In this section I will briefly review the neutrino physics and the effects that massive neutrinos have on the cosmic evolution and their impact on the cosmological observables described so far.

1.5.1 Neutrinos thermal history

A standard prediction of the hot big bang model is the existence of a relic sea of neutrinos, with a number density slightly below that of CMB photons. Produced in the early Universe by frequent weak interactions, neutrinos were kept in thermal equilibrium – with a Fermi-Dirac momentum spectrum – with the primaeval plasma until the rate of interactions falls below the expansion rate of the Universe at $T_{\rm dec} \simeq 2 - 4$MeV. After decoupling, the neutrino momenta and temperature scale

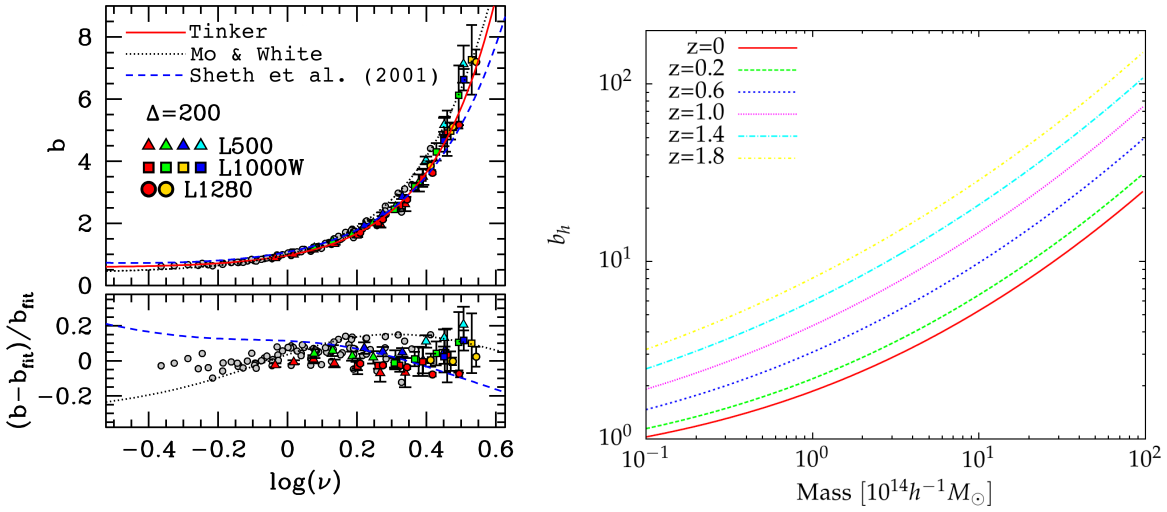

Figure 1.5: *Left* panel: Comparison between the halo-mass bias relations proposed by Mo and White (1996), Sheth et al. (2001) and Tinker et al. (2010) as a function of ν. Each point type indicates the results of a different simulation, and their colour, from left to right, go in order of increasing redshift from $z = 0$ to $z = 2.5$. In the bottom panel are shown the residual of the bias functions of Mo and White (1996) and Sheth et al. (2001), along with N-body simulations results, with respect to the fitting formula of Tinker et al. (2010). Figure from Tinker et al. (2010). *Right* panel: Halo-mass bias of Tinker et al. (2010), for $\Delta_m = 200$, as a function of the mass. Different curves correspond to different redshifts; from bottom to top: $z = 0, 0.2, 0.6, 1.0, 1.4, 1.8$.

identically with the expansion of the Universe, preserving their Fermi-Dirac spectrum. Due to the smallness of neutrino masses, $\lesssim 1\,\mathrm{eV}$ (see later), they were ultra-relativistic at $T_{\rm dec}$ and became non-relativistic only after recombination. Shortly after neutrino decoupling the plasma temperature drops below the electron mass favouring the $e^{\pm}$ annihilation into photons. The energy exchanged during these processes heats the photon gas but not the neutrinos which are assumed to be already completely decoupled. This settles the ratio of the photon to neutrino temperature after $e^{\pm}$ pairs disappearance to $T_\gamma/T_\nu = (11/4)^{1/3} \simeq 1.40102$. Once the neutrino temperature and spectrum are known, it is possible to compute the present day neutrino number density:

$$n_\nu = \frac{3}{11} n_\gamma = \frac{6\zeta(3)}{11\pi^2} T_\gamma^3, \tag{1.40}$$

which leads to $n_\nu = 113\text{cm}^{-1}$ for neutrinos and antineutrinos of each flavour. As for the neutrino energy density, in the relativistic and non-relativistic limit, it reads:

$$\begin{aligned}\rho_\nu(m_\nu \ll T_\nu) &= \frac{7\pi^2}{120}\left(\frac{4}{11}\right)^{\frac{4}{3}} T_\gamma^4 \\ \rho_\nu(m_\nu \gg T_\nu) &= m_\nu n_\nu\,,\end{aligned} \tag{1.41}$$

respectively. When relativistic, neutrinos contribute to the radiation energy density, while, after the non-relativistic transition, they contribute to the matter energy density. In the latter stage the energy density is a function of the masses of the neutrino species for which $m_{\nu,i} \gg T_\nu$. Their contribution to the radiation energy content is usually parametrized in terms of the effective number of neutrinos, N_{eff}, through the relation:

$$\rho_r = \rho_\gamma + \rho_\nu = \left[1 + \frac{7}{8}\left(\frac{4}{11}\right)^{4/3} N_{\text{eff}}\right]\rho_\gamma\,, \tag{1.42}$$

where the present value of the photon energy density, ρ_γ, is known from the measurement of the CMB temperature. The standard value for the effective number of neutrino is $N_{\text{eff}} = 3.046$, where three is the number of neutrinos sensitive to the weak interaction ($N_\nu^{\text{active}} = 2.9840 \pm 0.082$; The ALEPH Collaboration et al., 2005), and 0.046 accounts for a non-instantaneous decoupling process and flavour oscillation effects (Mangano et al., 2005). Any departure of N_{eff} from this value could indicate the presence of new physics beyond the standard model; adding an extra (thermalized) light fermion would contribute $\Delta N_{\text{eff}} = N_{\text{eff}} - 3.046 = 1$ (see later § 1.5.5), but more generally a non-integer ΔN_{eff} value could arise from different physics, such as lepton asymmetries (Hannestad et al., 2012), partial thermalisation of new fermions (Melchiorri et al., 2009), particle decay (Palomares-Ruiz et al., 2005), non-thermal production of dark matter (Hooper et al., 2012), gravity waves (Smith et al., 2006) or early dark energy (Calabrese et al., 2011).

Observationally, a first allowed range for N_{eff} is given by the comparison of the primordial abundances of light elements – in particular ^{4}He – predicted by the big bang nucleosynthesis (BBN) and experimental data. Basically, N_{eff} fix the expansion rate at BBN through its contribution to the radiation energy content. This in turn affects the freezing temperature of the neutron-to-proton ratio, thus changing the ^{4}He abundance. Recent measurements of primordial abundances constrain the extra radiation to $\Delta N_{\text{eff}} \lesssim 1$ at 2σ (Izotov et al., 2013; Cooke et al., 2014).

In addition, as will be shown later, independent constraints on $N_{\rm eff}$ at later epochs can be extracted from CMB observables, and to a lower extend, from observations of the LSS.

1.5.2 Neutrinos as dark matter

Provided that neutrinos are massive particles, they will contribute to the matter content of the Universe. Their present energy density in units of the critical value is:

$$\Omega_\nu = \frac{\rho_\nu}{\rho_c} = \frac{\sum m_\nu}{94.57 h^2 \mathrm{eV}}\,, \tag{1.43}$$

where $\sum m_\nu$ includes the masses of all neutrino species which are non-relativistic today. Oscillation experiments provide us measures of the mass-squared difference between massive species. Recent experiments, using solar and atmospheric neutrinos, quantified these difference as: $\Delta m^2_{12} = 7.5 \times 10^{-5}\,\mathrm{eV}^2$ and $|\Delta m^2_{23}| = 2.3 \times 10^{-3}\,\mathrm{eV}^2$ (e.g. Fogli et al., 2012; Forero et al., 2012). This means that at least two neutrino species are non-relativistic today, since both $(m^2_{12})^{1/2}$ and $|\Delta m^2_{23}|^{1/2}$ are larger than present neutrino temperature, $T_{\nu,0} = 1.95K \simeq 1.7 \times 10^{-4}\,\mathrm{eV}$. Unfortunately these experiments are insensitive to the absolute neutrino mass scale, and, depending on the sign of $|\Delta m^2_{23}|$, two mass spectra are possible: the normal mass hierarchy ($m_1 < m_2 < m_3$) for $\Delta m^2_{23} > 0$, and the inverted mass hierarchy (m_3, m_1, m_2) for $\Delta m^2_{23} < 0$. There exist two kind of laboratory experiments which are able to detect the absolute scale of neutrino masses. One type of experiment exploits the neutrinoless double beta decay, $(Z, A) \rightarrow (Z+2, A) + 2e^-$, a rare nuclear process where the lepton number conservation is violated, and that can occur if neutrinos are Majorana particles. The other kind of experiment searches for the kinematic signature of massive neutrino in ordinary beta decay, $n \rightarrow p + e + \bar{\nu}_e$. Combining the current limits from tritium beta decay experiments (e.g. $m_\nu < 2.3\,\mathrm{eV}$ at 95%C.L. Kraus et al., 2005), and the minimal neutrino mass allowed by oscillation experiments, the sum of the masses of the three active species is constrained in the range:

$$0.056\,(0.095)\,\mathrm{eV} \lesssim \sum_i m_i \lesssim 6\,\mathrm{eV}\,,$$

or, in terms of the energy density parameter:

$$0.0013\,(0.0022)\,\mathrm{eV} \lesssim \Omega_\nu \lesssim 0.13 \quad \text{with} \quad h \simeq 0.7$$

where the value of the lower limits is for a normal (inverted) hierarchy. As we will see shortly, cosmological data allow us to put stronger constraints on $\sum m_\nu$ thanks

to the mass-dependent imprints that neutrinos leave on cosmological observables.

1.5.3 Effects of massive neutrino on cosmology

Neutrino free-streaming

After decoupling, because of their large random velocities and collisionless nature, neutrinos can diffuse, leading to damping of density fluctuations on small scales. The proper length below which the damping effect becomes important, called free-streaming length, depends on the typical distance travelled by neutrinos in a time t after decoupling. In analogy with the definition of Jeans length (see §1.2.1 and Eq. (1.11)), we can define the neutrino free-streaming length (wavenumber) as:

$$\lambda_{fs}(t) = 2\pi\frac{a(t)}{k_{fs}(t)} = 2\pi\sqrt{\frac{2}{3}}\frac{v_{\rm th}(t)}{H(t)}\,, \qquad k_{fs}(t) = \left(\frac{4\pi G\bar{\rho}(t)a^2(t)}{v_{\rm th}^2(t)}\right)^{1/2}\,, \tag{1.44}$$

exploiting that their characteristic velocity, on average, is given by the thermal velocity $v_{\rm th}$. When neutrinos are relativistic, they travel at the speed of light and their free-streaming length is equal to the Hubble radius. After the non-relativistic transition, their thermal velocity scale as:

$$v_{\rm th} \equiv \frac{\langle p\rangle}{m_\nu} \simeq \frac{3.15T_\nu}{m_\nu} = \frac{3.15T_{\nu,0}}{m_\nu}\left(\frac{a_0}{a}\right) \simeq 158(1+z)\left(\frac{1{\rm eV}}{m_\nu}\right){\rm km\ s^{-1}}. \tag{1.45}$$

Including this relation in Eq. (1.44), the evolution of the neutrino free-streaming wavenumber in the matter or Λ dominated era reads:

$$k_{fs}(t) = 0.82\frac{\sqrt{\Omega_{\Lambda,0}+\Omega_{{\rm m},0}(1+z)^3}}{(1+z)^2}\left(\frac{m_\nu}{1{\rm eV}}\right)h\,{\rm Mpc^{-1}}. \tag{1.46}$$

Therefore, after the non-relativistic transition in the matter dominated era, for which $a_{\rm MD} \propto t^{2/3}$, the comoving free-streaming length decreases like $\lambda_{fs}/a \propto v_{\rm th}/(aH) \propto (a^2H)^{-1} \propto t^{-1/3}$. This implies that, for neutrinos becoming non-relativistic in the matter-dominated era, the comoving free-streaming wavenumber pass trough a minimum, $k_{\rm nr}$, at the time of the non-relativistic transition ($\langle p\rangle = 3.15T_\nu = m_\nu$):

$$k_{\rm nr} \simeq 0.018\Omega_{{\rm m},0}^{1/2}\left(\frac{m_\nu}{1{\rm eV}}\right)h{\rm Mpc^{-1}}. \tag{1.47}$$

Figure 1.6 shows the evolution of the comoving k_{fs} and horizon scale as a function of the scale factor for a model with $\sum m_\nu = 1.2\,{\rm eV}$. Modes inside the shaded area

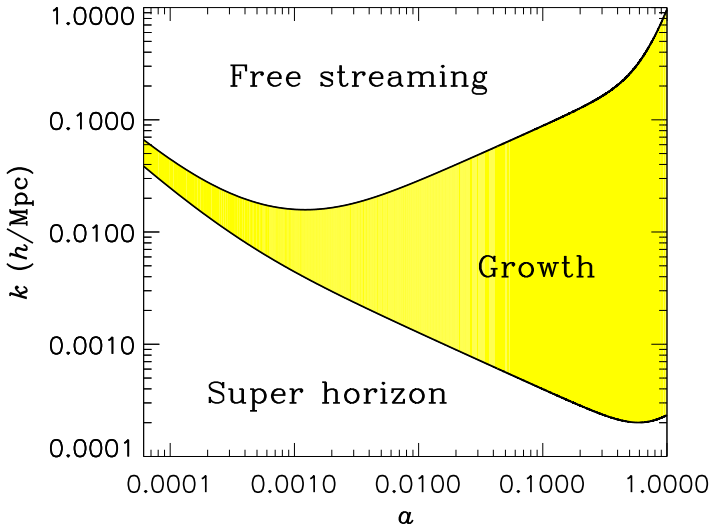

Figure 1.6: Evolution of the of the comoving k_{fs} (*top* curve) and horizon scale (*bottom* curve) as a function of the scale factor for a model with $\sum m_\nu = 1.2\,\mathrm{eV}$. Adapted from Shoji and Komatsu (2010).

can grow, being inside the horizon and on scale larger than the free-streaming length. Note that passed the point of minimum, $k_{\rm nr}$, the thermal velocity decreases with the scale factor, and the number of modes that can grow increases. On scale much larger than the free-streaming length ($k \ll k_{fs}$) the neutrino velocity can be considered as vanishing, and after the non-relativistic transition the neutrinos perturbation grow like those of CDM, as described in §1.2. In particular, modes with $k < k_{\rm nr}$ never experience the free-streaming damping, and evolve like in a pure ΛCDM model.

Signature of massive neutrinos on the matter power spectrum

We discuss now the difference between the power spectra computed in a cosmology with massless and three degenerate massive neutrinos, at fixed values of the other cosmological parameters.

We have seen that on large scales ($k \ll k_{\rm nr}$), the neutrino free-streaming can be always ignored, and the neutrino perturbations δ_ν evolve like that of CDM, which in the matter-dominated era grow as $\delta_{\rm cdm} \propto a$. Thus, if we vary Ω_ν keeping fixed $\Omega_{\rm m}$, the large-scale power spectrum remains unchanged.

Instead, for $k > k_{\rm nr}$ and $k > k_{\rm eq}$, the matter power spectrum in the presence

of massive neutrinos varies for different reasons. Firstly, since $\sim 1\,\mathrm{eV}$ neutrinos become non-relativistic after recombination, the matter-radiation equivalence occurs at different times. Defining the neutrino energy fraction $f_\nu = \Omega_\nu/\Omega_\mathrm{m}$, it turns out that the equivalence in presence of massive neutrino is delayed by $a_\mathrm{eq}^{f_\nu} = a_\mathrm{eq}^{f_\nu=0}/(1-f_\nu)^6$. Thus, the time during which matter perturbation can grow is shorter if $\Omega_\nu \neq 0$ (see §1.2).

Secondly, the neutrino perturbations do not contribute to the gravitational clustering below the free-streaming scale, so that, the neutrino component can be omitted from the Poisson equation (Eq. (1.8)). On the other side, they do contribute with their energy density to the expansion rate through the Friedmann equation (Eq. (1.3)). The net effect is a slowdown on such scales of the growth rate of CDM and baryon perturbations at late times. It can be proved that for $f_\nu \ll 1$, on scale $k \gg k_{fs}$ in the matter dominated era, the CDM perturbations grow like $\delta_\mathrm{cdm} \propto a^{1-3f_\nu/5}$ (see e.g. Lesgourgues and Pastor, 2006, for details). This last effect, rather than the damping of δ_ν, has the largest impact on the suppression of the matter power spectrum. At redshift $z \simeq 0$, the step like suppression of the power spectrum starts at $k \gtrsim k_\mathrm{nr}$, and saturates at $k \sim 1h\mathrm{Mpc}^{-1}$ to the value $P(k)^{f_\nu}/P(k)^{f_\nu=0} = 1-8f_\nu$ in the linear approximation (Hu et al., 1998) and reaches $P(k)^{f_\nu}/P(k)^{f_\nu=0} \simeq 1-10f_\nu$ taking into account non-linear effects (e.g. Brandbyge et al., 2010a; Viel et al., 2010). Therefore, a feature introduced by massive neutrinos is the scale dependence of the growth factor $D_+ = D(z,k)$. For a pure ΛCDM model, the shape of the matter power spectrum is fixed after the recombination era ($D_+ = D(z)$, Eq. (1.13)). In the presence of massive neutrinos, instead, the evolution of perturbations depends on the scale, making the shape of the matter power spectrum redshift dependent.

Figure 1.7 shows in the *left* panel the step-like suppression induced on the matter power spectrum by different values of $\sum m_\nu$, while in the *right* panel the scale dependence of the growth factor for two models with $\Omega_\nu = 0.02$ and $\Omega_\nu = 0.01$, respectively.

So far, we discussed the effects of the variation of $\sum m_\nu$ – or equivalently Ω_ν – on the matter power spectrum. In principle, the position, k_nr, and the size of the step-like suppression induced by each massive species in $P(k,z)$, have a small dependence on individual neutrino masses. However, the difference induced by a different mass-splitting scheme is so tiny that even for the most ambitious future surveys their detection is expected to be problematic (Lesgourgues et al., 2004;

[6] As will be explained later in §2.1, this effect is especially relevant to constrain neutrino properties with the CMB power spectrum.

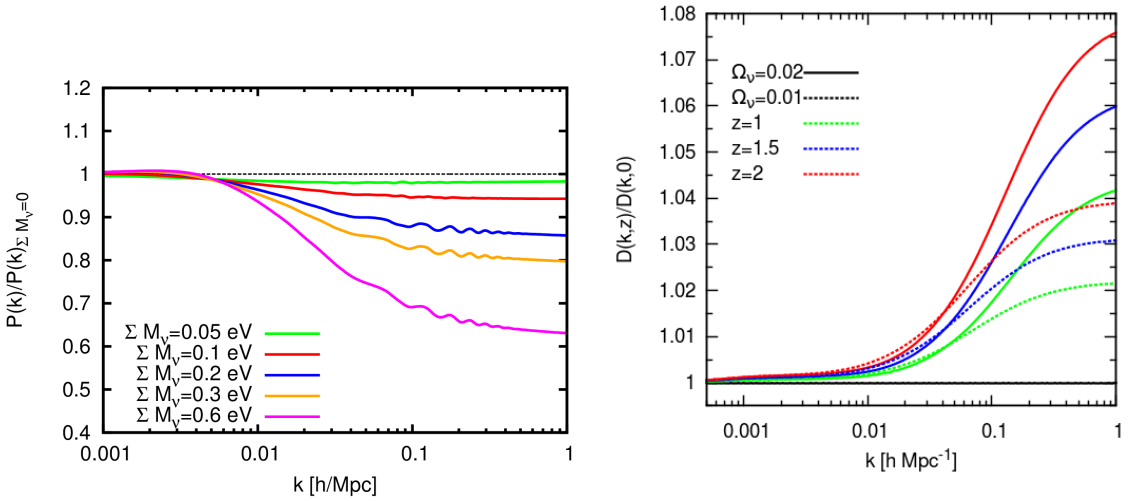

Figure 1.7: *Left* Panel: Ratio of the linear matter power spectrum at $z = 0$ for a cosmology with three degenerate massive neutrinos to that with massless neutrinos for different values of $\sum m_\nu$. *Right* Panel: Scale dependence of the linear growth factor. The curves have been obtained after normalizing $D(k, z)$ to $D(k \ll 0.001, z = 0)$. Solid (Dashed) curves correspond to a model with $\Omega_\nu = 0.02$ ($\Omega_\nu = 0.01$). The different colours are for: $z = 1$ (*green*), $z = 1.5$ (*blue*) and $z = 2$ (*red*). In both panels the curves have been computed using the Boltzmann code `CAMB` (Lewis et al., 2000).

Pritchard and Pierpaoli, 2008; Jimenez et al., 2010).

Similar effects of suppression, due to massive neutrinos are expected for the HMF, which we recall depends upon the power spectrum through σ_M (Eqs. (1.31) and (1.22)). Simply computing the HMF with one of the relation proposed in §1.3.2, the number of halos predicted is lower for larger neutrino mass, and the suppression is more pronounced in the exponential tail. The effect is due to the loss of power in the matter fluctuations which shifts the characteristic mass M^* at a given redshift to lower values (see §1.3.2). However, a naive application of these equations is not sufficient to recover an accurate HMF in cosmologies with non-vanishing neutrino masses. We will see later in Chapter 4 which prescription has to be used for the HMF to be in percent agreement with N-body simulations with $\sum m_\nu \neq 0$.

1.5.4 Current constraints on $\sum m_\nu$

Thanks to the effects that massive neutrinos have on the background evolution and structure formation, their signature can be detected in many observables of the

LSS, as well as of the CMB. As for the latter, for masses smaller than $\sim 0.6\,\mathrm{eV}$ neutrinos are still relativistic at recombination, and the effect of $\sum m_\nu \neq 0$ can appear only at the level of background evolution and secondary anisotropies. The two main physical effects that allow to bound $\sum m_\nu$ from CMB data are the early-ISW effect, which induces a dip in the CMB spectrum around $50 < \ell < 200$, and the lensing effect, which smooths the temperature power spectrum at $\ell > 1000$. The best measurement of CMB temperature anisotropies comes from the first release of the Planck satellite (Planck Collaboration, 2013d) which gives $\sum m_\nu < 0.66$ eV (95%CL) in combination with data from the high-resolution ($\ell > 2500$) CMB experiments ACT (Das et al., 2014) and SPT (Reichardt et al., 2012) (hereafter HighL), and from WMAP E-type polarization (Bennett et al., 2013) (hereafter WP), for a ΛCDM $+\sum m_\nu$ model. The capability of CMB data to constrain $\sum m_\nu$ is hampered by the degeneracy with Ω_Λ (or the derived H_0). Late-time geometric measurements, such as BAO scale or direct H_0 measurements, could help in reducing this degeneracy. Combining Planck+WP+HighL data with the latest BAO measurements from BOSS DR11 (Beutler et al., 2013), Giusarma et al. (2014) obtained the upper limit $\sum m_\nu < 0.25$ eV. Including also H_0 measurements from HST (Riess et al., 2011) the error further decreases to $\sum m_\nu < 0.22$ eV. However, it is worth to mention that the tension between Planck CMB and HST results, $H_0^{Planck} = 67.3 \pm 2.54\,\mathrm{km\,s^{-1}Mpc^{-1}}$ and $H_0^{HST} = 73.8 \pm 4.8\,\mathrm{km\,s^{-1}Mpc^{-1}}$, could lead to biased results. Finally, LSS datasets, probing the amplitude and evolution of matter fluctuations at low redshift, should provide even stronger constraints on $\sum m_\nu$ in combination with Planck. However, this is not the case since many probes of the low-redshift Universe seem to prefer a non-zero neutrino mass at odds with Planck data. In particular, the low σ_8 value derived form galaxy shear power spectrum (Heymans et al., 2013) , galaxy-galaxy lensing (Mandelbaum et al., 2013), redshift space distortion (RSD) (Beutler et al., 2013) and clusters abundance (Vikhlinin et al., 2009b; Rozo et al., 2010; Allen et al., 2011; Planck Collaboration, 2013a), could be interpreted as the effect of neutrinos with a total mass of $\sum m_\nu \simeq 0.3 - 0.4\,\mathrm{eV}$. For instance, Beutler et al. (2014) combining Planck temperature and lensing power spectra with BAO scale and RSD measurements, shear power spectrum and galaxy-galaxy lensing, found a $\geq 2\sigma$ preference for massive neutrinos, namely: $\sum m_\nu = 0.24 \pm 0.20$ eV (95%). Otherwise, the tension between CMB and LSS data can be driven by some systematics not properly taken into account in the analyses. I will come back to this point in Chapter 5, where a detailed analysis of the CMB data in combination with low-redshift probes measurements is presented.

1.5.5 Light sterile neutrinos

Light sterile neutrinos are not motivated by arguments of fundamental physics, but rather by a few anomalies in short baseline neutrino oscillation data, as in LSND (Aguilar-Arevalo and et al., 2001), MiniBooNE (Aguilar-Arevalo et al., 2010), reactor (Mention et al., 2011) and Gallium (Abdurashitov et al., 2006; Giunti et al., 2012) experiments. These anomalies can be explained with a neutrino having a mass squared difference of $\Delta m^2 \gtrsim 1\,\mathrm{eV}^2$. However, results from solar and atmospheric neutrino oscillations experiments ($\Delta m^2_{1,2/1,3} \lesssim 10^{-3}\,\mathrm{eV}^2$) require a fourth neutrino to admit $\Delta m^2 \gtrsim 1\,\mathrm{eV}^2$, while LEP results on the invisible decay width of the Z boson ($N_\nu^{\mathrm{active}} = 2.9840 \pm 0.082$: The ALEPH Collaboration et al., 2005) imply that the fourth neutrino, if it exists indeed, is a sterile neutrino. Yet, the aforementioned experiments have to deal with a number of evidences which clearly disfavour the extra sterile neutrino interpretation, the stronger coming from accelerator experiments like CDHSW (Dydak et al., 1984) or MINOS (Adamson and et al., 2011).

From the theoretical point of view the existence of sterile neutrinos arise naturally as a consequence of active neutrinos having non-zero masses. Once neutrino mass generation via the seesaw mechanism is put into the wider context of grand unification and leptogenesis, (light) sterile neutrinos in the mass range of eV and keV appear slightly less natural, but still a large class of models allows for their existence (see Abazajian et al., 2012, for a review).

From the cosmological side sterile neutrinos can be generated in the early Universe through various mechanisms, including resonant or non-resonant oscillations with the flavour neutrinos produced in the thermal bath. To account for their effects on cosmology two parameters are usually considered: the effective number of extra relativistic degree of freedom $\Delta N_{\mathrm{eff}} = N_{\mathrm{eff}} - 3.046$, and the effective sterile neutrino mass, $m_{\mathrm{s}}^{\mathrm{eff}}$. The former account for the sterile neutrino contribution to the radiation energy density (Eq. (1.42)) when they are in the relativistic regime, and its value depends on the number of sterile flavours and the level of thermalisation. The primary thermalisation process is the collisional production from active neutrinos that oscillate into sterile neutrinos. This process is favoured by large mixing angle(s) and large mass squared difference(s). For one extra sterile species, the values of the mass squared difference ($m_{\mathrm{s}} \sim 1\,\mathrm{eV}$) and mixing angles invoked to resolve reactor, Gallium ($\sin^2 2\Theta \gtrsim 0.1$) and accelerator ($\sin^2 2\Theta \sim 5 \times 10^{-3}$) anomalies suggest a full thermalisation of the sterile neutrinos in the early Universe (Langacker, 1989), and thus a contribution of $\Delta N_{\mathrm{eff}} = 1$ to the dark radiation. The relation between the parameter $m_{\mathrm{s}}^{\mathrm{eff}}$ and the physical mass m_{s} depends on the

production mechanism which generate the sterile neutrinos in the early Universe. For a thermally-distributed sterile neutrino the relation reads:

$$m_{\rm s}^{\rm eff} = (T_{\rm s}/T_\nu)^3 m_{\rm s} = (\Delta N_{\rm eff})^{3/4} m_{\rm s} \tag{1.48}$$

where $T_{\rm s}$ and T_ν represent the current temperature of the sterile and active neutrinos, respectively. Alternatively, if the sterile neutrino is distributed proportionally to the active species due to oscillations the physical mass can be expressed as $m_{\rm s}^{\rm eff} = (\Delta N_{\rm eff}) m_{\rm s}$, which corresponds to the Dodelson and Widrow (1994) scenario. In both cases for a fully thermalised sterile neutrino, $\Delta N_{\rm eff} = 1$, one gets $m_{\rm s}^{\rm eff} = m_{\rm s}$.

After decoupling, and when still relativistic, sterile neutrinos contribute to the radiation energy density modifying the equality redshift $z_{\rm eq}$ (Eq. (1.4)) according to:

$$1 + z_{\rm eq} = \frac{\Omega_{\rm m}}{\Omega_\gamma} \frac{1}{1 + 0.227 N_{\rm eff}}\,, \tag{1.49}$$

(see Eq. (1.42)). When non-relativistic, and for masses $m_{\rm s} \lesssim 1\,{\rm eV}$, sterile neutrinos acts similarly to the active ones suppressing the matter fluctuations on scale smaller than their free streaming length (Eq. (1.46)). Assuming one massive sterile neutrino, in addition to the two massless and one massive active neutrino with $m_\nu = 0.06\,{\rm eV}$, the Planck Collaboration (2013d) combining Planck+WP+HighL and BAO data found no evidence for the extra massive species: $m_{\rm s}^{\rm eff} < 0.42\,{\rm eV}$ and $\Delta N_{\rm eff} < 0.80$ (95% C.L.). Otherwise, including also datasets which are in tension with Planck CMB results such as H_0 measurements (which push for extra radiation) and cluster data (which prefers non-zero neutrino mass) various authors (e.g. Wyman et al., 2013; Battye and Moss, 2013; Hamann and Hasenkamp, 2013) found evidence for a sterile neutrino with $m_{\rm s}^{\rm eff} \sim 0.4 - 0.5\,{\rm eV}$ and dark radiation $\Delta N_{\rm eff} \sim 0.4 - 0.7$. Other constraints on sterile neutrino properties from CMB data in combination with LSS constraints – also accounting for systematics in the cluster analysis – will be presented in Chapter 5.

2

Cosmological probes

In the first Chapter the theory that describes the evolution of the background Universe and matter fluctuations has been presented. To exploit this theoretical framework to constrain cosmological model we need suitable cosmological probes to sample the underlying dark matter distribution and measure the Universe expansion over the cosmic time.

Thanks to the advancement in instrumentation technology and theory of cosmic structure formation, the last decades have witnessed the appearance of plenty of new cosmological probes (e.g. BAO scale and cosmic shear measurements) and refinement of old ones (e.g. CMB temperature and polarization anisotropies and cluster number counts). Still, the full exploitation of these cosmological data is hampered by our limited understanding of different astrophysical processes which take place at small scales modifying the observational properties of the structures under consideration.

Here I will present an overview of the cosmological probes used in the analysis presented in this Thesis, explaining their properties, observational techniques, and providing some recent results. Particular emphasis will be given to galaxy cluster surveys which is the probe mostly used for the results of this Thesis.

2.1 Cosmic Microwave Background

The Cosmic Microwave Background is widely recognized as one of the most powerful probes of cosmology and early Universe physics. Predicted by Gamow (1946),

the CMB is the relic radiation we receive from the surface of last scattering between photons and baryons at $z_{\rm d} \sim 1100$. The spectrum of the CMB is perfectly consistent with a blackbody spectrum with a temperature $T = 2.725\,\mathrm{K}$, resulting from the thermalisation of the photon-baryon plasma in the pre-recombination era, and the subsequent cooling of free-streaming CMB photons with the Universe expansion. Its anisotropies, observed as small temperature fluctuations across the CMB sky, carry the imprint of the density and metric perturbations present at the photon decoupling. After its first detection by Penzias and Wilson (1965) – which allowed to establish the modern paradigm of the hot big bang cosmology – the cosmological relevance of the CMB was rapidly realized and a series of experiments aimed to measure its anisotropies were started by the mid-70s. However, only twenty eight years after its discovery the COBE satellite has been able to detect the fluctuations of the order 10^{-5} in its temperature field. If from one side the small amplitude of the fluctuations has hampered their detection for several years, on the other side it allows to use the accurate theoretical predictions of the linear perturbation theory to tightly constrain cosmological parameters. The COBE results established the existence of a nearly scale-invariant spectrum of primordial fluctuations on angular scales larger than 7°, consistent with the predictions of inflationary cosmology, and has prompted new generations of sub-orbital (Boomerang, Maxima), ground based (DASI, CBI, ACT, SPT) and satellite (WMAP, Planck) experiments to map the CMB sky. Thanks to the huge amount and accuracy of CMB measurements available today, CMB data alone are able to provide constraints at percent level for all the six ΛCDM parameters. In what follows I will present the quantities observed in CMB surveys and the most recent constraints provided by the latter.

2.1.1 Observational quantities

Temperature anisotropies

The basic observable of the CMB is its intensity as a function of frequency and direction on the sky $\hat{\mathbf{n}}$, usually expressed in terms of temperature fluctuations $\Theta(\hat{\mathbf{n}}) = \Delta T/T$. If the cosmic density field is Gaussian, as predicted by many standard inflation scenarios and confirmed by observations, the multipole moments of the temperature fluctuation field

$$a_{\ell m} = \int \mathrm{d}\hat{\mathbf{n}} \mathrm{Y}^*_{\ell m}(\hat{\mathbf{n}}) \Theta(\hat{\mathbf{n}}) \tag{2.1}$$

are fully characterized by their power spectrum, $C_\ell = \langle |a_{\ell m}|^2 \rangle$. The maximum precision reachable for each measured C_ℓ is set, for an idealised full-sky survey, by

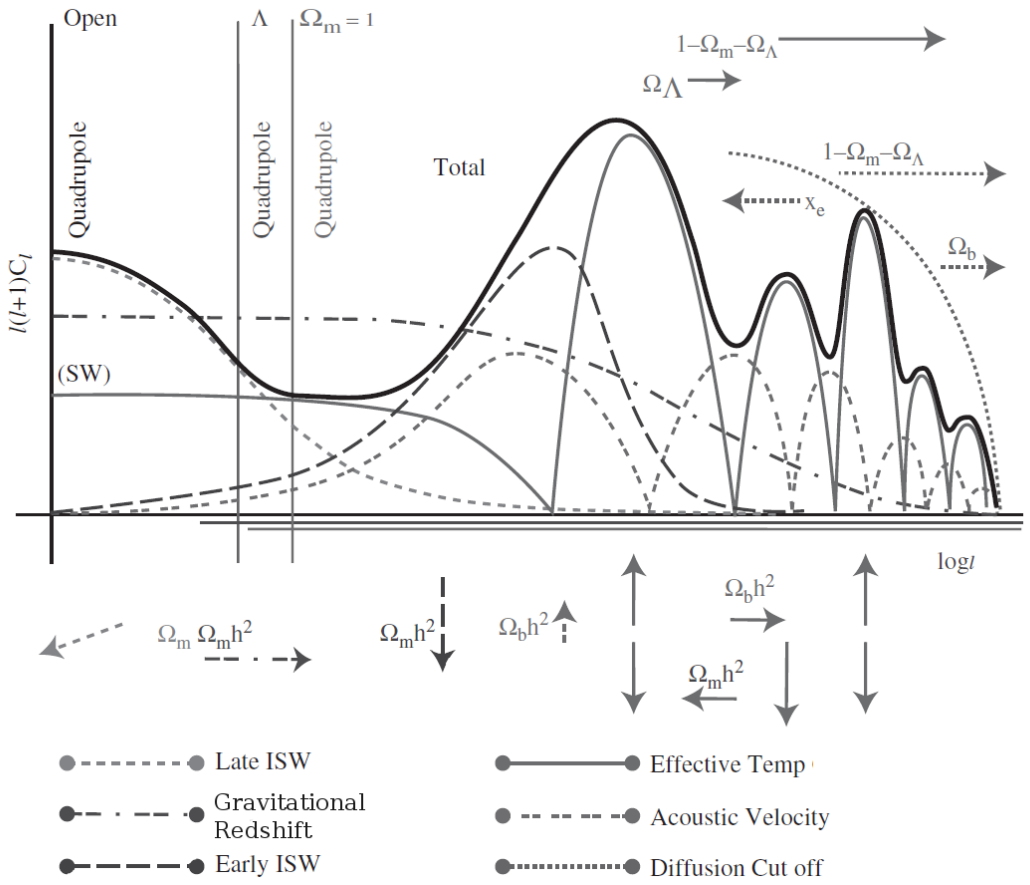

Figure 2.1: Contributions to the CMB temperature power spectrum of various physical processes and their dependence on Ω_m, Ω_b, Ω_Λ. Features in open models ($\Omega_k = 1 - \Omega_m - \Omega_\Lambda > 0$) are shifted to larger ℓ compared to flat ΛCDM (Λ) or EdS ($\Omega_m = 1$) models, represented here as a shift of the origin of the x-axis $\ell = 2$. Contributions from different physical processes are shown with different line styles (see legend). The arrows indicate the direction of change of the various contribution led by the increase of the model parameter written aside. For example, an increase of $\Omega_b h^2$ increases the heights if the first and third acoustic peaks, shifts the peaks to larger ℓ and increases the overall contribution of the acoustic velocity peaks. Figure from Mo et al. (2010) (see Hu, 1995, for the original version of the Figure).

the cosmic variance and is equal to $\Delta C_\ell = \sqrt{2/(2\ell+1)}C_\ell$.

As shown in Figure 2.1, several physical processes contribute to shape the CMB temperature spectrum; the main of these are described as follows:

Sachs-Wolfe effect and integrated Sachs-Wolfe effect. Since CMB photons comes to us from the last scattering surface at $z \sim 1100$, the angle subtended by the Hubble radius at decoupling, $\vartheta_d \simeq 1^\circ$ (or $\ell_d \simeq 200$), sets a characteristic angle over which the temperature fluctuations are entirely due to super-horizon metric perturbations. In particular, the observed temperature anisotropies at angular scales $\vartheta > \vartheta_d$ depend on: i) the intrinsic fluctuations of the photon density at decoupling, ii) the potential difference between the observer and the last scattering surface – gravitational redshift – and iii) the Doppler shift due to the velocity of the photon-baryon fluid at decoupling (double-dashed grey line in Figure 2.1; see later) and the relative motion of the observer to the CMB. The latter, caused by the solar system motion relative to the nearly isotropic blackbody field, produces a strong dipole signal, usually removed for the purposes of CMB anisotropies study. The temperature anisotropies resulting from the combination of the intrinsic temperature perturbations and gravitational redshifts are usually referred to as effective temperature perturbations (solid gray line in Figure 2.1). On large scales ($\ell \lesssim 200$), for a scale-invariant primordial power spectrum ($P_{\rm in} \propto k$; see Eq. (1.23)), the contribution to $\ell(\ell+1)C_\ell$ from the effective temperature perturbations is constant – Sachs-Wolfe effect (Sachs and Wolfe, 1967) – as shown in Figure 2.1 with the label (SW). Time variations of the potential – i.e. time-dependent metric perturbations – lead to an upturn of the spectrum at the lowest multipoles ($\ell \lesssim 10$). This effect, arising from the contribution of all the time-varying potential wells crossed by CMB photons in their path toward us, is known as Integrated Sachs-Wolfe effect (ISW). There are two possible way to generate such an ISW effect in the linear regime. At decoupling, when the contribution of the radiation to the total energy density is non-negligible, the density perturbations grow more slowly than the scale factor, which causes the potential to decay until the Universe is completely matter dominated. Being produced close to decoupling, these temperature fluctuations are referred to as the early ISW effect. Since potential evolution is relevant only for modes within the horizon the early ISW effect peaks roughly at the horizon scale at decoupling ($\ell \simeq 100$, see Figure 2.1). In open ($\Omega_{\rm k} > 0$) or flat ΛCDM universes, the linear gravitational potential starts to decays with time as the curvature and/or the cosmological constant become dynamically relevant. For a flat ΛCDM model this occurs at $z_\Lambda \simeq 0.3$ (see Eq. (1.5)). Because this kind of potential decay starts only at late time, its effect on the CMB is known as late ISW effect, and it is expected to peak roughly at the present horizon scale, i.e. $\ell \lesssim 10$ (see Figure 2.1).

Acoustic peaks. On sub-horizon scales $\vartheta < \vartheta_d$ the rich structure observed in the anisotropy spectrum is mainly a consequence of the acoustic oscillations of the tightly-coupled baryon-photon fluid in the pre-recombination era. Perturbations in the gravitational potential, dominated by the CDM component, drive the oscillations in the plasma, with photon pressure providing most of the restoring force and baryon giving some additional inertia (see §1.2.1). The frequency of the oscillations depends on the sound speed in the fluid, c_s (Eq. (1.17)). After recombination, photons can travel freely toward us, and the phases of the oscillations is imprinted in the CMB spectrum as a series of harmonic peaks (solid grey line in Figure 2.1 at $\ell \gtrsim 100$). The first peak corresponds to the mode that is caught in its first compression by recombination. The second peak corresponds to the mode that went through a full cycle of compression and rarefaction by recombination. The even peaks are generally of smaller amplitude because the rebound has to fight against baryon inertia. Also the Doppler effect due to the acoustic waves velocity contributes to the effective temperature fluctuations, but with a phase shift of $\pi/2$ which partially fills the troughs of the acoustic pattern (double-dashed grey line in Figure 2.1). The position of the acoustic peaks in C_ℓs are determined by the physical size of the sound horizon at decoupling , $l_\mathrm{s} \approx 100(\Omega_\mathrm{m}h^2)^{-1/2}(1+\mathscr{R})^{-1/2}$Mpc (see Eq. (1.17) for the definition of $\mathscr{R}$), and the angular diameter distance of the last scattering surface , $D_A(z_\mathrm{d}) = r(z_\mathrm{d})/(1+z_\mathrm{d})$. Thus, the position of the peaks depends on the geometry of the space and on the value of Ω_b. Furthermore, the value of Ω_b controls also the relative amplitude between even and odd peaks – through the contribution of the baryon inertia – and the depth of the valleys – through the contribution of the acoustic velocity. In addition, the heights of the acoustic peaks can be affected by the strength of the initial perturbations (A_s and n_s) , and by Ω_m through to the time evolution of the gravitational potential induced by the self-gravity of the acoustic perturbations.

Diffusion damping. We have seen in §1.2.1 that the imperfect coupling between baryons and photons during decoupling causes a damping of the perturbations at scales smaller than the damping (or Silk (1967)) scale, which corresponds to $\ell \gtrsim 2000$. Moreover, since the recombination process is not instantaneous, the last scattering surface has a finite thickness. This leads to a smearing of the anisotropies at the highest ℓs, corresponding to scales smaller than the width ($\Delta z \simeq 80$) of the recombination process, $\ell \gtrsim 1000$. Finally, re-scattering of CMB photons with free

electrons produced at reionization[1] suppresses exponentially the amplitude of the acoustic peaks, on scales smaller than the horizon size at reionization. The diffusion cut off is shown in Figure 2.1 with a grey dotted line, along with the effect led by an increase of the ionization fraction at reionization x_e, the latter affecting the photon diffusion length.

Secondary anisotropies: CMB lensing and Sunyaev-Zel'dovich effect. At angular scales smaller than few arc-minutes CMB temperature fluctuations are no longer dominated by primary effects at the surface of last scattering, but rather by the so-called secondary anisotropies which arise from the interaction of the CMB photons with the matter along the line of sight. The secondary anisotropies can be divided in two major families depending on the physical process which generate them. The first family arises from the interaction of the photons with gravitational potential wells, and it includes gravitational lensing and the late ISW effect. As for former, the gravitational deflection of CMB photons by intertwining non-linear structures causes a smoothing of the acoustic peaks up to 10% level at $\ell > 2000$, and generate small-scale power that dominates the primary anisotropies for $\ell > 4000$, where the diffusion damping is highly effective. Moreover, CMB lensing introduces non-Gaussianity in the four-point correlation function with a very specific and predictable shape, from which it is possible to reconstruct the power spectrum of the lensing potential $C_\ell^{\phi\phi}$ (see §2.4). The second family incorporates the effects of scattering of CMB photons with free electrons, such as reionization effects (e.g. Aghanim et al., 2008) and the Sunyaev and Zeldovich (1972) (SZ) effect. The SZ effect is related to the spectral distortion induced by the inverse Compton scattering between CMB photons and free electrons of a hot ionized gas (such as the intracluster medium, ICM). Specifically, cold photons in the Rayleight-Jeans tail of the blackbody body spectrum (radio wavelengths) are up-scattered by hot electrons to the Wein tail (submillimiter wavelengths), giving to the SZ contribution a distinct frequency signature which can be used to isolate it from other secondaries. Once isolated, the SZ signal can be used to constraints the amplitude of the matter fluctuations through its power spectrum (Komatsu and Seljak, 2002) or, as described in §2.2.3, to effectively detect and characterize clusters of galaxies. Along with the "thermal" SZ effect described above there exist also a "kinetic" SZ effect induced

[1] With the evolution of the cosmic structures, after a sufficient number of ionizing sources have formed, the ionized fraction of the gas in the Universe rapidly increases until hydrogen becomes highly ionized. This period, occurred roughly between $20 \lesssim z \lesssim 6$, is known as epoch of reionization.

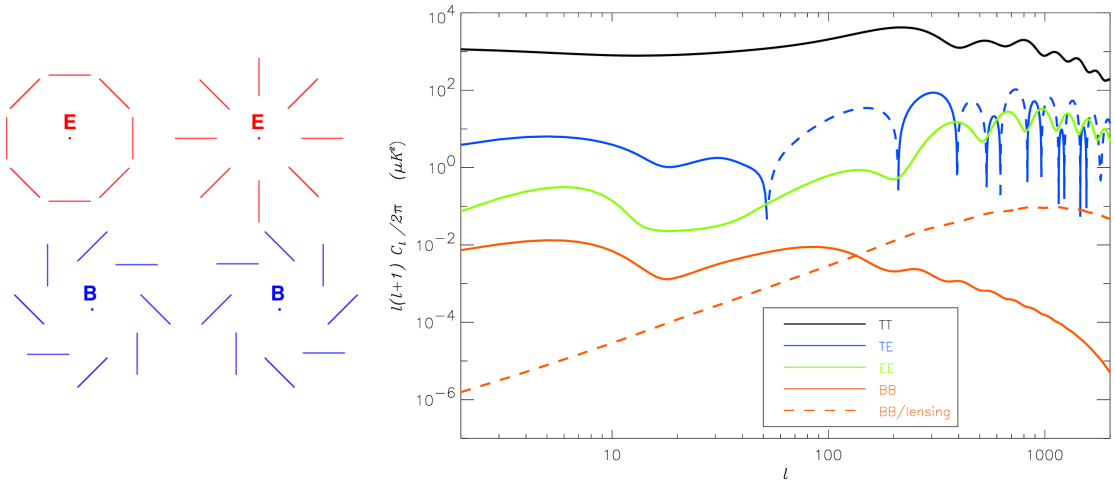

Figure 2.2: *Left* panel: Typical patterns of the E- and B-mode polarization, which display the opposite transformation properties under parity. *Righ* panel: The four observable CMB spectra: C_ℓ^{TT}, C_ℓ^{TE}, C_ℓ^{EE} and C_ℓ^{BB}. The dashed segments in the C_ℓ^{TE} spectrum (*blue* line) represent negative values. The *solid red* line labelled "BB" represents the contribution to the C_ℓ^{BB} from tensor perturbations ($r = 0.1$) while the *dashed red* line labelled "BB/lensing" represents the contribution expected from gravitational lensing. Figure from Kaplan (2003).

by the bulk motion of the cluster gas, which causes a smaller spectral distortion and it is usually treated in CMB analysis as foreground noise.

Polarization

The other key CMB observable is polarization. Thomson scattering of a radiation field with a quadrupole anisotropy produces linear polarization. The relevant epoch for the generation of polarization in the CMB is around recombination since at early times scattering is too efficient to allow a significant quadrupole to grow, while after recombination scatterings are very rare (until the universe reionizes). The CMB polarization signal is expected to have a r.m.s. of $\sim 5\mu$K, peaking at multipoles $\ell \simeq 1000$ (the angle subtended by the photon mean free path at last scattering). To study the polarization pattern of the CMB sky is convenient to decompose the polarization (vector) field in two components: a curl-free component, called E-mode, with no handedness, and a gradient-free component, called B-mode, with

handedness (see *left* panel of Figure 2.2). From their definition it follows that in absence of parity-violating physics, the two are uncorrelated. This leaves with three non-zero polarization spectra: the two auto-correlation C_ℓ^{EE} and C_ℓ^{BB} spectra, and the cross-correlation spectrum C_ℓ^{TE} between E and temperature anisotropies. These are shown in the *right* panel of Figure 2.2 in comparison with the temperature power spectrum to highlight the small amplitude of the polarization signal compared to the primary C_ℓ^{TT} spectrum. Scalar perturbations, produced by density and isocurvature fluctuations, generate positive parity polarization patterns, and therefore, can only produce E-mode polarization. The oscillating baryon-photon fluid results in a series of acoustic peaks in C_ℓ^{EE} at the troughs of C_ℓ^{TT} since the polarization anisotropies are sourced by the fluid bulk velocity which vanishes at density extrema. The C_ℓ^{TE} patterns comes from correlations between density and velocity perturbations on the last scattering surface – which can be both positive and negative – and is of larger amplitude than the E-mode signal. B-mode polarization can be induced by tensor perturbation, generated by the primordial gravitational waves predicted in the inflationary scenario, or by gravitational lensing due to the intertwining structures along the line of sight. A measurement of the gravitational waves power probes directly the energy scale of inflation. Therefore, detection of the B-mode polarization signal at $\ell \lesssim 100$ will allow to constrain this energy scale, usually parametrized with $r = A_\mathrm{t}/A_\mathrm{s}$, the tensor to scalar ratio of the amplitudes of the primordial spectra (see *solid red* line in Figure 2.2). At smaller scales ($\ell \gtrsim 100$) the weak lensing induced-B mode signal become dominant (*dashed red* line in Figure 2.2). Lensing does not produce nor rotate polarization, but warps its spatial distribution in a Gaussian-random fashion which blurs the original parity properties, thereby leaking E modes into B modes. This signal, in addition to galactic emission, is one of the major contamination for experiments devoted to the detection of the gravitational waves signal. The "bump" at low multipoles ($\ell \lesssim 20$) in the polarization spectra is due to the re-scattering of CMB photons at reionization. The position of this peak is set by the size of the horizon at reionisation, while its amplitude is determined by the duration of the ionization process.

2.1.2 Current constraints from CMB surveys

The Planck satellite belongs to the third generation of all sky CMB surveys after COBE and WMAP, and represents the state-of-the-art of CMB experiments. Results from the first data release (Planck Collaboration, 2013d), using measurements of the temperature ($\ell < 2500$) and lensing potential ($40 < \ell < 400$) power spectra, provide percent level constraints on the six base ΛCDM parameters (see Table 2.1),

Table 2.1: Constraints at 68% C.L. on the six base ΛCDM parameters from: Planck temperature power spectrum alone, combining Planck temperature and lensing potential spectra (Planck+lensing) or combining Planck temperature data with WMAP polarization at low multipoles (Planck+WP) and high resolution experiments SPT and ACT (Planck+WP+HighL). Data from (Planck Collaboration, 2013d). The six base parameters listed are: the physical cold dark matter and baryon energy densities $\Omega_c h^2$ and $\Omega_b h^2$, the ratio between the sound horizon and the angular diameter distance at decoupling Θ_s , the Thomson optical depth at reionization τ the scalar spectral index n_s and the amplitude of the primordial power spectrum A_s.

Parameter	Planck	Planck+lensing	Planck+WP	Planck+WP+HighL
$\Omega_b h^2$	0.02207 ± 0.00033	0.02217 ± 0.00033	0.02205 ± 0.00028	0.02207 ± 0.00027
$\Omega_c h^2$	0.1196 ± 0.0031	0.1186 ± 0.0031	0.1199 ± 0.0027	0.1198 ± 0.0026
$100\Theta_s$	1.04132 ± 0.00068	1.04141 ± 0.00067	1.04131 ± 0.00063	1.04132 ± 0.00063
τ	0.097 ± 0.038	0.089 ± 0.032	$0.089^{+0.012}_{-0.014}$	$0.091^{+0.013}_{-0.014}$
n_s	0.9616 ± 0.0094	0.9635 ± 0.0094	0.9603 ± 0.0073	0.9585 ± 0.0070
$\ln(10^{10} A_s)$	3.103 ± 0.072	3.085 ± 0.057	$3.089^{+0.024}_{-0.027}$	3.090 ± 0.025

and exhibit no evidence to favour any extension to the consensus cosmological model. For smaller angular scales ($2500 < \ell < 10^4$) the best CMB measurements up today are provided by the ground based experiments ACT and SPT (Das et al., 2014; Reichardt et al., 2012). Temperature anisotropies data from these experiments are often combined with those of all sky CMB surveys like WMAP and Planck (Planck+WP+HighL in Table 2.1) to improve parameters constraints, especially of those parameters affecting the shape of C_ℓ^{TT} at small angular scales (e.g. the total neutrino mass).

Although CMB polarization data alone have the potential to constrain cosmological parameters as temperature anisotropies data do, the current sensitivity of polarization experiments limits their constraining power. WMAP E-mode polarization spectra at low-multipoles ($\ell < 23$) (Bennett et al., 2013) have been used in combination with Planck C_ℓ^{TT} spectrum to improve the constraints on τ (see Planck+WP column in Table 2.1). At the time of writing this Thesis the Planck Collaboration has not yet released results from polarization measurements, but only shown an excellent visual agreement between their best-fit ΛCDM model and their C_ℓ^{TE} and C_ℓ^{EE} polarization spectra at $\ell > 100$. Similarly, a number of experiments (CAPMAP (Bischoff et al., 2008), QUAD (Brown et al., 2009), QUIET (QUIET Col-

laboration, 2012), BICEP1 (BICEP1 Collaboration, 2013), WMAP (Hinshaw et al., 2013), ACT (Naess et al., 2014)) demonstrated the quantitative agreement with ΛCDM prediction and placed upper limits on primordial and lensing B-modes. Hanson et al. (2013) using SPT data detected at 7.7σ significance the B-mode signal produced by gravitational lensing, while the Polarbear Collaboration (2014) provided its first measurement. Finally, the Bicep2 Collaboration (2014) announced the first detection of non-zero B-mode polarization at degree angular scale from primordial gravitational waves, which, if confirmed, would imply a tensor-to-scalar ratio value of $r = 0.20^{+0.07}_{-0.05}$ (cf. Planck Collaboration, 2014, which investigated the level of dust polarization in the BICEP2 experiment field and found a dust power of the same magnitude as reported by Bicep2 Collaboration (2014) over the same ℓ range, highlighting the need for assessment of the polarized dust signal.).

2.2 Clusters of galaxies

Among the different probes of the LSS, galaxy clusters have played a significant role in the definition of the "concordance" ΛCDM model, starting with the Zwicky (1933) discovery of dark matter in the Coma Cluster, passing through the ruling out of critical matter density models (e.g. White et al., 1993b; Borgani et al., 2001), up to the most recent cosmological constraints from large cluster surveys (e.g. Vikhlinin et al., 2009b; Mantz et al., 2010; Allen et al., 2011). As shown in Chapter 1, according to the hierarchical growth structure model, clusters are the largest and most recent objects that have undergone gravitational relaxation and entered into virial equilibrium. Arising from the high density peaks of the initial matter distribution, the galaxy cluster population bears the imprints of the statistical distribution of the initial perturbations, their subsequent growth and the dynamics of the collapse of dark matter halos. Thanks to this three-fold dependence galaxy clusters can supply cosmological information with a number of critical tests. Their mass and redshift distribution, depending on the amplitude and growth rate of density perturbations, as well as on the redshift evolution of the cosmic volume, can provide thigh constraints on the amplitude of the power spectrum σ_8, density parameters like Ω_m, Ω_Λ, Ω_ν, and modified gravity models. Furthermore, clustering of galaxy clusters, through its dependence on the halo bias and matter power spectrum, provides complementary information on the growth rate, shape and amplitude of the power spectrum, as well as constraints on the level of primordial non-Gaussianities. Finally, internal properties of clusters, such as baryon fraction or radial density profile, can be used to get insight on the nature of the dark energy and dark matter.

Galaxy clusters are multi-component systems consisting of dark matter and baryons in several phases (black holes, stars, cold, warm and hot gas and non-thermal plasma). From one side this multi-component nature challenges the study of the astrophysical processes which determine the observational properties of the structures inside the clusters. On the other side it offers multiple observable signals across the electromagnetic spectrum (Figure 2.3): at X-ray wavelengths, the diffuse hot intra cluster medium (ICM) shines due to the thermal bremsstrahlung emission; stellar emission from galaxies and intracluster light dominates the optical and near-infrared bands; at millimeter wavelengths, the hot plasma in the ICM distorts the CMB spectrum through the SZ effect (see §2.1.1).

In order to exploit clusters as cosmological tools, we need to determine the evolution of their space density, that is the number of clusters within given mass and redshifts ranges, per unit volume. Thus, besides an efficient method for detecting clusters over a wide range of redshifts, an observable estimator of the cluster mass – mass proxy – and a robust method to compute the selection function – i.e. the survey volume within which clusters are found – are needed. In particular, having a robust mass proxy which correlates tightly with the mass – i.e. with a low-scatter – is mandatory in large cluster surveys for which follow-up observations of individual clusters are feasible only for a small fraction of the detected objects. On the other side, follow-up data are needed to improve the accuracy of the calibration of the mass-proxy relation, and thus reduce the uncertainties in the mass estimation. In what fallows I will review the methodology used to build cluster samples in the optical/near-IR, X-ray and microwave bands, along with the statistical tools used to infer parameters constraints and some recent results.

2.2.1 Cluster surveys in the optical/near-IR band

Cluster identification

The optical identification has been the first technique used to detect clusters of galaxies since the end of the XVIII century, with the Charles Messier's (1784) and William Herschel's (1785) catalogues of nebulæ. The first extensive and statistical complete sample of galaxy clusters was built by Abell (1958) – later extended to the Southern hemisphere (Abell et al., 1989) – based on visual inspection of photographic plates. Clusters were identified as enhancements in the projected galaxy density and were characterized according to their richness – number of galaxy members – and estimated distance. With the advent of CCD imaging, purely visual inspection gives way to automated detection techniques, whose algorithms

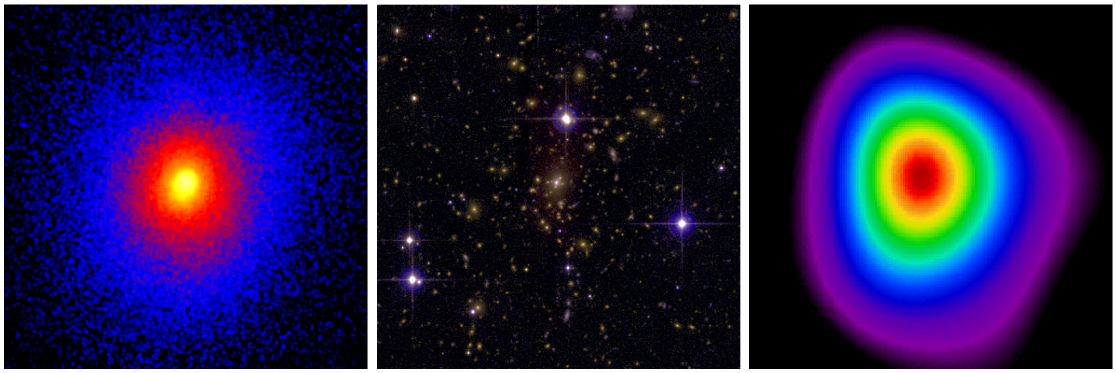

Figure 2.3: Images of the cluster Abell 1835 ($z = 0.25$) in the X-ray (*left*), optical (*center*) and millimeter (*right*) band, all centred on the X-ray peak position. Images respectively from: Chandra X-ray Observatory / A. Mantz, Canada France Hawaii Telescope / A. von der Linden et al., Sunyaev Zel'dovich Array / D. Marrone.

depend on the available photometric data. If only single band data are available the most used ones are the match filter methods (e.g. Postman et al., 1996; Lobo et al., 2000; Dong et al., 2008) which exploit prior knowledges of the luminosity profile typical of clusters to enhance the spatial galaxy overdensity at a given position. This method has been successfully applied to several surveys – e.g. ESO imaging survey (Olsen et al., 1999), SDSS (Bahcall et al., 2003; Szabo et al., 2011), 2MASS (Kochanek et al., 2003), XFS (Dietrich et al., 2007) – to detect clusters up to $z \sim 1$ and down to masses of order $\sim 10^{14} M_{\odot}$. However, projection effects and the loose relation between cluster richness and optical luminosity reduce the completeness and purity of these catalogues. An effective way to reduce the impact of projection effects rely on the use of multi-bands imaging. One way to exploit multi-colour data is to obtain photometric redshifts of galaxies; these in turn allow to detect clusters in 3-d space – two spatial coordinates and redshift – as groups of galaxies whose mutual distances do not exceed a chosen linking length (friend-of-friend percolation algorithm: Huchra and Geller, 1982; van Breukelen et al., 2006; Li and Yee, 2008; Farrens et al., 2011; Wen et al., 2012). Another efficient detection method which exploit colour information relies upon the existence of a *red sequence* for cluster galaxies in the colour-magnitude diagram (e.g. Gladders and Yee, 2000). The population of rich, relaxed clusters up to $z \sim 1$ is dominated by early type galaxies, placing them on a narrow and distinctive locus of the colour-magnitude diagram – the *red sequence* – which can be easily detected. The colour bands are chosen so as to bracket the redshifted 4000 Å break feature of galaxy spectra; there-

fore the choice of the colour-cuts enables the estimate of the redshift of the cluster. The cluster red sequence method has been applied for the first time using two wavebands to build the Red Sequence Cluster Survey catalogue (Gladders and Yee, 2005), and later applied to several photometric galaxy surveys including the *Spitzer* IRAC shallow survey (Eisenhardt et al., 2008) and SDSS (Koester et al., 2007; Hao et al., 2010; Rykoff et al., 2014). This technique has proven to be very effective in removing field galaxy contamination, however for un-relaxed, low-mass clusters, especially at $z \gtrsim 1$, the *red sequence* is not well established, and the method becomes less efficient.

Mass estimation

If spectroscopic or high-quality imaging data are available cluster masses can be estimated directly, by applying dynamical methods (e.g. Virial theorem, Jeans equation) in the first case, or analysing the gravitational lensing effect on background galaxies in the second.

The gravitational potential well generated by the cluster mass is the main driver of the orbital motion of the member galaxies, which can be treated as collisionless test particles of the local gravitational field. Using spectroscopic measurements of the cluster galaxies line-of-sight velocities, under the assumption of spherical symmetry and dynamical equilibrium, the mass enclosed within radius r can be estimated by means of the Jeans equation (e.g. Binney and Tremaine, 1987):

$$M(<r) = -\frac{r\sigma_r^2}{G}\left(\frac{\mathrm{d}\ln\sigma_r^2}{\mathrm{d}\ln r} + \frac{\mathrm{d}\ln n_{\mathrm{glx}}}{\mathrm{d}\ln r} + 2\beta\right), \tag{2.2}$$

where $n_{\mathrm{glx}}(r)$ is the galaxy number density, $\sigma_r(r)$ the radial velocity dispersion and $\beta(r) = 1 - \sigma_t^2/\sigma_r^2$, the relative difference between the radial and the tangential (σ_t) velocity dispersion, is the velocity anisotropy parameter. The latter, which quantifies the anisotropy of the orbits induced by e.g. dynamical friction, tidal effects or infall events, cannot be directly measured and it is determined by modelling the velocity dispersion profile or by considering higher-than-second-order moments of the velocity distribution (e.g. Merritt, 1987; van der Marel et al., 2000; Łokas and Mamon, 2003; Wojtak et al., 2005). Significant uncertainties for this mass estimator come from the assumption of dynamical equilibrium of the system and contaminations by spurious cluster members. Another technique, usually referred to as the caustic method (Diaferio and Geller, 1997), allows to estimate the mass from the projected phase-space distribution of cluster galaxies. In general

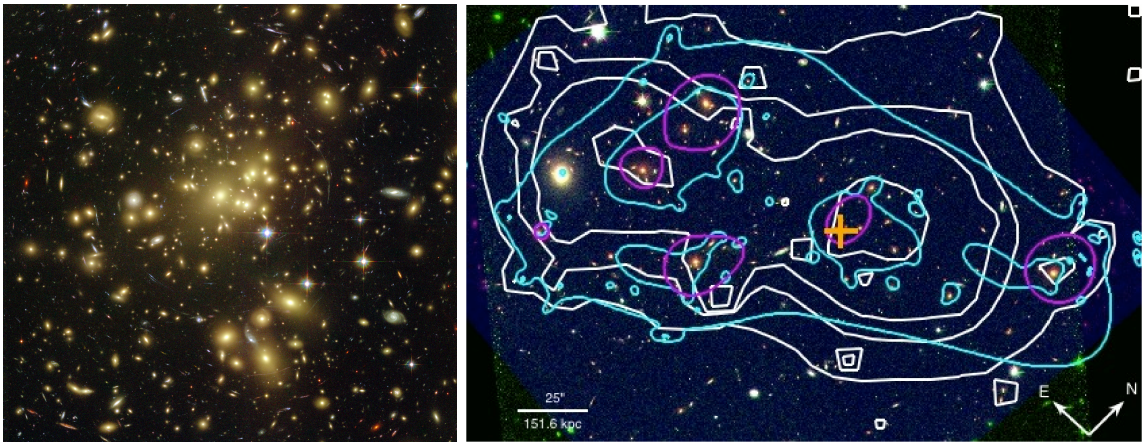

Figure 2.4: *Left* panel: HST image of the galaxy cluster Abell 1689. The long arcs around the cluster correspond to distorted images of background galaxies due to strong lensing effects. Credit: NASA/ESA. *Right* panel: Example of lensing mass reconstruction in the core of the galaxy cluster MACSJ0717.5+3745 obtained from 18 multi-passband images acquired with the Advanced Camera for Surveys aboard the HST. Cyan contours represent the mass distribution inferred in the strong lensing study by Limousin et al. (2012); white contours show the mass distribution obtained with the weak lensing analysis by Jauzac et al. (2012) using the orange cross as cluster centre. Magenta contours represent the K-band light distribution of the cluster. Image from Jauzac et al. (2012)

the "Jeans" and caustic methods have been shown to provide consistent results between them (Biviano and Girardi, 2003; Rines et al., 2003) and with lensing mass measurements (Natarajan and Kneib, 1996; Diaferio et al., 2005), while the agreement is poorer if compared with X-ray determined mass profiles (Benatov et al., 2006).

Gravitational lensing offers a direct way to probe directly the cluster potential insensitive to the dynamical state of the system. The gravitational lensing effect, predicted by the theory of general relativity, refers to distortion and/or magnification of distant galaxies images caused by the bending of light passing through clusters potential wells (see Hoekstra et al., 2013, for a recent review on this topic). In the so-called strong lensing regime, the deflection of the light is large enough to crate multiple images of the same source and arcs (see *left* panel of Figure 2.4). These strong lensing events are confined in the inner region of the cluster and enables precise measurements of the projected masses on scales enclosed by these

lensed images. At larger radii, the tidal gravitational field causes subtle distortion of the shape of background galaxies – weak lensing regime – resulting in a coherent alignment of the sources which can be quantified statistically with the so-called *shear* signal (see later §2.4). Probing different scales of the cluster, the combination of strong and weak lensing data greatly improve the calibration of the projected mass maps (Bradač et al., 2005; Meneghetti et al., 2010) (*right* panel of Figure 2.4). In both lensing regimes, accurate mass reconstructions are usually done by fitting the observed strong lensing features or the azimuthal shear signal with parametrized mass models (e.g. Kneib et al., 1996; Broadhurst et al., 2005; Hoekstra, 2007). Projection effect due to the matter distribution along the line of sight and triaxiality of the dark matter halos are the main source of uncertainty in lensing mass estimation (e.g. Meneghetti et al., 2010). Also relevant for the lensing analysis are: the knowledge of the redshifts of the source galaxies, to relate the observed shear signal to the lens mass, and the level of contamination by unlensed cluster galaxies, which will dilute the observed shear signal. Despite these limitations, lensing measurements provide currently the most reliable (unbiased) estimates of cluster masses and are widely used to accurately calibrate the mean mass-observable scaling relations (e.g. Johnston et al., 2007; Rozo et al., 2009; Rykoff et al., 2008; von der Linden et al., 2014).

In optical cluster studies, the most used mass proxies are the richness and luminosity, both measured summing up the number or the luminosities of the cluster member galaxies in a certain magnitude range and out to a certain radius from the cluster centre. With the availability of high-quality photometric data and highly efficient detection methods these two mass proxies have been proven to be as reliable tracers of cluster mass as X-ray luminosity (see below §2.2.2). Figure 2.5 shows an example of calibration between mass and optical/near-IR luminosity (*left* panel) and between mass and richness (*right* panel). The luminosity-mass relation, $L_{\rm opt} - M_{500}$, obtained by Popesso et al. (2005) from *i*-band SDSS data for a sample of clusters detected within the ROSAT All Sky Survey (RASS), shows a low intrinsic scatter of 30%, comparable to that of the X-ray luminosity (L_X) mass relation. The right panel shows the richness-mass relation from Andreon and Hurn (2010) obtained from the CIRS catalogue (Rines and Diaferio, 2006) of 53 X-ray selected clusters with spectroscopic SDSS data. Again the two quantities are tightly correlated with a scatter of 0.19 dex, comparable to that of the L_X-mass relation.

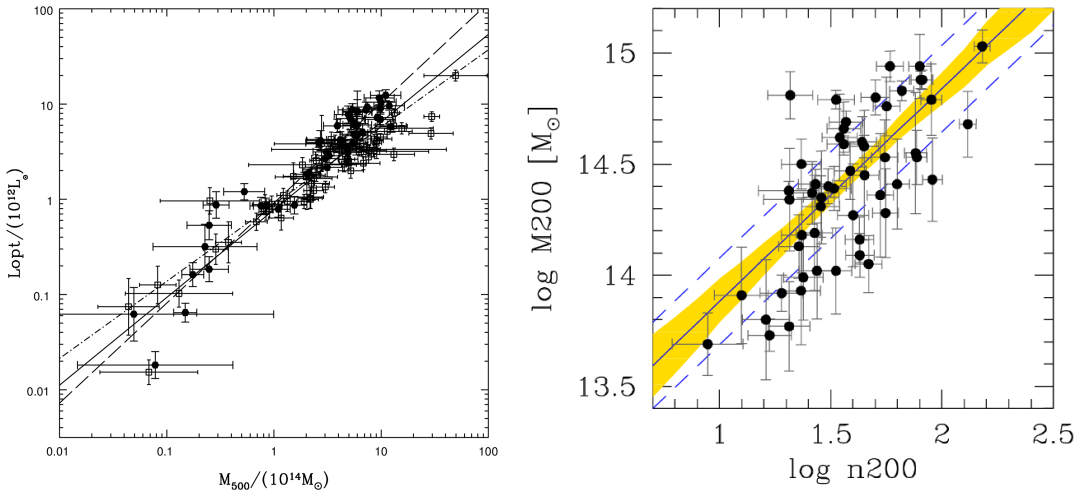

Figure 2.5: *Left* panel: $L_{op} - M_{500}$ relation in the *i* SDSS band from Popesso et al. (2005). Empty and filled squares correspond to mass estimates based on velocity dispersion analysis from spectroscopic data and on mass-X-ray temperature (T_X) relation, respectively. The three lines represent the best fit relation obtained using objects with masses estimated through the dynamical analysis (*dot-dashed* line), masses from the M-T_X relation (*dashed* line), or both (*solid* line). *Right* panel: richness-mass ($n_{200} - M_{200}$) relation obtained from the CIRS cluster catalogue (Rines and Diaferio, 2006) with dynamical mass measurements. The notation $n_{200} = n(r < r_{200})$ stands for the number of cluster galaxies observed within the cluster centric radius r_{200} (see Eq. (1.33)). The solid line marks the mean fitted regression line, while the dashed lines show the intrinsic scatter. The shaded region marks the 68% confidence region for the regression. From Andreon and Hurn (2010).

2.2.2 Cluster surveys in the X-ray band

Cluster identification

As mentioned at the beginning of this section, clusters are multi-component systems. Approximately $80 - 85\%$ of their mass is provided by DM, while only the $2 - 5\%$ is constituted by cool baryons in stars and galaxies. The remaining $\sim 15\%$ of the mass is provided by the diffuse Intracluster Medium (ICM). The ICM is a plasma, mostly composed by hydrogen and helium, heated by the cluster's gravitational energy at temperatures of $k_B T \simeq 2 - 10\,\mathrm{keV}$ (or $T \simeq 10^7 - 10^8\mathrm{K}$). At

these temperatures the gas light up in the X-ray band mainly due to the thermal bremsstrahlung emission, and, to a lesser extent, to emission lines of heavy elements and recombination processes. This allows to detect galaxy clusters as extended X-ray sources with a typical luminosity of $L_X \sim 10^{43} - 10^{45} \mathrm{erg\,s^{-1}}$. Furthermore, being the bremsstrahlung emissivity proportional to the square of the gas density, and given the relatively low surface density of X-ray sources, clusters are observed as high contrast objects in the X-ray sky, making X-ray selection less prone to projection effects than the optical one. On the other hand, the concentration of the X-ray emission could represent a problem for the detection of the faintest objects which are usually distinguished from point sources – mostly active galactic nuclei and star-forming galaxies – with proper detection algorithms (e.g. Rosati et al., 1995; Vikhlinin et al., 1998; Lazzati et al., 1999). Another inherent fundamental advantage of X-ray selection is the ability to define flux-limited samples with well-understood selection functions. The latter depends on the survey strategy and on the details of the adopted cluster finding algorithm (see Rosati et al., 2002, for a review). In particular, the effective area covered by a X-ray survey as a function of the flux (*sky coverage*) depends on the exposure time across the observed area, the degradation of the PSF[2] across the field of view and background noise, both instrumental and from unresolved astrophysical X-ray sources. Once the survey flux-limit and *sky coverage* are defined it is possible to compute the survey volume, which allows a reliable comparison between the theoretical and the observed cluster space density.

The first cluster catalogues used for cosmological studies were built using data from *Ariel V* and HEAO-1 all-sky surveys, and follow-up observations by the *Einstein Observatory* and *EXOSAT* (Edge et al., 1990; Gioia et al., 1990). In the 90's, the lunch of the ROSAT satellite allowed a significant step forward in X-ray surveys of clusters, thanks to the unprecedented sensitivity and spatial resolution, as well as low instrumental background, of its detector. The ROSAT all-sky surveys (RASS; Voges et al. (1999)) yielded a number of cluster catalogues exploited for cosmology which include: the Brightest Cluster Sample (BCS; Ebeling et al. (1998)) for the northern hemisphere; the ROSAT-ESO flux limited X-ray (REFLEX; Böhringer et al. (2004)) cluster survey in the southern hemisphere; the HIFLUGCS (Reiprich and Böhringer, 2002) and Massive Cluster Survey (MACS; Ebeling et al. (2010)) sample of X-ray brightest clusters at high Galactic latitudes. A number of X-ray cluster

[2]The Point Spread Function characterizes the response of an imaging instrument to a point source. For extended sources the observed image corresponds to the convolution of the PSF with the real image of the objects.

catalogues have also been constructed based on serendipitous discoveries in the pointed phase of the ROSAT mission, which covers much smaller areas than the RASS, but reach an order of magnitude or more fainter in flux. Notable among these are the ROSAT Deep Cluster Survey (RDCS; Rosati et al. (1998)) and the 400 Square Degree ROSAT PSPC Galaxy Cluster Survey (400d; Burenin et al. (2007)), both used to derive cosmological constraints. The sample of 1743 clusters identified by means of the all-sky survey and pointed observations of the ROSAT satellite are collected in the meta-catalogue MCXC by Piffaretti et al. (2011).

The current generation of X-ray satellites XMM-Newton, Chandra, and Suzaku, thanks to their improved angular and spectral resolution, have been extensively employed in follow-up observations to obtain spatially resolved spectra of individual clusters (e.g. Vikhlinin et al., 2009a; Pratt et al., 2010; Mantz et al., 2010; Arnaud et al., 2010). The XMM-Newton satellite has been used also to perform a number of cluster surveys, including: the XMM Cluster Survey (Romer et al., 2001), a serendipitous survey aimed at the detection of all galaxy clusters in all XMM archive fields, the multi-wavelength XMM Large-Scale Structure survey (Pierre et al., 2006), and the XMM Distant Cluster Project, a serendipitous survey dedicated to find and study clusters of galaxies at $z > 1$ (Fassbender, 2008). Moreover, several other studies have been carried out using XMM-Newton, Chandra, and the Swift/X-ray (deep) observations of small contiguous areas of the sky (e.g. Finoguenov et al., 2010; Adami et al., 2011) or pointed observations (e.g. Barkhouse et al., 2006; Peterson et al., 2009; Mehrtens et al., 2012; Tundo et al., 2012), providing cluster samples up to few hundreds objects and up to redshift $z \simeq 1.6$.

Masses from X-ray observations

For survey observations, the primary X-ray observables are flux, spectrum and spatial extent. The X-ray emitting ICM, tracing the matter inside clusters, provides information on the morphology of the system. Moreover, the dominant bremsstrahlung emissivity at frequency ν is proportional to:

$$\epsilon_\nu \equiv \frac{\mathrm{d}L}{\mathrm{d}V\mathrm{d}\nu} \propto n_e^2 g(\nu, T) T^{-1/2} \exp(-h\nu/k_B T) \tag{2.3}$$

where n_e is the number density of electrons and $g(\nu, T) \propto \ln(9k_B T/4h\nu)$ is the Gaunt factor. Therefore, the measured X-ray luminosity (L_X) of the cluster can be used to infer the mean temperature and density of the ICM, or, if spatially resolved spectra are available, their radial profiles. Under the assumption of a spherically symmetric distribution and hydrostatic equilibrium of the ICM, the measured gas

density and temperature profiles can be related to the total mass within the radius r through the formula:

$$M(<r) = -\frac{r}{G}\frac{k_B T(r)}{\mu m_p}\left(\frac{\mathrm{d}\ln\rho_{\rm gas}(r)}{\mathrm{d}\ln r} + \frac{\mathrm{d}\ln T(r)}{\mathrm{d}\ln r}\right), \tag{2.4}$$

with μ the mean molecular weight and m_p the proton mass. Thanks to the sensitivity of Chandra and XMM-Newton X-ray observatories, out to intermediate radii, measurements of the gas temperature and density profiles are possible for a fair number of clusters. While at larger radii ($r \gtrsim r_{500}$), where the X-ray emission is faint, the low and stable particle background of Suzaku allows the observation of the ICM emission in the cluster outskirts. Two main approaches are used to estimate hydrostatic masses. One uses parametrized fits to the observed projected surface brightness and spectral temperature data to compute the derivatives of Eq. (2.4) and thus the mass profile. A second approach assumes a functional form for the density profile (e.g. Navarro et al., 1997) and estimates the gas density profile from the measured X-ray surface brightness to recover the temperature profile from Eq. (2.4). The mass profile parameters are thus obtained by a χ^2 analysis of the recovered temperature profile and that measured from the spectral data. Hydrostatic mass measurements suffer for different sources of systematic biases, e.g. associated to departures from spherical symmetry, to biases in X-ray measurement of gas temperature (e.g. Mahdavi et al., 2008; Rasia et al., 2012), and, especially, to violation of hydrostatic equilibrium due to the presence non-thermal pressure support (e.g. Laganá et al., 2010; Shi and Komatsu, 2014). Comparison between hydrostatic and weak lensing masses indicates biases up to 20% between the two mass estimates, which tend to vanish when considering only the more relaxed systems (e.g. Mahdavi et al., 2013; Israel et al., 2014; Donahue et al., 2014).

Temperature profiles can be obtained only for a small number of clusters due to the long exposure time required. Indeed, while $\sim 10^2 - 10^3$ photons are sufficient to detect the cluster and measure its global temperature, reliable temperature profiles for hydrostatic mass measurements need $\sim 10^4$ photons. One of the main advantages of the X-ray selection is the observed strong correlation between X-ray observables – luminosity and temperature – and mass. These thigh relations among the observed cluster properties themselves ($L_X - T_X$) and mass ($L_X - M$, $T_X - M$) are expected for nearly self-similar systems, in which the thermodynamical properties of the ICM are determined only by gravity. In this case clusters of different sizes are the scaled version of each other, and so their observed properties. In the self-similar model, assuming spherical symmetry and hydrostatic equilibrium, the

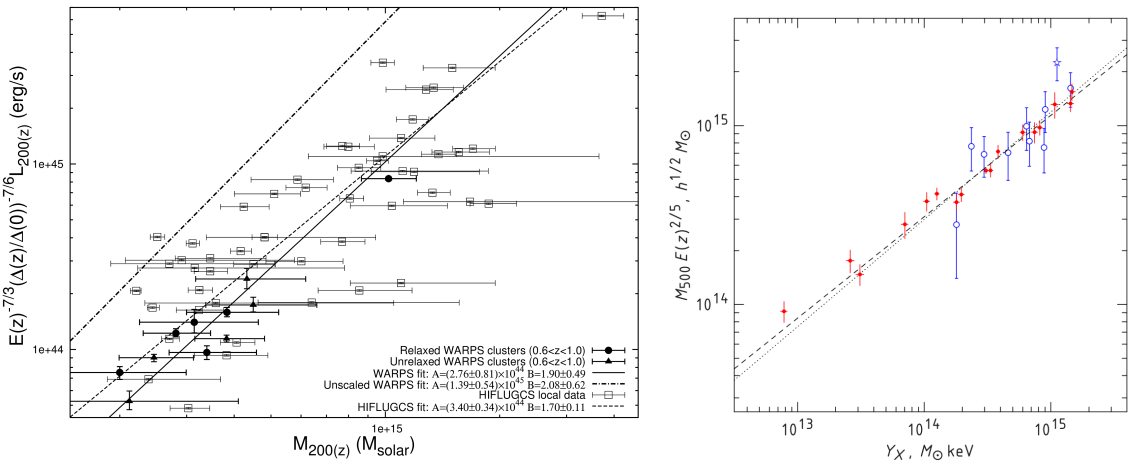

Figure 2.6: *Left* panel: $L_X - M_{200}$ relation for X-ray selected low-z HIFLUGCS and high-z WARPS clusters. Masses were estimated using hydrostatic equilibrium within $R_{200,c}$ and the luminosities within the same radius were scaled by the evolutionary factor predicted by the self-similar model. *Solid* and *dashed* lines correspond to the best-fit to the high-z and low-z sample, respectively. The *dot-dashed* line is the best-fit to the unscaled high-z sample and can be used to quantifies the goodness of the self-similar scaling. Image from (Maughan et al., 2006). *Right* panel: $M_{500} - Y_X$ relation obtained from 17 low-z, relaxed clusters observed with Chandra (Vikhlinin et al., 2009a). The hydrostatic masses in the y-axis are scaled by the evolutionary factor predicted by the self-similar model. The *dashed* and *dotted* line show a power low fit with free slope and fixing the slope to the self similar value, respectively. Also shown in the plot with open points are weak lensing mass measurements from Hoekstra (2007).

following relations hold:

$$M \propto T_X^{3/2} E(z)^{-1}\,, \quad L_X \propto T_X^2 E(z)\,, \quad M \propto L_X^{3/4} E(z)^{-7/4} \tag{2.5}$$

where $E(z)$ is the evolutionary factor given in Eq. (1.14) and the second and third relations hold for pure thermal bremsstrahlung emission. Several groups calibrated these relations observationally finding departures from the self-similar expectations. In particular, the $L_X - T_X$ relation exhibits a steeper slope than expected in the self-similar model ($L_X \propto T_X^{2.5-3}$) with a large scatter, unless of excising the contribution to the luminosity from the cluster central region which is often affected by radiative cooling (e.g. Markevitch, 1998; Pratt et al., 2009; Maughan et al., 2012). As

for the $L_X - M$ relation (and thus the $T_X - M$ relation) observations confirmed the correlation between X-ray luminosity and mass, although with some scatter and a slope slightly steeper than the self-similar scaling (see *left* panel of Figure 2.6), consistently with what found for the $L_X - T_X$ relation. Another X-ray mass proxy proposed by Kravtsov et al. (2006), and used in the analysis of Chapter 5, is the quantity $Y_X = M_{\rm gas} \times T_X$, which approximates the total thermal energy of the ICM. The goodness of this mass proxy relies on the fact that the total thermal energy is weakly disturbed by merger events. In the simplest self-similar model Y_X scales with the cluster mass as $M \propto Y_X^{3/5} E(x)^{-2/5}$. Hydrodynamical simulations (e.g. Nagai et al., 2007; Fabjan et al., 2011) and observations (e.g. Arnaud et al., 2007; Pratt et al., 2009) confirmed the expected self-similar scaling and the low scatter of the proxy (see *right* panel of Figure 2.6), and importantly, the low sensitivity of $Y_X - M$ relation to the dynamical state of the cluster. The agreement with the self-similar model further improve if Y_X is computed using T_X measured excising the core regions ($r \lesssim 0.15 R_{500}$) where the clusters is often affected by radiative cooling (Kravtsov and Borgani, 2012).

2.2.3 SZ cluster surveys

Cluster identification

We have seen in §2.1.1 that the SZ effect induces a distortion of the spectrum of CMB photons passing through the hot ICM. The magnitude of the SZ effect, which depends on the probability that a photon is scattered by an electron of the ICM ($\sigma_{\rm T} n_e$; see §1.2.2) and the fractional amount of energy gained in the interaction ($\Delta E/E = k_B T_e / m_e c^2$), is quantified by the Compton y-parameter:

$$y = \int {\rm d}l \frac{k_B T_e}{m_e c^2} n_e \sigma_{\rm T} \,, \tag{2.6}$$

where the integral is along the line of sight, and T_e, m_e and n_e are the electron temperature, mass and density, respectively. The temperature difference induced by the SZ effect relative to the mean CMB temperature, $T_{\rm CMB}$, is equal to:

$$\Delta T_{\rm SZ} = T_{\rm CMB} \cdot f_{\rm SZ}(\nu) \cdot y \,, \tag{2.7}$$

where $f_{\rm SZ}(\nu)$ encodes the distinctive frequency dependence of the thermal SZ effect, which leads to a decrement of the CMB intensity at $\nu \lesssim 220\,{\rm GHz}$, and a to corresponding increase above this frequency. Worthy of note, $\Delta T_{\rm SZ}$, which is proportional to the cluster pressure along the line of sight, is independent of redshift.

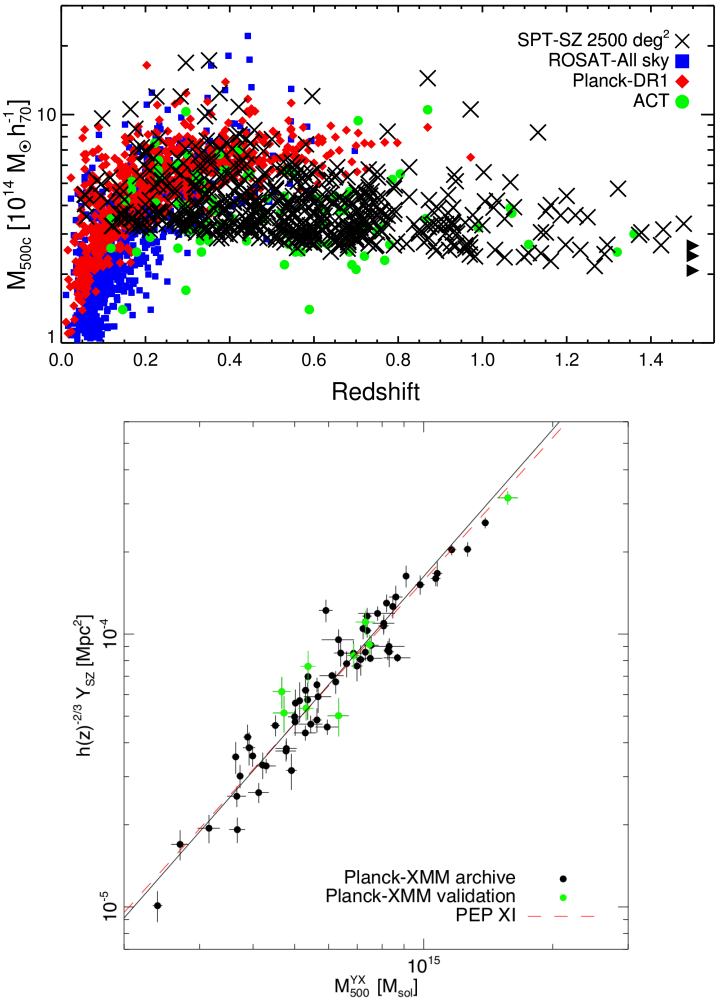

Figure 2.7: *Upper* panel: Comparison of SZ and X-ray cluster catalogues in the mass-redshift plane. Different marks correspond respectively to: 516 optically confirmed clusters from the 2500 deg^2 SPT-SZ catalogue (*crosses*; Bleem et al., 2014); 91 clusters from ACT survey (*points*; Hasselfield et al., 2013); 809 SZ-selected clusters from the Planck survey (*diamonds*; Planck Collaboration, 2013b); 740 X-ray selected clusters from the RASS (*squares*; Piffaretti et al., 2011). While the SPT and ACT data provide a nearly mass-limited samples, the cluster samples selected from ROSAT and Planck data are redshift-dependent owing to cosmological dimming of X-ray emission and the dilution of the SZ signal by the large Planck beams, respectively. Image from Bleem et al. (2014). *Lower* panel: $Y_{SZ} - M_{500}$ relation obtained from a sub set of 71 SZ-Planck clusters for which good quality XMM-Newton observation are available. Masses were estimated using the Y_X mass-proxy within r_{500}, while the integrated Comptonisation Y_{SZ} within the same radius is multiplied by the self-similar scaling in the y-axis. The *dashed* best fit line , obtained correcting the clusters flux for selection bias, has a slope of 1.79, slightly steeper than what expected (5/3) in the self-similar model . Figure from Planck Collaboration (2013b).

In other words, the SZ signal does not undergo surface brightness dimming, like the optical and X-ray ones, providing mass-limited cluster samples nearly independent of redshift (see *upper* panel of 2.7). The observed temperature distortions in the CMB caused by the thermal SZ effect are small, typically on the level of hundreds of μK for the most massive clusters. The development over the past decades of high-sensitivity bolometric cameras has enabled in 1999 the first spatially resolved observation of the SZ effect in a cluster (Komatsu et al., 1999; Pointecouteau et al., 1999), and in 2009 the first discovery of a previously unknown cluster in a blind SZ survey (Staniszewski et al., 2009). Nowadays, such discoveries have become routine, with catalogues produced by the ACT (Hasselfield et al., 2013), SPT (Bleem et al., 2014) and Planck (Planck Collaboration, 2013b) containing tens to hundreds of massive clusters out to $z \sim 1.5$ (*upper* panel of 2.7). Most of the detection algorithms are based on the matched-filter approach which, given priors on the cluster spectral and spatial characteristics, uses filters designed to maximize the SZ contrast over a set of observations containing contaminating signals (e.g. Melin et al., 2006). As for the cluster redshift, it is not directly measurable from the SZ map, and optical or X-ray follow-up observations are always necessary.

SZ-mass scaling relation

For every cluster detected in a SZ map it is possible to measure the integrated Comptonisation parameter Y_{SZ} over the solid angle $\Delta\Omega$ subtended by the object:

$$Y_{SZ} = \int_{\Delta\Omega} y \mathrm{d}\Omega = \frac{1}{D_A(z)^2} \frac{\sigma_T}{m_e c^2} \int k_B n_e T_e \mathrm{d}V \,, \tag{2.8}$$

where $D_A(z) = (1+z)r(z)$ is the cosmology dependent angular diameter distance. The volume integral of the electron pressure, $P_e = k_B n_e T_e$, in the r.h.s. of Eq. (2.8) corresponds to the total energy density of the ICM. Therefore, the parameter Y_{SZ} is expected to be strongly correlated to the cluster mass through the virial theorem, and relatively insensitive to the dynamical state of the system. Assuming hydrostatic equilibrium of the ICM and a self-similar model, the $Y_{SZ} - M$ scaling relation reads:

$$D_A(z)^2 Y_{SZ} \propto M^{5/3} E(z)^{2/3} \,. \tag{2.9}$$

Hydrodynamical simulations (e.g. Sehgal et al., 2010; Kay et al., 2012) and observations (Arnaud et al., 2010; Marrone et al., 2012) concordantly, show small departures from the simplest self-similar scaling (see *lower* panel of Figure 2.7), while the actual scatter ($\sim 20\%$) is usually larger than what predicted by hydrodynamical simulations. This increase is partially due to contaminations from small halos

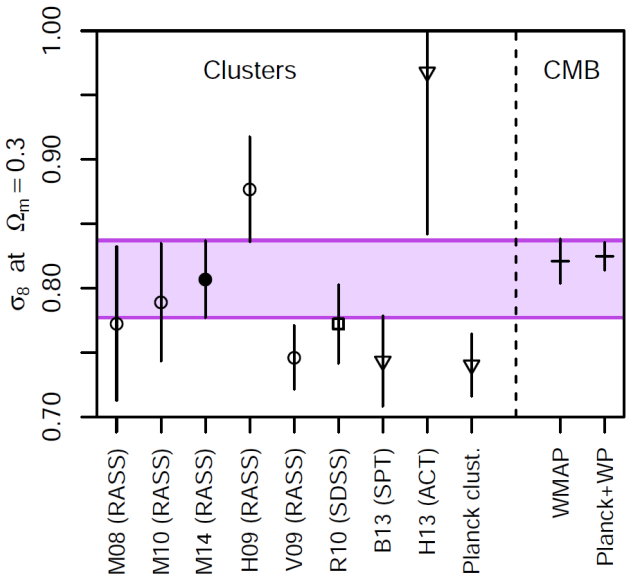

Figure 2.8: Comparison of a number of constraints on σ_8 at the common value of $\Omega_m = 0.30$, obtained from cluster datasets and CMB surveys: M08, Mantz et al. (2008); M10, Mantz et al. (2010); M14, Mantz et al. (2014); H09, Henry et al. (2009); V09, Vikhlinin et al. (2009b); R10, Rozo et al. (2010); B13, Benson et al. (2013); H13, Hasselfield et al. (2013); WMAP, Hinshaw et al. (2013); Planck+WP, Planck Collaboration (2013d). The shaded, horizontal band reflects the 68.3% confidence interval obtained by Mantz et al. (2014). Figure from Mantz et al. (2014).

along the line of sight, which are not resolved in SZ observations but contribute to the total signal.

2.2.4 Cosmological constraints from cluster surveys

Current constraints on cosmological parameters from cluster surveys are mainly obtained comparing the observed cluster abundance with the theoretical one. The latter is specified for a given cosmological model by the HMF, $n(M,z)$ (see §1.3.2), the comoving volume element, $\mathrm{d}V/\mathrm{d}z\mathrm{d}\Omega$, and the survey completeness, $X(M,z,\mathbf{\Omega})$ – which depends on the strategy and specifics of the survey– through the equation:

$$N_{i,j} = \int_{z_i}^{z_{i+1}} \mathrm{d}z \int_{\Delta\Omega} \mathrm{d}\Omega \frac{\mathrm{d}V}{\mathrm{d}z\mathrm{d}\Omega} \int_{M_j}^{M_{j+1}} dM\, X(M,z,\mathbf{\Omega})\, n(M,z)\,. \tag{2.10}$$

Table 2.2: Constraints at 68% C.L. on the cluster normalization condition, $\sigma_8\Omega^\alpha$, obtained from X-ray, optical and SZ cluster surveys assuming a ΛCDM model. The 4$^{\text{th}}$ and 5$^{\text{th}}$ columns present constraints for single parameter extensions to the standard ΛCDM model: the total neutrino mass, $\sum m_\nu$, and the dark energy equation of state (EoS), $w \equiv P_{\text{de}}/\rho_{\text{de}}$. Parameters listed without error bars are kept fixed in the analysis to the standard ΛCDM value. Upper limits are at 95% C.L.

Data	$\sigma_8(\Omega_{\text{m}}/0.27)^\alpha$	α	$\sum m_\nu$	w
X-ray (RASS) (Mantz et al., 2014)	0.82 ± 0.03	0.17	$< 0.22\,\text{eV}^{ab}$	-0.98 ± 0.15
X-ray (RASS) (Henry et al., 2009)	0.90 ± 0.04	0.30	0.0 eV	-1
X-ray (RASS) (Vikhlinin et al., 2009b)	0.784 ± 0.027	0.47	0.0 eV	-1.08 ± 0.15^c
Optical (SDSS) (Rozo et al., 2010)	0.806 ± 0.033	0.41	0.0 eV	-1.05 ± 0.34^c
SZ (SPT) (Benson et al., 2013)	0.767 ± 0.037	0.30	$0.12 \pm 0.9\,\text{eV}^{cd}$	-1.09 ± 0.36^{de}
SZ (ACT) (Hasselfield et al., 2013)	0.768 ± 0.025	0.30	$< 0.57\,\text{eV}^c$	-1.05 ± 0.11^c
SZ Planck Collaboration (2013a)	0.764 ± 0.025	0.30	$0.40 \pm 0.21\,\text{eV}^a$	-1

Note: ^{a} combined with Planck+WP data; ^{b} combined with ACT and SPT data (HighL); ^{c} combined with WMAP 7-year data (Komatsu et al., 2011); ^{d} combined with H_0 prior from HST (Riess et al., 2011); ^{e} combined with BBN prior on $\Omega_{\text{b}}h^2$ from Kirkman et al. (2003)

where $\Delta\Omega$ is the solid angle covered by the survey, and the subscripts i, j refer to the redshift and mass bin considered, respectively. This probe is particularly effective in constraining the parameters combination $\sigma_8\Omega_m^\alpha$, for which some recent results are presented in Table 2.2 and shown in Figure 2.8. Besides few exceptions, optical, X-ray and SZ surveys provide consistent results, which are, however, in tension with the most recent Planck CMB constraints for the standard ΛCDM model ($\sigma_8(\Omega_{\text{m}}/0.27)^{0.3} = 0.868 \pm 0.016$; Planck Collaboration, 2013d). This tension suggests either the need for new physics, systematics in the measurements, or a combination thereof; in Chapter 5 a detailed analysis of this issue is presented. The contribution of cluster surveys to cosmology is better seen in combination with other probes (e.g. CMB and BAO), thanks to the different scales and redshifts probed by the former. In particular, probing the amplitude and the growth of the matter fluctuations, the cluster abundance is sensitive to those parameters beyond the six ΛCDM ones, which affect the late time evolution ($z \lesssim 2$) of the cosmic structures at cluster scales. Examples of these are the total neutrino mass, the dark energy EoS (see 4$^{\text{th}}$and 5$^{\text{th}}$ columns of Table 2.2), the grow rate index (e.g. Mantz et al., 2014) and the level of non-Gaussianities (e.g. Benson et al., 2013).

A complementary probe to the cluster abundance is the clustering of clusters.

The observed clustering properties can be compared to the theoretical expectations by means of the halo-mass bias and matter power spectrum (see §1.4 and §3.3.2). Currently, the constraining power of this probe is limited by the relatively small number of clusters detected within a survey and/or the uncertainties in the mass measurements, and only limited efforts have been done to measure it (e.g. Hütsi, 2010; Balaguera-Antolínez et al., 2011). However, for upcoming cluster surveys, like e-ROSITA or Euclid, the cosmological information carried by the clustering properties of galaxy clusters is expected to improve considerably the constraining power of these datasets (e.g. Sartoris et al. 2012; see also Chapter 3).

2.3 Baryonic Acoustic Oscillations

In the last decade, the advent of large galaxy surveys provides a new robust method to measure cosmic distances alternative to the luminous-distance techniques such as those based on type Ia supernovae. As explained in §1.2.1, the acoustic oscillations of the baryon-photon plasma in the pre-recombination era imprint a characteristic scale in the clustering of matter – the BAO scale – determined by the distance travelled by the acoustic waves prior to the baryon-photon decoupling – the acoustic horizon, $r_s \simeq 150$Mpc (see e.g. Bassett and Hlozek, 2010, for a review). The exact size of this "standard ruler" depends on the baryon density and on the overall matter density. The baryon density affects the plasma inertia and hence its sound speed (Eq. (1.17)). The total matter density affects the cosmic expansion rate (Eq. (1.3)) and hence the redshift at which the baryon-photon decoupling occurs and the physical size of the BAO scale at different redshifts. The signal, therefore, relies on a simple, linear and well understood physics that can be calibrated by CMB anisotropy measurements and is quite insensitive to non-linear or astrophysical processing that typically occurs on much smaller scales. This makes experiments using the BAO signal relatively free of systematic errors, and moreover, provide a geometrical method to test cosmological models.

2.3.1 BAO scale detection and measurement

The challenge of this probe is primarily statistical: because this is a weak signal at a large scale, one needs to map enormous volumes of the universe of order $1[h^{-1}\text{Gpc}]^3$ to detect the BAO and obtain a precise distance measurement.

There are several tracers of the density field that can be used to this end. In general they are required to have: a strong spectroscopic signature to allow a fast

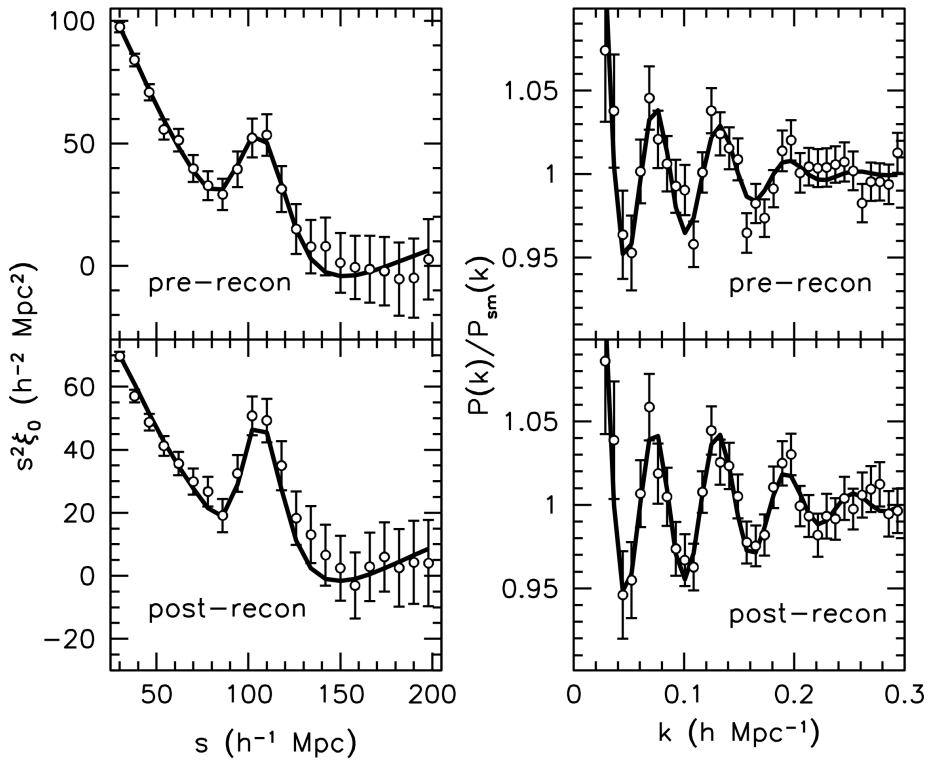

Figure 2.9: Two point correlation function (*left*) and power spectrum (*right*) as measured from the BOSS DR11 CMASS catalogue (*black* circles with error bars). The power spectrum is divided by a smoothed model without BAO to enhance the acoustic features. *Solid* lines show the best fit BAO model in each case. The top and bottom panels correspond to measurements obtained prior and after the reconstruction procedure, respectively. One can see that reconstruction has sharpened the acoustic features considerably for both $\xi(s)$ and $P(k)$. Figure from Anderson et al. (2014).

and accurate redshift determination; a high density and/or clustering bias, so that to reduce the Poisson noise and/or the required number density to detect the signal; and finally they should by easy to select. At low redshift ($z \lesssim 0.5$) Luminous Red Galaxies (LRGs) are an effective choice, thanks to their strong absorption feature (the 4000Å break), high surface brightness and high bias ($b \sim 2$). At redshift $z \gtrsim 1$, where the star formation rate of normal galaxies is ten time higher than the local one, emission-line galaxies become the ideal target. However, the low clus-

tering bias of these objects demands an higher target density compared to LRGs. Other possible tracers are clusters of galaxies and quasars; the former have a large bias but a low number density, the latter are particularly effective at high redshift being extremely luminous and easy to select. Cross-correlation among multiple sight-lines Ly-α forest in quasar spectra offers another possibility to probe the 3-dimensional structure between redshift $2 \lesssim z \lesssim 3$ (White, 2003; McDonald and Eisenstein, 2007). The challenge here is systematics, as one must control the continuum of the quasars emission and the spectrophotometry of the measurements, as well as possible theoretical systematics associated with the state of the intergalactic medium.

The BAO signal can be statistically measured from the two point correlation function[3], as a peak in correspondence of the acoustic scale, or from its Fourier transform, the power spectrum, where the single acoustic scale gives rise to a harmonic sequence of oscillations (see *top* panels of Figure 2.9). The statistical sensitivity of BAO measurements is limited by non-linear structure formation: non-linearities not only shift the peak position, but also smooth out and broaden the peak of the correlation function. This issue is commonly overcome applying a procedure to reconstruct the linear density field (e.g. Eisenstein et al., 2007; Padmanabhan et al., 2012, ; see *lower* panels of Figure 2.9). Briefly, the reconstruction procedure attempts to partially reverse the effects of non-linear growth of structure and large-scale peculiar velocities, using the measured galaxy density field and Lagrangian theory relations between density and displacement.

Depending on whether the separation is along the line of sight or in the transverse direction, distances in cosmology are measured in two different ways. Separations in the radial direction are estimated by measuring differences in cosmological redshift, $r_{||}(\bar{z}) = c\Delta z / H(\bar{z})$, while separations in the transverse direction are inferred by measuring angles in the sky, $r_{\perp}(\bar{z}) = (1+\bar{z}) D_A(\bar{z}) \Delta\Theta$. Thus, the BAO scale measured along the line of sight at the mean ensemble redshift $\bar{z}$ provides constraints on the Hubble parameter $H(\bar{z})$, while the transverse mode provides a measurements of the angular diameter distance $D_A(\bar{z})$. In the past, limited survey volume has made it difficult to analyse the differential clustering along the line of sight and transverse directions. As a result, most BAO analyses have been based on the spherically-averaged clustering statistics (e.g. Percival et al., 2010; Anderson et al., 2012; Padmanabhan et al., 2012), which only allow to measure $D_V(z)$, the

[3]The two point correlation function quantifies the excess clustering on a given scale relative to a uniform distribution with the same mean density.

spherically-averaged distance to redshift z, defined as

$$D_V(z) = \left[cz(1+z^2)D_A(z)^2 H(z)^{-1}\right]^{1/3} . \quad (2.11)$$

However, $H(z)$ is degenerate with $D_A(z)$ in this isotropic analysis, preventing a direct measurements of the expansion rate of the Universe. Moreover, the clustering of galaxies is not truly isotropic, as assumed in Eq. (2.11), due to both large-scale RSD and from assuming the wrong cosmology when calculating the 2-point statistic (Alcock and Paczynski, 1979). More recently, thanks to the larger volume probed by current galaxy surveys (e.g. SDSS-III), it has been possible to measure the anisotropic BAO signal and exploit the additional cosmological information to break the $H(z) - D_A(z)$ degeneracy (Beutler et al., 2013; Anderson et al., 2014, ; see Figure 2.10).

2.3.2 Current constraints from BAO scale measurements

The baryon acoustic peak method has become one of the most promising ways of studying the geometry of the Universe and the nature of dark energy. It complements the study of distant type Ia supernovae that discovered dark energy in the first place. The supernovae are easiest to measure at low redshift, where the total cosmic volume limits the acoustic peak method, while the latter gains in precision at higher redshift.

The first convincing detections of BAO came in 2005 from the SDSS Data Release 3 (DR3) and the final 2dFGRS samples (Eisenstein et al., 2005; Cole et al., 2005), providing constraints on both curvature and dark energy EoS parameters. Since these first detections, the clustering of successively larger SDSS spectroscopic samples has been analysed by several groups using different methods (e.g. Hütsi, 2006; Percival et al., 2010), reaching a precision of 1.9% in the measurement of the spherically-averaged distance D_V, applying the reconstruction technique (Padmanabhan et al., 2012; Xu et al., 2013). New BAO detections have recently been made in three other samples. Beutler et al. (2011) report a 2.4σ detection from the 6dFGS, obtaining a 4.5% distance measurement to $z = 0.1$, which combined with WMAP 7-years data (Komatsu et al., 2011) provide the constraints $w = -0.97 \pm 0.13$. Analysing data from the WiggleZ survey, Kazin et al. (2014) measured D_V in three redshift slices centred on $z = 0.44$, 0.60, and 0.73, with an accuracy of 4.8, 4.5 and 3.4 percent, respectively. Combining these data with Planck CMB measurements the authors obtained $w = -1.18^{+0.36}_{-0.19}$ and $100\Omega_k = -0.64^{+0.62}_{-0.55}$ assuming a wCDM or an open ΛCDM model. At the time of writing this Thesis, the state of the art in

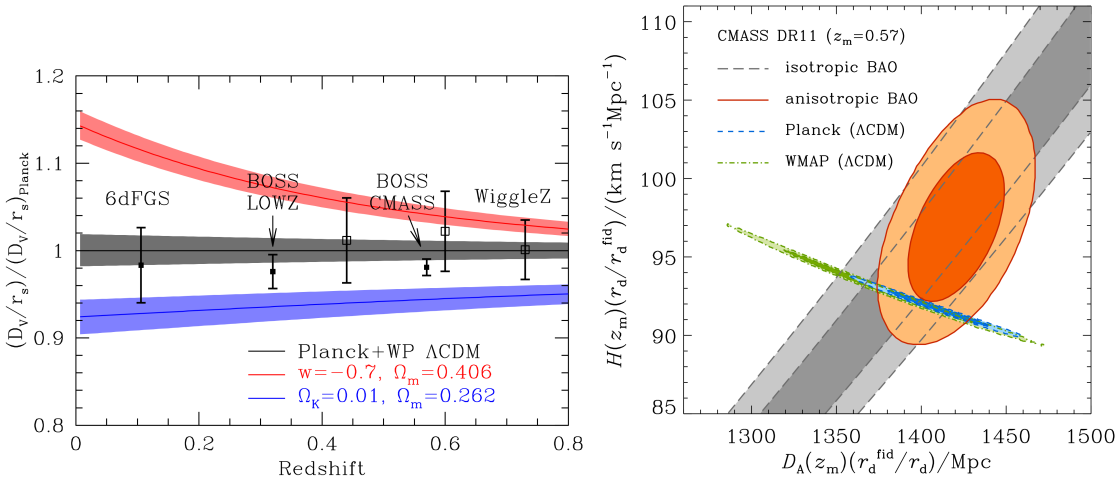

Figure 2.10: *Left* panel: the D_V/r_s measured from three recent galaxy surveys, divided by the best-fit flat ΛCDM prediction from the Planck data. Also shown in the figure to illustrate the capability of BAO measurements in constraining the dark energy EoS and curvature parameters, are the Planck results assuming a flat model with $w = -0.7$, as well as that for a closed ΛCDM Universe with $\Omega_k = -0.01$. All error bars are shown at 1σ. *Right* panel: comparison of the 68% and 95% confident regions in the $D_A(z = 0.57) - H(z = 0.57)$ plane obtained from the high-z BOSS sample ($\bar{z} = 0.57$) considering the isotropic (*grey* contours) or the anisotropic (*orange* contours) BAO signal. Also shown with *green* and BLUE contours the constraints from WMAP 9-years and Planck. Figures from Anderson et al. (2014).

BAO scale measurements is provided by SDSS-III BOSS DR11 sample, which contains nearly 10^6 galaxies in the redshift range $0.2 < z < 0.7$ across 8500deg^2. From the analysis of this survey Anderson et al. (2014) obtained 1% and 2% accuracy distance measurements at the median redshift $z = 0.57$ and $z = 0.32$; combined with Planck data these BAO measurements constrain the dark energy EoS and the curvature parameter to $w = -1.19 \pm 0.15$ and $100\Omega_k = 0.17 \pm 0.51$, respectively. Moreover, extracting the anisotropic BAO signal from the high-z BOSS sample further improves the constraints, yielding $w = -1.07 \pm 0.09$ and $100\Omega_k = 0.06 \pm 0.18$.

In the *left* panel of Figure 2.10 are shown the spherically-averaged distances D_V measured by these three galaxy surveys along with the Planck prediction for a ΛCDM model (*grey* shaded region). All the BAO results are consistent among them and with the Planck CMB measurements. Also shown in the Figure 2.10

to illustrate the utility of BAO measurements for constraining the w and Ω_k parameters, are the Planck predictions for a wCDM model with $w = -0.7$ (*red* shaded region) and a closed ΛCDM Universe with $\Omega_k = -0.01$ (*blue* shaded region). In the *right* panel of Figure 2.10 are compared the 68% and 95% confidence regions in the $D_A(z) - H(z)$ plane obtained from the isotropic (*grey* contours) and anisotropic (*orange* contours) BAO analysis of the high-z BOSS sample (CMASS). The anisotropic BAO signal partially breaks the $D_A(z) - H(z)$ degeneracy allowing to place individual constraints on the two parameters.

Finally, even if with a lower statistical significance, the BAO signal has been detected also in the distribution of clusters (Hütsi, 2010; Veropalumbo et al., 2014), and at high redshift, $z \gtrsim 2$, using the Ly-α forest in quasar spectra (e.g. Slosar et al., 2013; Delubac et al., 2014) and cross-correlation between quasars and the Ly-α forest (Font-Ribera et al., 2014), finding consistent and competitive results with the BAO scale measurements performed with other tracers.

Redshift Space Distortions

Another observable provided by galaxy surveys is the Redshift Space Distortion (RSD). The radial distance of a galaxy is derived by measuring its redshift, which depends on its relative velocity with respect to the observer, and so include both the Hubble recession and its peculiar velocity. The line of sight component of this additional velocity cannot be easily separated from the Hubble flow and contaminates the measurement of radial separations between galaxies, making the observed clustering of galaxies anisotropically distorted. These distortions are referred to as RSDs (see Hamilton, 1998, for a review). The anisotropic pattern of RSDs in galaxy clustering allows to extract information on the peculiar velocities which are directly related to the gravitational potential perceived by the galaxies. Given the amount of matter in the Universe, the theory of general relativity provide a clear and testable prediction for the amplitude of this anisotropic signal, which can be used to constrain the parameters combination:

$$f(z)\sigma_8(z) = \frac{\mathrm{d}\sigma_8(z)}{\mathrm{d}\ln a}\,. \tag{2.12}$$

In the last decade, galaxy redshift surveys became large enough to test this prediction and make RSD measurements useful to place constraints on the cosmological growth rate (e.g. Peacock et al., 2001; Hawkins et al., 2003; Guzzo et al., 2008; Blake et al., 2011; Samushia et al., 2012; Beutler et al., 2012; Reid et al., 2012; Chuang et al., 2013). Latest RSD constraints on the growth rate are provided by Beutler

et al. (2013) using $\sim 7 \times 10^5$ galaxies in the redshift range $0.43 < z < 0.7$ detected within the SDSS-III BOSS survey. The authors obtain $f\sigma_8 = 0.419 \pm 0.044$ at the effective redshift $z_{\rm eff} = 0.57$; this result, as well as most growth of structure constraints obtained in other galaxy surveys or using different low-redshift probes (e.g. cosmic shear and cluster abundance), lies below the Planck prediction for a ΛCDM model.

2.4 Cosmic shear

The cosmic shear denotes tiny shape distortions of distant galaxy images that arise from gravitational lensing of light by the LSS of the Universe. It is a cumulative, anisotropic gravitational shear effect that a light bundle experiences by passing through cosmic structures on the way from the galaxy to the observer. This well understood physical effect, potentially, is one of the most powerful probes of cosmology, allowing not only the direct study of dark matter, but also, through the study of the growth of structures, a unique probe of gravity and dark energy on large scales. However, shortly after its first detection, cosmic shear has turned out to be one of the most challenging signal to be interpreted for cosmological parameter inference (see e.g. the reviews by Hoekstra and Jain, 2008; Weinberg et al., 2013, and references therein).

2.4.1 Cosmic shear principles

Although the lensing effect is very weak, it modifies the shapes of galaxies in a coherent manner and can therefore be detected, analysed statistically, and interpreted within a cosmological model. The coherent distortion of background images (shear) can be related to the underlying matter density distribution through the theory of general relativity (e.g. Bartelmann and Schneider, 2001, for a detailed review). Briefly, under the weak field and Born approximations, the deflection angle of a light ray, $\delta\vec{\vartheta}$, arising from all the potential gradient along the line of sight, $\nabla_\perp \Phi(\chi)$, between the observer and the source is given by:

$$\delta\vec{\vartheta} = \vec{\vartheta}_I - \vec{\vartheta}_S = \frac{2}{c}\int_0^{\chi_S} \mathrm{d}\chi \frac{D_A(\chi_S - \chi)}{D_A(\chi_S)} \nabla_\perp \Phi(\chi)\,, \tag{2.13}$$

where $\vec{\vartheta}_I$ and $\vec{\vartheta}_S$ are the observed image and true source positions in the sky, and the integral is computed along the radial distance, χ, between the observer and the source, χ_S. Eq. (2.13) clearly shows that the weak lensing distortions are related

to the projected gravitational potential along the line of sight. However, since we only know the position of the observed image but not true position of the source, the deflection angle cannot be directly measured. The observable quantities are the distortions, $\partial\delta\vec{\vartheta}/\partial\vec{\vartheta}_I$, induced by these deflections, which at lowest order are given by the Laplacian of the so called deflection, or lensing, potential ψ:

$$\frac{\partial\delta\vec{\vartheta}}{\partial\vec{\vartheta}_I} = \frac{\partial^2\psi(\vec{\vartheta},\chi_S)}{\partial\vartheta_{Ii}\partial\vartheta_{Ij}} \equiv \psi_{,ij} \quad \text{with} \quad \psi(\vec{\vartheta},\chi_S) = \frac{2}{c}\int_0^{\chi_S} \mathrm{d}\chi \frac{D_A(\chi_S-\chi)}{D_A(\chi_S)D_A(\chi)}\Phi(D_A(\chi)\vec{\vartheta},\chi)\,. \tag{2.14}$$

Thus, in linear approximation, the remapping of the source's surface brightness into the image's surface brightness can be described by the Jacobian matrix:

$$\mathscr{A}(\vec{\vartheta}) = \frac{\partial\vec{\vartheta}_S}{\partial\vec{\vartheta}_I} = \left(\delta^D_{ij} + \psi_{,ij}\right) = \begin{pmatrix} 1-\kappa-\gamma_1 & -\gamma_2 \\ -\gamma_2 & 1-\kappa+\gamma_1 \end{pmatrix} \tag{2.15}$$

where we defined the convergence $\kappa = \nabla^2\psi/2$, and the complex shear $\gamma = \gamma_1 + i\gamma_2$, with $\gamma_1 = (\psi_{,11} - \psi_{,22})/2$ and $\gamma_2 = \psi_{,12}$. Note that in Fourier space holds the relation $\hat{\gamma}(\boldsymbol{\ell}) = -1/2(\ell_1 + i\ell_2)^2\hat{\psi}(\ell) = e^{i2\alpha}\hat{\kappa}(\boldsymbol{\ell})$. In the weak lensing regime, the convergence quantifies the magnification of an image, while the shear gives the ellipticity induced on an initially circular image. From Eq. (2.14) and the Poisson equation ($\nabla^2\Phi = 3H_0^2\Omega_\mathrm{m}\delta/2a$; Eq. (1.8)), it follows that for a redshift distribution of sources $p[z(\chi)]\mathrm{d}\chi$, between $0 < z < z(\chi_\mathrm{max})$, the convergence is related to the matter density contrast, δ, through:

$$\kappa(\vec{\vartheta}) = \int \mathrm{d}\chi p[z(\chi)]\kappa(\vec{\vartheta},\chi) = \int_0^{\chi_\mathrm{max}} \mathrm{d}\chi W(\chi)\delta(D_A(\chi)\vec{\vartheta},\chi)\,, \tag{2.16}$$

where the weight $W(\chi)$ is the lens efficiency defined as:

$$W(\chi) = \frac{3H_0^2\Omega_\mathrm{m}}{2c^2a(\chi)}D_A(\chi)\int_\chi^{\chi_\mathrm{max}} \mathrm{d}\chi_S\, p[z(\chi_S)]\frac{D_A(\chi_S-\chi)}{D_A(\chi_S)}\,. \tag{2.17}$$

Taking the Fourier transform of $\kappa(\vec{\vartheta})$, and computing the angular convergence (or shear) power spectrum in the flat sky approximations one gets:

$$C_{ij}(\ell) = \frac{\langle\hat{\kappa}(\boldsymbol{\ell})\hat{\kappa}^*(\boldsymbol{\ell}')\rangle}{(2\pi)^2\delta^D(\boldsymbol{\ell}-\boldsymbol{\ell}')} = \frac{\langle\hat{\gamma}(\boldsymbol{\ell})\hat{\gamma}^*(\boldsymbol{\ell})\rangle}{(2\pi)^2\delta^D(\boldsymbol{\ell}-\boldsymbol{\ell}')} = \int_0^{\chi_\mathrm{max}} \mathrm{d}\chi \frac{W_i(\chi)W_j(\chi)}{D_A(\chi)^2}P_\delta\left(\frac{\ell}{D_A(\chi)},\chi\right) \tag{2.18}$$

where i and j denote the redshift bins the sources belong to. The power spectrum $C_{ij}(\ell)$, illustrated for a ΛCDM and wCDM model in Figure 2.11, can therefore be used to constrain the 3D matter power spectrum, P_δ.

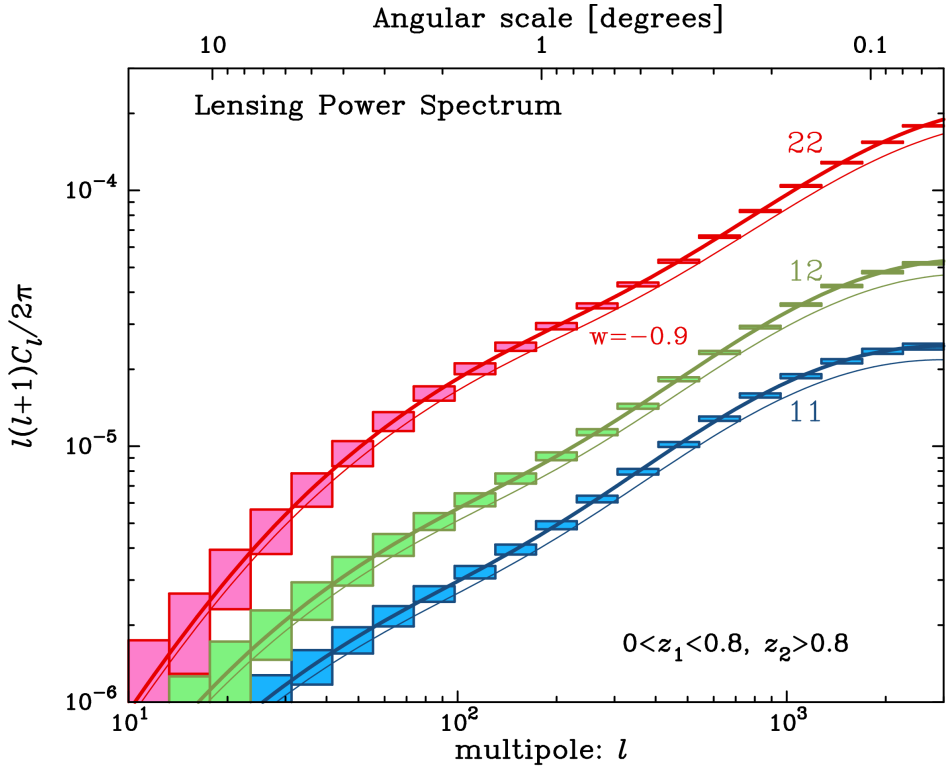

Figure 2.11: Shear power spectra obtained from a galaxy sample splits into two redshift bins. Shown are two auto-spectra, labelled (11) and (22), and one cross-spectrum, labelled (12), following the notation of Eq. (2.18). The solid curves are predictions for the fiducial WMAP 7-years ΛCDM model. The boxes show the expected measurement error considering the sample variance and intrinsic ellipticity errors (see Eq. (2.19)) for a 5000 deg^2 survey. To emphasise the capability of this probe in distinguish different dark energy models, the thin lines show the predictions for a model with $w = -0.9$. Figure from Hoekstra and Jain (2008).

2.4.2 Shear measurement

The cosmic shear signal can be measured only statistically correlating the ellipticities of a large number of galaxies. The observed ellipticity of a galaxy, $\epsilon_{\rm obs}$, is the result of the sum of its intrinsic ellipticity, $\epsilon_{\rm s}$, and the shear distortion, γ[4]. The observed angular two-point correlation function, $\hat{\xi}^{ab}(\vartheta)$, obtained averaging over

[4]For the sake of clarity here we assume the weak lensing limit: $\gamma, \kappa \ll 1$; the actual quantity which contributes to the observed ellipticity is the reduced shear $g = \gamma/(1-\kappa)$ (see Eq. (2.15))

all galaxy pairs (a, b) separated by angle ϑ, is thus related to the two-point shear correlation function $\langle \gamma^a \gamma^b \rangle$ through:

$$\hat{\xi}^{ab}(\vartheta) = \langle \epsilon^a_{\rm obs} \epsilon^b_{\rm obs} \rangle = \langle \epsilon^a_{\rm s} \epsilon^b_{\rm s} \rangle + \langle \epsilon^a_s \gamma^b \rangle + \langle \gamma^a \epsilon^b_{\rm s} \rangle + \langle \gamma^a \gamma^b \rangle \tag{2.19}$$

The function $\langle \gamma\gamma \rangle$, which corresponds to the Fourier transform of Eq. (2.18), is the quantity we want to measure being directly related to the underlying matter power spectrum of density fluctuations. However, the intrinsic alignment term $\langle \epsilon_{\rm s} \epsilon_{\rm s} \rangle$, and the shape-shear correlation term $\langle \epsilon_s \gamma \rangle$ cannot be neglected in tomographic or 3D shear measurements. In particular, the intrinsic alignment term arises from close pairs galaxies which could be aligned by the tidal forces of DM structures surrounding them; the shape-shear correlation term is relevant for galaxies separated by large physical distances, where the same structure responsible for the shear of the background galaxy causes the alignment of the nearby galaxy (Hirata and Seljak, 2004). The impact of the former can be mitigated, if redshift information is available, down-weighting the signal of physically close pairs (e.g. King and Schneider, 2002; Heymans and Heavens, 2003). The latter can be disentangled from the shear signal looking at the different redshift dependence of the two (e.g. Joachimi and Schneider 2008; cf. also Bridle and King 2007).

One of the most challenging task in the cosmic shear analysis is the shape measurements of faint galaxy images. The shape and the size of images are affected by the PSF of the telescope optics and, for ground based surveys, also by the atmospheric turbulence (the so called *seeing*). A number of techniques have been developed to address this problem, which can be divided in two classes. One class of methods is to measure moments of the galaxy image, and relate, e.g. the quadrupole moments, to the shear, given a model for the PSF (see Massey et al., 2007a, and references therein). The other class of methods starts with a set of models for a galaxy (e.g., an elliptical Sersić profile, or a linear combination of basis images), then simulates the observational procedure and finally performs a χ^2 analysis to find the model which best fits the data (e.g. Refregier, 2003; Miller et al., 2007). For both strategies to be efficient an exquisite knowledge of the PSF is required. Besides the aforementioned issue related to the PSF correction and intrinsic alignment contaminations, another sources of systematics in shear measurements is the photometric redshift error.

2.4.3 Recent results from cosmic shear surveys

The modern era of lensing studies was introduced by the availability of arrays of large-format CCDs. Cosmic shear was detected for the first time in 2000 by four

Table 2.3: A summary of cosmic shear results from optical survey. Note that some of the listed results are independent analyses or extensions of the same datasets and hence are not independent. Errors are to be intended at 68% C.L. if not otherwise stated.

Reference & Telescope/instrument	Result	
	ΛCDM model	extended models
Bacon et al. (2000) – WHT/EEV-CCD	$\sigma_8 = 1.5 \pm 0.5$ (@$\Omega_m = 0.3$)	
Van Waerbeke et al. (2000) – CFHT/UH8K	Detection[a]	
Wittman et al. (2000) – Blanco/BTC	Detection[b]	
Rhodes et al. (2001) – HST/WFPC2	$\sigma_8(\Omega_m/0.3)^{0.48} = 0.91^{+0.25}_{-0.30}$	
Hoekstra et al. (2002) – CFHT/CFH12K	$\sigma_8(\Omega_m/0.3)^{0.55} = 0.87^{+0.17}_{-0.23}$ (95%CL)	
Bacon et al. (2003) – Keck II/ESI + WHT	$\sigma_8(\Omega_m/0.3)^{0.68} = 0.97 \pm 0.13$	
Jarvis et al. (2003) – Blanco/BTC+MosaicII	$\sigma_8(\Omega_m/0.3)^{0.57} = 0.71^{+0.12}_{-0.16}$ (2σ)	
Hamana et al. (2003) – Subaru/SuprimeCam	$\sigma_8(\Omega_m/0.3)^{0.37} = 0.78^{+0.55}_{-0.25}$ (95%CL)	
Heymans et al. (2005) – HST/ACS	$\sigma_8(\Omega_m/0.3)^{0.65} = 0.68 \pm 0.13$	
Massey et al. (2005) – WHT/PFIC	$\sigma_8(\Omega_m/0.3)^{0.5} = 1.02 \pm 0.15$	
Semboloni et al. (2006) – CFHT/MegaCam	$\sigma_8 = 0.89 \pm 0.06$ @$\Omega_m = 0.3$	
Massey et al. (2007b) – HST/ACS	$\sigma_8(\Omega_m/0.3)^{0.44} = 0.866^{+0.085}_{-0.068}$	
Fu et al. (2008) – CFHT/MegaCam	$\sigma_8(\Omega_m/0.3)^{0.64} = 0.70 \pm 0.04$	
Schrabback et al. (2010) – HST/ACS	$\sigma_8(\Omega_m/0.3)^{0.51} = 0.75 \pm 0.08$	$w < -0.41$ (90%)CL
Huff (2012) – SDSS	$\sigma_8 = 0.636^{+0.109}_{-0.154}$ @$\Omega_m = 0.265$	
Lin et al. (2012) – SDSS	$\sigma_8(\Omega_m/0.3)^{0.7} = 0.64^{+0.08h}_{-0.12}$	
Jee et al. (2013) – Mayall+CTIO/Mosaic	$\sigma_8 = 0.833 \pm 0.034$[c]	
Kilbinger et al. (2013) – CFHT/MegaCam	$\sigma_8(\Omega_m/0.27)^{0.6} = 0.79 \pm 0.03$	$w = -0.72^{+0.20}_{-0.24}$,$100\Omega_k = -0.5 \pm 1.1$[d]
Heymans et al. (2013) – CFHT/MegaCam	$\sigma_8(\Omega_m/0.27)^{0.46} = 0.77^{+0.03}_{-0.04}$	$w = -1.05 \pm 0.33$,$100\Omega_k = -0.2 \pm 0.8$[d]
Kitching et al. (2014) – CFHT/MegaCam	$\sigma_8(\Omega_m/0.27)^{0.46} = 0.69 \pm 0.22$	$w = -1.23 \pm 0.34$[d]

[a]Consistent with $\Omega_m = 0.3$ (Λ or open), cluster normalized; $\Omega_m = 1, \sigma_8 = 1$ excluded.
[b]Consistent with ΛCDM or OCDM, but not with *COBE* normalized to $\Omega_m = 1$.
[c]Other parameters fixed to WMAP 7-year values.
[d]Combined with WMAP 7-year data.

independent groups (Bacon et al., 2000; Kaiser et al., 2000; Van Waerbeke et al., 2000; Wittman et al., 2000). Over the same period, a number of studies were carried out yielding the first cosmological constraints on the parameter combination $\sigma_8(\Omega_m)^\alpha$ (see Table 2.3). However, results from these early studies highlighted the need for a deeper understanding of the complex systematics – ranging from optical distortions in telescopes to intrinsic galaxy alignments – which affect this kind of measurements. Great progresses have been made in overcoming these difficulties over the last years. Current constraints, obtained from different datasets (SDSS, CFHTLenS) and using different analysis methods, provide consistent results, competitive with those obtained with other probes of the LSS. These constraints are currently sufficiently accurate and robust to be used, in combination with other datasets (e.g. CMB), to test several extension of the ΛCDM model, such as dark

energy or massive neutrino models (3rd column of Table 2.3; see also Chapter 5), or modifications of gravity as well (e.g. Simpson et al., 2013). Similarly to cluster number counts results, the parameter combination $\sigma_8(\Omega_m)^\alpha$ inferred from shear measurements is in tension with the most recent Planck CMB constraints. A possible way to alleviate this tension is to extend the cosmological model to massive neutrinos, as will be shown in Chapter 5 exploiting CFHTLenS data. As for the next generation surveys, the Euclid mission is expected to improve considerably the constraints provided by shear measurements (Laureijs et al., 2011): being a space-based mission, Euclid imaging will not be affect by *seeing* effects that seriously limit current observations from ground, allowing shape measurements for ~ 1.5 billion galaxies.

Finally, worth to mention is the 25σ detection of lensing signal on the CMB performed by the Planck Collaboration (2013e). The authors used the temperature-gradient correlations induced by lensing to reconstruct a map of the CMB lensing potential, which provides an integrated measure of the mass distribution back to the CMB last-scattering surface. The power spectrum of the lensing potential derived from this reconstruction is in good agreement with expectations from the best-fit ΛCDM for the Planck temperature power spectrum, and supplies degeneracy-breaking power for parameter constraints: it improves CMB-alone constraints on curvature by a factor of two and also partly breaks the degeneracy between the amplitude of the primordial perturbation and the optical depth to reionization (see 3rd column of Table 2.1).

2.5 Ly-α forest

Absorption spectra of distant luminous quasars (QSOs) provide a means to probe the properties of the intergalactic medium (IGM)[5] at high redshift through the analysis of the so called Ly-α forest (see e.g. Ferrara and Pandolfi, 2014, for a review). Briefly, the UV light of a distant quasar – in the wavelengths blue-wards of the Ly-α emission line, $\lambda < 1216$Å – traversing the IGM towards the observer could be absorbed by intervening bunches of neutral hydrogen atoms once the photons are redshifted – due to cosmic expansion – to the proper transition frequency. This scattering process is equivalent to an effective opacity of the medium, with an optical depth proportional to the number density of neutral hydrogen atoms which

[5]With the term IGM we refer to the baryonic matter (gas) which is not part of collapsed objects, such as galaxies. When the IGM falls from the filamentary structures of the cosmic web into galaxy clusters it heats up to temperatures of order $10^7 - 10^8$K, and it is referred to as Intracluster Medium.

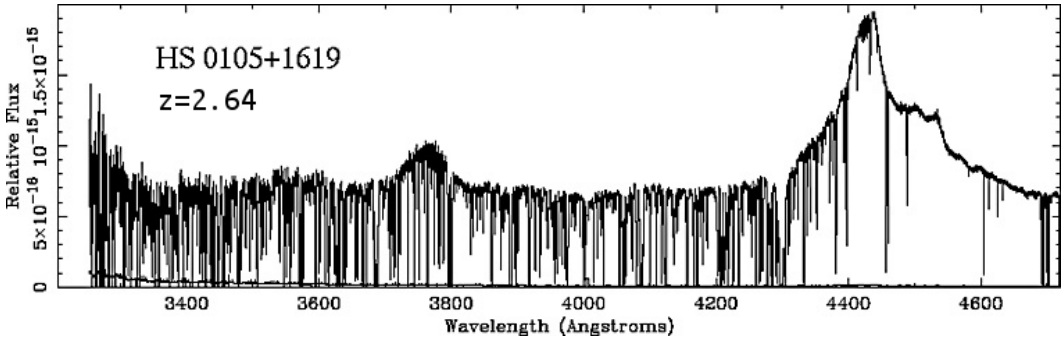

Figure 2.12: The Ly-α forest in the spectrum of the high redshift QSO HS 0105+1619 observed with the Keck-I HIRES spectrograph. The peak at 4426Å=1216Å$(1+2.62)$ corresponds to the Ly-α emission line. The features present in the part of the spectrum red-ward of the Ly-α emission are absorption lines from heavy elements (e.g. carbon, silicon, nitrogen, oxygen, iron). Figure adapted from O'Meara et al. (2001).

compose the cloud. Thus, the Ly-α forest, that is the series of absorption features observed in QSOs spectra at wavelengths corresponding to $1216(1+z_a)$Å, where z_a is the redshift of the absorbers, can be used to map the distribution of the IGM (see Figure 2.12). In particular, the transmitted flux can be related to the gas density which is a biased tracer of the underlying DM distribution. Therefore, the clustering statistics of the flux can be used to constrain the shape and amplitude of the matter power spectrum and measure the structure growth at redshifts inaccessible to other LSS probes such as cosmic shear or clusters (e.g. Croft et al., 2002; Viel et al., 2004a). From the theoretical side, several physical processes must be taken into account to model properly the relation between transmitted flux and matter fluctuations. These are usually calibrated using hydrodynamic cosmological simulations, and since the physical conditions are only mildly non-linear, uncertainties in their effects are not a major source of concern (e.g. Borde et al., 2014a). On the observational side, the primary complication is the need to estimate the unabsorbed continuum of the quasar, relative to which the absorption is measured. For statistical analyses of large QSO samples there are strategies for mitigating the bias caused by continuum errors (e.g. Slosar et al., 2011). Nonetheless, residual uncertainties from continuum determination can be significant compared to the precision of measurements.

One of the earliest study which employed Ly-α data was performed by Croft et al. (1999) using 19 QSOs spectra. The authors found an amplitude and slope of

the power spectrum which was consistent with a COBE-normalised ΛCDM model with a primordial scale invariant fluctuation amplitude. With the availability of an ever increasing number of QSOs spectra, several groups (e.g. Nusser and Haehnelt, 2000; Pichon et al., 2001; Zaldarriaga et al., 2001; Viel et al., 2004a) started to work with Ly-α data, improving the analysis methods and developing different statistical tool for cosmological inference (e.g. Viel et al., 2004b; Lidz et al., 2006). A substantial breakthrough was achieved with the measurement of the Ly-α forest power spectrum based on 3300 SDSS QSOs spectra from data releases one and two by McDonald et al. (2005). Probing the matter density fluctuations on small scale, the Ly-α forest has been readily recognized as a powerful tool to constrain neutrino properties (see also Chapter 5). For instance, Seljak et al. (2006) uses SDSS Ly-α forest data in combination with CMB and SNe measurements to constrains the total neutrino mass, finding $\sum m_\nu < 0.17$ (95% CL). A further step forward has been made thanks to the recently released data from the SDSS-III BOSS. This survey has been specifically designed to target quasars at redshift $z > 2$, and to obtain spectra of many more of them than in the previous phases of SDSS. Slosar et al. (2011), using the first 14000 quasars of the BOSS survey, performed a detailed measurement of the Ly-α power spectrum in 3D redshift space. With the data release 9, containing more than 60000 quasars, the measurement of the redshift space power spectrum has been extended up to the scales of the BAO, yielding the highest redshift measurement of the BAO peak position and providing new constraints on the expansion history of the Universe (Busca et al., 2013; Slosar et al., 2013). The most updated results are the one provided by Palanque-Delabrouille et al. (2013), who measured the one-dimensional power spectrum of the transmitted flux of BOSS DR11 QSOs, and inferred $\sigma_8 = 0.83 \pm 0.03$ and $n_s = 0.97 \pm 0.02$, a factor 3 improvement in precision with respect to earlier SDSS constraints of McDonald et al. (2005).

3

Constraining neutrino properties with the Euclid galaxy cluster survey

As explained in §1.5, neutrino oscillation experiments have provided conclusive evidence for neutrinos having non-zero masses – through the measurement of the mass squared difference between neutrino species – but current terrestrial experiments are capable of giving only loose constraints on their absolute mass scale ($0.06\text{eV} \lesssim \sum m_\nu \lesssim 6\text{eV}$). On the other hand, cosmological data provide a means to constrain neutrino masses due to the effects neutrinos induce on background evolution and growth of structures: relativistic neutrinos affect the pre-recombination Universe and thus the statistical properties of the CMB anisotropies, whereas, when they become non-relativistic, neutrinos suppress matter density fluctuations at small scales. Given these multiple effects massive neutrinos leave an imprint on many cosmological probes, ranging from CMB anisotropies to cosmic shear, clusters and Ly-α forest, which are currently used to constrain their properties. In particular, the upper limit on the total neutrino mass, accordingly to different recent studies, lies in the range $\sum m_\nu \lesssim 0.2 - 0.6\,\text{eV}$ (95% CL) (e.g. Seljak et al., 2006; Zhao et al., 2013; Xia et al., 2012; Riemer-Sørensen et al., 2013; Hinshaw et al., 2013; Joudaki, 2012; Burenin and Vikhlinin, 2012; Zhao et al., 2012; Planck Collaboration, 2013d; Wyman et al., 2013; Battye and Moss, 2013; Beutler et al., 2014; Giusarma et al., 2014; Mantz et al., 2014), depending on the probes and datasets employed. Moreover, the number of active neutrinos is known to be three to high precision through the measurement of the invisible width of the Z boson at LEP (The ALEPH Collaboration et al., 2005), nevertheless, there exist several scenarios which

allow the effective number of neutrinos to be different from its standard value, $N_{\rm eff} = 3.046$ (e.g. Steigman, 2013). Current Planck CMB data alone do not favour non-standard values of $N_{\rm eff}$, there are, however, several studies (e.g. Burenin, 2013; Hamann and Hasenkamp, 2013; Wyman et al., 2013; Battye and Moss, 2013) that including different probes of the LSS in their analyses found results which go in the opposite direction.

We have seen in §2.2 that galaxy clusters, thanks to their capability of probing the amplitude and growth of structures on scales of $\sim 10\,$Mpc, provide a powerful tool to constrain the neutrino properties. However, while current constraints based on galaxy cluster data rely on relatively small samples of clusters identified at redshift below one (e.g. Burenin et al., 2007; Rozo et al., 2009), next generation of X-ray (e.g. eROSITA[1]), Sunyaev-Zeldovich (e.g. CCAT[2], SPT-3G) and optical (e.g. DES[3], LSST[4], PanSTARRS[5], Euclid [6]) surveys is expected to increase by orders of magnitude the number of galaxy clusters detected, further extending the probed range of redshift up to $z \sim 2$. Such large cluster surveys will provide tight constraints on cosmological parameters, independent and complementary to those recovered from other cosmological probes. In this Chapter we explore the cosmological information contained in the cluster catalogue that will be provided by the photometric redshift survey of ESA's Euclid mission, which has been approved for lunch in 2020. Specifically, we will make use of cluster number counts and cluster power spectrum to derive forecast errors on the total neutrino mass and effective number of neutrino species. Moreover, we will assess how much extended models (wCDM and open ΛCDM), or an uncertain knowledge of the relation between mass and observable, degrade the constraints on neutrino properties.

The Chapter is organized as follows. In Section 3.1, we briefly explain the physical and observable effects of $N_{\rm eff}$ and $\sum m_\nu$. In Section 3.2 we introduce the Euclid mission, and specify the characteristics of the Euclid cluster survey used in the analysis. Section 3.3 describes the formalism which we used to compute the cluster number counts (§3.3.1) and power spectrum (§3.3.2), while in § 3.3.3 we outline our forecasting procedure. Our results for different cosmological model are presented in Section 3.4, and finally in Section 3.5 we draw our conclusions. The results presented in this Chapter have been published in Costanzi Alunno Cerbolini

[1] http://www.mpe.mpg.de/eROSITA
[2] http://www.ccatobservatory.org/index.cfm
[3] http://www.darkenergysurvey.org/
[4] http://www.lsst.org/lsst/
[5] http://pan-starrs.ifa.hawaii.edu/public/
[6] http://www.euclid-ec.org/

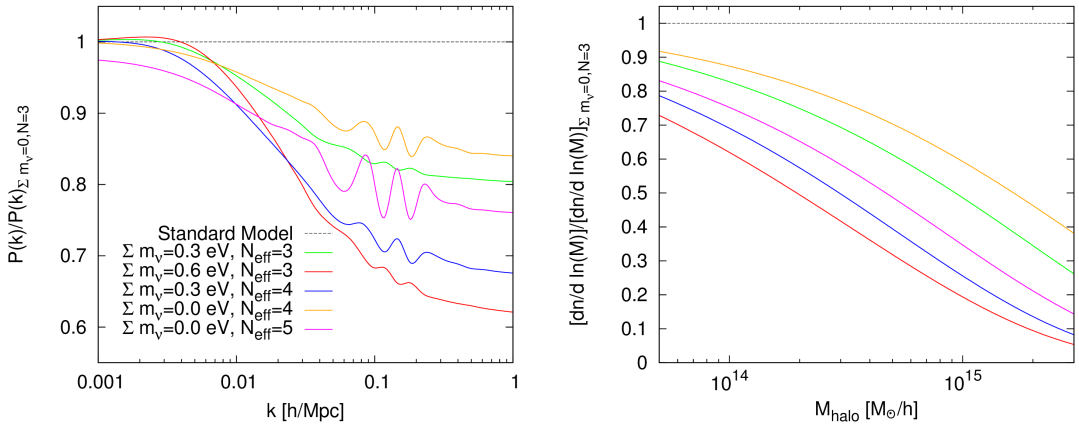

Figure 3.1: Effects of the variation of $\sum m_\nu$ and $N_{\rm eff}$ (keeping the number of massive species equal to three) on the linear matter power spectrum and halo mass function at $z = 0$. The y-axis represents the ratio of the linear matter power spectrum (*left*) and HMF (*right*) obtained for different values of $\sum m_\nu$ and $N_{\rm eff}$ to the standard results for a ΛCDM model with $\sum m_\nu = 0$ and $N_{\rm eff} = 3.046$. All other parameters $(\Omega_{\rm m}, \Omega_\Lambda, H_0, n_{\rm s}, \Delta^2_{\rm R}, \tau)$ are kept fixed to the WMAP 9-yr best-fit values for ΛCDM. Both an increase of $\sum m_\nu$ or $N_{\rm eff}$ determines a suppression of the matter power spectrum and HMF, making the effects of the two parameters degenerate for these two observables.

et al. (2013) on the "Journal of Cosmology and Astroparticle Physics".

3.1 Effects of varying $\sum m_\nu$ and $N_{\rm eff}$

We already seen in §1.5.3 that massive neutrinos affect both the background evolution, by changing the expansion rate and the time of matter-radiation equality, and the structure formation, through the free-streaming effect. These effects produce a suppression of the matter power spectrum at small scales (*left* panel of Figure 3.1), and in turn, a reduction of the number density of massive halo (*right* panel of Figure 3.1)

Similarly, a variation of $N_{\rm eff}$ affects the expansion rate and shifts the matter-radiation equality, through Eq. (1.42). We recall here that the epoch of equality sets the time at which sub-horizon DM density fluctuations can start to growing under the action of gravity (see §1.2). Such modification is seen in the matter power

spectrum as a shift to larger scale of its peak, which is determined by the size of the particle horizon at the time of matter-radiation equality. Moreover, since on sub-Hubble scales density fluctuations grow more efficiently during matter dominated epoch (i.e. after equality), the matter power spectrum is suppressed on small scales relatively to large scales (left panel of Figure 3.1). These effects, in turn, determine a suppression of the halo mass function (right panel of Figure 3.1), especially in the high mass end.

Comparing the various curves in Figure 3.1 obtained for different combinations of $\sum m_\nu$ and $N_{\rm eff}$, it is clear that the effects induced by these two parameters on the matter power spectrum and HMF are almost degenerate. Thus, we expect the constraints on the total neutrino mass and the effective number of neutrinos from power spectrum and HMF analyses to be highly correlated.

To actually detect the signature of massive neutrinos in the matter power spectrum and HMF we need a cosmic tracer of such quantities. As mentioned in the introduction we will use the cluster number counts and cluster power spectrum to this end. In the next sections, after having introduced the Euclid mission, the formalism used to quantify the two observables and the forecasting procedure will be described.

3.2 The Euclid survey

Euclid is a Medium Class mission of the ESA Cosmic Vision 2015-2025 programme, planned for lunch in 2020. Thanks to its three imaging and spectroscopic instruments working in the visible and near-infrared bands, Euclid will cover 15,000 square degrees of extragalactic sky with the wide survey, thereby providing high-quality images from visual imaging for more than a billion galaxies, accurate photometric redshifts from near-IR imaging photometry (in combination with ground-based data) for about 2×10^8 galaxies and about 5×10^7 spectroscopic redshift at $z > 0.7$ from near-IR slitless spectroscopy. The primary driver for the Euclid mission is to understand the accelerated expansion of the Universe and the rate of structure growth. To this end the mission is optimised for two independent primary cosmological probes: cosmic shear (see §2.4) and BAO (see §2.3). In addition, the Euclid survey will yield data of several complementary cosmological probes, among which, galaxy clusters.

To fulfil the scientific goals for the cosmic shear survey, Euclid has been designed to measure the shapes of ~ 30 galaxies per square arc-minute, with a median redshift greater than 0.8, in one broad visible R+I+Z band ($550 - 920$ nm)

down to AB mag 24.5 (10σ). To reach the full potential of the weak lensing technique the required photometric redshift accuracy for these galaxies is $\sigma_z/(1+z) \leqslant 0.05$. This level of accuracy is achieved by using three additional Euclid near-IR bands (Y, J, H in the range $0.92 - 2.0$ micron) reaching AB mag 24 (5σ) in each, complemented by ground-based photometry in visible bands derived from public data or through collaborations with projects such as DES, KiDS, and Pan-STARRS.

The spectroscopic survey has been optimised for the detection of the BAOs. By using a slitless spectrometer, with a spectral resolution of $\lambda/\Delta\lambda \sim 250$ and limiting line flux of 3×10^{-16}ergs^{-1}cm^{-2}, Euclid will target Hα emitting galaxies providing spectroscopic redshifts for over $3,500$ galaxies per square degree with an accuracy of $\sigma_z/(1+z) \leqslant 0.001$ and a completeness higher than 45 per cent.

As for the galaxy cluster survey, the most efficient method to build the Euclid galaxy cluster catalogue relies on the analysis of the photometric data. To predict cosmological constraints from the expected sample of galaxy clusters, we use the analytic selection function adopted in the Euclid *Red-Book* (Laureijs et al., 2011) to forecast the contribution of the cluster survey to the cosmological constraints. The computation of the selection function is based on using the luminosity function of cluster galaxies to compute the number of galaxies expected within R_{200c}[7] down to the $H_{AB} = 24$ magnitude limit reached in the photometric survey, as a function of the cluster mass and the cluster redshift.

Specifically, we use an average of the K_s-band luminosity functions of nearby clusters, evaluated within R_{500c} by Lin et al. (2003), which we then evolve passively with redshift (Lin et al., 2006). We transform the K_s magnitudes into the H_{AB} band by using the mean colour for cluster galaxies. Integrating the luminosity function down to the apparent magnitude limit of the survey we obtain the number density of cluster galaxies within R_{500c}. Then, after appropriate scaling and multiplication by the corresponding sphere volume, we obtain the number of cluster galaxies within a sphere of radius R_{200c}. Given the direct relation between cluster mass M_{200c} and radius R_{200c}, we obtain the number of observable galaxies for a cluster of given mass at any redshift.

In practice, this procedure is equivalent to adopting a scaling relation between a cluster mass M_{200c} and richness, a relation which evolves with redshift because of passive evolution of the cluster population, and where the knowledge of the luminosity function allows the richness to be estimated down to the redshift-dependent absolute magnitude limits that correspond to the fixed apparent magnitude limit

[7]Recall that R_{200c} is defined as the radius encompassing an average density equal to 200 times the cosmic critical density at a given redshift.

of the survey.

We then calculate the predicted number of fore-/back-ground galaxies within a cylinder of angular radius corresponding to R_{200c} at the cluster redshift, and of length equal to ± 3 times the photometric redshift error, with the idea that photometric redshifts will be used to reduce the fore-/back-ground. The signal-to-noise (S/N) for cluster detection is then obtained from the ratio between the number of cluster galaxies and the rms of the number of fore-/back-ground galaxies. The latter is contributed by both Poisson noise and cosmic variance.

Assuming $S/N = 3$ for the fiducial limiting signal-to-noise for a reliable cluster detection turns into a selection function which provides $M_{\rm lim,200c}(z)$ defined as the limiting mass within R_{200c} for a cluster to be included in the survey. As a result, one finds $M_{\rm lim,200c}(z) \simeq 1.6 \times 10^{14} M_\odot$ at $z > 0.5$, while decreasing at lower redshift, reaching $\simeq 5 \times 10^{13} M_\odot$ at $z = 0.2$ (see dashed line in Figure 3.2). Even though a $S/N = 3$ level may look optimistic the selection function adopted in this work is derived using a simplistic analytical model which does not take into account any sophisticated algorithm for cluster detection, and without making use of the full information available (e.g. from cluster density profiles, luminosity functions, red sequence and spectroscopic data). Therefore, the chosen limiting signal-to-noise is likely to represent a conservative estimate, and we can assume the cluster sample to be 100% complete and pure. Clearly, a detailed assessment of the completeness and purity of the cluster sample should require a detailed analysis of the performance of different cluster detection algorithms when applied to the Euclid survey, which is beyond the aim of this paper. Moreover, as discussed in Rozo et al. (2010), what matters in parameter estimation is not the level of the survey completeness and purity, but the uncertainty in their calibration. Thus, the assumption of a 100% pure and complete sample for $S/N \geq 3$ can be considered as assuming that purity and completeness will be accurately measured in this regime (see Sartoris et al., 2014, for further details).

3.3 The analysis method

A standard method in cosmology to constrain model parameters from survey data is to compute the probability that an observed quantity, such as the cluster abundance or power spectrum, is reproduced by a theoretical model described by a set of parameters (Bayesian inference approach). Otherwise, in forecast analyses, for which no real data yet exist, two approaches are commonly employed; in one case, given the specifics of the planned survey and a fiducial cosmological model,

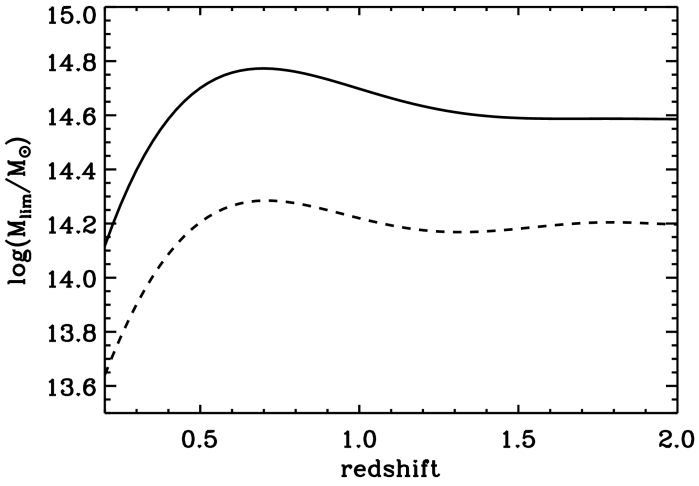

Figure 3.2: Galaxy cluster selection function for the Euclid photometric survey, expressed as the limiting mass for a cluster to be included in the survey as a function of redshift, $M_{\mathrm{lim,200c}}(z)$. Dashed and solid lines represent the limiting mass for detection thresholds S/N=3 and 5, respectively. Figure from Sartoris et al. (2014).

a synthetic set of data of the survey is generated and then used to parameter inference in the same fashion of real data. The other approach exploits the Fisher matrix formalism in which the confidence level on parameter measurement can be estimated from the derivatives of the observables with respect to the model parameters around the best fit point. Even though the Fisher Matrix technique has the advantage of allowing for a quick, analytic estimate of the confidence limits, on the other hand it approximates the likelihood function as a multivariate Gaussian function of the model parameters. In general, this turns out to be a coarse approximation since the likelihood function can be highly non-Gaussian (e.g. Perotto et al., 2006); moreover the results obtained with this technique depend on the step chosen in the calculation of numerical derivatives with respect to the parameters (e.g. Wolz et al., 2012). For these reasons we choose to use the first approach in our analysis. Specifically: *i*) we computed the mock cluster power spectrum and number counts for a Euclid-like photometric survey; *ii*) these are then used to build the likelihood functions of the two observables, and finally *iii*) the likelihoods are sampled by means of a Monte Carlo Markov Chain (MCMC) technique to obtain forecast constraints. In what follows the models and procedure used to perform this analysis

are described.

3.3.1 Cluster number counts

Following Eq. (2.10), the number of clusters expected for a survey having sky coverage $\Delta\Omega$ with an observed mass between $M^{ob}_{\mathrm{l,m}}$ and $M^{ob}_{\mathrm{l,m+1}}$ and redshift between z_{l} and $z_{\mathrm{l+1}}$ can be expressed as:

$$N_{l,m} = \Delta\Omega \int_{z_{\mathrm{l}}}^{z_{\mathrm{l+1}}} \mathrm{d}z \, \frac{\mathrm{d}V}{\mathrm{d}z} \int_{M^{ob}_{\mathrm{l,m}}}^{M^{ob}_{\mathrm{l,m+1}}} \mathrm{d}M^{ob} \times \int_0^{\infty} \mathrm{d}M \, n(M,z) \, p(M^{ob}\|M) \,, \tag{3.1}$$

where we approximated the survey completeness function with $X(M,z,\mathbf{\Omega}) = \int \mathrm{d}M^{ob} p(M^{ob}\|M)$. In this notation $M^{ob}_{\mathrm{l,m=0}}$ is equal to $M_{\mathrm{lim}}(z)$, the minimum value of the observed mass for a cluster to be included in the survey discussed in §3.2. To compute Eq. 3.5 we convert $M_{\mathrm{lim,200c}}(z)$, computed following the procedure outlined in §3.2, to $M_{\mathrm{lim,200m}}(z)$ – the limiting mass within a radius encompassing an overdensity equal to 200 times the mean density of the Universe – consistently with the chosen halo mass function (see below). To this end we follow the recipe given in Hu and Kravtsov (2003), assuming a NFW profile (Navarro et al., 1997) as halo density profile and using their fitting formula (C11).

The integral over the observed mass is computed within bins having width $\Delta \log M = 0.2$, extending from $M_{\mathrm{min}}(z)$ to $10^{15.8} h^{-1} M_{\odot}$, whereas the integral over the redshift is evaluated in bins of width $\Delta z = 0.2$ between $z = 0.2$ and $z = 2$. The sky coverage is set to the required area for the wide Euclid survey $\Delta\Omega = 15,000 \mathrm{deg}^2$ (Laureijs et al., 2011). For $n(M,z)$ we adopt the expression provided by Tinker et al. (2008), with mass function parameters obtained for overdensity $\Delta_{\mathrm{m}} = 200$ with respect to the mean density of the universe (see their Table 2). Moreover, to take into account massive neutrino effects, we follow the prescription used by many authors[8] (e.g. Brandbyge et al., 2010b; Marulli et al., 2011; Ichiki and Takada, 2012; Villaescusa-Navarro et al., 2013) neglecting the weakly clustering neutrino component when calculating the halo mass ($M_{\mathrm{halo}} = 4\pi r^3 \rho/3$, with $\rho = \rho_{\mathrm{m}} - \rho_{\nu}$). Many other calibrations of the halo mass function from simulations have

[8] In Chapter 4 a refined calibration of the HMF in cosmology with massive neutrino, based on a later study, is presented. As will be explained later, this improved HMF calibration entails a second order effect on the absolute number of clusters predicted for a given cosmological model. The net effect of this change in clusters count on parameters constraints is to shift the confidence contours with respect to the results obtained with the standard HMF calibration. Such an effect is not relevant for forecast analyses, for which the best-fit values of the parameters are set by the chosen fiducial model.

been presented by several authors (e.g. Sheth and Tormen, 1999; Jenkins et al., 2001; Warren et al., 2006; Crocce et al., 2010). However, for the purposes of this work the choice of the best-calibrated mass function has a minor impact. Indeed the forecast errors depend primarily on the number of clusters expected for a given cosmological model, which is far more sensitive to the exponential shape of the mass function rather than to the calibration details of the mass function. The factor $p(M^{ob}\|M)$ takes into account the uncertainties that a scaling relation introduces in the knowledge of the true cluster mass. Following the prescription of Lima and Hu (2005), $p(M^{ob}\|M)$ gives the probability of assigning to a cluster of true mass M an observed mass M^{ob}, as inferred from a giving scaling relation. Under the assumption of a lognormal-distributed intrinsic scatter around the nominal scaling relation with variance $\sigma^2_{\ln M}$, the probability can be written as:

$$p(M^{ob}\|M) \;=\; \frac{\exp[-x^2(M^{ob})]}{M^{ob}\sqrt{(2\pi\sigma^2_{\ln M})}}\,, \tag{3.2}$$

where

$$x(M^{ob}) \;=\; \frac{\ln M^{ob} - B_{\rm M} - \ln M}{\sqrt{(2\sigma^2_{\ln M})}}\,. \tag{3.3}$$

Here the parameter $B_{\rm M}$ represents the fractional value of the systematic bias in the mass estimate. Moreover, according to Sartoris et al. (2010) we assume the following parametrization for redshift dependencies of the halo mass bias and variance (we do not consider a possible mass dependence of these parameters):

$$\begin{aligned} B_{\rm M}(z) &= B_{\rm M,0}(1+z)^{\alpha} \\ \sigma_{\ln M}(z) &= \sigma_{\ln M,0}(1+z)^{\beta}\,. \end{aligned} \tag{3.4}$$

In our formalism, we have four nuisance parameters, $B_{\rm M,0}$, $\sigma_{\ln M,0}$, α and β, which can be allowed to vary along with the other cosmological parameters during the forecast procedure (see § 3.4.4).

Including Eq. 3.2 into Eq. 3.1 it follows that:

$$N_{\rm l,m} = \frac{\Delta\Omega}{2}\int_{z_{\rm l}}^{z_{\rm l+1}} {\rm d}z\,\frac{dV}{dz}\int_0^{\infty} {\rm d}M\, n(M,z)\times[{\rm erfc}(x_{\rm l,m}) - {\rm erfc}(x_{\rm l,m+1})]\,, \tag{3.5}$$

where ${\rm erfc}(x)$ is the complementary error function. For Euclid data, the photometric redshift measurements will be calibrated using a combination of the spectroscopic survey and ground-based visual bands photometry, with an expected limiting precision of $\sigma(z) \sim 0.05(1+z)$ (Laureijs et al., 2011). While this error refers to

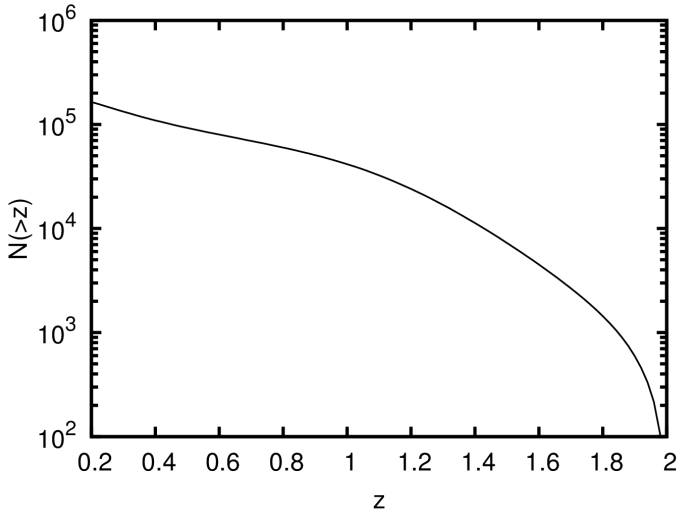

Figure 3.3: The cumulative cluster redshift distribution as predicted by the reference cosmological model and the reference values for the mass nuisance parameters (see Table 3.1), for the Euclid cluster survey.

the photometric redshift of a single galaxy, the redshift of a cluster identified in the photometric survey should be reduced by a factor $N^{1/2}$, where N is the number of galaxies assigned to the cluster. For a typical cluster at $z \sim 1.0$ with $N \sim 100$ detected galaxies the error is reduced by a factor 10, leading to $\sigma(z) \sim 0.01$. Thus in the following, we assume that the errors on cluster redshift measurements can be neglected.

An additional effect on the number counts is induced by line-of-sight peculiar velocities, which can scatter redshifts by $\delta z \sim 0.003$ for velocities of $\sim 1000\,\mathrm{km\ s^{-1}}$. However, since the redshift bins adopted in the analysis have a width of $\Delta z = 0.2$, i.e. far larger than the δz value associated to the peculiar velocities, it is a fair assumption to neglect this effect.

From Eq. 3.5, using this survey specifics and fiducial parameter values listed in Table 3.1, we expect that Euclid will find of order 1.5×10^5 cluster with a S/N better than 3, between $z = 0.2$ and $z = 2.0$, with $\sim 4 \times 10^4$ having $z > 1$ (see Figure 3.3).

3.3.2 Cluster power spectrum

In order to include information from the clustering of galaxy clusters, we calculate the averaged cluster power spectrum within a given redshift interval using the

expression:

$$\bar{P}_1^{cl}(k,z) = \frac{\int_{z_l}^{z_{l+1}} \mathrm{d}z \, \frac{\mathrm{d}V}{\mathrm{d}z} \, n^2(z) \, P^{cl}(k,z)}{\int_{z_l}^{z_{l+1}} \mathrm{d}z \, \frac{\mathrm{d}V}{\mathrm{d}z} \, n^2(z)} \,, \tag{3.6}$$

where $n(z) = \int_0^\infty dM n(M,z) \times \mathrm{erfc}(x_{\mathrm{l,m=0}})$ is the comoving number density of clusters that are included in the survey at redshift z (e.g. Majumdar and Mohr, 2004). The cluster power spectrum $P^{cl}(k,z)$ is expressed in terms of the underlying matter power spectrum $P(k,z)$ according to $P^{cl}(k,z) = b_{\mathrm{eff}}^2(z) \, P(k,z)$; the term of proportionality b_{eff} is the cluster mass function averaged linear bias, defined as:

$$b_{\mathrm{eff}}(z) = \frac{\int_0^\infty dM n(M,z) \, \mathrm{erfc}(x_{\mathrm{l,m=0}}) \, b(M,z)}{\int_0^\infty dM \, n(M,z) \, \mathrm{erfc}(x_{\mathrm{l,m=0}})} \,. \tag{3.7}$$

For the linear bias of dark matter halos, $b(M,z)$, we adopt the fitting function of Tinker et al. (2010) (Eq. (1.39)) for overdensity $\Delta = 200$ (see their table 2). The linear matter power spectrum $P(k,z)$ is computed with the publicly available software package `CAMB` (Lewis et al., 2000), which takes correctly into account the effect of massive neutrinos also in a mild non-linear regime (Bird et al., 2012).

As for the effect of errors in photometric redshifts, they are expected to introduce a smearing in the power spectrum at small scales (see e.g. Hütsi, 2010), thus degrading the information carried by clustering analysis. Consistently with the number counts analysis we neglect in the following the effect of uncertainties in redshift measurements, thereby not accounting for the damping of the power spectrum due to photometric redshift errors. In order to avoid contribution to the matter power spectrum and scale-dependent bias introduced by non-linearities, we do not include in our analysis modes with wavenumbers larger than $k_{\mathrm{max}} = 0.1\,\mathrm{Mpc}^{-1}$ (Percival and White, 2009). Although massive free-streaming neutrinos mainly affects the power spectrum at small scales (§1.5), a value of k_{max} larger than $\sim 0.3\,\mathrm{Mpc}^{-1}$ would not increase significantly the sensitivity of the survey. Indeed, given the level of Poisson noise associated to the cluster distribution (see Eq. 3.10, and Figure 3.4), higher frequency modes are not adequately sampled and, therefore, adding them to the analysis does not add significant information (Sartoris et al., 2010). As for the minimum value of the wavenumber we impose $k_{\mathrm{min}} = 0.003\,\mathrm{Mpc}^{-1}$; again, using a smaller value of k_{min} does not change the final results, since extremely large scales are not sampled by the surveys. According to the Euclid specifics the average cluster power spectrum is evaluated in the redshift range $0.2 < z < 2.0$, considering 9 bins of width $\Delta z = 0.2$ each. Finally,

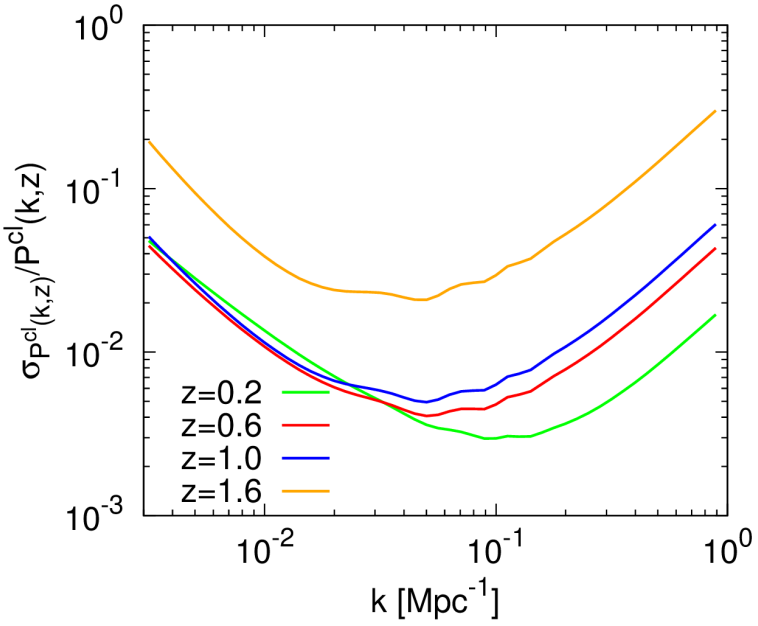

Figure 3.4: Wavenumber dependence of the relative error of the cluster power spectrum, $\sigma_{\bar{P}^{cl}}/\bar{P}^{cl}$ defined as in Eq. 3.10, at four different redshift: $z = 0.2, 0.6, 1.0, 1.6$, from bottom to top curves, respectively.

in our analysis we neglect the correction to the power spectrum due to redshift space distortion effects.

3.3.3 Forecasting

The forecast is based on the Bayesian inference technique, for which a likelihood function of the mock data is first constructed and then sampled in order to estimate the marginalized probability distribution of the parameters. To explore the parameter space by means of Monte Carlo Markov Chains we use the publicly available code `CosmoMC`[9] (Lewis and Bridle, 2002), where we included a module for the calculation of the cluster number counts and power spectrum likelihoods.

Our most general parameter space is:

$$\mathbf{\Theta} \equiv (\Omega_b h^2, \Omega_c h^2, \Theta_s, \tau, n_s, \log[10^{10} A_s], f_\nu N_{\rm eff}, \Omega_k, w, B_{M,0}, \sigma_{\ln M,0}, \alpha, \beta) \qquad (3.8)$$

[9] http://cosmologist.info/cosmomc/

Table 3.1: Fiducial parameter values.

$\Omega_b h^2$	$\Omega_c h^2$	Θ_s	τ	n_s	$\log[10^{10} A_s]$	f_ν
0.02253	0.1122	1.0395	0.085	0.967	3.18	0

N_{eff}	Ω_k	w	$B_{M,0}$	$\sigma_{\ln M,0}$	α	β
3.046	0	-1	0	0.45	0	0

where the first six are the usual standard ΛCDM parameters: the physical baryon $\Omega_b h^2$ and cold dark matter $\Omega_c h^2$ densities, the ratio (multiplied by 100) between the sound horizon ant the angular diameter distance at decoupling Θ_s, the reionization optical depth τ, the scalar spectral index n_s and the amplitude of initial power spectrum A_s. Besides these parameters we performed several forecasts for different extensions of the minimal cosmological model, by fitting (along with the other parameters): the neutrino density fraction $f_\nu = \Omega_\nu / \Omega_c$, the effective number of neutrino species N_{eff}, the spatial curvature Ω_k and the dark energy equation of state parameter w. Finally, in order to assess the effect of the uncertain knowledge of the mass-observable relation we consider also the case in which the four nuisance parameter are treated as fitting parameters to be determined along with the cosmological ones.

Throughout this paper, our reference model is chosen to be a flat ΛCDM model with three neutrino species. The fiducial ΛCDM parameter values are listed in Table 3.1, consistently with the WMAP-7+BAO+H_0 best-fit model by Komatsu et al. (2011). These fiducial parameter values are also consistent with the latest WMAP 9-year best-fit model (Hinshaw et al., 2013) and within 2σ with the Planck results (Planck Collaboration, 2013d).

As for the nuisance parameters, clusters mass within Euclid survey will be estimated using photometric richness as a cluster mass proxy. An accurate calibration of the scaling relation between richness and mass will be provided by weak lensing mass measurements within the Euclid survey. We note that different authors calibrated the presence of a possible bias in weak lensing mass measurements by resorting to cosmological simulations of galaxy clusters (Becker and Kravtsov, 2011; Rasia et al., 2012). The results of these analyses converge to indicate that a small, but sizeable, underestimate in weak lensing masses, is induced by projection effects and amounts to 5–10%. For the purpose of the present analysis we prefer to assume that weak lensing provides an unbiased calibration of the mass–richness relation, thus fixing $B_{M,0} = 0$ as a reference value for the mass bias. For the intrinsic

scatter we assume $\sigma_{\ln M,0} = 0.45$ as estimated by Rozo et al. (2009) by demanding consistency between available weak lensing and X-ray measurements of the maxBCG clusters, and the X-ray luminosity-mass relation inferred from the 400d X-ray cluster survey. The intrinsic scatter has the effect of increasing the number of clusters included in the survey. Indeed, the number of low-mass clusters that are up-scattered above the survey mass limit is always larger than the number of rarer high-mass clusters which are down-scattered below the same mass limit (e.g. Cunha, 2009). Because so far there are no evidences for the evolution of the nuisance parameters we adopt $\alpha = 0$ and $\beta = 0$ as reference values, thus making the minimal assumption of constant bias and scatter with redshift. When the nuisance parameters are left free we consider two cases: one with strong prior on the evolution parameters, with α and β not allowed to vary with respect to their reference value, and the other one with no prior knowledge of their value. The latter turns out to be a conservative assumption in view of the large number of clusters for which mass measurements from weak lensing will be available from Euclid (Laureijs et al., 2011). As such, the corresponding uncertainties expected on cosmological parameters should be regarded as upper limits of the error introduced by the uncertainties in the relation between cluster richness and mass. The cluster power spectrum and number counts of the mock data are assumed to be equal to the theoretical cluster power spectrum (Eq. (3.6)) and number counts (Eq. (3.5)) of the fiducial model.

Since we are interested only in parameter error estimation, we define our likelihood functions $\mathcal{L}$ of the observable O as

$$\chi^2_{\rm eff} \equiv -2\ln\mathcal{L} = \sum_{i,j} \frac{O^{\rm obs}_{ij} - O^{\rm th}_{ij}}{\sigma^2_{O_{ij}}}\,, \tag{3.9}$$

in such a way that $\chi^2_{\rm eff}$ is equal to zero for the fiducial parameter values. In the previous equation $O^{\rm obs}_{ij}$ denotes the observed cluster power spectrum, $\bar{P}^{\rm obs}_{cl}(k_i, z_j)$ (number counts, $N^{\rm obs}(M_i, z_j)$), while $O^{\rm th}_{ij}$ is the theoretical cluster power spectrum (number counts) of Eq. 3.6 (Eq. 3.5). The statistical error associated to the observed galaxy cluster power spectrum in a bin centred on (k_i, z_j) (Feldman et al., 1994) reads:

$$\sigma^2_{P^{cl}_{ij}} = \frac{(2\pi)^2(\bar{P}^{\rm th}_{cl}(k_i,z_j))^2}{V_{\rm sur}(z_j)k_i^2\Delta k}\left[1 + \frac{1}{n(z_j)\bar{P}^{\rm th}_{cl}(k_i,z_j)}\right]^2\,, \tag{3.10}$$

where $V_{\rm sur}(z_j)$ is the comoving survey volume within the redshift bin centred on z_j, and Δk is the size of the bins in wavenumber space. In this way, constraints at

redshift z are mostly contributed by wave-numbers k, which maximize the product $n(z)P_{cl}^{\rm obs}(k,z)$ (see Figure 3.4). The average cluster power spectrum is computed by integrating over redshift intervals having constant width $\Delta z = 0.2$. This choice of binning represents a compromise between the need of extracting the maximum amount of information from clustering evolution and request of negligible covariance between adjacent z-intervals (e.g. Stril et al., 2010). Indeed, the definition of Eq. 3.9 holds only if the contribution from different redshift slices carry statistically independent information. As for the statistical error of the observed number counts for a given mass and redshift bin centred in (M_i, z_j), we consider only the Poissonian noise, $\sigma^2_{N^{cl}_{ij}} = N^{\rm th}(M_i, z_j)$, neglecting the contribution from sample variance, which accounts for the clustering of clusters due to large scale structure. Given the large volume to be probed by the Euclid survey ($\sim 100h^{-3}\,$Gpc) and the exponential suppression of cluster number density for mass larger than the maximum cluster mass, the shot-noise errors dominate over sample variance for the most of mass and redshift bins (see Hu and Kravtsov, 2003, also for a more rigorous definition of the number counts covariance matrix). Finally, since number counts and power spectrum probe the same mass density field, the covariance between the two is expected to be different from zero. In practice, it has been shown (e.g. Fang and Haiman, 2007) that these two observables have in fact negligible covariance.

Because the full parameter space is quite large and some parameters are poorly constrained by LSS observations, we perform our forecast combining the Euclid-like cluster catalogue with Planck-like data[10]. The mock CMB TT, EE and TE power spectra have been simulated following the procedure of Perotto et al. (2006) according to the specifications presented in the Planck *Blue-Book* (Planck Collaboration, 2006, page 4, Table 1.1) based on 14 months of observations, using the three frequency channels with the lowest foreground levels at 100GHz, 143GHz and 217GHz, and a sky fraction of $f_{\rm sky} = 0.80$. In order to avoid problems with foreground signal, beam uncertainties, etc., we cut-off the spectra at $\ell_{\rm max} = 2000$.

[10] At the time of performing this analysis the first Planck data release has not been published yet. However, the fiducial values adopted in this work are consistent within 2σ with the mean values obtained by the Planck Collaboration (2013d). For this data release the authors did not use polarization spectra, so a direct comparison of our forecast with the actual constraints from Planck is not possible. Nevertheless, for a ΛCDM+m_ν model, using Planck temperature power spectrum in combination with a WMAP-9year polarization low-multipole likelihood the authors obtained $\sum m_\nu < 0.933$ (95%CL), compatible with our expected error. The actual Planck data will be used in the analysis proposed in Chapter 5

3.4 Analysis and results

Having defined the reference cosmological model and the specifics of Euclid survey we now present forecast errors on neutrino parameters for various extensions of the minimal ΛCDM model. For each of the cases that we describe here below, we run four independent chains, requiring the fulfillment of the Gelman & Rubin Gelman and Rubin (1992) criteria with $R - 1 \leqslant 0.03$ as convergence test.

3.4.1 Three massive neutrinos: ΛCDM+m_ν

We start by considering the scenario with three degenerate massive neutrino species. A degenerate mass spectrum is justified on one side by the smallness of the mass difference measured, on the other by the incapability of the Euclid cluster data to probe directly the neutrino mass hierarchy, as we will explain later in § 3.4.2. In Table 3.2 we report the 68% and 95% CL bounds on $\sum m_\nu$ derived from different data sets: Planck only, cluster power spectrum only, cluster number counts and power spectrum (hereafter Euclid-Cl), and the combination of Planck and Euclid-Cl. When only cluster power spectrum data are considered we obtain a quite loose 2σ upper limit on $\sum m_\nu$ of 1.20 eV. Otherwise, the information contained in cluster number counts alone is unable to constrain the total neutrino mass, but it greatly improves the error on $\sum m_\nu$ once added to cluster power spectrum data, mainly thanks to the tight constraints provided on σ_8 (see left panel of Figure 3.5). Specifically, the upper limit for $\sum m_\nu$ shrinks by a factor ~ 4 to 0.35 eV (95%CL). This error is comparable to the present constraints obtained combining CMB and LSS probes, and of the same order of magnitude of the error expected for Planck. Regarding parameter degeneracies for the galaxy cluster dataset, the total neutrino mass is correlated with all the cosmological parameter affecting the galaxy power spectrum shape (i.e. $\Omega_{\rm m}$, σ_8, $n_{\rm s}$; see red contours in Figure 3.5 and Figure 3.6).

The main power of constraints in cosmological parameters indeed originate from the joint analysis of galaxy cluster and CMB datasets. In this case the error on $\sum m_\nu$ is reduced to 31 meV; an improvement of more than one order of magnitude that would allow a 2σ detection of the total neutrino mass even in the minimal normal hierarchy scenario ($\sum m_\nu \simeq 0.06$ eV). The reason for such an improvement can be easily understood by looking at the right panel of Figure 3.5 which shows the 68% and 95% confidence regions in the $(\sum m_\nu - \sigma_8)$ plane from Planck data, Euclid-Cl data and the combination of the two. Taken independently, the CMB and galaxy cluster data exhibit significant degeneracies in this plane, but the nearly orthogonal degeneracy directions allow their combination to provide tight constraint on these

Table 3.2: Constraints on $\sum m_\nu$ for ΛCDM+m_ν model from Planck, cluster power spectrum ($P^{cl} - only$), Euclid-Cl (cluster number counts and power spectrum) data, and the combination of the two data sets Euclid-Cl+Planck. Because the parameter τ is not constrained by Euclid data, when CMB measurements are not included τ is kept fixed to its fiducial value.

Model		ΛCDM+m_ν			
Data		Planck	$P^{cl}-$only	Euclid-Cl	Euclid-Cl+Planck
$\sum m_\nu$ [eV]	68% CL	< 0.41	< 0.41	< 0.17	< 0.017
	95% CL	< 0.74	< 1.20	< 0.35	< 0.031

parameters, and in particular on the neutrino mass. When Planck priors are added to the Euclid-Cl constraints, all degeneracies are either resolved or largely reduced (see blue contours in Figure 3.5 and Figure 3.6). Similar levels of sensibility on $\sum m_\nu$ are also expected combining Euclid galaxy or cosmic shear power spectrum measurements with Planck CMB data (e.g. Carbone et al., 2011; Audren et al., 2012; Hamann et al., 2012).

3.4.2 Varing $N_{\rm eff}$: ΛCDM+m_ν+$N_{\rm eff}$

We now explore the scenario with massive neutrinos and $N_{\rm eff}$ effective number of neutrino species. Again, we distribute the sum of neutrino masses equally among three active species ($N_\nu = 3$), and we treat additional contribution to $N_{\rm eff}$ as massless, such that $N_{\rm eff} = 3 + \Delta N_{\rm eff}$, with the prior $\Delta N_{\rm eff} \geqslant 0$. While the choice of keeping N_ν fixed does not affect constraints from CMB measurements (what matters is $N_{\rm eff}$), it could change the sensitivity to $\sum m_\nu$ and $N_{\rm eff}$ based on galaxy clusters data. Indeed, changing N_ν would change the mass of each massive neutrino and thus its free-streaming lenght beyond which the power spectrum is suppressed (see Eq. (1.46)). We checked the case with fixed $\Delta N_{\rm eff}$ and N_ν as free parameter and we find no qualitative changes in our results. This means that the data are not sensitive to the exact position of the break in the power spectrum induced by free-streaming neutrinos, and thus to the neutrino mass hierarchy. Table 3.3 shows the joint constraints on the sum of neutrino masses and on the effective number of neutrino species from Planck data alone and the combination of Planck and Euclid-Cl datasets. Looking at Planck data alone, the quality of the constraints on $\sum m_\nu$ are nearly unchanged from the single-parameter extensions discussed earlier, as it would be expected for independent parameters. Indeed, $\sum m_\nu$ and $N_{\rm eff}$ are con-

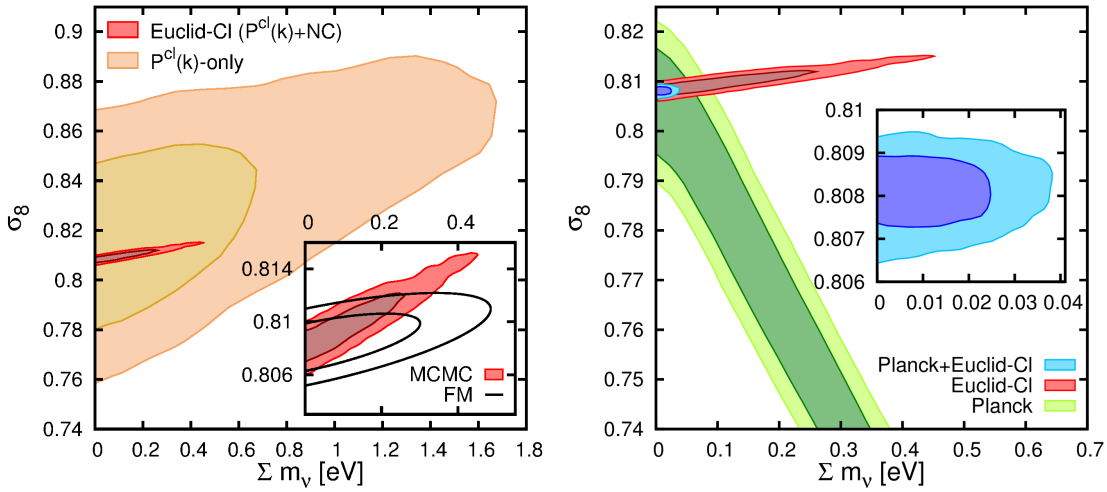

Figure 3.5: The 68% and 95% CL contours in the $(\sum m_\nu$-$\sigma_8)$ plane for a ΛCDM+m_ν model. Left panel: contours from cluster power spectrum (large contours; P^{cl}-only) and the combination of cluster power spectrum and number counts (small contours; Euclid-Cl). The insert plot shows a zoom of the confidence contours given by the Euclid-Cl dataset compared with the contours obtained from the Fisher Matrix technique using the same dataset. Right panel: contours from Planck (*green*), Euclid-Cl (*red*) and Planck+Euclid-Cl (*blue*) datasets. The insert plot shows a zoom of the confidence contours obtained from the Planck+Euclid-Cl datasets.

Table 3.3: Constraints on $\sum m_\nu$ and $N_{\rm eff}$ for ΛCDM+m_ν+$N_{\rm eff}$ model.

Model		ΛCDM+m_ν+$N_{\rm eff}$	
Data		Planck	Euclid-Cl+Planck
$\sum m_\nu$ [eV]	68% CL	< 0.42	< 0.022
	95% CL	< 0.78	< 0.040
$N_{\rm eff}$	95% CL	< 3.36	< 3.14

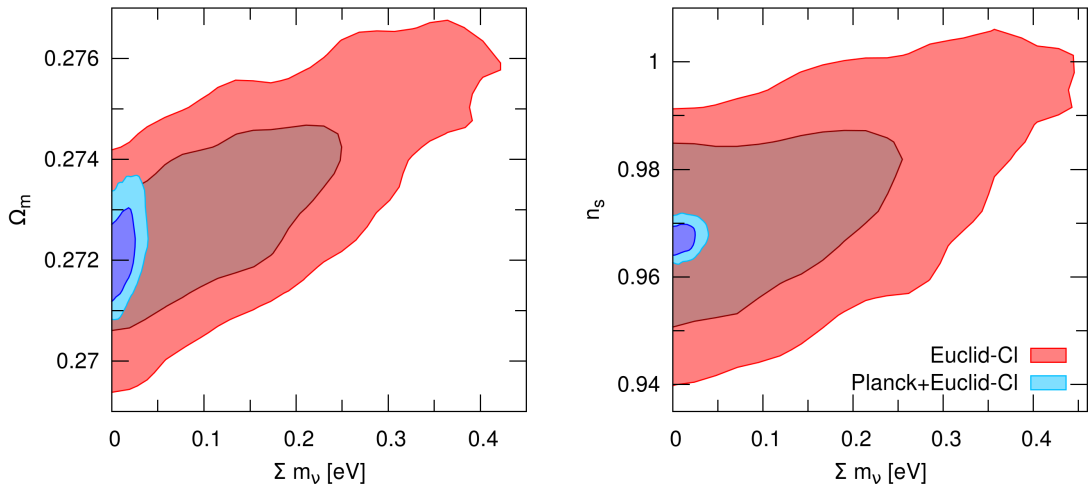

Figure 3.6: The 68% and 95% CL contours in the $\sum m_\nu - (\Omega_{\rm m}, n_{\rm s})$ planes for a ΛCDM+m_ν model, from Euclid-Cl (red contours) and the Planck+Euclid-Cl (blue contours) datasets. When only Euclid-Cl dataset is used the parameter τ, which is not constrained by this data, is kept fixed to its fiducial value 0.085.

strained by different features in the CMB spectra: the early integrated Sachs-Wolfe effect for $\sum m_\nu$, the damping scale and the position of the acoustic peaks for $N_{\rm eff}$ (see e.g. Hinshaw et al., 2013, and references therein). However, since both $\sum m_\nu$ and $N_{\rm eff}$ have similar effects on the matter power spectrum (§ 3.1), the correlation of the two degrades the upper bound on the sum of neutrino masses inferred from Euclid-Cl+Planck data by $\sim 30\%$ to $\sum m_\nu < 0.040[\rm eV]$ at 95%CL. With this accuracy, it would still be possible a $2\,\sigma$ detection of neutrino masses in the minimal normal hierarchy scenario. Constraining $N_{\rm eff}$ is mainly achieved through CMB measurements of the redshift of the matter-radiation equality z_{eq} and the baryon density $\Omega_{\rm b}h^2$. However, keeping z_{eq} and $\Omega_{\rm b}h^2$ fixed as $N_{\rm eff}$ increases can be achieved by increasing the cold dark matter density $\Omega_{\rm c}h^2$, which displays a large correlation with $N_{\rm eff}$ (Hou et al., 2011). Euclid-Cl data alone are unable to provide constraints on the number of effective species. However, the inclusion of clusters dataset allows to significantly improve the measurements of $\Omega_{\rm m}h^2$ (by constraining σ_8), thus reducing the 2σ error on the effective number of neutrino by a factor larger than 2.5 from 0.36 to 0.14 (see right panel of Figure 3.7). After the inclusion of Euclid-Cl data $N_{\rm eff}$ still exhibits strong degeneracies with many cosmological parameters (e.g. $\Omega_{\rm m}h^2$, H_0 and $n_{\rm s}$), and a correlation of ~ 0.5 with $\sum m_\nu$ (see left panel of Figure 3.7).

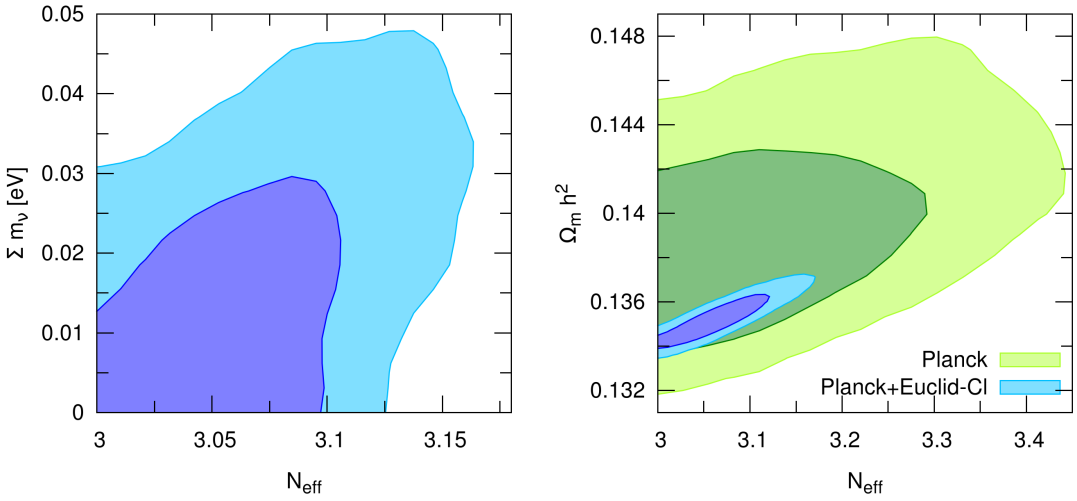

Figure 3.7: The 68% and 95% CL contours in the $N_{\rm eff} - (\Omega_{\rm m}, \sum m_\nu)$ planes for a ΛCDM+m_ν+$N_{\rm eff}$ model, from: Planck (green contours) and Planck+Euclid-Cl (blue contours) data.

Table 3.4: Constraints on $\sum m_\nu$ and $N_{\rm eff}$ for the two parameter extensions $(w, \Omega_{\rm k})$ from Euclid-Cl+Planck datasets.

Data		Planck+Euclid-Cl	
Model		wCDM+m_ν+$N_{\rm eff}$	ΛCDM+m_ν+$N_{\rm eff}$+$\Omega_{\rm k}$
$\sum m_\nu$ [eV]	68% CL	< 0.024	< 0.024
	95% CL	< 0.046	< 0.046
$N_{\rm eff}$	95% CL	< 3.16	< 3.17

3.4.3 Extended models: wCDM+m_ν+$N_{\rm eff}$ and curved Universe

Next, we consider how the constraints on $\sum m_\nu$ and $N_{\rm eff}$ are affected when additional degrees of freedom are introduced in the cosmological model. The effect on $(\sum m_\nu, N_{\rm eff})$ of adding these degree of freedom to the ΛCDM+m_ν+$N_{\rm eff}$ model are shown in Figure 3.8 and listed in Table 3.4. We start by considering a constant dark energy equation of state ($w \equiv P_{\rm de}/\rho_{\rm de} \neq -1$). In this case the evolution of the

Hubble parameter reads:

$$H(z) = H_0\Big[\Omega_{de}(1+z)^3 \exp\left[3\int_0^z \frac{w}{1+z'}dz'\right] + \Omega_k(1+z)^2 + \Omega_m(1+z)^3 + \Omega_r(1+z)^4\Big]^{1/2}, \tag{3.11}$$

which reduces to Eq. (1.14) for $w = -1$. Therefore, changing the value of w affects the expansion rate of the Universe, and in turn, the growth of structure through Eq. (1.13). Neutrino properties ($\sum m_\nu, N_{eff}$) and w are generally degenerate because they can both affect the shape of the matter and CMB power spectra (e.g. Xia et al., 2007). Looking at Figure 3.9 (a), we indeed see this degeneracy in the plane $N_{eff} - w$, which displays a correlation of ~ 0.5, whereas the parameters w and $\sum m_\nu$ show almost no correlation. The Euclid clusters catalog, probing the evolution of the LSS up to $z \sim 2$, will be able to put tight constraints on the dark energy equation of state; we find for the combination of Planck and Euclid-Cl data: $-1.011 < w < -0.987$ (95%CL). Given the small uncertainty on w the constraints on neutrino mass and effective number of species are only slightly degraded when w is allowed to vary; the 95% CL upper limit for N_{eff} is relaxed from 3.14 to 3.16 due to the degeneracy with w. Whereas, the 95% CL upper limit for $\sum m_\nu$ undergoes only a small degradation from 0.040 eV to 0.046 eV, caused by the weak constraints on parameters that are correlated with $\sum m_\nu$ induced by the extension of the parameter space. Secondly, we relax the prior on the curvature of the universe by considering the case ΛCDM+m_ν+$N_{eff}+\Omega_k$. Since current data do not support departures from the flat ΛCDM model either through $\Omega_k \neq 0$ or $w \neq -1$, we introduce these parameters separately. From the combination of Planck and Euclid-Cl datasets we obtain, for the curvature parameter, the following constraint: $-0.0024 < \Omega_k < 0.0024$ (95%CL). As CMB power spectrum suffer from a well known "geometrical degeneracy" (e.g. Bond et al., 1997; Zaldarriaga et al., 1997), Euclid-CL data considerably improves the error on Ω_k breaking such degeneracy thanks to the tight constraint on Ω_m (given by the growth information encoded in the dataset). The spatial curvature mainly affects the expansion rate via the Friedmann equation, as well as the total neutrino mass and number of effective species do. As it can be seen in Figure 3.9 (b), this results in a correlation with both $\sum m_\nu$ and N_{eff} of the order of ~ 0.5 and ~ 0.6, respectively. Despite these quite large degeneracies with Ω_k, the small error associated to the curvature parameter leads to a slight relaxation of the constraints on neutrino properties: the upper limit for neutrino mass degrades by $\sim 10\%$, passing from 0.040 eV to 0.046 eV (95%CL), while the 2σ error on N_{eff} shift from 0.14 to 0.17, a 20% degradation.

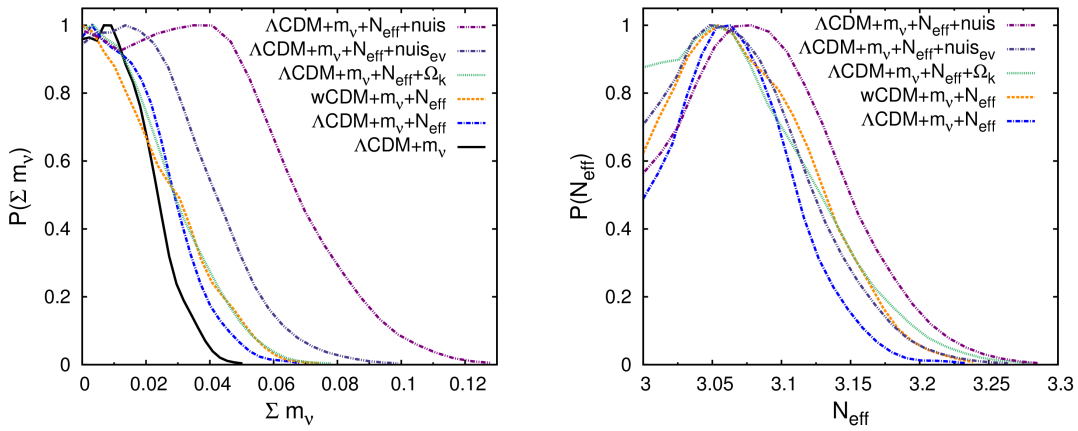

Figure 3.8: The marginalized one-dimensional posteriors for $\sum m_\nu$ (left) and $N_{\rm eff}$ (right) for different parameter extensions from the combination of Euclid-Cl and Planck datasets.

Table 3.5: Constraints on $\sum m_\nu$ and $N_{\rm eff}$ for ΛCDM+m_ν+$N_{\rm eff}$ models with free nuisance parameters.

Data		Planck+Euclid-Cl	
Model		ΛCDM+m_ν+$N_{\rm eff}$+nuis	ΛCDM+m_ν+$N_{\rm eff}$+nuis$_{\rm ev}$
$\sum m_\nu$ [eV]	68% CL	< 0.049	< 0.031
	95% CL	< 0.083	< 0.056
$N_{\rm eff}$	95% CL	< 3.18	< 3.16

Thus, in both cases, the parameter extension entails a relaxation of the constraints on $\sum m_\nu$ and $N_{\rm eff}$; nonetheless, given the high accuracy with which w and $\Omega_{\rm k}$ are expected to be measured, the survey would still allow a 2σ detection of neutrino mass in the minimal normal hierarchy scenario and reveal the presence of possibles extra relativistic species.

3.4.4 Nuisance parameters

Finally, to assess the effect of an uncertain knowledge of cluster masses on $\sum m_\nu$ and $N_{\rm eff}$ constraints, we treat the ΛCDM+$m_\nu + N_{\rm eff}$ case with the four nuisance parameters as fitting parameters, following the so-called self-calibration method (e.g. Majumdar and Mohr, 2004; Lima and Hu, 2005; Sartoris et al., 2012). The results

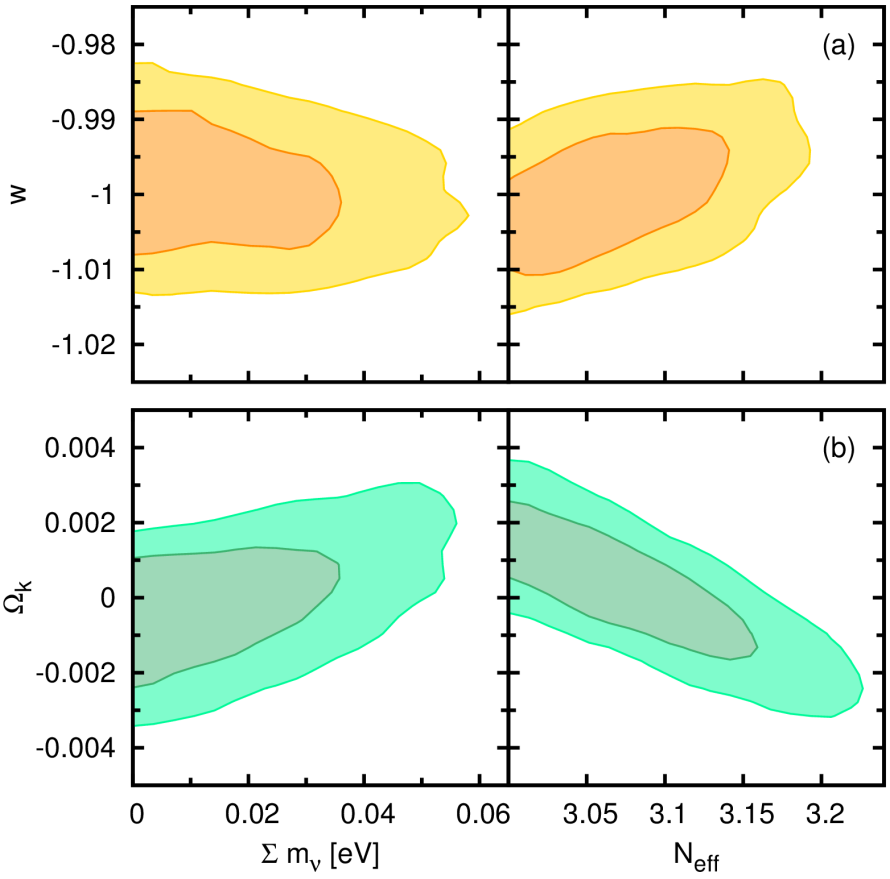

Figure 3.9: Joint two dimensional marginalized constraints on w (a) and Ω_k (b) against $(\sum m_\nu, N_{\rm eff})$ at 68% and 95% CL. The confidence regions are respectively for the extended parameter space wCDM+m_ν+$N_{\rm eff}$ and ΛCDM+m_ν+$N_{\rm eff}+\Omega_k$, using data from Euclid-Cl+Planck.

are listed in Table 3.5. We start with the the over-conservative assumption of no priors on all the four nuisance parameters (ΛCDM+m_ν+$N_{\rm eff}$+nuis model). The uncertainties on scaling relation parameters compromise our ability to recover the halo mass function from cluster data, thus reducing the cosmological information achievable from cluster number counts. This results in a larger error for the parameters that are primarily constrained by cluster number counts, in particular for σ_8, the normalization of the power spectrum. Looking at Figure 3.10 (left panel), the constraints on σ_8 are relaxed by a factor of ~ 10 compared to the ΛCDM+m_ν+$N_{\rm eff}$ model, and the parameter recovers a large degeneration with $\sum m_\nu$ of the order of ~ 0.65. This effect, along with the degradation of other parameters errors (e.g. $\sigma(\Omega_{\rm m})$), entails a relaxation of the upper limit for $\sum m_\nu$ by a factor larger than two, from 0.040 eV to 0.083 eV. With these loose constraints, in the case of minimal normal hierarchy scenario, it would not be possible to have a 2σ detection of neutrino mass. Because the constraints on neutrino mass from cluster number counts relay on the evolution of the high-mass end of the mass function, $\sum m_\nu$ is rather degenerate with α and β, the two nuisance parameters which control the evolution of the systematic bias and intrinsic scatter (see Eq. 3.4). To emphasize the role played by the uncertain redshift evolution of the nuisance parameter on the determination of $\sum m_\nu$ we show in Figure 3.10 the contours for a model with α and β kept fixed (ΛCDM+m_ν+$N_{\rm eff}$+nuis$_{ev}$ model). In this case the degradation of the total neutrino mass constraints with respect the ΛCDM+m_ν+$N_{\rm eff}$ model is only of $\sim 40\%$, from 0.040 eV to 0.056 eV. In other words, an accurate knowledge of the redshift evolution of the nuisance parameter improves the 2σ upper limit of $\sum m_\nu$ by $\sim 33\%$ compared to the previous case with no prior on the nuisance parameters.

Likewise, the forecast error on $N_{\rm eff}$ is influenced by the loss of constraining power of the cluster number counts data, even if to a lesser extent than the bounds on $\sum m_\nu$, since the constraints on $N_{\rm eff}$ are primarily contributed by CMB measurements. The 2σ upper limit shifts from $N_{\rm eff} < 3.14$ to $N_{\rm eff} < 3.16$ and $N_{\rm eff} < 3.18$, in the model with strong evolution prior and free nuisance parameters, respectively. In these case the degradation is mainly due to the larger error associated to $\Omega_{\rm m}h^2$, which is highly degenerate with $N_{\rm eff}$ as explained in Section 3.4.2 and shown in Figure 3.10 (right panel). We remind that the results for the model with no prior have to be regarded as an upper limit on the error introduced by the uncertain knowledge of the scaling relation; nevertheless, these results highlight the importance of having robust calibration of the scaling relation, and in particular of their evolution with redshift, to fully exploit the cosmological information contained in the Euclid cluster catalog.

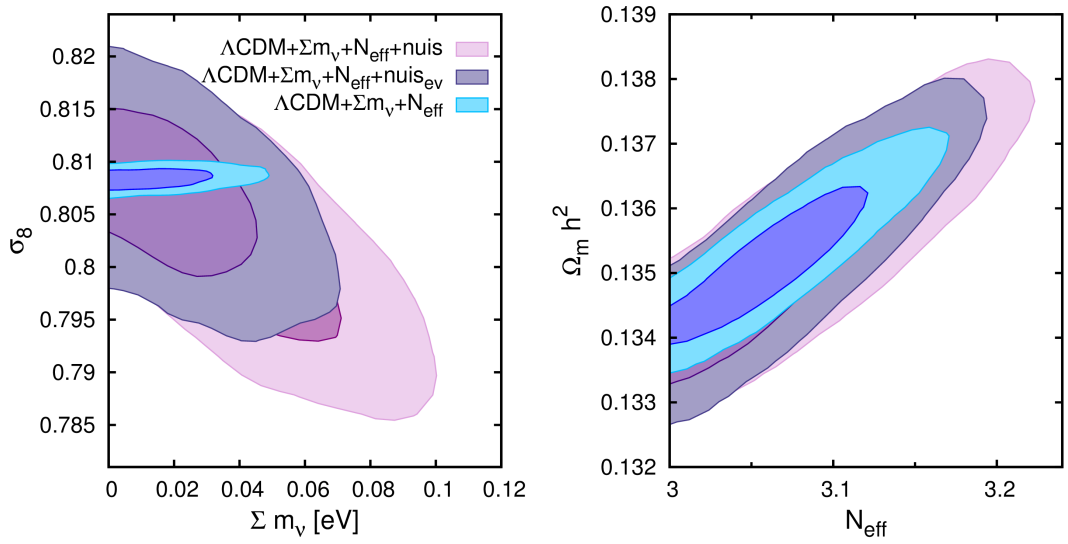

Figure 3.10: Joint two dimensional marginalized constraints on the planes $(\sum m_\nu - \sigma_8)$ and $(N_{\rm eff} - \Omega_{\rm m} h^2)$ at 68% and 95% CL from Euclid-Cl+Planck data. The confidence regions are for the ΛCDM+m_ν+$N_{\rm eff}$ model discussed in 3.4.2 (small blue contours) and the two extended model with nuisance parameters: all nuisance float (larger light violet contours) and fixed evolution parameters α and β (dark violet contours).

3.5 Conclusions

In this Chapter, we presented forecasts on the capability of the future Euclid photometric galaxy cluster survey, in combination with Planck-like data, to provide constraints on neutrino properties. Specifically, we rely on two observables: the cluster number counts and their power spectrum. Our analysis is based on the Markov Chain Monte Carlo methods rather than the Fisher Matrix technique, which results in more reliable error bars. We start by considering a reference ΛCDM model in agreement with the results of WMAP 9-year.

In order to study possible degeneracies with $\sum m_\nu$, besides the ΛCDM model with massive neutrino, we also consider models with $N_{\rm eff}$ effective number of relativistic species, a constant dark energy equation of state w and curvature. Following the self-calibration approach, along with the other cosmological parameter, we decide to explore also the effect of leaving free the nuisance parameters that describe the relation between cluster optical richness and mass, its scatter and redshift

evolution.

Our results can be summarized as follows:

- From the combination of Euclid number counts and clustering data we predict a 2σ upper limits for the total neutrino mass of $\sum m_\nu < 0.35\,\mathrm{eV}$, comparable with present constraints from the combination of CMB and LSS probes (e.g. Zhao et al., 2012; Wyman et al., 2013; Battye and Moss, 2013; Beutler et al., 2014; Giusarma et al., 2014; Mantz et al., 2014). When Planck data are added to the Euclid-Cl ones the error on $\sum m_\nu$ is reduced by a factor larger than 10 to $\sum m_\nu < 0.031\,\mathrm{eV}$. With this accuracy the total neutrino mass could be detected at 2σ level even in the minimal normal hierarchy scenario. The large improvement is due to the different degeneracies present between Euclid and Planck that are broken once the two experiments are combined.

- Because the effective number of neutrino species is degenerate with the sum of neutrino masses, varying N_{eff} entails a relaxation of 2σ error bars on $\sum m_\nu$ by $\sim 30\%$ in the Planck+Euclid-Cl case. Still, the 2σ error is lower than the minimum neutrino mass admitted by neutrino oscillation experiments. The Euclid-Cl dataset is unable to constraints N_{eff} by itself, but improves the 2σ upper limits on N_{eff} from 3.36 using Planck-only, to 3.14 in the Planck+Euclid-Cl case. The improvement is mainly due to the tighter constraints on $\Omega_{\mathrm{m}}h^2$ provided by the Euclid-Cl datasets.

- In models with varying w or Ω_{k} the 2σ error on $\sum m_\nu$ is relaxed only by $\sim 10\%$. In both cases the high accuracy with which w or Ω_{k} are constrained by the Planck+Euclid-Cl data prevents the error on $\sum m_\nu$ from being largely degraded. As for N_{eff}, the parameter shows a correlation of the order of ~ 0.5 with both w and Ω_{k}, which shifts the 2σ upper limit for N_{eff} to 3.16 and 3.17, respectively.

- When nuisance parameters are considered in a conservative way (no prior) our ability to recover the halo mass function from cluster data is compromised. The degradation of cosmological information results in a ~ 2 times larger 2σ error for neutrino masses ($\sum m_\nu < 0.083\,\mathrm{eV}$) and a degradation of $\sim 30\%$ of the 2σ error on the effective number of neutrinos ($N_{\mathrm{eff}} < 3.18$). In this case the accuracy would not be sufficient for detecting the total neutrino mass with good significance in the minimal normal hierarchy scenario. Whereas, assuming a perfect knowledge of the redshift evolution of the nuisance parameters we partially recover the informations contained in cluster

number counts data. In this case the 2σ upper limit for $\sum m_\nu$ is degraded only by 40% to $\sum m_\nu < 0.056\,\mathrm{eV}$, while the 2σ error on the effective number of neutrinos degrades by $\sim 15\%$ to $N_{\mathrm{eff}} < 3.16$.

It is worth reminding that in our analysis we did not include the effect of redshift space distortions in the distribution of galaxy clusters induced by peculiar velocities. This effect should be in principle included when forecasting the cosmological constraining power of future cluster surveys; indeed, as demonstrated by Sartoris et al. (2012), the inclusion of redshift space distortions carries significant cosmological information through the growth rate of density perturbations.

As a concluding remark, we emphasize once again the importance to provide an accurate calibration of the scaling relation between the observable quantity on which cluster selection is based, optical richness in this case, and cluster mass. Thanks to the exquisite imaging quality expected for the Euclid survey, weak lensing masses for individual objects will be available for a significant fraction of the clusters identified from the photometric selection. At the same time, staking analysis will provide an accurate calibration of the relation between weak lensing masses and richness. For this reason, the Euclid cluster survey will represent a powerful complement to galaxy clustering and cosmic shear analyses to constrain cosmology through the growth of perturbations.

4

Massive neutrinos and the mass function of galaxy clusters

Among the different probes of the LSS, galaxy clusters have played a significant role in the definition of the "concordance" ΛCDM model (e.g. Allen et al., 2011; Kravtsov and Borgani, 2012), and many ongoing (Planck, SPT, DES), upcoming and future (eROSITA, LSST, Euclid) surveys will aim to use their abundance and spatial distribution to strongly constrain cosmological parameters. In order to fully exploit for cosmology the ever growing number of clusters detected, it is mandatory to have a reliable theoretical prediction for the cluster abundance (the halo mass function, HMF), together with an accurate calibration of the observable-mass relation. As for the former, since the pioneering work of Press and Schechter (1974) many forms for the HMF have been proposed in literature (e.g. Sheth and Tormen, 1999; Jenkins et al., 2001; Reed et al., 2007; Warren et al., 2006; Tinker et al., 2008; Crocce et al., 2010; Watson et al., 2013), often calibrated against large suites of cosmological simulations (§1.3.2). Despite the great improvement of the numerical results over the past decade many sources of systematic errors still affect the HMF, including finite simulation volume, mass and force resolution, baryonic physics and massive neutrino effects. In this Chapter we focus on the consequences of non-vanishing neutrino masses.

The effects of neutrino mass on the HMF has already been studied in several works (Brandbyge et al., 2010b; Marulli et al., 2011; Ichiki and Takada, 2012; Villaescusa-Navarro et al., 2013). Brandbyge et al. (2010b) measured the HMF from N-body simulations incorporating massive neutrinos using a hybrid scheme to sim-

ulate neutrino particles. They showed that the HMF in models with massive neutrinos can be well reproduced by the Sheth and Tormen (1999) mass function by using $\rho_{\rm cdm} = \rho_{\rm m} - \rho_\nu$, instead of $\rho_{\rm m}$, when establishing the relation between the halo mass and the top-hat window function radius ($M = 4\pi\rho R^3/3$, see Section 4.2 for details). Those results were later independently verified by Marulli et al. (2011) and Villaescusa-Navarro et al. (2013) using a different set of N-body simulations. More recently, Ichiki and Takada (2012) investigated the gravitational collapse of a spherical region in a massive neutrino cosmology, showing that neutrinos play a negligible role in the process. This led to the conclusion that the cold dark matter power spectrum should be used to compute the r.m.s. of the matter perturbations, $\sigma(M)$, required to predict the HMF. In Castorina et al. (2014) this was tested against N-body simulations, resulting in an excellent agreement.

In this Chapter we explore how the improved calibration of the HMF in cosmology with massive neutrinos affect the determination of cosmological parameters from galaxy clusters data. Firstly, using a suite of N-body simulations incorporating massive neutrinos as particles, we show that the abundance of halos, identified using the Spherical Overdensity (SO) algorithm (see §1.3.2), is well reproduced by the Tinker et al. (2008) fitting formula once the cold dark matter mean density and linear power spectrum are used, in agreement with Castorina et al. (2014) and the work of Ichiki and Takada (2012). The reason to use SO halos, rather than Friends-of-Friend (FoF) halos as in Castorina et al. (2014), is that the mass proxy in X-ray and SZ measurements is calibrated with spherically defined objects. Secondly, we use our findings to investigate the implications for cosmological parameter inference using cluster number counts. As a case study, we choose the Planck SZ-selected sample of clusters Planck Collaboration (2013b), for which we perform a Monte Carlo Markov Chain analysis in order to compare constraints obtained using different prescriptions for the HMF.

The results presented in this Chapter have been published in Costanzi et al. (2013). This is the last of a series of three papers. The first paper (Villaescusa-Navarro et al., 2014) introduces a large set of numerical simulations incorporating massive neutrinos as particles. It then studies the effect of neutrino masses on the spatial distribution of dark matter halos, finding that halo bias, as typically defined w.r.t. the underlying *total* matter distribution, exhibits a scale-dependence on large scales for models with massive neutrinos. In addition, Villaescusa-Navarro et al. (2014) investigates as well massive neutrinos effects on the spatial distribution of galaxies by constructing mock galaxy catalogues using a simple halo occupation distribution (HOD) model. In the second paper of the series Castorina et al. (2014) the universality of the HMF and of linear bias in massive neutrino cosmologies

Name	$\sum m_\nu$ [eV]	Box $[h^{-1}\mathrm{Mpc}]$	Ω_m	Ω_b	Ω_Λ	Ω_ν	h	n_s	$N_\mathrm{CDM}^{1/3}$	$N_\nu^{1/3}$	σ_8 $(z=0)$
H6	0.60	1000	0.2708	0.050	0.7292	0.0131	0.7	1.0	512	512	0.675
H3	0.30	1000	0.2708	0.050	0.7292	0.0066	0.7	1.0	512	512	0.752
H0	0.00	1000	0.2708	0.050	0.7292	0	0.7	1.0	512	0	0.832
H6s8	0.06	1000	0.2708	0.050	0.7292	0.0131	0.7	1.0	512	512	0.832

Table 4.1: Summary of the simulations used in the present work.

is discussed in terms of halo catalogues determined with the Friends-of-Friends algorithm on the simulations introduced in Villaescusa-Navarro et al. (2014). It is shown that the proper variable to describe the HMF of a massive neutrino model is the variance of *cold* dark matter perturbations, rather than the total ones (i.e. including neutrinos) typically assumed in previous analyses Brandbyge et al. (2010b); Marulli et al. (2011); Villaescusa-Navarro et al. (2013). If the correct prescription is used then the HMF becomes nearly universal with respect to the neutrino mass. The paper discusses also similar results for the bias of halos at large scales, which is found to be almost scale independent and universal when expressed in terms of CDM quantities alone.

The Chapter is organized as follows. In Section 4.1 we describe the numerical simulations we have used to calibrate the HMF of dark matter halos identified using the SO criterion. The halo mass functions for the different cosmological models and the procedure used to compute them are shown in Section 4.2. The implications of our results, in terms of cluster number counts, are presented in Section 4.3, while the likelihood analysis is shown in Section 4.4. Finally, we draw the main conclusions of this Chapter in Section 4.5.

4.1 N-body simulations

The analysis presented in this Chapter has been obtained using a subset of a large suite of N-body simulations presented in Villaescusa-Navarro et al. (2014), whose main features are summarized below.

The N-body simulations, containing CDM and neutrino particles, have been run using the TreePM code `GADGET-3`, which is an improved version of the code `GADGET-2` Springel (2005). The TreePM algorithm (e.g. Xu, 1995) is an hybrid tech-

nique, where short-range forces are computed with the so called "tree" method[1] (e.g. Appel, 1985; Barnes and Hut, 1986; Dehnen, 2000), while long-range forces are determined with Fourier techniques (Particle-Mesh (PM) methods, e.g. Hockney and Eastwood, 1981; Klypin and Shandarin, 1983; White et al., 1983). The neutrinos have been simulated using the so-called *particle-based* implementation. In this implementation, neutrinos are treated as an extra set of particles, in the same way as the CDM, with the difference that, at the starting redshift of the simulation, the neutrinos receive an extra thermal velocity component obtained by random sampling the neutrino Fermi-Dirac linear momentum distribution. On small scales, the force affecting the neutrinos is computed using the short-range Tree force; this feature is required to correctly account for the clustering of neutrinos within dark matter halos and to reproduce the neutrino halos down to small scales (Villaescusa-Navarro et al., 2013). This *particle-based* approach is better suited to study the effects of massive neutrinos on the spatial distribution of dark matter halos since it allows to capture the fully non-linear regime, as opposed to the so-called *grid method* used in earlier studies (Brandbyge and Hannestad, 2009; Viel et al., 2010; Marulli et al., 2011), in which neutrinos only contribute to the long distance force through the PM method.

The starting redshift of the simulations was set to $z = 99$. The initial conditions were generated at that redshift by displacing the particles positions from a regular cubic grid, using the Zel'dovich approximation (Zel'dovich, 1970). We incorporate the effects of baryons into the CDM particles by using a transfer function that is a weighted average of the transfer functions of the CDM and the baryons, obtained directly from the Boltzmann solver code `CAMB` (Lewis et al., 2000). The gravitational softening of each particle type is set to 1/30 of their mean inter-particle linear spacing. For each simulation we saved snapshots at redshifts 0, 0.5, 1 and 2.

The different cosmological models used for this paper are shown in Table 4.1, together with the values of their cosmological parameters. Each simulation consists of eight independent realizations obtained by generating the initial conditions using different random seeds. The size of the cosmological boxes are 1 h^{-1}Gpc for all the simulations. The cosmological models span from a massless neutrino model (H0) to cosmologies with $\sum m_\nu = 0.3$ eV (H3) and $\sum m_\nu = 0.6$ eV (H6 and H6s8). Although observational constraints prefer a value of $\sum m_\nu$ smaller than 0.30 eV, a value of 0.60 eV is not completely unreasonable, as the latest results of Planck Col-

[1] In tree codes particles are hierarchically grouped following a tree-like-scheme (*root*, *branch*, *leaf*) according to their mutual distances; in this way only the gravitational interaction between nearby particles needs to be treated individually, while the gravitational force of distant groups of particles can be accounted for by means of a single multipole force.

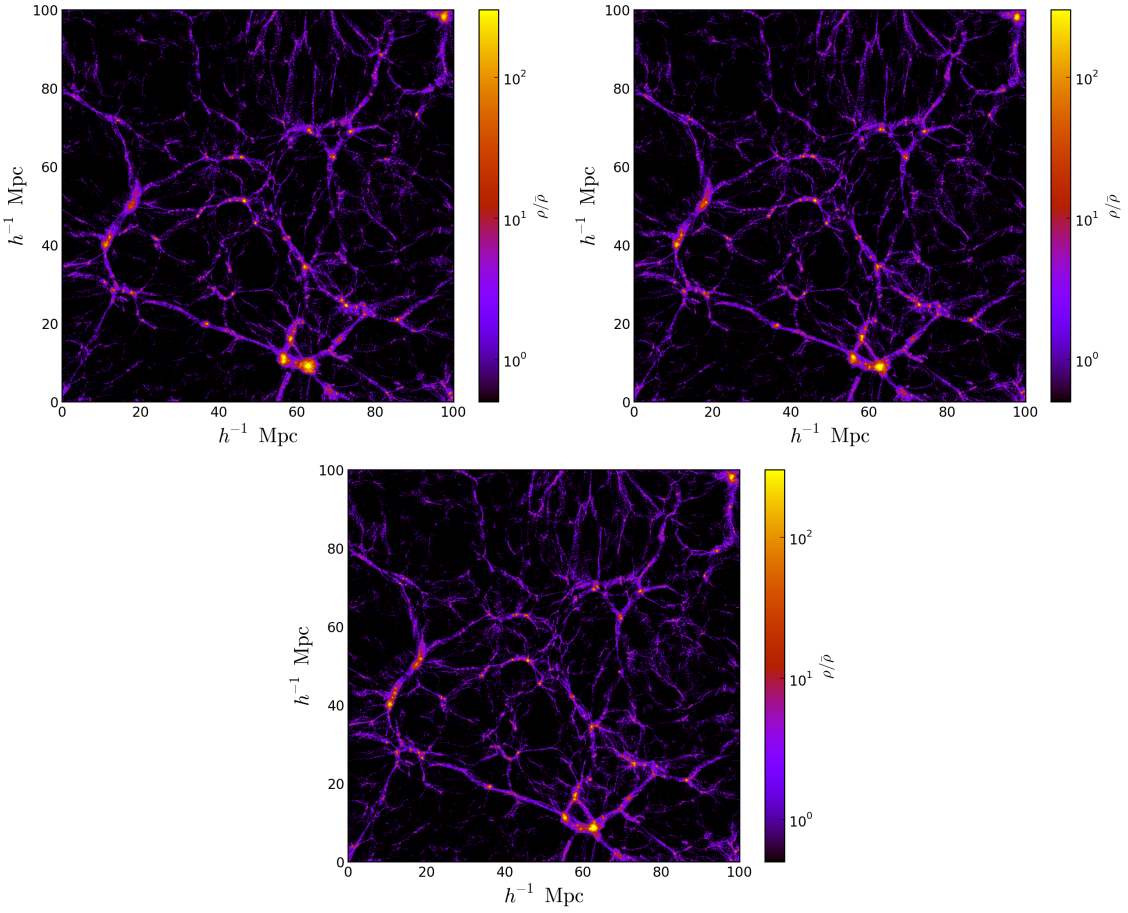

Figure 4.1: Density slices extracted from three simulations shearing the same initial conditions but with different total neutrino mass: $\sum m_\nu = 0.0\,\mathrm{eV}$ (*top left* panel), $\sum m_\nu = 0.3\,\mathrm{eV}$ (*top right* panel) and $\sum m_\nu = 0.6\,\mathrm{eV}$ (*lower* panel). The panels show the project CMD overdensities ($\rho/\bar{\rho} = 1 + \delta$; *colour coded*) at $z = 0$ obtained from the three simulations for boxes of $100h^{-1}$ comoving Mpc aside.

laboration (2013d) indicate. The simulations H6, H3 and H0 share the value of the large-scale power spectrum normalisation A_s, whereas the value of this parameter has been tuned in the simulation H6s8 to obtain the same value of σ_8 of the simulation H0. The value of the parameter σ_8 depends on the neutrino masses since the amplitude of the power spectrum is fixed on large scales, thus, models with higher neutrino masses will have a lower value of σ_8. The values of the other cosmological parameters are common to all the simulations: $\Omega_{\rm m} = \Omega_{\rm cdm} + \Omega_{\rm b} + \Omega_\nu = 0.2708$, $\Omega_{\rm b} = 0.05$, $\Omega_\Lambda = 1 - \Omega_{\rm m} = 0.7292$, $h = 0.7$ and $n_s = 1.0$. In all the simulations the value of the parameter $\Omega_{\rm cdm}$ is given by $\Omega_{\rm m} - \Omega_{\rm b} - \Omega_\nu$, i.e. is fixed by requiring that the total matter density of the Universe is the same for all the cosmological models. The number of CDM particles is 512^3, and for the models with massive neutrinos the number of neutrinos is also 512^3. The masses of the CDM particles are $5.6 \times 10^{11}\ h^{-1} M_\odot$ for the model H0, while for the others model the masses are slightly different since the value of $\Omega_{\rm cdm}$ varies from model to model.

In Figure 4.1 are shown illustrative slices extracted at $z = 0$ from three simulations with the same parameters of the simulations H0 ($\sum m_\nu = 0.0\,$eV), H3 ($\sum m_\nu = 0.3\,$eV) and H6 ($\sum m_\nu = 0.6\,$eV), shearing the same initial density field – i.e. generated using the same random seeds. Looking at the densest regions (*yellowest* areas), one can see that increasing the neutrino mass (*clockwise*) the structures become less evolved, in particular at the knots of the cosmic web, where the neutrino free-streaming suppresses the growth of structures (see §1.5.3).

4.2 The halo mass function

The dark matter halos used to compute the HMFs have been identified using the `SUBFIND` algorithm (Springel et al., 2001). Even though `SUBFIND` is capable of identifying all the halos and sub-halos from a given particle distribution, we have used it to identify spherical overdensity (SO) halos. The virial radius of a given dark matter halo corresponds to the radius within which the mean density is $\Delta_{\rm m}$ =200 times the mean density of the Universe at that redshift. We restrict our analysis to SO halos containing at least 32 particles.

`SUBFIND` has only been run on top of the CDM particle distribution. This is equivalent to neglect the contribution of neutrinos to the masses of the dark matter halos. Such assumption is supported by different studies (Ringwald and Wong, 2004; Brandbyge et al., 2010b; Villaescusa-Navarro et al., 2011, 2013) which have shown that the contribution of massive neutrinos to the total mass of dark matter halos is below the percent level for the neutrino mass range relevant for this paper.

We have explicitly checked that the contribution of neutrinos with $\sum m_\nu = 0.6$ eV to the total masses of dark matter halos ranges from 0.01% for halos with $M_{200} \simeq 10^{13}\,h^{-1}M_\odot$, to 0.5% for the most massive halos with $M_{200} \simeq 10^{15}\,h^{-1}M_\odot$. To make sure that our results are not affected by selecting the halos on top of the CDM particle distribution we have run SUBFIND on top of the total matter (i.e. CDM plus neutrinos) density field. We find that the HMF of SO halos changes by less than 0.5% on a very wide range of masses. However, the masses of some low mass halos are slightly changed when including neutrinos. This is because some of these low mass halos contain many unbound neutrino particles, which bias the estimate of their masses by an unreasonable amount. This effect is less important for more massive halos and/or for simulations in which the number of neutrino particles is much larger than the number of CDM particles. In order to avoid this spurious contamination in the masses of some dark matter halos we decided to rely on the halo catalogues obtained by running SUBFIND just on top of the CDM particle distribution.

Having built the DM halo catalogues we can now compute the HMFs for the various simulations with massless and massive neutrinos. We recall here that the comoving number density of dark matter halos per unit mass at redshift, $n(M,z)$, is commonly parametrized as follows:

$$n(M,z) = f(\sigma,z)\frac{\rho}{M}\frac{\mathrm{d}\ln\sigma^{-1}(M,z)}{\mathrm{d}M}\,, \tag{4.1}$$

where ρ is the comoving mean density of the Universe and $\sigma(M,z)$ is defined as:

$$\sigma^2(M,z) = \frac{1}{2\pi^2}\int_0^\infty \mathrm{d}k\,k^2 P(k,z)W^2(k,R)\,, \tag{4.2}$$

with $P(k,z)$ being the linear matter power spectrum at redshift z, and $W(k,R)$ the Fourier transform of the top-hat window function of radius R. The relationship between the halo mass, M, and the radius in the top-hat window function is given by $M = 4\pi\rho R^3/3$.

Our aim here is to compare the results of the left and right-hand side of eq. (4.1). The left-hand side is directly measured from the N-body simulations, whereas the right-hand side can be computed using a fitting formula for the function $f(\sigma,z)$ together with some prescriptions for cosmological models with massive neutrinos. We calculate the left-hand side of eq. (4.1) by approximating the quantity $\mathrm{d}n(M,z)/\mathrm{d}M$ by $\triangle n(M,z)/\triangle M$, where the width of the mass intervals has been chosen to be $\triangle\log(M) = 0.2$. The comoving number density of dark matter halos in a given mass interval $\triangle n(M,z)$ has been directly obtained from the N-body

halo catalogue. In order to compute the right-hand side of eq. (4.1) we need the following three ingredients: *i*) the function $f(\sigma, z)$; *ii*) the value of ρ to establish the relation between the halo mass and the radius in the top-hat window function and *iii*) the linear matter power spectrum $P(k, z)$.

Since we are considering SO halos, we compare our N-body results to the fitting formula of Tinker et al. (2008) (Eq. (1.36)), also defined in terms of SO halos, with best-fit parameters for the overdensity $\Delta_{\rm m} = 200$, according to the chosen halo identification criterion.

In a standard ΛCDM cosmology the quantities ρ and $P(k)$ appearing in eqs. (4.1, 4.2) are evaluated for the total dark matter field. However, it is not obvious which quantities have to be used for a model with massive neutrinos. The work of Brandbyge et al. (2010b) demonstrated that the abundance of dark matter halos in massive neutrino cosmologies cannot be reproduced by the Sheth and Tormen (1999) fit if the *total* matter density and linear power spectrum were used when calculating the r.h.s. of eq. (4.1). The authors proposed to use, instead, the mean cold dark matter density $\rho_{\rm cdm}$, computing, however, the variance $\sigma^2(M, z)$ still in terms of the total matter power spectrum. Such prescription, that we will refer to as the *matter prescription*, was later corroborated by several works Marulli et al. (2011); Villaescusa-Navarro et al. (2013).

More recently, Ichiki and Takada (2012) studied the gravitational collapse of a spherical region in a massive neutrino cosmology, showing that neutrinos play a negligible role in the process and leading to the conclusion that the cold dark matter power spectrum should be used to predict the HMF. Indeed, Castorina et al. (2014) shown that, for Friends-of-Friends (FoF) halos, a good agreement between the Crocce et al. (2010) fitting formula and the same suite of N-body simulations used in this analysis is obtained if both ρ and $P(k)$ are computed in terms of CDM quantities alone. We call this the *cold dark matter prescription* for massive neutrino cosmologies, and it has been show in Castorina et al. (2014) that it is the only way of obtaining a mass function that is nearly universal with respect to changes in the background cosmology.

We now compare the abundance of dark matter halos from the N-body simulations with the Tinker et al. (2008) prediction evaluated with both the matter and cold dark matter prescriptions. We emphasize that for cosmologies with massless neutrinos the above two prescriptions become the same. We show the results of this comparison in Figure 4.2 where the data points correspond to the mean of the mass function, $n(M)$, measured from eight realizations while the error bars represent the error on the mean. Predictions using the Tinker et al. (2008) fitting formula along with the matter and cold dark matter prescriptions are shown by

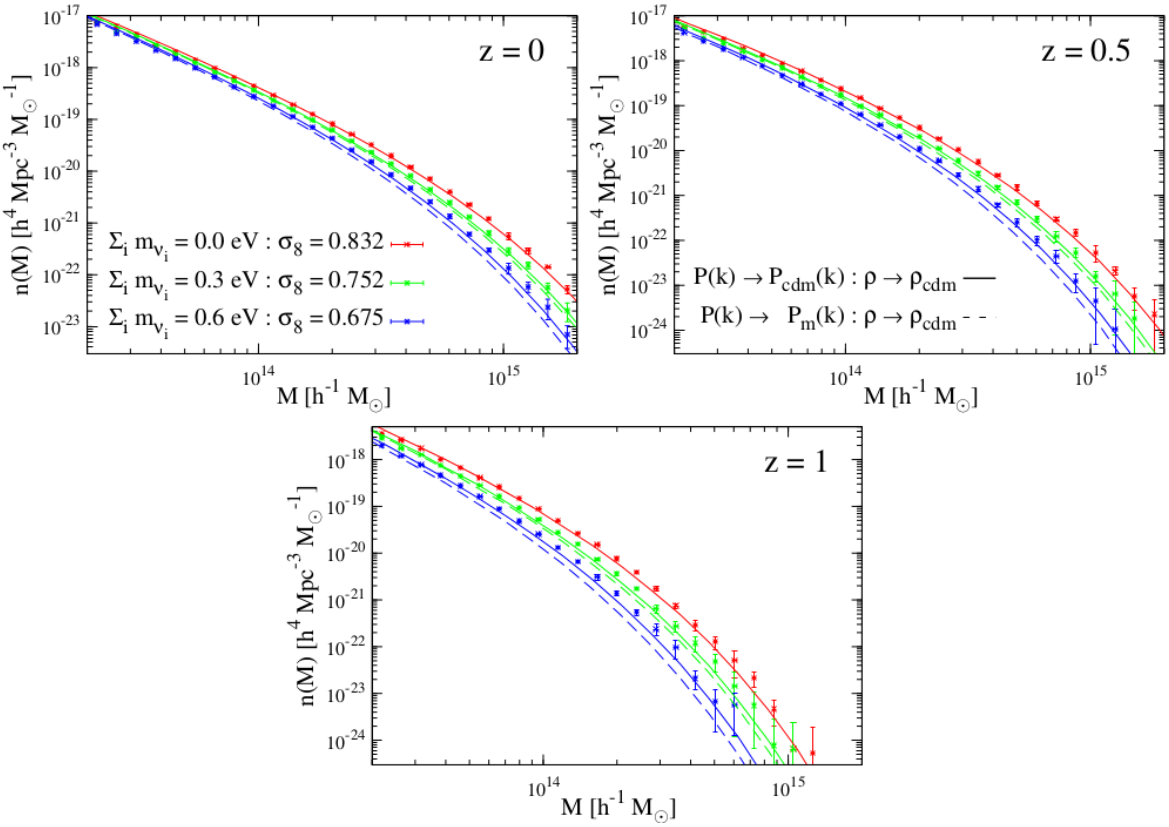

Figure 4.2: Mass function of dark matter halos identified using the SO criterion for different cosmological models at redshifts $z = 0$ (upper-left), $z = 0.5$ (upper-right) and $z = 1$ (bottom). The points show the halo mass function obtained from the N-body simulations with massless neutrinos (red) and with neutrinos with masses $\sum m_\nu = 0.3$ eV (green) and $\sum m_\nu = 0.6$ eV (blue). The error bars represent the dispersion around the mean value obtained from the eight independent realizations for each cosmological model. The results of using the Tinker et al. (2008) fitting formula along with the matter and cold dark matter prescriptions (see text for details) are displayed with dashed and solid lines, respectively.

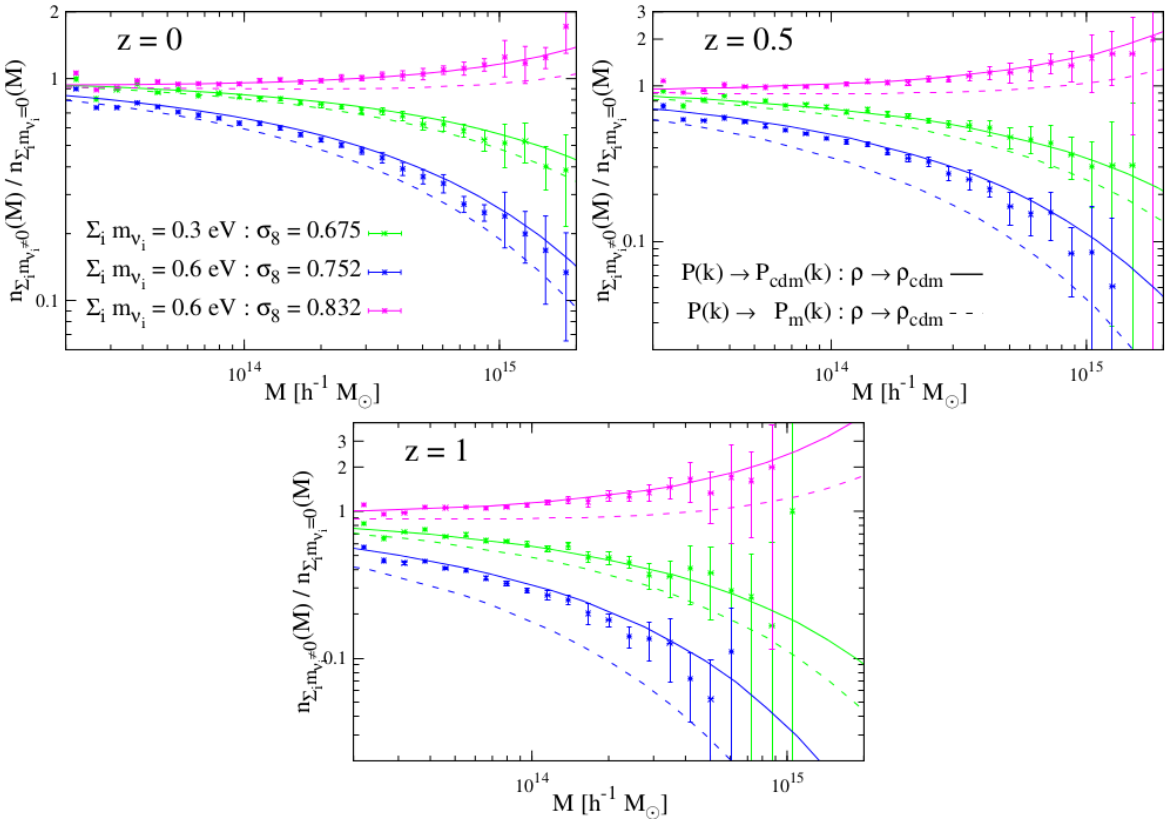

Figure 4.3: Ratio between the HMF for cosmologies with massive neutrinos to the halo mass function for the cosmological model with massless neutrinos (reference model). The points represent the results from the N-body simulations whereas the solid and dashed lines correspond to the ratios between the HMFs computed using the Tinker et al. (2008) fitting formula together with the *cold dark matter prescription* and the *matter prescription* for cosmologies with massive neutrinos, respectively.

the dashed and solid lines, respectively. We show the results at redshifts 0, 0.5 and 1 for the simulations H0, H3 and H6 (results at $z > 1$ are noisy). For clarity we do not display the results of the simulation H6s8 since they are very close to those of the simulation H0.

We find that the cold dark matter prescription reproduces much better the abundance of dark matter halos extracted from the N-body simulations. The agreement between the Tinker et al. (2008) fitting formula (plus the *cold dark matter prescription* for massive neutrinos) and our results is pretty good at $z = 0$, while at higher redshift is a bit poorer. We note that the differences between the results from the N-body simulations and the Tinker et al. (2008) fitting formula along with the cold dark matter prescription are almost independent of the cosmological model, likely arising from the different method used to identify the SO halos with respect to Tinker et al. (2008). In addition, Castorina et al. (2014) shown that the HMF for FoF halos ($b = 0.2$) using the same N-body simulations is very well reproduced (within a 10%) by the fitting formula of Crocce et al. (2010) at all redshifts. We emphasize that the use of a different HMF will not change the main conclusions of this Chapter.

In Figure 4.3 we show the ratio of the HMF for cosmologies with massive neutrinos to the HMF for the cosmology with massless neutrinos. We find that the abundance of SO halos is very well reproduced by the Tinker et al. (2008) fitting formula once the cold dark matter prescription is used for cosmologies with massive neutrinos.

4.3 An application to cluster number counts

A different prescription for the HMF can affect the constraints on cosmological parameters provided by cluster number counts by changing the number of clusters predicted for a given cosmology and survey.

From Eq. (2.10) it follows that the number of cluster expected to be detected within a survey with sky coverage $\Delta\Omega$ in a redshift bin $[z_i, z_{i+1}]$ can be expressed as:

$$N(z_i) = \int_{z_i}^{z_{i+1}} \mathrm{d}z \int_{\Delta\Omega} \mathrm{d}\Omega \frac{\mathrm{d}V}{\mathrm{d}z\mathrm{d}\Omega} \int_0^\infty dM\, X(M, z, \mathbf{\Omega})\, n(M, z)\,, \tag{4.3}$$

where, we recall, $\mathrm{d}V/\mathrm{d}z\mathrm{d}\Omega$ is the comoving volume element per unit redshift and solid angle, $X(M, z, \mathbf{\Omega})$ is the survey completeness and $n(M, z)$ is the HMF. Again, we adopt the Tinker et al. (2008) functional form for the mass function defined in eq. (1.36) with the best-fit parameters for the overdensity $\Delta = 200$.

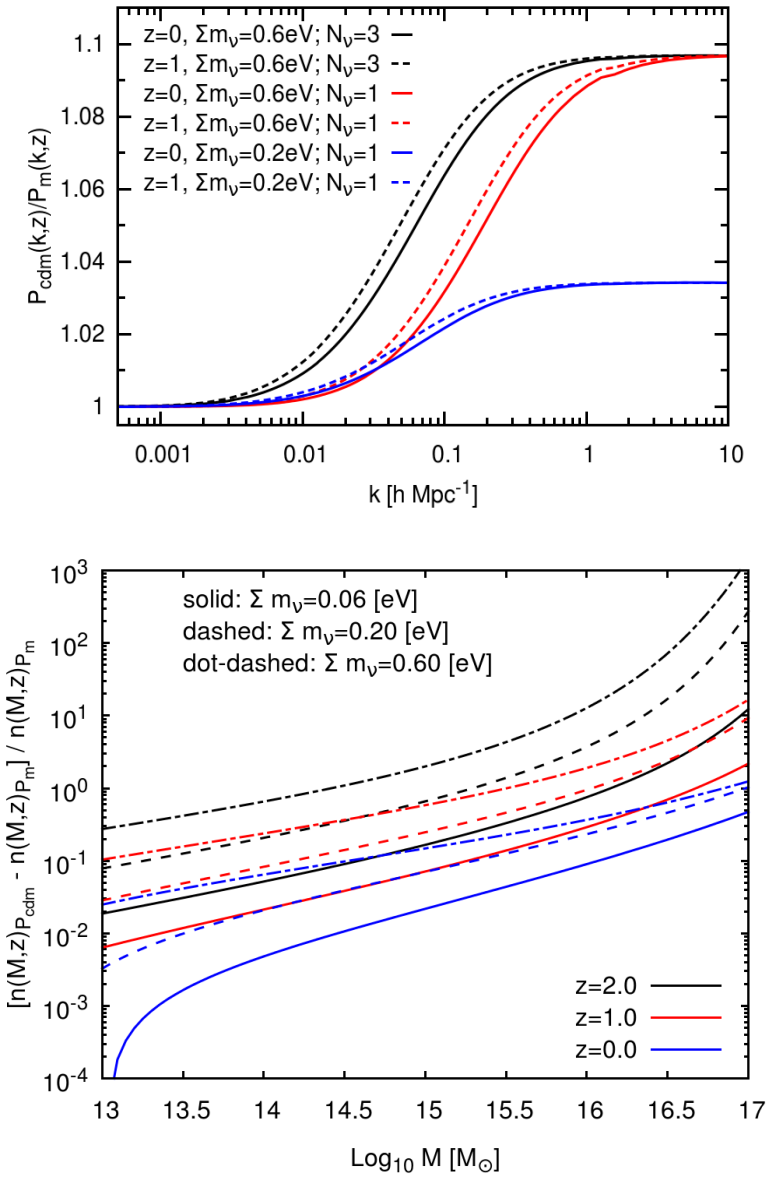

Figure 4.4: *Upper* panel: Ratio of the CDM (Eq. (4.5)) to the matter power spectrum as a function of the wavenumber k, for two different redshifts, $z = 0$, 1, total neutrino masses, $\sum m_\nu = 0.6$, 0.2 eV, and numbers of massive species, $N_\nu = 1$, 3; keeping fixed $\sum m_\nu$ and varying N_ν, corresponds to change the individual neutrino mass, $m_\nu = \sum m_\nu / N_\nu$ (for degenerate neutrino species). *Upper* panel: Residual of the HMF computed using the *CDM* prescription with respect to the HMF computed using the *matter* prescription, at redshift $z = 0$, 1 and 2, and for three total neutrino mass, $\sum m_\nu = 0.06$, 0.20 , 0.60 eV, assuming one massive neutrino.

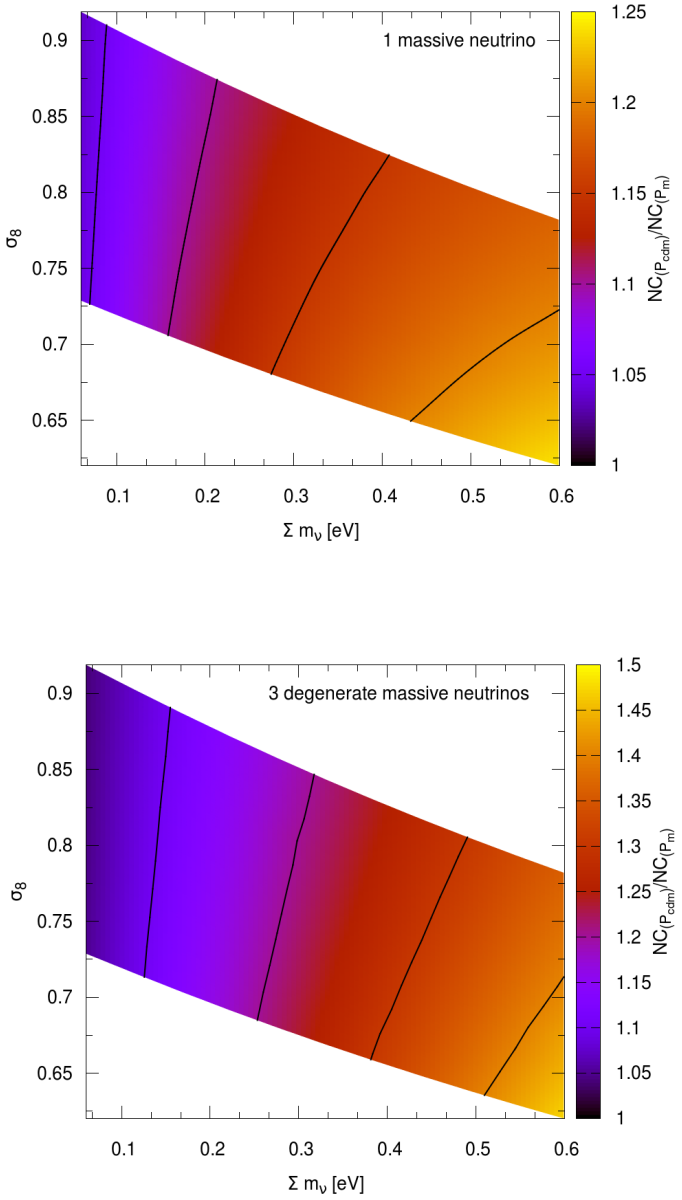

Figure 4.5: Ratio of the number counts obtained using the CDM over the matter prescription for different combinations of ($\sum m_\nu - \sigma_8$) values (*colour-coded*) and different neutrino mass splitting: one massive neutrino (*upper* panel) and three degenerate massive neutrinos (*lower* panel). For a given cosmology, the cold dark matter prescription predicts a larger number of clusters, especially for high neutrino mass and cosmology with three massive neutrinos. Black curves trace constant values of the ratio; from the left to the right: 1.05, 1.10, 1.15, 1.20 (*upper* panel); 1.1, 1.2, 1.3, 1.4 (*lower* panel).

Since we are interested in the relative change of $N(z)$ due to the different HMF prescription adopted in its computation, the completeness function can be simply expressed as:

$$X(M, z, \mathbf{\Omega}) = \int_{M_{\rm lim}(z)}^{\infty} {\rm d}M^{\rm ob} p(M^{\rm ob} \| M)\,, \tag{4.4}$$

where the lower limit in the mass integral, $M_{\rm lim}(z)$, represents the minimum value of the observed mass for a cluster to be included in the survey, and $p(M^{ob}\|M)$, already defined in Eq. (3.2), gives the probability that a cluster of true mass M has a measured mass given by M^{ob}, accordingly to the uncertainties introduced by the scaling relation between observable and mass.

We now turn to the implications of the prescription choice on the HMF prediction. By replacing $P_{\rm m}(k,z)$ with $P_{\rm cdm}(k,z)$ one neglects the suppression of the total DM density fluctuations on scales smaller than their free-streaming length (see *upper* panel of Figure 4.4), the scale below which neutrinos cannot cluster due to their high thermal velocity (§1.5.3). The magnitude of the suppression depends on the sum of the neutrino masses (see *blue* and *red* curves), while the scale below which it takes place depends on the individual neutrino mass (see *black* and *red* curves) and on redshift (see *solid* and *dashed* curves), through the free-streaming length (Eq. (1.46)). This in turn affects the halo mass function by shifting the maximum cluster mass (i.e. the scale beyond which the halo mass function is exponentially suppressed) to larger values, thus increasing the predicted number of rare massive clusters. The effect is larger for larger total neutrino mass, larger number of massive neutrinos and higher redshift (see *lower* panel of Figure 4.4).

In Figure 4.5 we show the ratio (colour coded) of the cluster counts predicted using the $P_{\rm cdm}(k,z)$ (*CDM* prescription) over the one predicted using $P_{\rm m}(k,z)$ (*matter* prescription) for different combinations of ($\sum m_\nu - \sigma_8$) values and for two neutrino mass split schemes: a single massive neutrino (*upper* panel) and three degenerate massive neutrinos (*lower* panel). In the former case the total neutrino mass is assigned to one neutrino species ($m_1 = \sum m_\nu$ and $m_2 = m_3 = 0$), in the latter one it is equally split among three massive species ($m_{\rm i} = \sum m_\nu/3$ with $i = 1,2,3$). The plots have been obtained by varying $\sum m_\nu$ and A_s and keeping fixed $\Omega_{\rm m}$, $\Omega_{\rm b}$, τ, H_0 and n_s to the Planck mean value (see Table 2.1, *Planck*+WP). In order to mimic a Planck SZ-cluster survey, we computed the number counts integrating eq. (4.3) between $0.0 < z < 1.0$ with a sky coverage $\Delta\Omega = 27.000$ deg^2 and we approximated the Planck SZ-cluster completeness function using as lower limit in eq. (4.4) the limiting mass $M_{\rm lim}(z)$[2] provided by the Planck Collaboration (2013a) (dashed black

[2]Following the recipe given in Hu and Kravtsov (2003), the limiting mass has been converted to

line in their Figure 3). Moreover, since we are simply interested in quantify the relative effect of using an improved HMF calibration we assumed no uncertainties in the estimation of the true mass ($M = M^{\rm ob}$) and we set $B_{\rm M} = 0$ and $\sigma^2_{\ln M} \to 0$ in eq. (3.2). Power spectra have been computed using `CAMB` (Lewis et al., 2000), where $P_{\rm cdm}(k,z)$ has been obtained exploiting the relation

$$P_{\rm cdm}(k,z) = P_{\rm m}(k,z)\left(\frac{\Omega_{\rm cdm}T_{\rm cdm}(k,z)+\Omega_{\rm b}T_{\rm b}(k,z)}{\Omega_{\rm cdm}+\Omega_{\rm b}}\frac{1}{T_{\rm m}(k,z)}\right)^2, \tag{4.5}$$

with $T_{\rm cdm}$, $T_{\rm b}$ and $T_{\rm m}$ being the CDM, baryon and total matter transfer functions, respectively.

Assuming one massive neutrino, changing the matter power spectrum to the cold dark matter one in the HMF prediction increases the expected number of clusters by $\sim 5\%$ in the minimal normal hierarchy scenario ($\sum m_\nu = 0.06\,$eV), reaching differences of $\sim 20\%$ for masses of $\sum m_\nu \sim 0.4\,$eV. Considering instead three degenerate massive neutrinos, the CDM prescription gives even a larger correction to the cluster counts: the splitting of the total neutrino mass between three species causes the free-streaming length to increase (see Eq. (1.46)), therefore widening the range in which $P_{\rm m}(k,z)$ is suppressed with respect to $P_{\rm cdm}(k,z)$. As a result, the difference in cluster counts computed with the two prescriptions reaches $\sim 30\%$ for neutrino mass of the order of $\sum m_\nu = 0.4\,$eV. For a given cosmology the magnitude of the ratio slightly depends also on the specifics of the survey: a lower $M_{\rm lim}(z)$ would entail a larger difference between the expected number of clusters computed with the two different calibrations, due to the larger mass range over which $n(M,z)$ would be integrated in the computation of $N(z)$.

The difference in the predictions in turn affects the degeneracy between cosmological parameters. An example of this effect is shown in Figure 4.6, in the $(\sum m_\nu - A_s)$ plane (*upper* panel) and the corresponding $(\sum m_\nu - \sigma_8)$ plane (*lower* panel). The curves correspond to constant number counts obtained using $P_{\rm m}(k,z)$ (black) or $P_{\rm cdm}(k,z)$ (red) in the HMF definition, following the same procedure of Figure 4.5 to compute the expected number of clusters and keeping the other cosmological parameters ($\Omega_{\rm m}$, $\Omega_{\rm b}$, τ, H_0, n_s) fixed to the Planck mean value. Solid and dashed curves are for models with one massive neutrino and three degenerate massive neutrinos, respectively. The different slope of the curves indicates a different degeneracy direction between parameters. Consistently with the results

$M_{\rm lim,200}(z)$ – the limiting mass within a radius encompassing an overdensity equal to 200 times the mean density of the Universe – consistently with the chosen HMF.

shown in Figure 4.5 the change in the slope is more pronounced in the case of three massive neutrinos.

As illustrated in the next Section both these effects can contribute to modify the information on cosmological parameters inferred from cluster data in models with massive neutrinos.

4.4 Implications for cosmological constraints

The ultimate aim of an analytic expression for the HMF is to link the observed abundance of galaxy clusters to the underlying cosmology. As already stated, the recently released Planck data indicate some tension between the cosmological parameters preferred by the primary CMB temperature measurements and those obtained from cluster number counts using X-ray (Vikhlinin et al., 2009b), optical richness (Rozo et al., 2010) and SZ-selected clusters (Benson et al., 2013; Hasselfield et al., 2013; Planck Collaboration, 2013a). In particular, the values of σ_8 and Ω_m inferred from cluster analyses are found to be lower than the values derived from CMB data. It has been argued that this discrepancy could be due to a wrong calibration of cluster mass (see e.g. Henry et al., 2009; Rozo et al., 2013) or alternatively it may indicate the need to extend the minimal ΛCDM to massive neutrinos (Planck Collaboration, 2013a; Wyman et al., 2013; Battye and Moss, 2013; Hamann and Hasenkamp, 2013). In the latter case, the results presented in this paper could in principle affect derived cosmological constraints which relies on an incorrect calibration of the HMF in cosmological models with massive neutrinos. In fact, in all previous cluster studies, the variance of the total dark matter field has been used to put constraints on neutrino masses. In Section 4.3 we have shown that, given a background cosmology, using the "wrong"prescription for the HMF could lead to differences up to 30% in the expected number of cluster. However that is not the the only reason to use the variance of the CDM field. Indeed, a key assumption in previous cosmological analyses of clusters counts is that the shape of the HMF is independent of the underlying cosmology, and the same functional form can be used through all the parameter space. In Castorina et al. (2014) it has been shown that universality of the HMF with respect to neutrino masses, and more in general cosmology, is recovered only if the cold dark matter prescription is adopted.

In order to assess the effects of the cold dark matter prescription on the parameter estimation we choose as a case study the sample of 188 SZ-selected clusters with measured redshift published in the Planck SZ Catalogue (Planck Collabora-

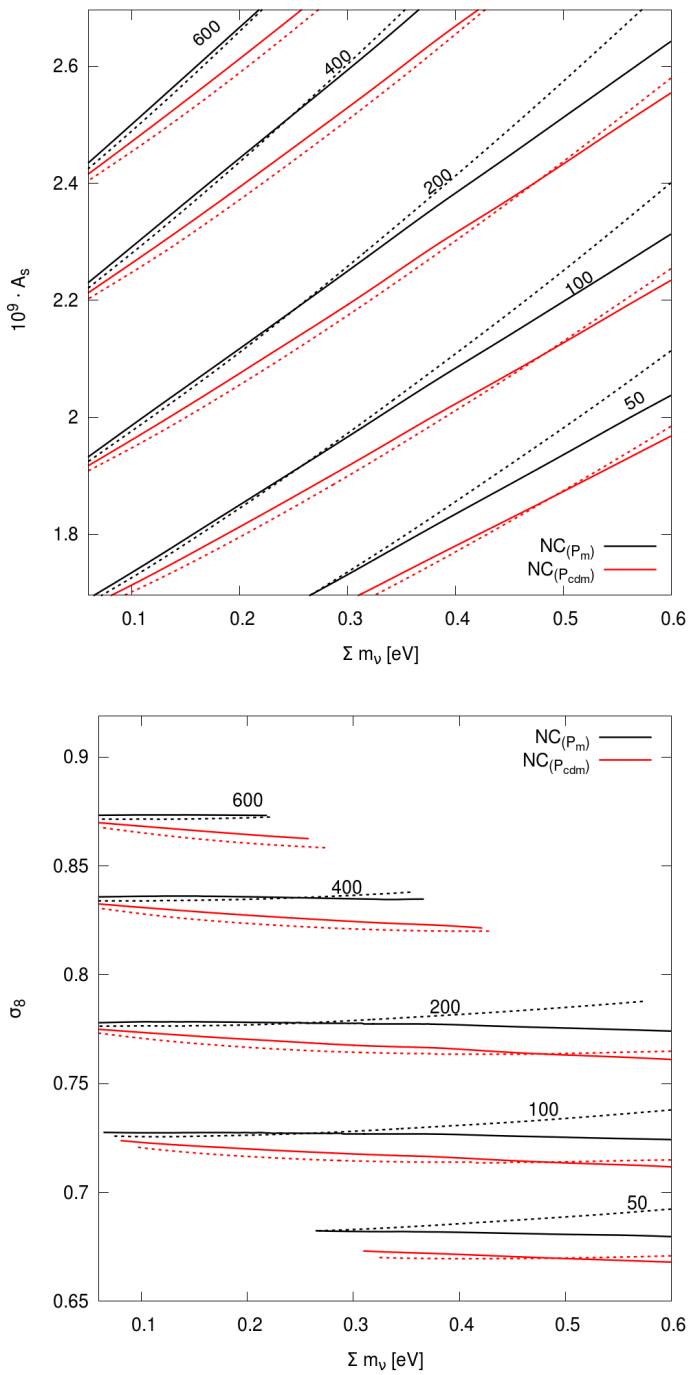

Figure 4.6: Curves of constant number counts ($N = 600$, 200, 100 and 50, top to bottom) in the plane $\sum m_\nu - 10^9 \cdot A_s$ (*upper panel*) and in the plane $\sum m_\nu$ - σ_8 (*lower panel*), for the two prescriptions for the HMF, matter (*black*) and cold dark matter (*red*) and for two neutrino mass splitting schemes, single massive neutrino (*solid lines*) and three degenerate massive neutrinos (*dashed lines*). The different slope of the black and red curves shows the different degeneracy direction between parameters in the prescriptions.

tion, 2013b). The cosmological constraints have been obtained using the likelihood function for Poisson statistics (Cash, 1979):

$$\ln L(N^{\rm obs}|N^{\rm th}) = \sum_{i=1}^{N_{\rm bin}} \left[N_i^{\rm obs} \ln(N_i^{\rm th}) - N_i^{\rm th} - \ln(N_i^{\rm obs}!) \right] , \tag{4.6}$$

where $N_i^{\rm obs}$, $N_i^{\rm th}$ represent respectively the number of clusters observed and theoretically predicted in the i-th redshift bin. The redshift range has been divided in $N_{\rm bin} = 10$ bins of width $\Delta z = 0.1$ between $z = 0.0$ and $z = 1.0$, also including in the analysis redshift bins with no observed clusters. We computed the predicted number of clusters , $N_i^{\rm th}$, for a Planck-like SZ-cluster survey following the procedure described in Section 4.3. The parameter space has been explored by means of the Monte Carlo Markov Chain technique using the publicly available code `CosmoMC`[3] (Lewis and Bridle, 2002), where we included a module for the computation of the likelihoods function described above. Since we are interested in the effects that a different prescriptions for the HMF has on parameter constraints rather than the constraints themselves, we kept fixed $\Omega_{\rm b}h^2 = 0.022$, $\tau = 0.085$ and $n_s = 0.963$, allowing only $\Omega_{\rm cdm}h^2$, θ, $\log(10^{10} \cdot A_s)$ and $\sum m_\nu$ to vary. For the same reason we neglect errors on nuisance parameters, which have been kept fixed to $B_{\rm M} = 0$ and $\sigma^2_{\ln M} = 0.2$ in order to roughly reproduce the mean values of $\Omega_{\rm m}$ and σ_8 obtained by the Planck Collaboration with Planck-SZ+BAO+BBN data (Planck Collaboration, 2013a). We also checked that our results in the $\Omega_{\rm m} - \sigma_8$ plane fixing $\sum m_\nu$ to 0.06 eV were in good agreement with those obtained by the Planck Collaboration. Finally, due to the weak sensitivity of the cluster sample to some cosmological parameters, we set a Gaussian prior on the total neutrino mass, $\sum m_\nu = 0.06 \pm 1.0\,{\rm eV}$, and one on the expansion rate, $H_0 = 68.9 \pm 3.0$ km/s/Mpc (from BAO measurements Addison et al., 2013). Note that the actual Planck cluster likelihood is not publicly available. Therefore, a quantitative comparison with the SZ Planck cluster results is not possible. However, since we are presenting results in terms of relative effects between different HMF calibrations, we expect that our findings will be robust and could be quantitatively similar to those to be derived with a more accurate likelihood analysis.

The joint constraints on the $\Omega_{\rm m}$-σ_8 plane resulting from this analysis are shown in Figure 4.7 with green contours for the CDM prescription and blue contours for the matter prescription. The left panel is for a model with one massive neutrino while the right one for a model with three degenerate massive neutrinos. The

[3] http://cosmologist.info/cosmomc/

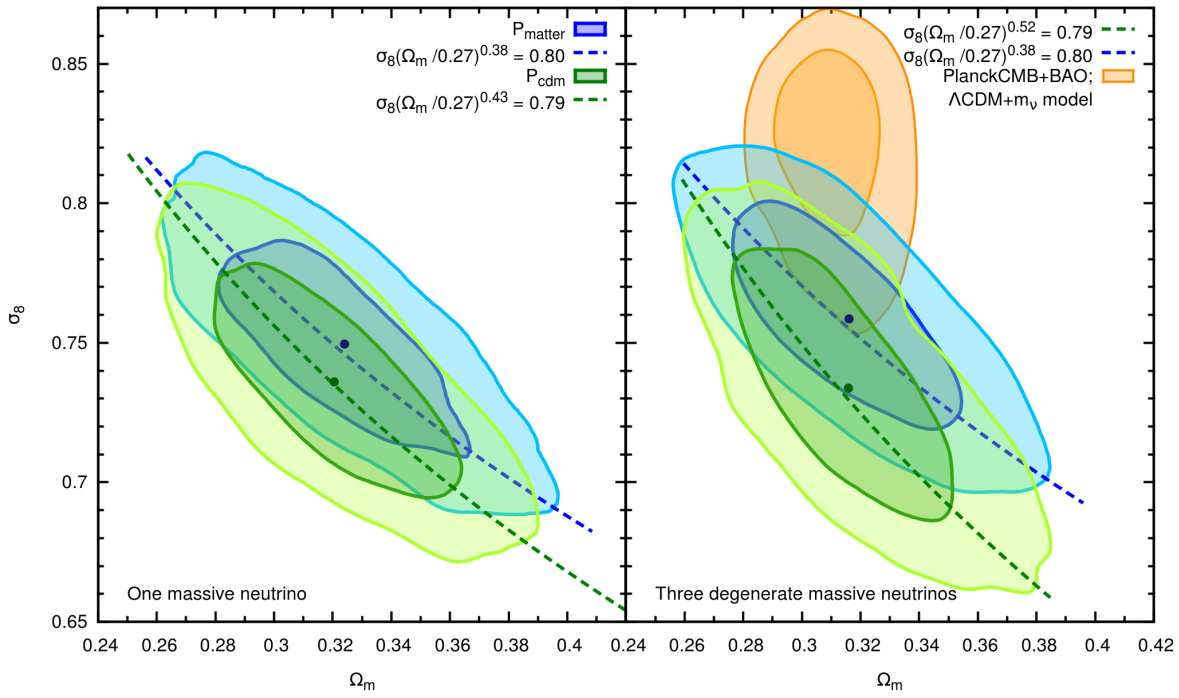

Figure 4.7: Comparison of the 68% and 95% C.L. contours in the $\Omega_m - \sigma_8$ plane and degeneracy curves obtained using the matter (*blue*) and cold dark matter (*green*) prescription. We show the results when the sum of the neutrino masses is split between one massive neutrino family (*left panel*) and three degenerate neutrino families (*right panel*). Also shown in the *right* panel in *orange* the contours from PlanckCMB+BAO datasets for a ΛCDM+$\sum m_\nu$ model.

dashed lines show the $\sigma_8(\Omega_m/027)^\gamma = S_8$ relation with γ and S_8 parameters obtained by fitting a power-law relation to the likelihood contours. Also shown in the right panel with orange contours are the constraints from Planck+WP+BAO datasets for a ΛCDM cosmology with free $\sum m_\nu$ [4]. While the constraining power of clusters is almost unaffected by different HMF prescriptions the degeneracy direction become steeper in the CDM case. For one massive neutrino the shift can be quantified as $\Delta\gamma = 0.05$, or $\Delta\sigma_8 = 0.01$. The effect is even larger when considering three massive neutrino, for which we obtain a shift of $\Delta\gamma = 0.14$ and $\Delta\sigma_8 = 0.02$. The different degeneracy of the CDM-case contours can be understood as follows: for our set of free parameters moving toward large Ω_m values in order to keep constant the number of clusters one has to compensate with lower σ_8 and larger $\sum m_\nu$ values. Using the CDM prescription, however, for a given matter density and neutrino mass the value of σ_8 which reproduces the right number of cluster is smaller than the one recovered using the matter prescription; moreover, the difference between σ_8 values inferred from the two HMF prescriptions increases with the total neutrino mass and is more pronounced when assuming three massive neutrinos (see Figure 4.6).

Using the orange contours as a reference one can see that the shift of the contours caused by the CDM prescription goes in the direction of increasing the tension with the Planck+BAO results. This means that when using the CDM prescription in trying to reconcile the Planck CMB measurements with cluster number counts, when extending the ΛCDM model to massive neutrinos, a larger $\sum m_\nu$ value will result from the combination of the two datasets.

The effects of the usage of the CDM prescription on parameter estimation are clearly visible but with low statistical significance for the cluster sample chosen for this work. However, owing to the much stronger constraining power expected from upcoming and future cluster surveys, corrections to the σ_8-Ω_m degeneracy direction of the order of $\Delta\gamma \sim 0.1$ would offsets the resulting constraints by a statistically significant amount (Costanzi Alunno Cerbolini et al., 2013; Khedekar and Majumdar, 2013).

4.5 Conclusions

In this Chapter, by using a set of large box-size N-body simulations containing CDM and neutrinos particles, we have studied the abundance of dark matter halos,

[4] Chains publicly available at http://www.sciops.esa.int/.

identified using the SO criterion, in cosmological models with massive neutrinos. The SO halos have been extracted from the N-body simulations by running the SUBFIND algorithm on top of the CDM particle distribution to avoid spurious mass contamination in the low mass halos from unbounded neutrino particles. We have however explicitly checked that our results do not change if SUBFIND is run on top of the total matter density field. We have compared the abundance of dark matter halos in cosmologies with massless and massive neutrinos with the Tinker et al. (2008) fitting formula along with the *matter prescription* and the *cold dark matter prescription*. In both prescriptions we use $\rho_{\rm cdm} = \rho_{\rm m} - \rho_\nu$ instead of $\rho_{\rm m}$ when setting the relation between the halo mass and the radius in the top-hat window function: $M = 4\pi\rho_{\rm cdm}R^3/3$. However, in the *cold dark matter prescription* we use the CDM linear power spectrum, $P_{\rm cdm}$, when computing the value of $\sigma(M,z)$, whereas in the *matter prescription* we use the total matter linear power spectrum, $P_{\rm m}$.

We find that the abundance of SO halos is much better reproduced by the Tinker et al. (2008) fitting formula once the *cold dark matter prescription* is used, in agreement with the claims of Ichiki and Takada (2012) and the results of Castorina et al. (2014). The agreement is very good at $z = 0$ while it worsens a bit at higher redshift. Once we present the results as ratios of the HMFs for cosmologies with massive neutrinos to the HMFs for cosmologies with massless neutrinos the agreement with theoretical predictions improves significantly at all redshifts. We stress that the conclusions of this paper are not affected if a different HMF fitting formula was used.

We have investigated the effects that the *cold dark matter prescription* has on theoretical predictions of number counts and on the estimation of cosmological parameter from cluster samples. By using the Tinker et al. (2008) fitting formula for the HMF we computed the expected number of clusters for a Planck-like SZ-cluster survey. We found that for a cosmology with massive neutrinos the predicted number of clusters is higher when using the cold dark matter prescription with respect to the results obtained by using the matter prescription. For a given value of $\Omega_{\rm m}$ the effect is more pronounced for large neutrino masses and in the case of a splitting of the total neutrino mass between three degenerate species. Assuming one massive neutrino family (and two massless neutrino families) the difference in the predicted number counts between the two prescriptions is nearly 20% for $\sum m_\nu \sim 0.4\,{\rm eV}$, while it reaches $\sim$ 30% in models with three degenerate massive neutrinos.

The different prediction for the HMF in turn affects the degeneracy direction between cosmological parameters and the mean values inferred from the cluster sample. To quantify these effects we use as a case study the Planck sample of 188

SZ-selected clusters with measured redshifts. We performed a Monte Carlo Markov Chains analysis for the parameters $\Omega_{\rm cdm}h^2$, θ, $\log(10^{10}\cdot A_s)$ and $\sum m_\nu$, both splitting the sum of the neutrino masses between one and three massive species. Looking at the combination $\sigma_8(\Omega_{\rm m}/0.27)^\gamma$, the cold dark matter prescription provides a steeper degeneracy direction (higher γ) which causes the σ_8 mean value to lower. The shift can be quantified as $\Delta\gamma = 0.05$ and $\Delta\gamma = 0.14$ for one and three massive neutrino respectively, or in terms of the σ_8 mean value as $\Delta\sigma_8 = 0.01$ and $\Delta\sigma_8 = 0.02$. The offset has a low statistical significance for the cluster sample used in this work but could entail a significant correction when the sample is combined with other probes or for large cluster samples that will be provided by future cluster surveys (see e.g. the results of Chapter 3). Furthermore, taking into account such an effect has the consequences of exacerbating the tension between the cosmological parameters derived from CMB data and those of cluster number counts (Planck Collaboration, 2013a).

5

Neutrino constraints: what large-scale structure and CMB data are telling us?

Results from Planck measurements of the CMB temperature anisotropies by themselves appear to be well described by the six standard ΛCDM parameters, and show no preference for extended models. However, as mentioned in Chapter 2, in the framework of the ΛCDM model, several probes of the low redshift Universe exhibit tension with the Planck results. In particular, Planck finds a larger and more precise value of the matter density at recombination than previous CMB data; this results in a lower value for the current expansion rate H_0, and a higher value of the matter density fluctuations σ_8. These changes lead to a $\sim (2-3)\sigma$ tension with direct measurements of H_0 (Riess et al., 2011) and σ_8 measurements from galaxy shear power spectrum (Heymans et al., 2013), galaxy-galaxy lensing (Mandelbaum et al., 2013), RSD (Beutler et al., 2013) and clusters abundance (Vikhlinin et al., 2009b; Rozo et al., 2010; Allen et al., 2011; Planck Collaboration, 2013a). Meanwhile, agreement with distance measurements from BAO suggests that the discrepancy cannot be resolved involving exotic dark energy models or curvature which modify the recent expansion history.

Beside unresolved systematic effects neutrinos can offer a possible means to relieve this tension. Sterile neutrinos change the expansion rate at recombination and hence the calibration of the standard ruler with which CMB and BAO observations infer distances, while massive neutrino, either sterile or active, suppress small scale clustering at late time, relieving the tension with σ_8 measurements (see §1.5). A number of studies have carried out joint analyses of various data combina-

tions finding that a neutrino mass of $0.3 - 0.4$ eV provides a better fit to CMB data with low redshift Universe measurements than the vanilla ΛCDM model (Burenin, 2013; Wyman et al., 2013; Battye and Moss, 2013; Hamann and Hasenkamp, 2013; Archidiacono et al., 2013; Beutler et al., 2014; Giusarma et al., 2014; Archidiacono et al., 2014), although these conclusions are not universally accepted (Feeney et al., 2013; Verde et al., 2013; Leistedt et al., 2014). While, none of these low redshift datasets combined individually with CMB measurements provide strong evidence for non-zero neutrino masses, the hint for neutrino mass is driven mainly by low redshift growth of structure constraints (e.g. from shear and RSD measurements or cluster number counts).

In particular, galaxy clusters offer a powerful complementary probe to the CMB and geometric probes as BAO thanks to the tight constraints provided on the parameters combination, $\sigma_8\Omega_{\rm m}^{\gamma}$. Most of the X-ray, Sunyaev-Zel'Dovich and optical cluster surveys yield consistent results favouring a value for the cluster normalization condition lower than the value derived from Planck data (see Table 2.2). This tension between Planck and cluster data and the combination with BAO results could be taken as an evidence for non-vanishing neutrino masses. However, the robustness of such constraints from cluster number counts depend on our capability to recover cluster masses from proxies and to have precise theoretical predictions for the spatial number density of halos. Thus it is worth to investigate possible sources of systematic errors in cluster data which could lead to misinterpretation of the results and to assess which combination of low-redshift datasets with CMB data prefers a non-zero neutrino mass within a given cosmological model.

In this Chapter the reliability of neutrino mass constraints, either active or sterile, from the combination of different low redshift Universe probes with measurements of CMB anisotropies is discussed. In order to avoid misleading results due to model dependence of the constraints, instead of adding priors obtained from cosmological data within a ΛCDM model (e.g. Battye and Moss, 2013; Hamann and Hasenkamp, 2013; Beutler et al., 2014; Giusarma et al., 2014), we performed a full likelihood analysis for all the datasets employed in this analysis. In particular for the clusters data analyses we took into account the effect of possible bias in the mass estimation and adopted different prescriptions for the HMF. As for the latter, we considered the correction to the HMF proposed by Ichiki and Takada (2012) and Castorina et al. (2014) for cosmology with massive neutrinos discussed in Chapter 4. Moreover, we investigated how the different calibration of the HMF due to baryonic feedback processes presented in Cui et al. (2014) affects the cosmological constraints.

The Chapter is organized as follows: Section 5.1 describes the cosmological

models and datasets used in this work; in Section 5.2 we present and discuss our results, and finally, in Section 5.3 we draw the main conclusions . The results of this analysis have been published in Costanzi et al. (2014).

5.1 Cosmological data analysis

5.1.1 Models

The baseline scenario analysed in this work is a ΛCDM model with three degenerate massive neutrinos, defined by the parameters:

$$\{\Omega_c h^2, \Omega_b h^2, \Theta_s, \tau, n_s, \log(10^{10} A_s), \sum m_\nu\} . \tag{5.1}$$

Note that given the current precision of cosmological constraints from available data, the effect of mass splitting is negligible and the degenerate model can be assumed without loss of generality (see e.g. Jimenez et al., 2010). We then consider a scenario with a massive sterile neutrino component which has been suggested as a possible solution for the reactor (Mention et al., 2011), Gallium (Abdurashitov et al., 2006; Giunti et al., 2012) and accelerator (Aguilar-Arevalo and et al., 2001) anomalies in neutrino oscillation experiments. Reactor and Gallium experiments prefer a new mass squared difference of $\Delta m^2 \gtrsim 1$ eV^2, while various accelerator experiments constrain Δm^2 to be ~ 0.5 eV^2 (see Abazajian et al., 2012, and reference therein). For this model we assume one massive active neutrino with $\sum m_\nu = 0.06$ eV (the minimum mass allowed by neutrino oscillation experiments) and we introduce two parameters to describe the extra hot relic component: the effective number of extra relativistic degree of freedom, $\Delta N_{\rm eff} = N_{\rm eff} - 3.046$, and the effective sterile neutrino mass, $m_s^{\rm eff}$. We recall here that the former parametrizes any contribution to the radiation energy content besides photons and the three standard neutrinos ($N_{\rm eff}^{\rm active} = 3.046$) in the radiation dominated era (see Eq. (1.42)); thus, an extra thermalised light fermion would contribute $\Delta N_{\rm eff} = 1$, but more generally a non-integer $\Delta N_{\rm eff}$ value could arise from different physical phenomena. As already mentioned in §1.5.5, the large values of the mass squared differences and mixing angles invoked to resolve reactor, Gallium ($\sin^2 2\Theta \gtrsim 0.1$) and accelerator ($\sin^2 2\Theta \sim 5 \times 10^{-3}$) anomalies suggest a fully thermalisation of the sterile neutrino in the early Universe Langacker (1989), and thus a contribution of $\Delta N_{\rm eff} = 1$ to the dark radiation. Depending on the production mechanism which generate the sterile neutrino the parameter $m_s^{\rm eff}$ is related to the physical mass, m_s, through Eq. (1.48) – in the case of thermally-distributed sterile neutrino – or by the relation

$m_s^{\rm eff} = (\Delta N_{\rm eff}) m_s$ – Dodelson-Widrow scenario (Dodelson and Widrow, 1994). In both cases for a fully thermalised sterile neutrino, $\Delta N_{\rm eff} = 1$, the effective and the physical mass are equal. In this analysis we adopted the prior $m_s^{\rm eff}/(\Delta N_{\rm eff})^{3/4} < 10$ eV in order to avoid a degeneracy between very massive neutrinos and cold dark matter.

5.1.2 Data and analysis

In order to investigate how different datasets combinations constrain the neutrino properties we used for this analysis: two different CMB datasets to constrain the early Universe physics, BAO scale measurements as geometric probe, and cluster abundance, Ly-α forest and cosmic shear measurements to probe the growth of structures (see Chapter 2 for a concise review on these probes). Specifically, the parameters constraints presented here have been obtained by means of the Monte Carlo Markov Chain technique using the publicly available code `CosmoMC` (Lewis and Bridle, 2002) for various combinations of the following datasets:

CMB – We considered CMB temperature and polarization measurements from 9-year WMAP data release (hereafter WMAP9) (Hinshaw et al., 2013) or, alternatively, temperature power spectrum from the Planck satellite (Planck Collaboration, 2013d) combined with large-scale TE- and EE-polarization power spectra from WMAP9 (hereafter Planck). These datasets are analysed using the likelihood functions provided by the Planck Collaboration (2013c), and publicly available at Planck Legacy Archive[1] and marginalizing over the foreground nuisance parameters. The helium abundance is computed as a function of $\Omega_b h^2$ and $N_{\rm eff}$, following the Big Bang Nucleosynthesis theoretical predictions. In the Planck analysis we fix the lensing spectrum normalization parameter to its standard ΛCDM value $A_L = 1$[2], if not otherwise stated. The WMAP9 dataset is not sensitive to the gravitational lensing signal since its effects can be detected only at large multipoles.

BAO – We include the most recent and accurate measurements of the BAO scales from BOSS Data Release 11 (Anderson et al., 2014). Exploiting a sample of nearly one million galaxies observed over 8500 square degree between redshift $0.2 < z < 0.7$, DR11 results provides percent level constraints on the peak position

[1] http://pla.esac.esa.int/pla/aio/planckProducts.html

[2] In the Planck analysis the parameter A_L modulates the lensing effect in the temperature power spectrum (see §2.1.1), and scales the amplitude of the power spectrum of the lensing potential.

of the spherically averaged galaxy correlation function at redshift $z = 0.32$ and $z = 0.57$. The likelihood function associated to this dataset is estimated using the likelihood code distributed with the `CosmoMC` package.

Shear – We use the 6-bin tomography angular galaxy shear power spectra data from the CFTHLenS survey (Heymans et al., 2013)[3]. The survey spans over 154 square degrees in five optical bands, with shear and photometric redshift measurements for a galaxy sample with a median redshift of $z = 0.70$. Constraints from this datasets are derived using a modified version of the `CosmoMC` module [4] for the weak lensing COSMOMS 3D data (Lesgourgues et al., 2007). The code has been substantially modified in order to reproduce the analysis described in Heymans et al. (2013) which makes use of 21 sets of cosmic shear correlation functions associated to 6 redshift bins, each spanning the angular range of $1.5 - 35$ arcmin, to extract cosmological information. Specifically, the likelihood function has been computed as:

$$-2\ln\mathcal{L} = (\hat{\boldsymbol{\xi}}^{ij}_{\pm}(\vartheta) - \boldsymbol{\xi}^{ij}_{\pm}(\vartheta))^T \boldsymbol{C}^{-1} (\hat{\boldsymbol{\xi}}^{ij}_{\pm}(\vartheta) - \boldsymbol{\xi}^{ij}_{\pm}(\vartheta))\,, \tag{5.2}$$

where $\hat{\boldsymbol{\xi}}^{ij}_{\pm}(\theta)$ and $\boldsymbol{\xi}^{ij}_{\pm}(\theta)$[5] are the observed and theoretical auto/cross-correlation functions for the redshift bins i, j and angular separation θ, respectively. The covariance matrix, $\boldsymbol{C}$, provided by the authors (Heymans et al., 2013), have been estimated using the 3-D N-body lensing simulations of Harnois-Déraps et al. (2012). As in Heymans et al. (2013), when computing the theoretical correlation functions $\boldsymbol{\xi}^{ij}_{\pm}(\theta)$ we accounted for the contribution from both intrinsic alignment of physically nearby galaxies and the shear-shape correlation for galaxies separated by large physical distances along the line of sight, following the model proposed by Bridle and King (2007). This model, which is based on a fitting approach, has the advantage of needing only one additional nuisance parameter, marginalized over in the analysis, to predict both the intrinsic alignment contributions to the shear correlation functions. We verified that our module reproduces well the results presented in Heymans et al. (2013) for a ΛCDM model.

[3] http://cfhtlens.org/astronomers/cosmological-data-products

[4] http://www.astro.caltech.edu/ rjm/cosmos/cosmomc/

[5] The two point statistics used here are defined as $\xi_{\pm}(\vartheta) = \langle\epsilon_t\epsilon_t\rangle(\vartheta) \pm \langle\epsilon_\times\epsilon_\times\rangle(\vartheta)$ where ϵ_t and $\epsilon_\times$ are the tangential and cross ellipticity of each pair of correlated objects, respectively; these two point statistics are related to the shear power spectrum of Eq. (2.18) by the relation: $\xi^{ij}_{\pm}(\vartheta) = \int \mathrm{d}\ell\,\ell/2\pi J(\ell\vartheta)_{0/4} C_{ij}(\ell)$.

Ly-α – We rely on the SDSS Ly-α forest data from (McDonald et al., 2005) to constrain the amplitude, slope and curvature of the linear matter power spectrum at scale $k = 0.009\,\mathrm{s\ km^{-1}}$ and redshift $z = 3$. We combine this dataset by implementing the Ly-α likelihood code distributed with the `CosmoMC` package. The module has been updated to work with the new version of `CosmoMC` and it has been implemented with the patch written by A. Slosar [6] in order to support extended model analysis. Note that this data set does not include the most recent BOSS data of Palanque-Delabrouille et al. (2013) that will soon provide an updated value of the upper limits obtained in Seljak et al. (2006), by using a new technique to sample the parameter space (Borde et al., 2014b) and hydro simulations that incorporate massive neutrinos (Rossi et al., 2014).

Clusters – Constraints from galaxy clusters are obtained exploiting the CCCP catalogue presented in (Vikhlinin et al., 2009a). The catalogue consists of X-ray *Chandra* observations of 37 clusters with $\langle z \rangle = 0.55$ derived from the 400 deg^2 *ROSAT* survey and 49 brightest $z \approx 0.05$ clusters detected in the *ROSAT* All-Sky Survey, which provide a robust determination of the cluster mass function at low and high redshifts. To derive cosmological constraints we developed our own module for `CosmoMC` following the fitting procedure outlined in Vikhlinin et al. (2009a). For the cluster masses we use Y_x proxy mass estimations (Kravtsov et al., 2006, see §2.2.2), which allows us to implement the X-ray luminosity-mass relation calibrated by Vikhlinin et al. (2009a) needed to compute the survey volume as a function of the mass. The theoretical abundance of massive halo is computed using the Tinker et al. (2008) HMF (Eq. (1.36)), where the coefficient of the fitting formula were obtained interpolating Table 2 of Tinker et al. (2008) for halos with $\Delta_{\rm mean} = \Delta_{\rm critical}/\Omega_{\rm m} = 500/\Omega_{\rm m}$, according to the cluster mass definition of Vikhlinin et al. (2009a). For the parameter inference we used the likelihood function of Eq. (4.6) for purely Poissonian statistics (Cash, 1979). We verified that our analysis reproduces accurately the results of Burenin and Vikhlinin (2012) for the combination of WMAP 7-year and CCCP cluster data. To properly take into account the effects of massive neutrinos on the HMF calibration, we neglect the weakly clustering neutrino component when calculating the halo mass, as suggested by many authors (e.g. Brandbyge et al., 2010b; Marulli et al., 2011; Villaescusa-Navarro et al., 2013). Moreover, following Ichiki and Takada (2012) and Castorina et al. (2014), and according to the results of Chapter 4, the variance of the matter perturbations,

[6] http://www.slosar.com/aslosar/lya.html

required to predict the HMF, is computed using only the cold dark matter and baryon linear power spectrum, in order to neglect the suppression of the matter density fluctuations on scales smaller than the neutrino free-streaming length. As shown in Chapter 4 these corrections entail an increase of the HMF with respect to the previous calibration. This effect is larger for larger neutrino masses and higher number of massive neutrino species. In turn, the increase in the HMF affects the resulting constraints on cosmological parameters, e.g. by steepening the $\sigma_8 - \Omega_{\rm m}$ degeneracy direction, thereby reducing the σ_8 mean value. Besides these modifications to the original analysis of Vikhlinin et al. (2009a) we test the effect of other sources of systematics. To address the impact on clusters constraints due to baryonic feedback processes we implement the correction to the HMF proposed by Cui et al. (2014); the net effect of baryonic processes is to generate shallower density profiles and a corresponding decrease of halo masses with respect to the dark matter only case used to fit the HMF (e.g. Jenkins et al., 2001; Reed et al., 2007; Warren et al., 2006; Tinker et al., 2008; Crocce et al., 2010). This effect is taken into account correcting the halo masses through a mass dependent fit to the halo mass variation induced by baryonic processes. Similar studies have been carried out by different groups (Cusworth et al., 2014; Velliscig et al., 2014; Vogelsberger et al., 2014; Martizzi et al., 2014) that found consistent results (cf. also Martizzi et al., 2014).

The main source of systematic errors is related to the uncertainty in cluster mass measurements. For the catalogue used in this work cluster masses have been inferred by using a scaling relation between total mass and the product of hot intracluster gas mass and temperature, as inferred from X-ray observations. This scaling relation has been calibrated by resorting to X–ray hydrostatic mass measurements for nearby galaxy clusters (see Vikhlinin et al., 2009a, for details). However, mass measurements from X–ray measurements suffer for different sources of possible systematic biases, e.g. associated to departures from spherical symmetry, to biases in X-ray measurement of gas temperature (e.g. Mahdavi et al., 2008; Rasia et al., 2012), or to violation of hydrostatic equilibrium due to the presence non-thermal pressure support (e.g. Laganá et al., 2010; Shi and Komatsu, 2014).

To consider this uncertainty we introduce a nuisance bias parameter defined as $M^{est}/M^{true} = B_M$, which is varied in the range $[0.8 : 1.0]$ when included in the fit. This prior accounts for the constraints on the mass bias from Israel et al. (2014) and Donahue et al. (2014) obtained comparing *Chandra* X-ray masses with MMT/Megacam weak lensing masses of 8 clusters between redshift $0.39 - 0.80$ and CLASH weak lensing masses of 20 clusters between redshift $0.2 - 0.5$, respectively. A different range for the mass bias, $B_M \simeq 0.7 \pm 0.1$, is suggested by the

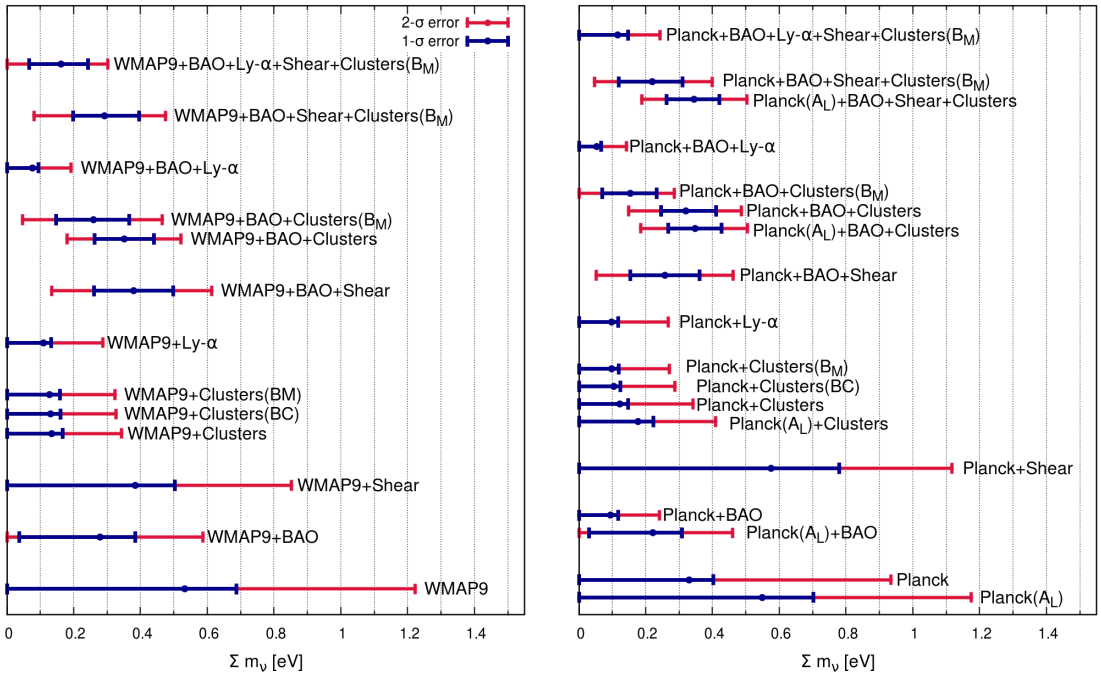

Figure 5.1: Summary of the 1σ and 2σ errors on $\sum m_\nu$ obtained from the dataset combinations discussed in Section 5.2.1 within a ΛCDM+$\sum m_\nu$ model.

analysis by von der Linden et al. (2014) which however uses X-ray masses derived from XMM–Newton temperature measurements. Temperature measurements from XMM–Newton could be systematically lower with respect to those obtained from *Chandra* observations, as discussed by Nevalainen et al. (2010), Schellenberger et al. (2014) and Donahue et al. (2014), thus providing a larger mass bias.

5.2 Results

For each of the cases that we describe here below, we run four independent chains, requiring the fulfilment of the Gelman and Rubin (1992) criteria with $R - 1 \leqslant 0.03$ as convergence test. The best fit values were obtained with the `BOBYQA` maximisation routine provided in `CosmoMC`. If not otherwise stated, errors and upper limits reported in the following text have to be intended at 95% confidence level.

Table 5.1: Constraints on $\Omega_{\rm m}$, σ_8 and $\sum m_\nu$ for a ΛCDM+$\sum m_\nu$ model combining different datasets. Errors are reported at 68% confidence level for σ_8 and $\Omega_{\rm m}$, and both 68% and 95% confidence level for $\sum m_\nu$. Notations included in parenthesis denote modifications to the standard setting: (BC) stands for the baryon correction to the HMF, while (B_M) and ($A_{\rm L}$) indicate analyses with the bias or lensing signal parameter marginalized out.

Dataset	$\Omega_{\rm m}$	σ_8	$\sum m_\nu$[eV]	
			68%CL	95%CL
WMAP9	$0.347^{+0.043}_{-0.079}$	$0.714^{+0.091}_{-0.068}$	< 0.68	< 1.22
WMAP9+Cluster	$0.264^{+0.010}_{-0.017}$	$0.780^{+0.027}_{-0.016}$	< 0.17	< 0.34
WMAP9+Cluster(B_M)	$0.275^{+0.014}_{-0.020}$	$0.793^{+0.029}_{-0.019}$	< 0.16	< 0.33
WMAP9+Cluster(BC)	$0.271^{+0.011}_{-0.017}$	$0.789^{+0.026}_{-0.017}$	< 0.16	< 0.33
WMAP9+BAO	$0.304^{+0.009}_{-0.011}$	$0.759^{+0.062}_{-0.043}$	$0.28^{+0.11}_{-0.24}$	< 0.59
WMAP9+Shear	$0.305^{+0.029}_{-0.055}$	$0.726^{+0.061}_{-0.046}$	< 0.50	< 0.85
WMAP9+Ly-α	$0.320^{+0.026}_{-0.033}$	$0.830^{+0.025}_{-0.021}$	< 0.13	< 0.29
WMAP9+BAO+Cluster	$0.298^{+0.009}_{-0.009}$	$0.735^{+0.015}_{-0.032}$	$0.35^{+0.09}_{-0.09}$	$0.35^{+0.17}_{-0.17}$
WMAP9+BAO+Cluster(B_M)	$0.298^{+0.009}_{-0.009}$	$0.765^{+0.024}_{-0.028}$	$0.26^{+0.11}_{-0.11}$	$0.26^{+0.20}_{-0.20}$
WMAP9+BAO+Shear	$0.303^{+0.010}_{-0.010}$	$0.724^{+0.028}_{-0.028}$	$0.38^{+0.12}_{-0.12}$	$0.38^{+0.23}_{-0.24}$
WMAP9+BAO+Ly-α	$0.305^{+0.009}_{-0.009}$	$0.833^{+0.021}_{-0.019}$	< 0.09	< 0.19
WMAP9+BAO+Cluster(B_M)+Shear	$0.297^{+0.010}_{-0.010}$	$0.752^{+0.017}_{-0.022}$	$0.29^{+0.11}_{-0.9}$	$0.29^{+0.18}_{-0.21}$
WMAP9+BAO+Ly-α+Shear+Cluster(B_M)	$0.289^{+0.008}_{-0.08}$	$0.787^{+0.019}_{-0.017}$	$0.16^{+0.08}_{-0.09}$	< 0.30
Planck	$0.355^{+0.025}_{-0.061}$	$0.775^{+0.077}_{-0.032}$	< 0.40	< 0.93
Planck+Cluster	$0.272^{+0.008}_{-0.018}$	$0.782^{+0.027}_{-0.013}$	< 0.15	< 0.34
Planck+Cluster(B_M)	$0.287^{+0.011}_{-0.015}$	$0.802^{+0.025}_{-0.012}$	< 0.12	< 0.27
Planck+Cluster(BC)	$0.278^{+0.009}_{-0.017}$	$0.790^{+0.026}_{-0.013}$	< 0.14	< 0.32
Planck+BAO	$0.309^{+0.009}_{-0.009}$	$0.819^{+0.027}_{-0.016}$	< 0.12	< 0.24
Planck+Shear	$0.358^{+0.051}_{-0.078}$	$0.708^{+0.093}_{-0.082}$	< 0.78	< 1.12
Planck+Ly-α	$0.329^{+0.018}_{-0.024}$	$0.831^{+0.024}_{-0.015}$	< 0.12	< 0.27
Planck+BAO+Cluster	$0.300^{+0.010}_{-0.010}$	$0.741^{+0.015}_{-0.018}$	$0.32^{+0.09}_{-0.07}$	$0.32^{+0.17}_{-0.17}$
Planck+BAO+Cluster(B_M)	$0.300^{+0.007}_{-0.009}$	$0.791^{+0.020}_{-0.018}$	$0.15^{+0.08}_{-0.08}$	< 0.28
Planck+BAO+Shear	$0.306^{+0.010}_{-0.011}$	$0.763^{+0.025}_{-0.024}$	$0.26^{+0.10}_{-0.10}$	$0.26^{+0.20}_{-0.21}$
Planck+BAO+Ly-α	$0.310^{+0.008}_{-0.008}$	$0.836^{+0.016}_{-0.014}$	< 0.07	< 0.14
Planck+BAO+Cluster(B_M)+Shear	$0.300^{+0.009}_{-0.011}$	$0.770^{+0.021}_{-0.021}$	$0.22^{+0.09}_{-0.10}$	$0.22^{+0.17}_{-0.18}$
Planck+BAO+Ly-α+Shear+Cluster(B_M)	$0.293^{+0.009}_{-0.010}$	$0.798^{+0.018}_{-0.014}$	< 0.15	< 0.24
Planck($A_{\rm L}$)	$0.358^{+0.040}_{-0.067}$	$0.716^{+0.081}_{-0.066}$	< 0.70	< 1.17
Planck($A_{\rm L}$)+Cluster	$0.276^{+0.010}_{-0.022}$	$0.769^{+0.032}_{-0.018}$	< 0.22	< 0.41
Planck($A_{\rm L}$)+BAO	$0.307^{+0.010}_{-0.010}$	$0.778^{+0.047}_{-0.033}$	$0.22^{+0.09}_{-0.19}$	< 0.46
Planck($A_{\rm L}$)+BAO+Cluster	$0.301^{+0.009}_{-0.009}$	$0.734^{+0.016}_{-0.015}$	$0.35^{+0.08}_{-0.08}$	$0.35^{+0.15}_{-0.16}$
Planck($A_{\rm L}$)+BAO+Shear+Cluster	$0.300^{+0.009}_{-0.010}$	$0.733^{+0.016}_{-0.014}$	$0.35^{+0.08}_{-0.08}$	$0.35^{+0.15}_{-0.16}$

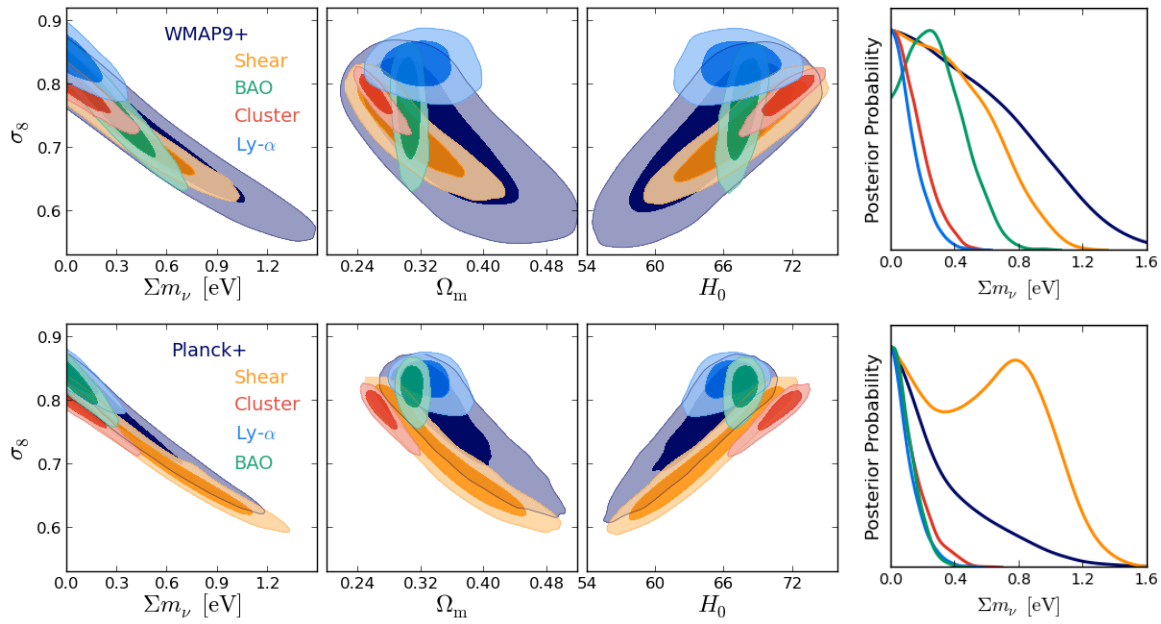

Figure 5.2: *Left* -Joint 68% and 95% CL contours in the $\sigma_8 - (\Omega_m, H_0, \sum m_\nu)$ planes for a ΛCDM+$\sum m_\nu$ model from the combination of WMAP9 (*upper* panels) or Planck (*lower* panels) data with different low redshift Universe probes. *Right* - Posterior probability distribution for $\sum m_\nu$ from the same data combination.

5.2.1 Massive neutrinos

We first turn our attention to the degenerate active neutrino case, whose results are summarized in Table 5.1 and Figure 5.1. To illustrate how different probes of the low redshift Universe combined with CMB measurements constrain cosmological parameters we use them one by one, before combining them together (see Figure 5.2 and Figure 5.3, respectively).

Combing with WMAP9

The upper panels of Figure 5.2 show constraints on the $\sigma_8 - (\sum m_\nu, \Omega_m, H_0)$ planes and the 1D likelihood distribution of $\sum m_\nu$ for several datasets combined with WMAP9 as CMB data. None of them exhibit tension with WMAP9 results nor evidence for non-zero neutrino mass. The stronger constraint on the neutrino mass, $\sum m_\nu < 0.29$ eV, comes from the inclusion of Ly-α data, due to the high σ_8 value pre-

ferred by this dataset. Similar results (on $\sum m_\nu$) involve the inclusion of cluster data which shrinks and shifts the $\sigma_8 - \Omega_{\rm m}$ contours toward lower values requiring small values for the total neutrino mass, $\sum m_\nu < 0.34$ eV. Repeating the analysis with a free mass bias parameter (Cluster(B_M) hereafter) or taking into account the baryon correction to the HMF (Cluster(BC) hereafter) slightly increases the σ_8 and $\Omega_{\rm m}$ values (see left panel of Fig 5.4) without significantly affecting the bound on $\sum m_\nu$ nor its best fit values. In the latter case the errors on σ_8 and $\Omega_{\rm m}$ remain unchanged while the suppression of the HMF with respect to the standard case causes the shift of the two parameters. Conversely, the inclusion of B_M in the fit relaxes the bounds on σ_8 and $\Omega_{\rm m}$ and shifts their contours owing to the low value assumed by the bias, $B_M \sim 0.9$. On the other hand, BAO data shows a mild preference for larger neutrino mass (see right panel of Fig 5.2) which displaces the neutrino bounds to higher values, $\sum m_\nu < 0.59$ eV, reason for that being the tight constraints on $\Omega_{\rm m}$ and the low σ_8 value allowed by this datasets combination. Shear measurement, as cluster number counts, provides constraints on $\sigma_8\Omega_{\rm m}^\gamma$ but with a poorer constraining power than clusters data and with a degeneracy direction more similar to the one given by WMAP9 data; therefore the inclusion of this dataset entails only a small improvement on neutrino mass constraints.

We discuss now the constraints obtained from the joint analyses of different probes of the low redshift Universe. The results are presented in the upper panels of Fig 5.3. Both the additions of cluster and shear datasets to the WMAP9+BAO joint analysis result in a larger than 2σ preference for massive neutrino yielding $\sum m_\nu = 0.35 \pm 0.17$ eV and $\sum m_\nu = 0.38^{+0.23}_{-0.24}$ eV, respectively. Also when the bias parameter is marginalized out the combination WMAP9+BAO+Cluster(B_M) shows a 2σ evidence for non-zero neutrino masses, although with larger error bars and a lower mean value: $\sum m_\nu = 0.26 \pm 0.20$ eV. The result can be understood as follows: the BAO scale measurements basically fix the matter density parameter thus breaking the $\sigma_8 - \Omega_{\rm m}$ degeneracy typical of cluster and shear constraints. The tight constraints obtained for these two parameters along with the large value of $\Omega_{\rm m}$ (driven by the BAO data) and small value of σ_8 (driven by cluster abundance or shear measurements) are compensated with a large value of $\sum m_\nu$. At variance, Ly-α data prefers large value of the power spectrum normalization, and when joined with WMAP9+BAO data the large $\Omega_{\rm m}$ and σ_8 values inferred require small neutrino masses yielding the upper limit $\sum m_\nu < 0.19$ eV. The further inclusion of shear data in the WMAP9+BAO+Cluster(B_M) analysis does not improve substantially the error on the neutrino mass, but decreases σ_8 by ~ 0.01 thus favouring slightly larger neutrino masses and increasing to 3σ the significance of the mass detection.

Finally we jointly analyse the WMAP9, BAO, Ly-α, shear and cluster data in-

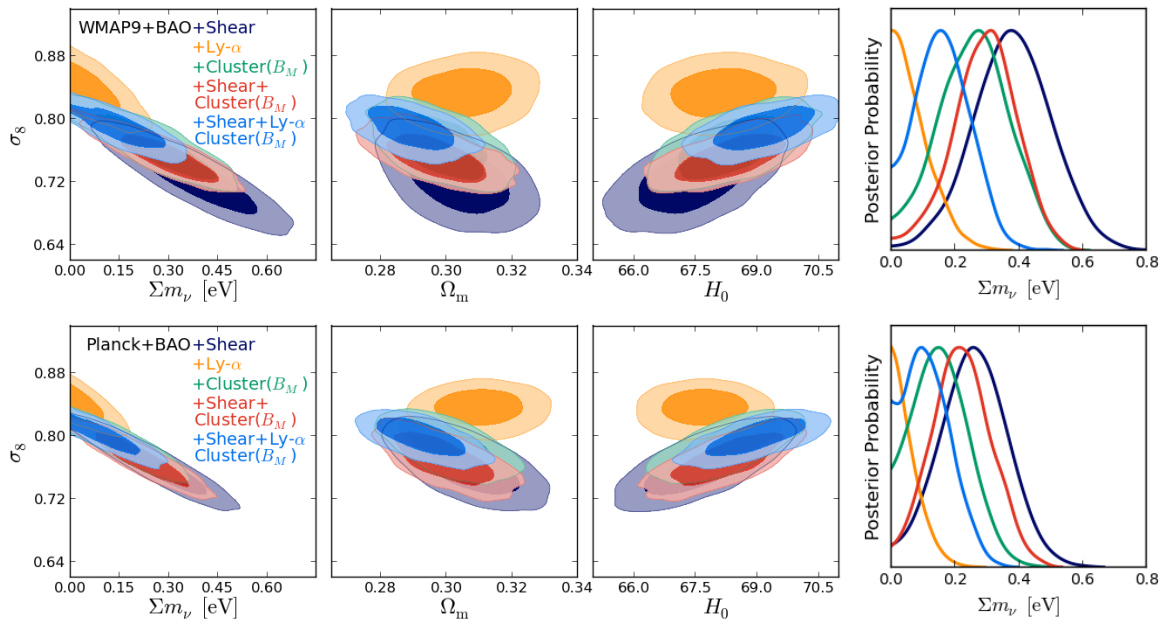

Figure 5.3: *Left* -Confidence contours at 68% and 95% CL in the $\sigma_8 - (\Omega_m, H_0, \sum m_\nu)$ planes when combining WMAP9 (*upper* panels) or Planck (*lower* panels) with many different probes of the low redshift Universe within a ΛCDM+$\sum m_\nu$ model. *Right* - Posterior probability distribution for $\sum m_\nu$ from the same datasets.

cluding B_M into the fit obtaining $\sum m_\nu < 0.30$ eV. The addition of Ly-α forest measurements raises the power spectrum normalization by ~ 0.04 which causes a shift of the neutrino mass toward lower values and reduces to 1σ the significance of the mass detection. We decided not to combine Ly-α and cluster data without marginalizing over the bias since the WMAP9+BAO+Ly-α and WMAP9+BAO+Cluster data are already in tension by more than 2σ (see upper panels of Figure 5.3).

Combining with Planck

Now we repeat the same analysis but replacing the WMAP9 dataset with Planck. The results are summarized in Table 5.1 and shown in the lower panels of Fig 5.2 and Fig 5.3. Planck provides not only tighter cosmological constraints than WMAP9 data but it also prefers a larger matter density parameters, which in turn lowers the derived H_0 value and increases the power spectrum normalization. For datasets which are consistent with Planck measurements, i.e. BAO and Ly-α, the

combination with this CMB data yields lower upper limits on the neutrino mass: $\sum m_\nu < 0.27$ eV and $\sum m_\nu < 0.24$ eV for Planck+Ly-α and Planck+BAO, respectively. In this case the CMB+BAO combination does not show preference for large neutrino mass thanks to the larger value and tighter constraints on σ_8 provided by Planck. Conversely, the addition of shear or cluster data, which prefer lower σ_8, shifts the contours outside the region allowed by Planck by 1σ and 2σ, respectively. This indicates that the extension to massive neutrino is not sufficient to bring the two datasets in agreement with Planck measurements. The shear measurements does not improve the constrains on $\sum m_\nu$, while clusters number counts yields an upper limit of 0.34 eV . Including in the cluster analysis the baryon correction to the HMF increases by few percents the σ_8 and $\Omega_{\rm m}$ values improving the fit by $\Delta\chi^2 \simeq 2$, but it is not sufficient to relieve the tension between the two datasets. Allowing the bias to vary causes the contours to move towards the region allowed by Planck bringing the datasets in better agreement at the expense of a large mass bias, $B_M \sim 0.8$. In this case the best fit χ^2 is reduced by ~ 9 with respect to the standard Planck+Cluster analysis and, as expected for consistent datasets, the errors shrink giving an upper limit of $\sum m_\nu < 0.27$ eV.

As above we start now to combine different probes of the low redshift Universe at the same time. The main results are shown in the lower panels of Figure 5.3. Similar to the previous results the inclusion of cluster or shear datasets in the Planck+BAO joint analysis results in a preference for massive neutrinos at more than 2σ. We obtain $\sum m_\nu = 0.32 \pm 0.17$ eV combining Planck, BAO and cluster data and $\sum m_\nu = 0.26^{+0.20}_{-0.21}$ eV replacing the latter with shear data. However, looking at the lower panels of Figure 5.2 it is clear that the large mean value of $\sum m_\nu = 0.32$ eV obtained from Planck+BAO+Cluster is driven by the tension between Planck+BAO and cluster constraints. In other words, the resulting constraints cannot be used to claim a significant detection of the neutrino mass, but rather they represent a compromise solution between discrepant datasets. Indeed, if we repeat the analysis marginalizing over the bias the best fit improves by $\Delta\chi^2 \simeq 11$ – in this case the Planck+BAO and Planck+Cluster(B_M) contours overlap; see middle panel of Figure 5.4 – and we obtain only a mild preference for massive neutrino at 1σ and an upper limit of $\sum m_\nu < 0.28$ eV at 2σ. A very tight upper limit of $\sum m_\nu = 0.14$ eV results instead from the combination of Planck with BAO and Ly-α data in agreement with the previous results obtained from WMAP9 data. Then we add progressively the shear and Ly-α constraints to the joint analysis Planck+BAO+Cluster(B_M). Again the inclusion of shear measurements after cluster data does not alter significantly the error on $\sum m_\nu$, but lowers by ~ 0.02 the

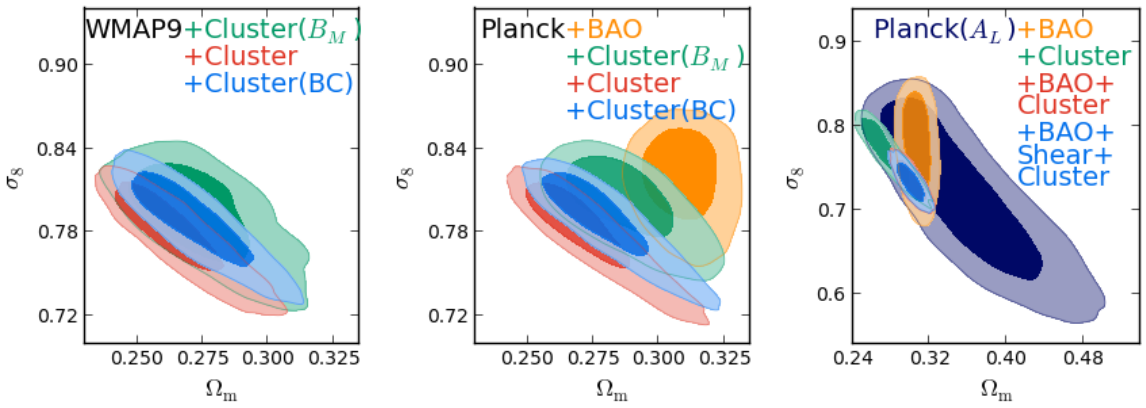

Figure 5.4: *Left-Middle panel* - Comparison of the confidence contours at 68% and 95% CL in the $\sigma_8 - \Omega_m$ plane within a ΛCDM+$\sum m_\nu$ model when combining WMAP9 (*left* panel) or Planck (*middle* panel) with cluster data using different prescriptions: the standard one (*Cluster*), the baryon correction (*Cluster(BC)*) or marginalizing over the bias (*Cluster*(B_M)). In the *middle* panel are also shown the confidence contours for the joint analysis Planck+BAO: only when B_M is allowed to vary the Planck+BAO and Planck+Cluster(B_M) regions overlap. *Right panel* - Joint 68% and 95% CL constraints on $\sigma_8 - \Omega_m$ for different dataset combined with Planck with the A_L-lensing signal marginalized out.

power spectrum normalization boosting the total neutrino mass to $\sum m_\nu = 0.22^{+0.17}_{-0.18}$ eV, thus providing a 2σ evidence for massive neutrinos. Instead, the shift to higher σ_8 value induced by the Ly-α dataset pushes again the mean neutrino mass toward lower value and wipes out the neutrino mass detection yielding $\sum m_\nu < 0.24$ eV.

Another possible way to relieve the tension between Planck and clusters data is to marginalize over the lensing contribution to the temperature power spectrum, parametrized by the parameter A_L. The Planck Collaboration reported some anomalies when A_L is included in the fit: for a ΛCDM+A_L model they found $A_L = 1.22^{+0.25}_{-0.22}$ (Planck Collaboration, 2013d), which is at 2σ from the expected value of one and 1σ away from the lensing signal extrapolated from the 4-point function $A_L^{\phi\phi} = 0.99^{+0.11}_{-0.10}$. Since Planck constraints on neutrino mass mainly relay on lensing information (massive neutrinos increase the expansion rate at $z \gtrsim 1$ suppressing clustering on sub-horizon scales at non-relativistic transition; see e.g. Planck Collaboration, 2013d) marginalizing over A_L significantly degrades the error on $\sum m_\nu$. Moreover, the preferred value of $A_L > 1$ shifts by $\sim 1\sigma$ the $\Omega_m - \sigma_8$ contours

bringing Planck in much better agreement with cluster and shear data (see right panel of Figure 5.4). The joint analysis Planck($A_{\rm L}$)+Cluster gives $\sum m_\nu < 0.41$ eV with an improved best fit with respect to the Planck+Cluster analysis of $\Delta\chi^2 \simeq 16$, while Planck($A_{\rm L}$)+BAO yields $\sum m_\nu < 0.46$ eV with a mild preference for massive neutrinos similar to the results obtained in combination with WMAP9. Combining Planck($A_{\rm L}$) with cluster and BAO yields $\sum m_\nu = 0.35^{+0.15}_{-0.16}$ eV: the tight constraints on σ_8 and $\Omega_{\rm m}$ provided by the combination of cluster and BAO data along with the low value of power spectrum normalization preferred by the former and large value of the matter density parameter preferred by the latter require large neutrino masses to bring the two datasets into agreement. The further inclusion of shear data, whose degeneracy direction between σ_8 and $\Omega_{\rm m}$ overlaps the one inferred from Planck($A_{\rm L}$) data, does not change the parameter constraints nor shift their preferred values. For this analysis we did not consider the Ly-α dataset which exhibits a larger than 2σ tension with Planck($A_{\rm L}$)+Cluster and Planck($A_{\rm L}$)+shear results in the $\sigma_8 - \Omega_{\rm m}$ plane due to the large value of the power spectrum normalization favoured by Ly-α forest data.

5.2.2 Extra sterile massive neutrinos

We now explore the scenario with an extra sterile neutrino component. Table 5.2 and Figure 5.5 summarize the results obtained for the various data combinations. For this cosmological model we employed only Planck as CMB dataset since the constraints obtained from WMAP9 are much weaker than Planck ones. With the same logic adopted in the previous Section we start combining single dataset with the CMB data and then we add them progressively. The inclusion of $N_{\rm eff}$ in the fit opens new parameter degeneracies which relax the Planck contours and bring the cluster and shear constraints in better agreement with the CMB data. In particular, $N_{\rm eff} > 3.046$ increases the radiation energy content (see Eq. 1.42) and affects the expansion rate of the Universe thus relaxing the bounds on H_0 and the scalar spectral index, with which $N_{\rm eff}$ is positively correlated. When cluster constraints are included we find a mild preference for massive sterile neutrino $m_{\rm s}^{\rm eff} = 0.54 \pm 0.26$ eV (68%), and a 2σ hint for extra dark radiation $\Delta N_{\rm eff} = 0.84^{+0.63}_{-0.60}$. At variance with the Planck+Cluster joint analysis performed in the previous Section – i.e. within a ΛCDM+$\sum m_\nu$ model – this time the Planck+Cluster combination does not exhibit strong tension with the Planck results, which improves the χ^2 best fit by $\simeq 11$ (e.g. compare the $\sigma_8 - \Omega_{\rm m}$ panels of Figure 5.2 and Figure 5.6). This fact, along with the lower σ_8 and larger $H_0 - n_s$ values preferred by cluster data and the positive correlation between $m_{\rm s}^{\rm eff}$ and $\Delta N_{\rm eff}$, accounts for the shift of the two parameters

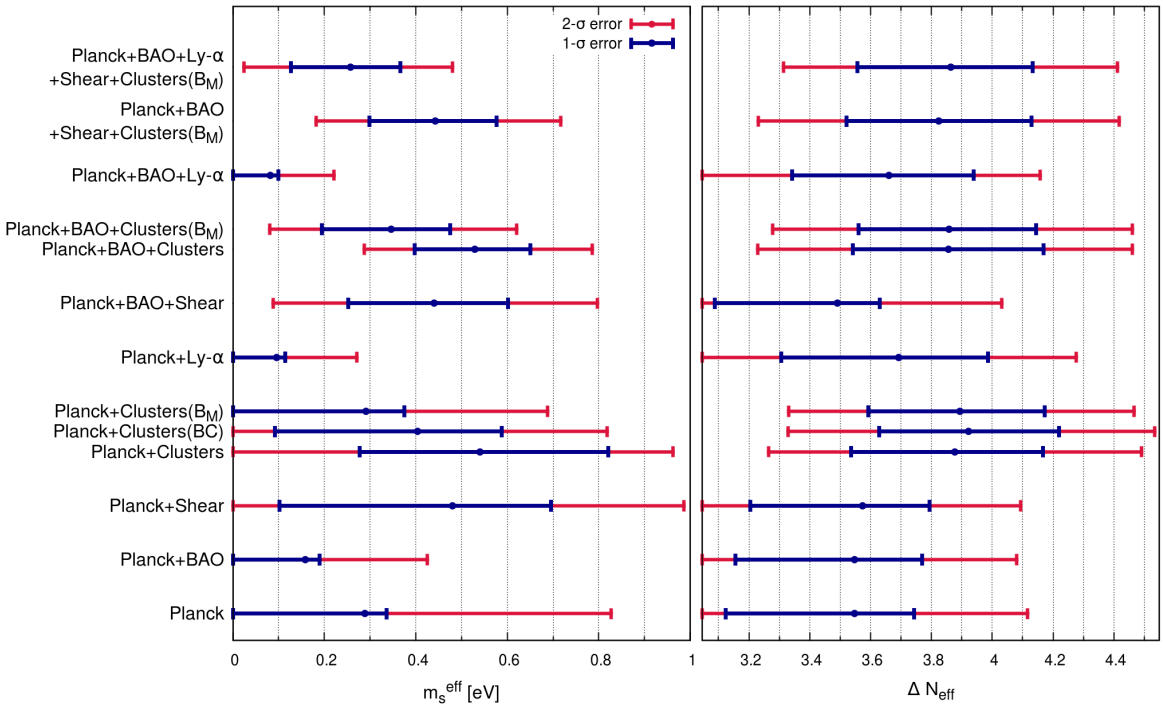

Figure 5.5: Summary of the 1σ and 2σ errors on $m_{\rm s}^{\rm eff}$ and $N_{\rm eff}$ obtained from the dataset combinations discussed in Section 5.2.2 for a ΛCDM+$m_{\rm s}^{\rm eff}$+$N_{\rm eff}$ model with one massive neutrino of mass $m_\nu = 0.06$ eV.

Table 5.2: Constraints on $\Omega_{\rm m}$, σ_8, $m_{\rm s}^{\rm eff}$ and $\Delta N_{\rm eff}$ for a ΛCDM model with massive sterile neutrino using different datasets. Errors are reported at 68% confidence level for σ_8 and $\Omega_{\rm m}$, and both 68% and 95% confidence level for $m_{\rm s}^{\rm eff}$ and $\Delta N_{\rm eff}$. Notations included in parenthesis denote modifications to the standard setting: (BC) stands for the baryon correction to the HMF, while (B_M) corresponds to analyses with the mass bias parameter marginalized out.

Dataset	$\Omega_{\rm m}$	σ_8	$m_{\rm s}^{\rm eff}$[eV]		$\Delta N_{\rm eff}$	
			68%CL	95%CL	68%CL	95%CL
Planck	$0.322^{+0.025}_{-0.030}$	$0.800^{+0.052}_{-0.031}$	< 0.34	< 0.86	$0.49^{+0.18}_{-0.42}$	< 1.07
Planck+Cluster	$0.304^{+0.026}_{-0.027}$	$0.745^{+0.023}_{-0.037}$	$0.54^{+0.26}_{-0.26}$	< 0.98	$0.84^{+0.32}_{-0.32}$	$0.84^{+0.63}_{-0.60}$
Planck+Cluster(B_M)	$0.295^{+0.019}_{-0.028}$	$0.794^{+0.040}_{-0.032}$	< 0.38	< 0.69	$0.85^{+0.28}_{-0.30}$	$0.85^{+0.56}_{-0.57}$
Planck+Cluster(BC)	$0.296^{+0.023}_{-0.028}$	$0.770^{+0.031}_{-0.036}$	$0.40^{+0.31}_{-0.19}$	< 0.81	$0.88^{+0.30}_{-0.29}$	$0.88^{+0.61}_{-0.60}$
Planck+BAO	$0.306^{+0.009}_{-0.009}$	$0.818^{+0.033}_{-0.026}$	< 0.19	< 0.43	$0.50^{+0.22}_{-0.39}$	< 1.04
Planck+Shear	$0.309^{+0.028}_{-0.028}$	$0.752^{+0.037}_{-0.043}$	$0.48^{+0.22}_{-0.38}$	< 0.99	$0.53^{+0.22}_{-0.37}$	< 1.30
Planck+Ly-α	$0.309^{+0.023}_{-0.024}$	$0.843^{+0.021}_{-0.021}$	< 0.11	< 0.27	$0.65^{+0.30}_{-0.38}$	< 1.49
Planck+BAO+Cluster	$0.303^{+0.009}_{-0.009}$	$0.744^{+0.013}_{-0.014}$	$0.53^{+0.12}_{-0.13}$	$0.53^{+0.26}_{-0.24}$	$0.81^{+0.31}_{-0.32}$	$0.81^{+0.60}_{-0.63}$
Planck+BAO+Cluster(B_M)	$0.303^{+0.007}_{-0.009}$	$0.782^{+0.020}_{-0.018}$	$0.35^{+0.13}_{-0.15}$	$0.35^{+0.27}_{-0.27}$	$0.81^{+0.29}_{-0.30}$	$0.81^{+0.60}_{-0.58}$
Planck+BAO+Shear	$0.305^{+0.09}_{-0.010}$	$0.753^{+0.023}_{-0.022}$	$0.44^{+0.16}_{-0.19}$	$0.44^{+0.34}_{-0.35}$	$0.45^{+0.14}_{-0.40}$	< 0.99
Planck+BAO+Ly-α	$0.305^{+0.09}_{-0.010}$	$0.844^{+0.020}_{-0.019}$	< 0.10	< 0.22	$0.61^{+0.28}_{-0.32}$	< 1.11
Planck+BAO+ Shear+Cluster(B_M)	$0.303^{+0.009}_{-0.009}$	$0.759^{+0.017}_{-0.020}$	$0.44^{+0.14}_{-0.14}$	$0.44^{+0.28}_{-0.26}$	$0.78^{+0.31}_{-0.30}$	$0.78^{+0.60}_{-0.59}$
Planck+BAO+Ly-α Shear+Cluster(B_M)	$0.293^{+0.009}_{-0.008}$	$0.794^{+0.016}_{-0.016}$	$0.26^{+0.11}_{-0.13}$	$0.26^{+0.22}_{-0.24}$	$0.82^{+0.27}_{-0.31}$	$0.82^{+0.55}_{-0.55}$

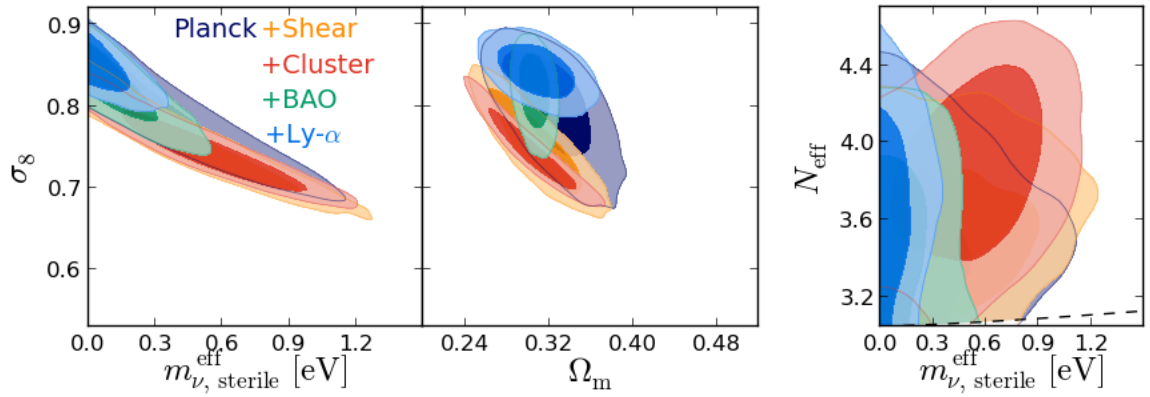

Figure 5.6: Two dimensional likelihood contours at 68% and 95% CL for $\sigma_8 - (\Omega_{\rm m}, m_{\rm s}^{\rm eff})$ and $N_{\rm eff} - m_{\rm s}^{\rm eff}$ from Planck combined with different probes of the low redshift Universe within a ΛCDM+$m_{\rm s}^{\rm eff}$+$\Delta N_{\rm eff}$ model. The dashed line shown in the $N_{\rm eff} - m_{\rm s}^{\rm eff}$ plane represent the prior on the physical sterile neutrino mass: $m_{\rm s}^{\rm eff}/(\Delta N_{\rm eff})^{3/4} < 10$ eV .

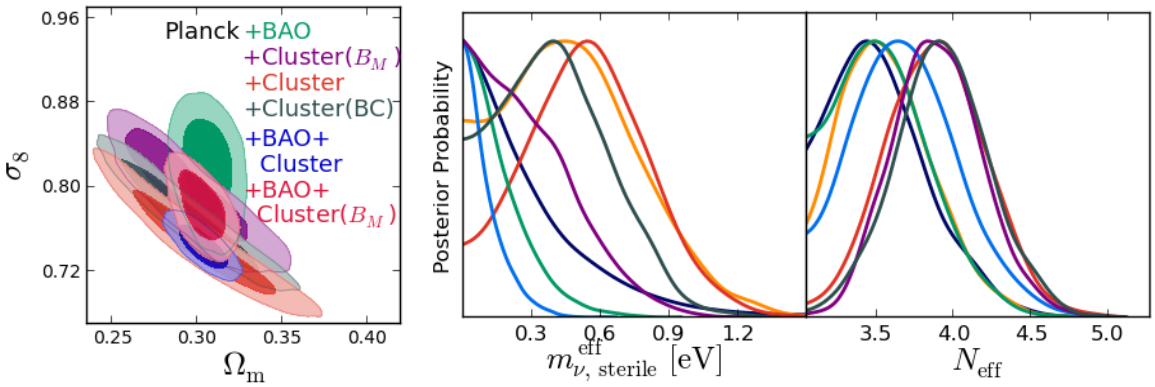

Figure 5.7: *Left* panel - Comparison of the two dimensional likelihood contours at 68% and 95% CL in the $\sigma_8 - \Omega_{\rm m}$ plane from the joint analysis of Planck or Planck+BAO and cluster data using different prescriptions for the HMF: the standard one (*Cluster*), the baryon correction (*Cluster(BC)*) or marginalizing over the bias (*Cluster*(B_M)). *Right* panels - Posterior probability distributions for $m_{\rm s}^{\rm eff}$ and $N_{\rm eff}$ from single datasets combined with Planck within a ΛCDM+$m_{\rm s}^{\rm eff}$+$\Delta N_{\rm eff}$ model. The colour coding of the lines is the same of Figure 5.6 and the *left* panel of this figure.

with respect to the Planck-only analysis (see Figure 5.6). Analogous constraints on $m_{\rm s}^{\rm eff}$ are provided by the inclusion of shear measurements which lowers the σ_8 mean value, while leaving the bounds on n_s and H_0, and thus on $\Delta N_{\rm eff}$, unaffected with respect to the Planck-only results. If we consider the Planck+Cluster analysis, the BC to the HMF results in a 1σ shift of the power spectrum normalization toward higher values which reduces the $m_{\rm s}^{\rm eff}$ mean value, while keeping the constraints on $N_{\rm eff}$ and the best fit value almost unchanged (see Figure 5.7). Similarly, but with an increased magnitude, if we repeat the analysis marginalizing over the bias the preferred σ_8 value shifts by 2σ at the expense of a large value for the bias, $B_M \sim 0.8$, wiping out the former 1σ preference for $m_{\rm s}^{\rm eff}$ larger than zero. For this analysis we find a mild improvement of the best fit value of $\Delta\chi^2 \simeq 5$ with respect to the standard one. At odds the inclusion of BAO data reduces the error on $\Omega_{\rm m}$ and slightly increases the σ_8 mean value with respect to the Planck-only analysis. This results in tighter constraints for the sterile neutrino mass, $m_{\rm s}^{\rm eff} < 0.43$ eV, and leaves almost unchanged the bounds on $\Delta N_{\rm eff}$. When joined to the Planck analysis the Ly-α data constrains σ_8 in the high values region allowed by Planck data and slightly increases the $n_{\rm s}$ and H_0 mean values. This entails an upper limit of 0.27 eV for the effective sterile neutrino mass and a $\sim 20\%$ increase of the $\Delta N_{\rm eff}$ mean values.

We start now to combine Planck CMB measurements with different low redshift probes. The main results of these analyses are shown in Figure 5.8. Also shown in the $N_{\rm eff} - m_{\rm s}^{\rm eff}$ plane are the $m_{\rm s}^{\rm eff}$ values motivated by reactor and Gallium anomalies ($m_{\rm s}^{\rm eff} \sim 1$ eV) and accelerator anomaly ($m_{\rm s}^{\rm eff} \sim 0.70$ eV), for a fully-thermalised sterile neutrino component ($\Delta N_{\rm eff} = 1$). As for the ΛCDM+$\sum m_\nu$ model, including BAO data in the Planck+Cluster or Planck+Shear analyses provides a 2σ evidence for massive sterile neutrino – $m_{\rm s}^{\rm eff} = 0.53^{+0.26}_{-0.24}$ eV and $m_{\rm s}^{\rm eff} = 0.44^{+0.34}_{-0.35}$ eV, respectively – reason for that being the tight constraints on $\Omega_{\rm m}$ from BAO measurements, which allow to break the $\sigma_8 - \Omega_{\rm m}$ degeneracy, and the low σ_8 mean value preferred by cluster and shear data. As for $\Delta N_{\rm eff}$ the Planck+BAO+Shear combination shows only a mild preference for $\Delta N_{\rm eff} > 0$, while the Planck+BAO+Cluster joint analysis, driven by the large $n_{\rm s}$ value required by cluster data, favours at 2σ an extra dark radiation component. However, even if not as strong as for the ΛCDM+$\sum m_\nu$ model, the Planck+BAO and Planck+Cluster results still exhibits a $\sim 1\sigma$ tension (see *right* panel of Figure 5.7), which could drive the large $m_{\rm s}^{\rm eff}$ value obtained from the combination of the three datasets. Interestingly, at variance with the ΛCDM+$\sum m_\nu$ analysis, the 2σ detection of massive sterile neutrino remains also if we repeat the Planck+BAO+Cluster analysis including the uncertainty in the mass bias. In this

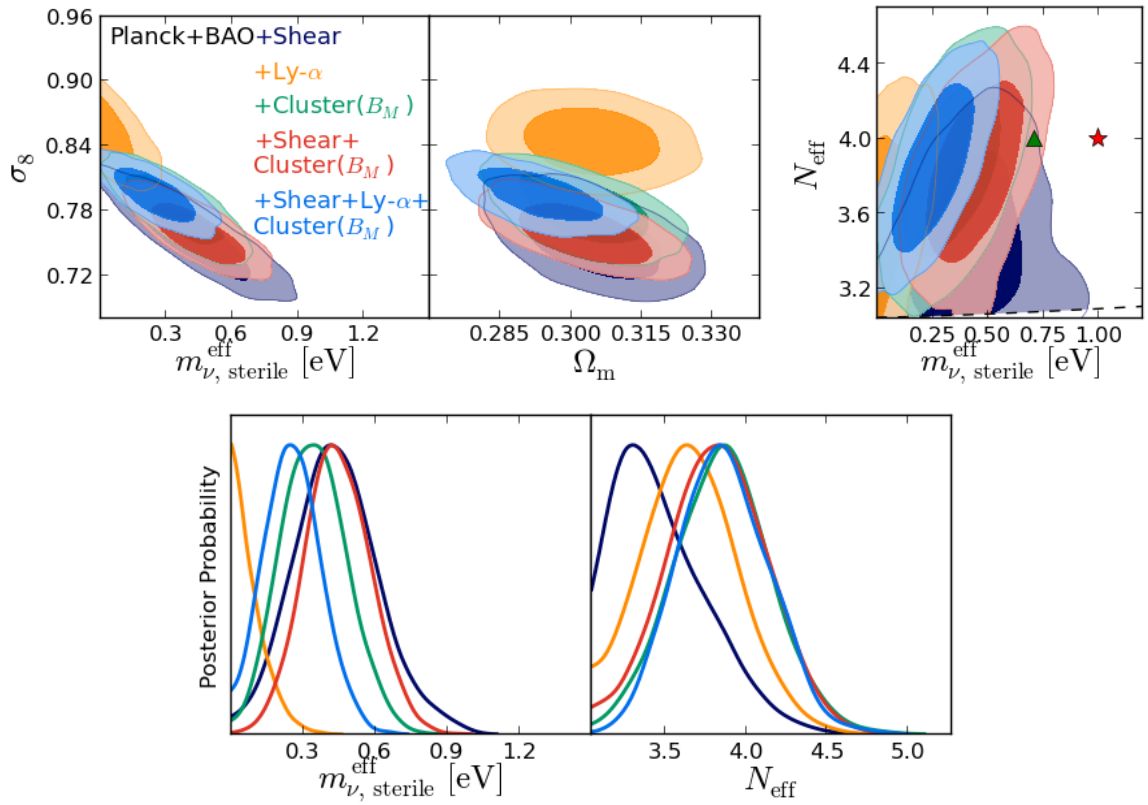

Figure 5.8: *Upper* panels - Confidence contours at 68% and 95% CL in the $\sigma_8 - (\Omega_{\rm m}, m_{\rm s}^{\rm eff})$ and $N_{\rm eff} - m_{\rm s}^{\rm eff}$ planes from Planck combined with various probes of the low redshift Universe within a ΛCDM+$m_{\rm s}^{\rm eff}$+$\Delta N_{\rm eff}$ model. Also shown in the $N_{\rm eff} - m_{\rm s}^{\rm eff}$ plane the value of the effective sterile neutrino masses suggested by accelerator (*green triangle*) and reactor and Gallium (*red star*) anomalies assuming $\Delta N_{\rm eff} = 1$. *Lower* panels - 1D likelihood distributions for $m_{\rm s}^{\rm eff}$ and $N_{\rm eff}$ for the same datasets combinations.

case Planck, BAO and cluster(B_M) results are in good agreement and the inclusion of cluster data in the Planck+BAO joint analysis does not shift the contours outside the region allowed by the latter but only shrinks the errors, as expected for consistent datasets. Compared to the previous analysis without mass bias the fit improves by $\Delta\chi^2 \simeq 5$. The inclusion of B_M in the fit increases the σ_8 mean value by ~ 0.04 which involves a decrease of $\sim 35\%$ of the mean effective sterile neutrino mass, $m_{\rm s}^{\rm eff} = 0.35 \pm 0.27$ eV, while leaving unaffected the bounds on $\Delta N_{\rm eff}$. This datasets combination rejects at more than 3σ the vanilla ΛCDM model, which is located at the origin of $N_{\rm eff} - m_{\rm s}^{\rm eff}$ plane in Figure 5.8, but it also disfavours a sterile neutrino mass of $m_{\rm s}^{\rm eff} \sim 0.70$ eV as suggested by accelerator experiments, and even more strongly rejects the value of $m_{\rm s}^{\rm eff} \sim 1$ eV motivated by reactor and Gallium experiments. The further inclusion of shear measurements has the effect of favour a slightly lower value of σ_8, which increases the mean sterile neutrino mass by 30% with respect to the Planck+BAO+Cluster(B_M) analysis, thus strengthening the evidence for a light sterile neutrino species. Moreover, this shift is sufficient to bring the $N_{\rm eff} - m_{\rm s}^{\rm eff}$ confidence contours in agreement with the sterile neutrino mass motivated by accelerator experiments within 2σ. As in the massive active neutrino scenario, the inclusion of Ly-α data on the Planck+BAO analysis leads to opposite results. The large value of σ_8 preferred by Ly-α data requires small value for the sterile neutrino mass to be consistent with the Planck+BAO constraints. This provides a thigh upper limit of 0.22 eV on $m_{\rm s}^{\rm eff}$ in agreement with the standard ΛCDM predictions. Finally, we add the Ly-α datasets to the combination Planck+BAO+Shear+Cluster(B_M) finding $m_{\rm s}^{\rm eff} = 0.26^{+0.22}_{-0.24}$ eV. The Ly-α contours are in tension with the Planck+BAO+Shear+Cluster(B_M) results at more than 1σ, and these constraints on $m_{\rm s}^{\rm eff}$ reflect the compromise between the low σ_8 mean value preferred by shear and cluster data and the large one inferred from Ly-α data. As for $\Delta N_{\rm eff}$, the inclusion of the Ly-α data does not shift its mean value but helps to reduce the errors giving $\Delta N_{\rm eff} = 0.82 \pm 0.55$, that is a larger than 2σ preference for extra dark radiation.

5.3 Conclusions

In this Chapter we presented neutrino mass constraints, either for an active and sterile neutrino scenario, from the combination of CMB measurements with low redshift Universe probes. We employed for this analysis CMB measurements from WMAP9 or Planck in combination with BAO scale measurements from BOSS DR11, galaxy shear power spectrum from CFTHLenS, SDSS Ly-α forest power spectrum

constraints and cluster mass functions from *Chandra* observations. At variance with previous similar studies, which included in their analysis constraints derived within a vanilla ΛCDM model, we performed a full likelihood analysis for all the datasets employed in this work in order to avoid model dependence of the constraints. Moreover, in the cluster data analysis we properly took into account the impact of massive neutrino in the HMF calibration and we investigated the effects on cosmological constraints of the uncertainty in the mass bias and re-calibration of the HMF due to baryonic feedback processes as suggested in Cui et al. (2014).

For both neutrino scenarios assumed and CMB datasets employed, we found that none of the constraints from the LSS data, combined on a one-by-one basis, with CMB measurements provide strong – i.e. larger than 2σ – evidence for massive neutrino. From the joint analysis Planck+Cluster we obtained $\sum m_\nu < 0.34$ eV but we emphasize that the extensions to three massive active neutrinos is not sufficient to bring the dataset in agreement with Planck results. Indeed the extension to massive neutrinos does not improve the fit of the combination of Planck and galaxy cluster data, with respect to the vanilla ΛCDM model. Taking into account the effect of baryons on the HMF calibration or the uncertainty in the mass bias increases the σ_8 mean value improving the fit with respect to the standard analysis of $\Delta\chi^2 \simeq 2$ and $\Delta\chi^2 \simeq 9$, respectively. In the latter case constraints from Planck CMB and galaxy clusters agree within 1σ, with their combination preferring a vanishing neutrino mass. Alternatively, the Planck and cluster datasets can be brought in agreement marginalizing over the lensing contribution to the temperature power spectrum. In this case the Planck's $\sigma_8 - \Omega_m$ contours relax and shift by $\sim 1\sigma$, improving the χ^2 best fit value by ~ 16 with respect to the Planck+Cluster analysis. Similarly, assuming an extra sterile neutrino species, which introduces in the fit the additional parameter $\Delta N_{\rm eff}$, relaxes the Planck's bounds reducing the discrepancy with cluster results by $\Delta\chi^2 \simeq 11$ with respect to the same data combination in a ΛCDM+$\sum m_\nu$ model. From this analysis we obtained a 1σ preference for non vanishing neutrino mass and $\Delta N_{\rm eff} = 0.84^{+0.63}_{-0.60}$. Including also the mass bias in the fit further improves the agreement between Planck and cluster datasets by $\Delta\chi^2 \simeq 5$ at the expense of an higher σ_8 mean value which cancels the former 1σ detection of massive neutrinos. Preference for non-vanishing neutrino mass at more than 2σ were found instead combining CMB and BAO measurements with shear or cluster data. The BAO constraints break the $\sigma_8 - \Omega_m$ degeneracy typical of cluster and shear data while the low σ_8 mean value preferred by the latter is compensated by large neutrino mass. However, for the ΛCDM+$\sum m_\nu$ model, the large neutrino mass obtained from the joint analysis Planck+BAO+Cluster is driven by the tension between Planck+BAO and cluster constraints. Indeed, in-

cluding the mass bias parameter in the fit reduces the $\sum m_\nu$ mean value by 50% wiping out the 2σ preference for massive neutrino, but increasing the χ^2 best fit value by ~ 11. For the sterile neutrino case, when considering the uncertainty in the mass bias, the fit is improved by $\Delta\chi^2 \simeq 5$ at the expenses of a lower mean neutrino mass but still with a preference for an extra massive neutrino, $m_{\rm s}^{\rm eff} = 0.35 \pm 0.27{\rm eV} - \Delta N_{\rm eff} = 0.81^{+0.60}_{-0.58}$. The significance of the detection increases further including simultaneously shear and cluster data. For a ΛCDM model with three degenerate massive neutrinos we obtained $\sum m_\nu = 0.29^{+0.18}_{-0.21}$ eV from the combination WMAP9+BAO+Shear+Cluster(B_M), while replacing WMAP9 with Planck measurements we got $\sum m_\nu = 0.22^{+0.17}_{-0.18}$ eV, or $\sum m_\nu = 0.35^{+0.15}_{-0.16}$ eV marginalizing over the lensing signal. For the sterile neutrino case, from the combination Planck+BAO+Shear+Cluster(B_M), we found $m_{\rm s}^{\rm eff} = 0.44^{+0.28}_{-0.26}$eV and $\Delta N_{\rm eff} = 0.78^{+0.60}_{-0.59}$, that is a larger than 3σ rejection of the vanilla ΛCDM model. Assuming a fully thermalised sterile neutrino these constraints reject at even higher significance a 1.0 eV sterile neutrino as motived by reactor and Gallium anomalies, while a neutrino mass of 0.7 eV as suggested by accelerator anomaly is within the 2σ errors. Conversely, the Ly-α measurements tend to increase the σ_8 mean value with respect to the CMB data analyses, which in turn entails a preference for vanishing neutrino masses to be consistent with the other parameters constraints. For the active neutrino scenario we got $\sum m_\nu < 0.19$ eV and $\sum m_\nu < 0.14$ eV combining BAO, Ly-α and WMAP9 or Planck dataset, respectively. Similarly, for the sterile neutrino model we obtained $m_{\rm s}^{\rm eff} < 0.22$eV and $\Delta N_{\rm eff} < 1.11$. The full data combination provides neutrino mass constraints which reflects the compromise between the σ_8 values preferred by shear and cluster data and those inferred from Ly-α measurements. For the ΛCDM+$\sum m_\nu$ model we obtained only an upper limit on the total neutrino mass independently from the CMB dataset employed, while in the sterile neutrino scenario we still found a 2σ preference for an extra massive species, $m_{\rm s}^{\rm eff} = 0.26^{+0.22}_{-0.24}{\rm eV} - \Delta N_{\rm eff} = 0.82 \pm 0.55$.

In summary, these results highlight that current CMB and LSS probes point towards a significant detection of the sterile neutrino mass and dark radiation unless the constraints on σ_8 provided by clusters and shear data turn out to be biased toward lower values. As for clusters, this could be due to a possible underestimate of the cluster mass bias. As for cosmic shear, an underestimate of σ_8 could be induced by a misinterpretation of the intrinsic alignment signal. On the other hand new BOSS results from the 1D Ly-α flux power spectrum or Planck CMB data – e.g. due to a different foreground removal technique (Spergel et al., 2013) – could strengthen or weaken the evidence for non-vanishing neutrino masses.

More in general, this analysis highlights the potential that current cosmological data already have to set rather stringent constraints on neutrino masses, which could even challenge the results from laboratory experiments, but these are hampered by systematics which need to be better controlled and understood. This becomes even more important in view of future surveys (eROSITA, SPT3G, DES, DESI, Euclid), that thanks to the large amount of data to be provided will bring down the statistical errors by large factors. As for cluster cosmology, the ever increasing number of high quality weak lensing data is expected to provide in the near term well characterized and unbiased constraints on the absolute cluster mass calibration. From the theoretical side, refined cosmological simulations which properly accounts for neutrino and baryonic physics will be crucial to improve the calibration of the HMF and modelling of the shear and Ly-α forest flux power spectrum.

6

Conclusions

In the last decade the wealth and accuracy of cosmological data from measurements of the CMB, LSS and related probes allowed to determine with high precision the six parameters of the concordance ΛCDM model. Yet, more than 90% of the content of the Universe is in the form of unknown dark matter and dark energy components, while tensions between constraints inferred from high and low redshift Universe probes require either a reassessment of their systematics, extensions of the standard ΛCDM paradigm, or a combination thereof. The joint analysis of different cosmological probes provides a means to address these issues, thanks to different scales and redshifts probed, and the different sources of systematics affecting them.

In this Thesis we derived cosmological constraints for the combination of CMB data with different probes of the LSS, focusing on massive neutrino constraints from galaxy cluster surveys.

This analysis has been motivated by the following considerations: neutrino oscillation experiments provided clear evidence for neutrino masses, but terrestrial experiments can only set loose constraints on their absolute mass scale. On the other hand, cosmology provides several tools to test the neutrino properties; among these, galaxy clusters, probing the growth of structures at low redshift, are particularly well suited to constrain their total mass, thanks to the effects that neutrinos induce on the structure formation.

Indeed, current neutrino constraints from cluster data are already competitive with those inferred from other low redshift probes, while next future cluster surveys, increasing by more than one order of magnitude the number of cluster de-

tected, are expected the improve considerably their constraining power. Moreover, the discrepancy between the growth of structures inferred from cluster number counts – as well as from cosmic shear and RSDs measurements – and that extrapolated from Planck CMB data within the ΛCDM model, can be accounted for by massive neutrinos, though, possible systematics in the cluster mass estimates or in the theoretical predictions of the cluster abundance, hamper the interpretation of these results.

As stated in the Introduction, we dealt with three issues throughout this Thesis: *i*) the capability of the forthcoming ESA's Euclid cluster surveys in constraining the neutrino properties; *ii*) the calibration of the HMF in cosmology with massive neutrinos and its effects on cosmological constraints from cluster data, and *iii*) the reliability of neutrino mass constraints from the combination of CMB data with low-redshift Universe probes and their role in the tension between CMB and LSS results.

The first point has been discussed in Chapter 3. We first created cluster number counts and power spectrum mock data for the Euclid photometric cluster survey; then, by means of the MCMC technique we derived cosmological constraints for a ΛCDM $+\sum m_\nu$ model from the combination of these two observables, along with Planck-like CMB data. It turns out that, thanks to the large number of clusters that Euclid is expected to detect, it will be possible to constrain the total neutrino mass to $\sum m_\nu < 0.35\,\mathrm{eV}$ (95%CL) using Euclid cluster data alone, and to $\sum m_\nu < 0.031\,\mathrm{eV}$ (95%CL) including also Planck CMB measurements. The factor 10 improvement yielded by the data combination, resulting from the nearly orthogonal degeneracy directions between cluster and CMB constraints, highlights the complementarity of these two probes. Remarkably, this level of accuracy would allow a 2σ detection of the neutrino mass even in the minimal normal hierarchy scenario ($\sum m_\nu \simeq 0.06\,\mathrm{eV}$). We thus considered several extensions to the ΛCDM $+\sum m_\nu$ model to assess possible degeneracies with the neutrino mass parameter, including: a non-standard effective number of neutrinos ($N_{\mathrm{eff}} \neq 3.046$), dark energy models ($w \neq -1$), and curved geometries ($\Omega_k \neq 0$). Thanks to the constraining power given by the combination of Euclid and Planck datasets none of these model extensions affect considerably the error on $\sum m_\nu$, which remains smaller than the minimal normal hierarchy mass. Finally, to explore the effects of an uncertain knowledge of the relation between cluster mass and optical richness, we also treated the ΛCDM+m_ν+N_{eff} case with free nuisance parameters, which parametrize the uncertainties on the cluster mass determination. Adopting the over-conservative assumption of no prior knowledge on the nuisance parameters the loss of information from cluster number

counts leads to a large degradation of neutrino constraints. In particular, the upper bounds for $\sum m_\nu$ are relaxed by a factor larger than two, $\sum m_\nu < 0.083\,\mathrm{eV}$ (95%CL), hence compromising the possibility of detecting the total neutrino mass with good significance. These results confirm the potential that a large optical/near-IR cluster survey, like that to be carried out by Euclid, could have in constraining neutrino properties, and stress the importance of a robust measurement of masses, e.g. from weak lensing within the Euclid survey, in order to fully exploit the cosmological information carried by such survey.

This analysis represent a first step toward the development of an effective pipeline for the analysis of the real Euclid cluster data. Further refinements are required, including a more accurate selection function which accounts for the geometry of the survey and the detection algorithm employed for the cluster detection, or a proper treatment of the photometric redshift errors and uncertainties in the completeness and purity levels of the cluster sample. Moreover, in our analysis we did not include RSDs, which have been proven to increase the cosmological information which can be extrapolated from the cluster power spectrum analysis (Sartoris et al., 2012). Finally, a better modelling of the structure formation in non-linear regime would allow to extend the range probed in the cluster power spectrum analysis to small-scale modes, the latter being particularly relevant to constrain the neutrino properties.

In Chapter 4 we considered the second issue. Exploiting a set of N-body simulations including CDM and neutrino particles, we showed that the standard form of the HMF matches the halo abundance recovered from simulations with massive neutrinos once the variance of the smoothed density field, which enters in the HMF definition, is computed neglecting the weakly clustering neutrino component, as proposed by Ichiki and Takada (2012). In particular, we showed that the HMF computed with this improved prescription becomes nearly universal – i.e. model independent – with respect to the total neutrino mass. We thus applied our findings to a Planck-like SZ survey to asses the impact of the improved HMF calibration on the theoretical prediction of cluster number counts. We found that the number of clusters predicted to be detected within the survey is lower when using the standard HMF prescription. The difference between the two HMF calibrations increases with the total neutrino mass and number of massive species, and reaches $\sim 30\%$ for three degenerate massive neutrinos with total mass $\sum m_\nu \simeq 0.4\,\mathrm{eV}$. We then moved to the implication for cluster constraints, considering as a case study the sample of 188 SZ-Planck clusters used in Planck Collaboration (2013a) for cosmological parameter inference. Once we had checked that our approximated like-

lihood reproduces well the Planck results, we compared the constraints on the parameter combination $\sigma_8(\Omega_m/0.27)^\gamma$ – the relation constrained by cluster number counts data – obtained with the two HMF prescriptions. We found that, in cosmology with massive neutrinos, the improved HMF calibration provides a steeper degeneracy directions between σ_8 and Ω_m, which results in a lower mean value for the matter power spectrum normalization. The offset has low statistical significance for the dataset employed for this analysis but could become significant for future large cluster samples or when deriving constraints from the joint analysis of cluster data with other probes. The results of this analysis therefore stress the relevance of having a well-calibrated HMF in order to recover unbiased cosmological parameters from cluster datasets in massive neutrino cosmologies.

As a further refinement, the calibration of the HMF should be tested against N-body simulations including multiple extensions of the ΛCDM paradigm – e.g. massive neutrino and dark energy or modified gravity models – to assess the universality of the HMF and the reliability of constraints from cluster data within these models.

Chapter 5 concerns the third point mentioned. To assess to what extent massive neutrinos, either active or sterile, provide a means to relieve the tension between CMB data and low redshift growth of structure measurements, we combined Planck or WMAP 9-year CMB data with several low redshift probes, including: BAO measurements from BOSS DR11, galaxy shear measurements from CFHTLenS, SDSS Ly-α forest constraints and galaxy cluster mass function from *Chandra* observations. At odds with recent similar studies, to avoid model dependence of the constraints, we perform a full likelihood analysis for all the datasets employed. In particular, for the cluster data analysis we employed the HMF calibration presented in Chapter 4 for cosmologies with massive neutrinos and we considered the effects on cosmological constraints induced by the uncertainty in the mass bias and re-calibration of the HMF due to baryonic feedback processes. We found that none of the low redshift probes alone provide evidence for massive neutrino in combination with CMB measurements, while a larger than 2σ detection of non zero neutrino mass, either active or sterile, is achieved combining cluster or shear data with CMB and BAO measurements. Yet, the significance of the detection exceeds 3σ if we combine all four datasets. However, even including massive neutrinos in the model the shear and cluster data exhibit a ~ 1 and $\sim 2\sigma$ tension with Planck measurements, respectively. The discrepancy with cluster data is alleviated, but not resolved, taking in to account the correction to the HMF due to baryonic feedback processes; whereas, considering the uncertainty in the mass

bias reduces the significance of the tension below 1σ, wiping out the preference for non-vanishing neutrino masses. The significance of the neutrino mass detection is larger in the sterile neutrino scenario, for which the inclusion of $N_{\rm eff}$ in the fit opens new parameter degeneracies which relax the Planck contours and bring the cluster and shear constraints in better agreement with the CMB data. For the combination of Planck, BAO, shear and cluster datasets the vanilla ΛCDM model is rejected at more than 3σ and a sterile neutrino mass as motivated by accelerator anomaly is within the 2σ errors. Conversely, the Ly-α data favour vanishing neutrino masses and from the data combination Planck+BAO+Ly-α we got the tight upper limits $\sum m_\nu < 0.14\,{\rm eV}$ and $m_s^{\rm eff} < 0.22\,{\rm eV}$ – $\Delta N_{\rm eff} < 1.11$ (95%CL) for the active and sterile neutrino model, respectively. Finally, results from the full data combination reflect the tension between the σ_8 constraints obtained from cluster and shear data and that inferred from Ly-α forest measurements. In the active neutrino scenario for both CMB datasets employed, the full data combination yields only an upper limits on $\sum m_\nu$, while assuming an extra sterile neutrino we still got preference for non-vanishing mass, $m_s^{\rm eff} = 0.26^{+0.22}_{-0.24}\,{\rm eV}$, and dark contribution to the radiation content, $\Delta N_{\rm eff} = 0.82 \pm 0.55$. The results of this analysis thus endorse massive sterile neutrinos as a means to relax the tension between CMB and LSS datasets and emphasize once again the relevance of having a reliable theoretical prediction for the halo abundance and a well-calibrated mass-proxy relation to infer unbiased constraints from cluster data.

However, many aspects need to be further investigated. For instance, the tension between the growth of structures inferred at $z \sim 2$ from Ly-α forest data and that inferred from shear and cluster data at $z \lesssim 1$ suggests the presence of systematics in one or more of these probes. Furthermore, the $\sim 1\sigma$ offset between the $\Omega_{\rm m}$, H_0 and σ_8 mean values obtained from WMAP 9-year and Planck data still needs to be understood, as well as the large amplitude of lensing signal inferred from the Planck temperature spectrum. Hopefully, the next Planck data release, which includes also polarization data, will shed light on these issues. Finally, other model extensions – e.g. wCDM+$\sum m_\nu$ – which could provide better fits to the data combination than those examined in Chapter 5, should be investigated.

Possible immediate developments of this Thesis work comprise: the extension of the analysis to modified gravity models to asses if clusters can help in breaking the degeneracy between the total neutrino mass and the $f(R)$ parameter; the preparation of a pipeline for the Euclid data where the cluster dataset can be combined with cosmic shear and galaxy clustering measurements, the latter being the primary probes of the mission.

Summarizing, the results presented in this Thesis highlight the decisive contribution that galaxy clusters in combination with other probes gives, and are expected to give in the next future, to the definition of the underlying cosmological model, as well as the criticality which hamper their cosmological usage. In particular, the accuracy of the mass estimation is one of the main limitation for the exploitation of galaxy clusters as cosmological tools. In this respect, panchromatic observations of clusters will provide a way to test the accuracy of the various mass inference techniques and reduce the systematic errors. At the same time larger cluster samples covering wider redshift ranges, as the ones expected from ongoing and next future cluster surveys, will allow to improve considerably the calibration of the mass-proxy relations. Also for the theoretical side there is ample room for improvement: the development of ever more accurate numerical methods and semi-analytical models is expected to improve the predictive power of cosmological simulations including baryonic physics effects and physics beyond the standard ΛCDM model. In turns this will provide more accurate calibrations for the theoretical functions used for parameter inference – e.g. the HMF and non-linear matter power spectrum – extending their effectiveness to a broader range of scales and class of cosmological models. Moreover, improvements in numerical simulation results will allow a better understanding of some systematics affecting the cluster mass measurements, such as projection effects and non-thermal pressure support, as well as the computation of accurate selection functions for specific surveys, as will be the case of the Euclid mission.

At the same time, similar progresses are expected for several other cosmological probes, thanks to both larger sets of data and improvements in theoretical modelling, while innovative instruments, such as the Square Kilometre Array – the radio interferometer for the 21cm line detection currently in progress – will open new observational windows on the Universe. All this bodes for a less “dark” future for precision cosmology.

Bibliography

K. N. Abazajian, M. A. Acero, S. K. Agarwalla, and et al. Light Sterile Neutrinos: A White Paper. *ArXiv e-prints*, April 2012.

J. N. Abdurashitov, V. N. Gavrin, S. V. Girin, , and et al. Measurement of the response of a Ga solar neutrino experiment to neutrinos from a Ar37 source. *Physical Review C*, 73(4):045805, April 2006. doi: 10.1103/PhysRevC.73.045805.

G. O. Abell. The Distribution of Rich Clusters of Galaxies. *Astrophysical Journal Supplement*, 3:211–+, May 1958. doi: 10.1086/190036.

G. O. Abell, H. G. Corwin, Jr., and R. P. Olowin. A catalog of rich clusters of galaxies. *Astrophysical Journal Supplement*, 70:1–138, May 1989. doi: 10.1086/191333.

C. Adami, A. Mazure, M. Pierre, P. G. Sprimont, C. Libbrecht, F. Pacaud, N. Clerc, T. Sadibekova, J. Surdej, B. Altieri, P. A. Duc, G. Galaz, A. Gueguen, L. Guennou, G. Hertling, O. Ilbert, J. P. Le Fèvre, H. Quintana, I. Valtchanov, J. P. Willis, M. Akiyama, H. Aussel, L. Chiappetti, A. Detal, B. Garilli, V. Lebrun, O. Lefèvre, D. Maccagni, J. B. Melin, T. J. Ponman, D. Ricci, and L. Tresse. The XMM-LSS survey: optical assessment and properties of different X-ray selected cluster classes. *Astronomy and Astrophysics*, 526:A18, February 2011. doi: 10.1051/0004-6361/201015182.

P. Adamson and et al. Active to Sterile Neutrino Mixing Limits from Neutral-Current Interactions in MINOS. *Physical Review Letters*, 107(1):011802, July 2011. doi: 10.1103/PhysRevLett.107.011802.

G. E. Addison, G. Hinshaw, and M. Halpern. Cosmological constraints from baryon acoustic oscillations and clustering of large-scale structure. *ArXiv e-prints*, April 2013.

N. Aghanim, S. Majumdar, and J. Silk. Secondary anisotropies of the CMB. *Reports on Progress in Physics*, 71(6):066902, June 2008. doi: 10.1088/0034-4885/71/6/066902.

A. Aguilar-Arevalo and et al. Evidence for neutrino oscillations from the observation of anti-neutrino(electron) appearance in a anti-neutrino(muon) beam. *Phys.Rev.*, D64:112007, 2001. doi: 10.1103/PhysRevD.64.112007.

A. A. Aguilar-Arevalo, et al., and The MiniBooNE Collaboration. Measurement of the neutrino neutral-current elastic differential cross section on mineral oil at $E_\nu \sim 1$GeV. *Physical Review D*, 82(9):092005, November 2010. doi: 10.1103/PhysRevD.82.092005.

C. Alcock and B. Paczynski. An evolution free test for non-zero cosmological constant. *Nature*, 281:358, October 1979. doi: 10.1038/281358a0.

S. W. Allen, A. E. Evrard, and A. B. Mantz. Cosmological Parameters from Observations of Galaxy Clusters. *Annual Review of Astronomy & Astrophysics*, 49:409–470, September 2011. doi: 10.1146/annurev-astro-081710-102514.

R. A. Alpher and R. C. Herman. On the Relative Abundance of the Elements. *Physical Review*, 74:1737–1742, December 1948. doi: 10.1103/PhysRev.74.1737.

L. Anderson, E. Aubourg, S. Bailey, D. Bizyaev, M. Blanton, A. S. Bolton, J. Brinkmann, J. R. Brownstein, A. Burden, A. J. Cuesta, L. A. N. da Costa, K. S. Dawson, R. de Putter, D. J. Eisenstein, J. E. Gunn, H. Guo, J.-C. Hamilton, P. Harding, S. Ho, K. Honscheid, E. Kazin, D. Kirkby, J.-P. Kneib, A. Labatie, C. Loomis, R. H. Lupton, E. Malanushenko, V. Malanushenko, R. Mandelbaum, M. Manera, C. Maraston, C. K. McBride, K. T. Mehta, O. Mena, F. Montesano, D. Muna, R. C. Nichol, S. E. Nuza, M. D. Olmstead, D. Oravetz, N. Padmanabhan, N. Palanque-Delabrouille, K. Pan, J. Parejko, I. Pâris, W. J. Percival, P. Petitjean, F. Prada, B. Reid, N. A. Roe, A. J. Ross, N. P. Ross, L. Samushia, A. G. Sánchez, D. J. Schlegel, D. P. Schneider, C. G. Scóccola, H.-J. Seo, E. S. Sheldon, A. Simmons, R. A. Skibba, M. A. Strauss, M. E. C. Swanson, D. Thomas, J. L. Tinker, R. Tojeiro, M. V. Magaña, L. Verde, C. Wagner, D. A. Wake, B. A. Weaver, D. H. Weinberg, M. White, X. Xu, C. Yèche, I. Zehavi, and G.-B. Zhao. The clustering of galaxies in the SDSS-III Baryon Oscillation Spectroscopic Survey: baryon acoustic oscillations in the Data Release 9 spectroscopic galaxy sample. *Montly Notices of the Royal Astronomical Society*, 427:3435–3467, December 2012. doi: 10.1111/j.1365-2966.2012.22066.x.

L. Anderson, É. Aubourg, S. Bailey, and et al. The clustering of galaxies in the SDSS-III Baryon Oscillation Spectroscopic Survey: baryon acoustic oscillations in the Data Releases 10 and 11 Galaxy samples. *Montly Notices of the Royal Astronomical Society*, 441:24–62, June 2014. doi: 10.1093/mnras/stu523.

S. Andreon and M. A. Hurn. The scaling relation between richness and mass of galaxy clusters: a Bayesian approach. *Montly Notices of the Royal Astronomical Society*, 404:1922–1937, June 2010. doi: 10.1111/j.1365-2966.2010.16406.x.

A. W. Appel. An Efficient Program for Many-Body Simulation. *SIAM Journal on Scientific and Statistical Computing, vol. 6, no. 1, January 1985, p. 85-103.*, 6:85–103, January 1985.

M. Archidiacono, N. Fornengo, C. Giunti, S. Hannestad, and A. Melchiorri. Sterile neutrinos: Cosmology versus short-baseline experiments. *Physical Review D*, 87 (12):125034, June 2013. doi: 10.1103/PhysRevD.87.125034.

M. Archidiacono, N. Fornengo, S. Gariazzo, C. Giunti, S. Hannestad, and M. Laveder. Light sterile neutrinos after BICEP-2. *Journal of Cosmology and Astroparticle Physics*, 6:031, June 2014. doi: 10.1088/1475-7516/2014/06/031.

M. Arnaud, E. Pointecouteau, and G. W. Pratt. Calibration of the galaxy cluster M{500}-Y{X} relation with XMM-Newton. *Astronomy and Astrophysics*, 474:L37–L40, November 2007. doi: 10.1051/0004-6361:20078541.

M. Arnaud, G. W. Pratt, R. Piffaretti, H. Böhringer, J. H. Croston, and E. Pointecouteau. The universal galaxy cluster pressure profile from a representative sample of nearby systems (REXCESS) and the Y_{SZ} - M_{500} relation. *Astronomy and Astrophysics*, 517:A92, July 2010. doi: 10.1051/0004-6361/200913416.

B. Audren, J. Lesgourgues, S. Bird, M. G. Haehnelt, and M. Viel. Neutrino masses and cosmological parameters from a Euclid-like survey: Markov Chain Monte Carlo forecasts including theoretical errors. *ArXiv e-prints*, October 2012.

D. J. Bacon, A. R. Refregier, and R. S. Ellis. Detection of weak gravitational lensing by large-scale structure. *Montly Notices of the Royal Astronomical Society*, 318:625–640, October 2000. doi: 10.1046/j.1365-8711.2000.03851.x.

D. J. Bacon, R. J. Massey, A. R. Refregier, and R. S. Ellis. Joint cosmic shear measurements with the Keck and William Herschel Telescopes. *Montly Notices of the Royal*

Astronomical Society, 344:673–685, September 2003. doi: 10.1046/j.1365-8711.2003.06877.x.

D. J. Bacon, A. N. Taylor, M. L. Brown, M. E. Gray, C. Wolf, K. Meisenheimer, S. Dye, L. Wisotzki, A. Borch, and M. Kleinheinrich. Evolution of the dark matter distribution with three-dimensional weak lensing. *Montly Notices of the Royal Astronomical Society*, 363:723–733, November 2005. doi: 10.1111/j.1365-2966.2005.09420.x.

N. A. Bahcall, T. A. McKay, J. Annis, R. S. J. Kim, F. Dong, S. Hansen, T. Goto, J. E. Gunn, C. Miller, R. C. Nichol, M. Postman, D. Schneider, J. Schroeder, W. Voges, J. Brinkmann, and M. Fukugita. A Merged Catalog of Clusters of Galaxies from Early Sloan Digital Sky Survey Data. *Astrophysical Journal Supplement*, 148:243–274, October 2003. doi: 10.1086/377167.

A. Balaguera-Antolínez, A. G. Sánchez, H. Böhringer, C. Collins, L. Guzzo, and S. Phleps. The REFLEX II galaxy cluster survey: power spectrum analysis. *Montly Notices of the Royal Astronomical Society*, 413:386–400, May 2011. doi: 10.1111/j.1365-2966.2010.18143.x.

W. A. Barkhouse, P. J. Green, A. Vikhlinin, D.-W. Kim, D. Perley, R. Cameron, J. Silverman, A. Mossman, R. Burenin, B. T. Jannuzi, M. Kim, M. G. Smith, R. C. Smith, H. Tananbaum, and B. J. Wilkes. ChaMP Serendipitous Galaxy Cluster Survey. *Astrophysical Journal*, 645:955–976, July 2006. doi: 10.1086/504457.

J. Barnes and P. Hut. A hierarchical O(N log N) force-calculation algorithm. *Nature*, 324:446–449, December 1986. doi: 10.1038/324446a0.

M. Bartelmann and P. Schneider. Weak gravitational lensing. *Physics Reports*, 340:291–472, January 2001. doi: 10.1016/S0370-1573(00)00082-X.

B. Bassett and R. Hlozek. *Baryon acoustic oscillations*, page 246. 2010.

R. A. Battye and A. Moss. Evidence for massive neutrinos from CMB and lensing observations. *ArXiv e-prints*, August 2013.

M. R. Becker and A. V. Kravtsov. On the Accuracy of Weak-lensing Cluster Mass Reconstructions. *Astrophysical Journal*, 740:25–+, October 2011. doi: 10.1088/0004-637X/740/1/25.

L. Benatov, K. Rines, P. Natarajan, A. Kravtsov, and D. Nagai. Galaxy orbits and the intracluster gas temperature in clusters. *Montly Notices of the Royal Astronomical Society*, 370:427–434, July 2006. doi: 10.1111/j.1365-2966.2006.10490.x.

C. L. Bennett, M. Halpern, G. Hinshaw, N. Jarosik, A. Kogut, M. Limon, S. S. Meyer, L. Page, D. N. Spergel, G. S. Tucker, E. Wollack, E. L. Wright, C. Barnes, M. R. Greason, R. S. Hill, E. Komatsu, M. R. Nolta, N. Odegard, H. V. Peiris, L. Verde, and J. L. Weiland. First-Year Wilkinson Microwave Anisotropy Probe (WMAP) Observations: Preliminary Maps and Basic Results. *Astrophysical Journal Supplement*, 148:1–27, September 2003. doi: 10.1086/377253.

C. L. Bennett, D. Larson, J. L. Weiland, N. Jarosik, G. Hinshaw, N. Odegard, K. M. Smith, R. S. Hill, B. Gold, M. Halpern, E. Komatsu, M. R. Nolta, L. Page, D. N. Spergel, E. Wollack, J. Dunkley, A. Kogut, M. Limon, S. S. Meyer, G. S. Tucker, and E. L. Wright. Nine-year Wilkinson Microwave Anisotropy Probe (WMAP) Observations: Final Maps and Results. *Astrophysical Journal Supplement*, 208:20, October 2013. doi: 10.1088/0067-0049/208/2/20.

B. A. Benson, T. de Haan, J. P. Dudley, C. L. Reichardt, K. A. Aird, K. Andersson, R. Armstrong, M. L. N. Ashby, M. Bautz, M. Bayliss, G. Bazin, L. E. Bleem, M. Brodwin, J. E. Carlstrom, C. L. Chang, H. M. Cho, A. Clocchiatti, T. M. Crawford, A. T. Crites, S. Desai, M. A. Dobbs, R. J. Foley, W. R. Forman, E. M. George, M. D. Gladders, A. H. Gonzalez, N. W. Halverson, N. Harrington, F. W. High, G. P. Holder, W. L. Holzapfel, S. Hoover, J. D. Hrubes, C. Jones, M. Joy, R. Keisler, L. Knox, A. T. Lee, E. M. Leitch, J. Liu, M. Lueker, D. Luong-Van, A. Mantz, D. P. Marrone, M. McDonald, J. J. McMahon, J. Mehl, S. S. Meyer, L. Mocanu, J. J. Mohr, T. E. Montroy, S. S. Murray, T. Natoli, S. Padin, T. Plagge, C. Pryke, A. Rest, J. Ruel, J. E. Ruhl, B. R. Saliwanchik, A. Saro, J. T. Sayre, K. K. Schaffer, L. Shaw, E. Shirokoff, J. Song, H. G. Spieler, B. Stalder, Z. Staniszewski, A. A. Stark, K. Story, C. W. Stubbs, R. Suhada, A. van Engelen, K. Vanderlinde, J. D. Vieira, A. Vikhlinin, R. Williamson, O. Zahn, and A. Zenteno. Cosmological Constraints from Sunyaev-Zel'dovich-selected Clusters with X-Ray Observations in the First 178 $\deg^2$ of the South Pole Telescope Survey. *Astrophysical Journal*, 763: 147, February 2013. doi: 10.1088/0004-637X/763/2/147.

F. Beutler, C. Blake, M. Colless, D. H. Jones, L. Staveley-Smith, L. Campbell, Q. Parker, W. Saunders, and F. Watson. The 6dF Galaxy Survey: baryon acoustic oscillations and the local Hubble constant. *Montly Notices of the Royal Astronomical Society*, 416:3017–3032, October 2011. doi: 10.1111/j.1365-2966.2011.19250.x.

F. Beutler, C. Blake, M. Colless, D. H. Jones, L. Staveley-Smith, G. B. Poole, L. Campbell, Q. Parker, W. Saunders, and F. Watson. The 6dF Galaxy Survey: z 0 measurements of the growth rate and σ_8. *Montly Notices of the Royal Astronomical Society*, 423:3430–3444, July 2012. doi: 10.1111/j.1365-2966.2012.21136.x.

F. Beutler, S. Saito, H.-J. Seo, J. Brinkmann, K. S. Dawson, D. J. Eisenstein, A. Font-Ribera, S. Ho, C. K. McBride, F. Montesano, W. J. Percival, A. J. Ross, N. P. Ross, L. Samushia, D. J. Schlegel, A. G. Sánchez, J. L. Tinker, and B. A. Weaver. The clustering of galaxies in the SDSS-III Baryon Oscillation Spectroscopic Survey: Testing gravity with redshift-space distortions using the power spectrum multipoles. *ArXiv e-prints*, December 2013.

F. Beutler, S. Saito, J. R. Brownstein, and et al. The clustering of galaxies in the SDSS-III Baryon Oscillation Spectroscopic Survey: Signs of neutrino mass in current cosmological datasets. *ArXiv e-prints*, March 2014.

BICEP1 Collaboration. Degree-Scale CMB Polarization Measurements from Three Years of BICEP1 Data. *ArXiv e-prints*, October 2013.

Bicep2 Collaboration. Detection of B-Mode Polarization at Degree Angular Scales by BICEP2. *Physical Review Letters*, 112(24):241101, June 2014. doi: 10.1103/PhysRevLett.112.241101.

J. Binney and S. Tremaine. *Galactic dynamics*. 1987.

S. Bird, M. Viel, and M. G. Haehnelt. Massive neutrinos and the non-linear matter power spectrum. *Montly Notices of the Royal Astronomical Society*, 420:2551–2561, March 2012. doi: 10.1111/j.1365-2966.2011.20222.x.

C. Bischoff, L. Hyatt, J. J. McMahon, G. W. Nixon, D. Samtleben, K. M. Smith, K. Vanderlinde, D. Barkats, P. Farese, T. Gaier, J. O. Gundersen, M. M. Hedman, S. T. Staggs, B. Winstein, and CAPMAP Collaboration. New Measurements of Fine-Scale CMB Polarization Power Spectra from CAPMAP at Both 40 and 90 GHz. *Astrophysical Journal*, 684:771–789, September 2008. doi: 10.1086/590487.

A. Biviano and M. Girardi. The Mass Profile of Galaxy Clusters out to ˜2r_{200}. *Astrophysical Journal*, 585:205–214, March 2003. doi: 10.1086/345893.

C. Blake, S. Brough, M. Colless, C. Contreras, W. Couch, S. Croom, T. Davis, M. J. Drinkwater, K. Forster, D. Gilbank, M. Gladders, K. Glazebrook, B. Jelliffe, R. J. Jurek, I.-H. Li, B. Madore, D. C. Martin, K. Pimbblet, G. B. Poole, M. Pracy,

R. Sharp, E. Wisnioski, D. Woods, T. K. Wyder, and H. K. C. Yee. The WiggleZ Dark Energy Survey: the growth rate of cosmic structure since redshift z=0.9. *Montly Notices of the Royal Astronomical Society*, 415:2876–2891, August 2011. doi: 10.1111/j.1365-2966.2011.18903.x.

L. E. Bleem, B. Stalder, T. de Haan, K. A. Aird, S. W. Allen, D. E. Applegate, M. L. N. Ashby, M. Bautz, M. Bayliss, B. A. Benson, S. Bocquet, M. Brodwin, J. E. Carlstrom, C. L. Chang, I. Chiu, H. M. Cho, A. Clocchiatti, T. M. Crawford, A. T. Crites, S. Desai, J. P. Dietrich, M. A. Dobbs, R. J. Foley, W. R. Forman, E. M. George, M. D. Gladders, A. H. Gonzalez, N. W. Halverson, C. Hennig, H. Hoekstra, G. P. Holder, W. L. Holzapfel, J. D. Hrubes, C. Jones, R. Keisler, L. Knox, A. T. Lee, E. M. Leitch, J. Liu, M. Lueker, D. Luong-Van, A. Mantz, D. P. Marrone, M. McDonald, J. J. McMahon, S. S. Meyer, L. Mocanu, J. J. Mohr, S. S. Murray, S. Padin, C. Pryke, C. L. Reichardt, A. Rest, J. Ruel, J. E. Ruhl, B. R. Saliwanchik, A. Saro, J. T. Sayre, K. K. Schaffer, T. Schrabback, E. Shirokoff, J. Song, H. G. Spieler, S. A. Stanford, Z. Staniszewski, A. A. Stark, K. T. Story, C. W. Stubbs, K. Vanderlinde, J. D. Vieira, A. Vikhlinin, R. Williamson, O. Zahn, and A. Zenteno. Galaxy Clusters Discovered via the Sunyaev-Zel'dovich Effect in the 2500-square-degree SPT-SZ survey. *ArXiv e-prints*, September 2014.

H. Böhringer, P. Schuecker, L. Guzzo, C. A. Collins, W. Voges, R. G. Cruddace, A. Ortiz-Gil, G. Chincarini, S. De Grandi, A. C. Edge, H. T. MacGillivray, D. M. Neumann, S. Schindler, and P. Shaver. The ROSAT-ESO Flux Limited X-ray (REFLEX) Galaxy cluster survey. V. The cluster catalogue. *Astronomy and Astrophysics*, 425:367–383, October 2004. doi: 10.1051/0004-6361:20034484.

J. R. Bond, S. Cole, G. Efstathiou, and N. Kaiser. Excursion set mass functions for hierarchical Gaussian fluctuations. *Astrophysical Journal*, 379:440–460, October 1991. doi: 10.1086/170520.

J. R. Bond, G. Efstathiou, and M. Tegmark. Forecasting cosmic parameter errors from microwave background anisotropy experiments. *Montly Notices of the Royal Astronomical Society*, 291:L33–L41, November 1997.

A. Borde, N. Palanque-Delabrouille, G. Rossi, M. Viel, J. S. Bolton, C. Yèche, J.-M. LeGoff, and J. Rich. New approach for precise computation of Lyman-α forest power spectrum with hydrodynamical simulations. *Journal of Cosmology and Astroparticle Physics*, 7:005, July 2014a. doi: 10.1088/1475-7516/2014/07/005.

A. Borde, N. Palanque-Delabrouille, G. Rossi, M. Viel, J. S. Bolton, C. Yèche, J.-M. LeGoff, and J. Rich. New approach for precise computation of Lyman-α forest power spectrum with hydrodynamical simulations. *Journal of Cosmology and Astroparticle Physics*, 7:005, July 2014b. doi: 10.1088/1475-7516/2014/07/005.

S. Borgani. Cosmology with clusters of galaxies. *ArXiv Astrophysics e-prints*, May 2006.

S. Borgani, P. Rosati, P. Tozzi, S. A. Stanford, P. R. Eisenhardt, C. Lidman, B. Holden, R. Della Ceca, C. Norman, and G. Squires. Measuring Ω_m with the ROSAT Deep Cluster Survey. *Astrophysical Journal*, 561:13–21, November 2001. doi: 10.1086/323214.

M. Bradač, P. Schneider, M. Lombardi, and T. Erben. Strong and weak lensing united. *Astronomy and Astrophysics*, 437:39–48, July 2005. doi: 10.1051/0004-6361:20042233.

J. Brandbyge and S. Hannestad. Grid based linear neutrino perturbations in cosmological N-body simulations. *Journal of Cosmology and Astroparticle Physics*, 5:002, May 2009. doi: 10.1088/1475-7516/2009/05/002.

J. Brandbyge, S. Hannestad, T. Haugbølle, and Y. Y. Y. Wong. Neutrinos in non-linear structure formation – the effect on halo properties. *Journal of Cosmology and Astroparticle Physics*, 9:14–+, September 2010a. doi: 10.1088/1475-7516/2010/09/014.

J. Brandbyge, S. Hannestad, T. Haugbølle, and Y. Y. Y. Wong. Neutrinos in non-linear structure formation - the effect on halo properties. *Journal of Cosmology and Astroparticle Physics*, 9:014, September 2010b. doi: 10.1088/1475-7516/2010/09/014.

S. Bridle and L. King. Dark energy constraints from cosmic shear power spectra: impact of intrinsic alignments on photometric redshift requirements. *New Journal of Physics*, 9:444, December 2007. doi: 10.1088/1367-2630/9/12/444.

T. Broadhurst, N. Benítez, D. Coe, K. Sharon, K. Zekser, R. White, H. Ford, R. Bouwens, J. Blakeslee, M. Clampin, N. Cross, M. Franx, B. Frye, G. Hartig, G. Illingworth, L. Infante, F. Menanteau, G. Meurer, M. Postman, D. R. Ardila, F. Bartko, R. A. Brown, C. J. Burrows, E. S. Cheng, P. D. Feldman, D. A. Golimowski, T. Goto, C. Gronwall, D. Herranz, B. Holden, N. Homeier, J. E.

Krist, M. P. Lesser, A. R. Martel, G. K. Miley, P. Rosati, M. Sirianni, W. B. Sparks, S. Steindling, H. D. Tran, Z. I. Tsvetanov, and W. Zheng. Strong-Lensing Analysis of A1689 from Deep Advanced Camera Images. *Astrophysical Journal*, 621:53–88, March 2005. doi: 10.1086/426494.

M. L. Brown, P. Ade, J. Bock, M. Bowden, G. Cahill, P. G. Castro, S. Church, T. Culverhouse, R. B. Friedman, K. Ganga, W. K. Gear, S. Gupta, J. Hinderks, J. Kovac, A. E. Lange, E. Leitch, S. J. Melhuish, Y. Memari, J. A. Murphy, A. Orlando, C. O'Sullivan, L. Piccirillo, C. Pryke, N. Rajguru, B. Rusholme, R. Schwarz, A. N. Taylor, K. L. Thompson, A. H. Turner, E. Y. S. Wu, M. Zemcov, and QUa D Collaboration. Improved Measurements of the Temperature and Polarization of the Cosmic Microwave Background from QUaD. *Astrophysical Journal*, 705:978–999, November 2009. doi: 10.1088/0004-637X/705/1/978.

R. A. Burenin. Possible indication for non-zero neutrino mass and additional neutrino species from cosmological observations. *Astronomy Letters*, 39:357–366, June 2013. doi: 10.1134/S1063773713060030.

R. A. Burenin and A. A. Vikhlinin. Cosmological parameters constraints from galaxy cluster mass function measurements in combination with other cosmological data. *Astronomy Letters*, 38:347–363, June 2012. doi: 10.1134/S1063773712060011.

R. A. Burenin, A. Vikhlinin, A. Hornstrup, H. Ebeling, H. Quintana, and A. Mescheryakov. The 400 Square Degree ROSAT PSPC Galaxy Cluster Survey: Catalog and Statistical Calibration. *Astrophysical Journal Supplement*, 172:561–582, October 2007. doi: 10.1086/519457.

N. G. Busca, T. Delubac, J. Rich, S. Bailey, A. Font-Ribera, D. Kirkby, J.-M. Le Goff, M. M. Pieri, A. Slosar, É. Aubourg, J. E. Bautista, D. Bizyaev, M. Blomqvist, A. S. Bolton, J. Bovy, H. Brewington, A. Borde, J. Brinkmann, B. Carithers, R. A. C. Croft, K. S. Dawson, G. Ebelke, D. J. Eisenstein, J.-C. Hamilton, S. Ho, D. W. Hogg, K. Honscheid, K.-G. Lee, B. Lundgren, E. Malanushenko, V. Malanushenko, D. Margala, C. Maraston, K. Mehta, J. Miralda-Escudé, A. D. Myers, R. C. Nichol, P. Noterdaeme, M. D. Olmstead, D. Oravetz, N. Palanque-Delabrouille, K. Pan, I. Pâris, W. J. Percival, P. Petitjean, N. A. Roe, E. Rollinde, N. P. Ross, G. Rossi, D. J. Schlegel, D. P. Schneider, A. Shelden, E. S. Sheldon, A. Simmons, S. Snedden, J. L. Tinker, M. Viel, B. A. Weaver, D. H. Weinberg, M. White, C. Yèche, and D. G. York. Baryon acoustic oscillations in the Lyα

forest of BOSS quasars. *Astronomy and Astrophysics*, 552:A96, April 2013. doi: 10.1051/0004-6361/201220724.

E. Calabrese, D. Huterer, E. V. Linder, A. Melchiorri, and L. Pagano. Limits on dark radiation, early dark energy, and relativistic degrees of freedom. *Physical Review D*, 83(12):123504, June 2011. doi: 10.1103/PhysRevD.83.123504.

C. Carbone, L. Verde, Y. Wang, and A. Cimatti. Neutrino constraints from future nearly all-sky spectroscopic galaxy surveys. *Journal of Cosmology and Astroparticle Physics*, 3:030, March 2011. doi: 10.1088/1475-7516/2011/03/030.

W. Cash. Parameter estimation in astronomy through application of the likelihood ratio. *Astrophysical Journal*, 228:939–947, March 1979. doi: 10.1086/156922.

E. Castorina, E. Sefusatti, R. K. Sheth, F. Villaescusa-Navarro, and M. Viel. Cosmology with massive neutrinos II: on the universality of the halo mass function and bias. *Journal of Cosmology and Astroparticle Physics*, 2:049, February 2014. doi: 10.1088/1475-7516/2014/02/049.

C.-H. Chuang, F. Prada, F. Beutler, D. J. Eisenstein, S. Escoffier, S. Ho, J.-P. Kneib, M. Manera, S. E. Nuza, D. J. Schlegel, D. P. Schneider, B. A. Weaver, J. R. Brownstein, K. S. Dawson, C. Maraston, and D. Thomas. The clustering of galaxies in the SDSS-III Baryon Oscillation Spectroscopic Survey: single-probe measurements from CMASS and LOWZ anisotropic galaxy clustering. *ArXiv e-prints*, December 2013.

J. D. Cohn and M. White. Dark matter halo abundances, clustering and assembly histories at high redshift. *Montly Notices of the Royal Astronomical Society*, 385: 2025–2033, April 2008. doi: 10.1111/j.1365-2966.2008.12972.x.

S. Cole, W. J. Percival, J. A. Peacock, P. Norberg, C. M. Baugh, C. S. Frenk, I. Baldry, J. Bland-Hawthorn, T. Bridges, R. Cannon, M. Colless, C. Collins, W. Couch, N. J. G. Cross, G. Dalton, V. R. Eke, R. De Propris, S. P. Driver, G. Efstathiou, R. S. Ellis, K. Glazebrook, C. Jackson, A. Jenkins, O. Lahav, I. Lewis, S. Lumsden, S. Maddox, D. Madgwick, B. A. Peterson, W. Sutherland, and K. Taylor. The 2dF Galaxy Redshift Survey: power-spectrum analysis of the final data set and cosmological implications. *Montly Notices of the Royal Astronomical Society*, 362: 505–534, September 2005. doi: 10.1111/j.1365-2966.2005.09318.x.

R. J. Cooke, M. Pettini, R. A. Jorgenson, M. T. Murphy, and C. C. Steidel. Precision Measures of the Primordial Abundance of Deuterium. *Astrophysical Journal*, 781: 31, January 2014. doi: 10.1088/0004-637X/781/1/31.

M. Costanzi, F. Villaescusa-Navarro, M. Viel, J.-Q. Xia, S. Borgani, E. Castorina, and E. Sefusatti. Cosmology with massive neutrinos III: the halo mass function and an application to galaxy clusters. *Journal of Cosmology and Astroparticle Physics*, 12:012, December 2013. doi: 10.1088/1475-7516/2013/12/012.

M. Costanzi, B. Sartoris, M. Viel, and S. Borgani. Neutrino constraints: what large-scale structure and CMB data are telling us? *Journal of Cosmology and Astroparticle Physics*, 10:081, October 2014. doi: 10.1088/1475-7516/2014/10/081.

M. Costanzi Alunno Cerbolini, B. Sartoris, J.-Q. Xia, A. Biviano, S. Borgani, and M. Viel. Constraining neutrino properties with a Euclid-like galaxy cluster survey. *Journal of Cosmology and Astroparticle Physics*, 6:020, June 2013. doi: 10.1088/1475-7516/2013/06/020.

M. Crocce, P. Fosalba, F. J. Castander, and E. Gaztañaga. Simulating the Universe with MICE: the abundance of massive clusters. *Montly Notices of the Royal Astronomical Society*, 403:1353–1367, April 2010. doi: 10.1111/j.1365-2966.2009.16194.x.

R. A. C. Croft, D. H. Weinberg, M. Pettini, L. Hernquist, and N. Katz. The Power Spectrum of Mass Fluctuations Measured from the Lyα Forest at Redshift z = 2.5. *Astrophysical Journal*, 520:1–23, July 1999. doi: 10.1086/307438.

R. A. C. Croft, D. H. Weinberg, M. Bolte, S. Burles, L. Hernquist, N. Katz, D. Kirkman, and D. Tytler. Toward a Precise Measurement of Matter Clustering: Lyα Forest Data at Redshifts 2-4. *Astrophysical Journal*, 581:20–52, December 2002. doi: 10.1086/344099.

W. Cui, S. Borgani, and G. Murante. The effect of active galactic nuclei feedback on the halo mass function. *Montly Notices of the Royal Astronomical Society*, 441: 1769–1782, June 2014. doi: 10.1093/mnras/stu673.

C. Cunha. Cross-calibration of cluster mass observables. *Physical Review D*, 79(6): 063009, March 2009. doi: 10.1103/PhysRevD.79.063009.

S. J. Cusworth, S. T. Kay, R. A. Battye, and P. A. Thomas. Impact of baryons on the cluster mass function and cosmological parameter determination. *Montly Notices*

of the Royal Astronomical Society, 439:2485–2493, April 2014. doi: 10.1093/mnras/stu105.

N. Dalal, O. Doré, D. Huterer, and A. Shirokov. Imprints of primordial non-Gaussianities on large-scale structure: Scale-dependent bias and abundance of virialized objects. *Physical Review D*, 77(12):123514, June 2008. doi: 10.1103/PhysRevD.77.123514.

S. Das, T. Louis, M. R. Nolta, G. E. Addison, E. S. Battistelli, J. R. Bond, E. Calabrese, D. Crichton, M. J. Devlin, S. Dicker, J. Dunkley, R. Dünner, J. W. Fowler, M. Gralla, A. Hajian, M. Halpern, M. Hasselfield, M. Hilton, A. D. Hincks, R. Hlozek, K. M. Huffenberger, J. P. Hughes, K. D. Irwin, A. Kosowsky, R. H. Lupton, T. A. Marriage, D. Marsden, F. Menanteau, K. Moodley, M. D. Niemack, L. A. Page, B. Partridge, E. D. Reese, B. L. Schmitt, N. Sehgal, B. D. Sherwin, J. L. Sievers, D. N. Spergel, S. T. Staggs, D. S. Swetz, E. R. Switzer, R. Thornton, H. Trac, and E. Wollack. The Atacama Cosmology Telescope: temperature and gravitational lensing power spectrum measurements from three seasons of data. *Journal of Cosmology and Astroparticle Physics*, 4:014, April 2014. doi: 10.1088/1475-7516/2014/04/014.

M. Davis and P. J. E. Peebles. A survey of galaxy redshifts. V - The two-point position and velocity correlations. *Astrophysical Journal*, 267:465–482, April 1983. doi: 10.1086/160884.

W. Dehnen. A Very Fast and Momentum-conserving Tree Code. *Astrophysical Journal Letters*, 536:L39–L42, June 2000. doi: 10.1086/312724.

T. Delubac, J. E. Bautista, N. G. Busca, J. Rich, D. Kirkby, S. Bailey, A. Font-Ribera, A. Slosar, K.-G. Lee, M. M. Pieri, J.-C. Hamilton, É. Aubourg, M. Blomqvist, J. Bovy, J. Brinkmann, W. Carithers, K. S. Dawson, D. J. Eisenstein, J.-P. Kneib, J.-M. Le Goff, D. Margala, J. Miralda-Escudé, A. D. Myers, R. C. Nichol, P. Noterdaeme, R. O'Connell, M. D. Olmstead, N. Palanque-Delabrouille, I. Pâris, P. Petitjean, N. P. Ross, G. Rossi, D. J. Schlegel, D. P. Schneider, D. H. Weinberg, C. Yèche, and D. G. York. Baryon Acoustic Oscillations in the Ly{\alpha} forest of BOSS DR11 quasars. *ArXiv e-prints*, April 2014.

A. Diaferio and M. J. Geller. Infall Regions of Galaxy Clusters. *Astrophysical Journal*, 481:633, May 1997. doi: 10.1086/304075.

A. Diaferio, M. J. Geller, and K. J. Rines. Caustic and Weak-Lensing Estimators of Galaxy Cluster Masses. *Astrophysical Journal Letters*, 628:L97–L100, August 2005. doi: 10.1086/432880.

J. P. Dietrich, T. Erben, G. Lamer, P. Schneider, A. Schwope, J. Hartlap, and M. Maturi. BLOX: the Bonn lensing, optical, and X-ray selected galaxy clusters. I. Cluster catalog construction. *Astronomy and Astrophysics*, 470:821–834, August 2007. doi: 10.1051/0004-6361:20077281.

S. Dodelson and L. M. Widrow. Sterile neutrinos as dark matter. *Physical Review Letters*, 72:17–20, January 1994. doi: 10.1103/PhysRevLett.72.17.

M. Donahue, G. M. Voit, A. Mahdavi, and et al. CLASH-X: A Comparison of Lensing and X-ray Techniques for Measuring the Mass Profiles of Galaxy Clusters. *ArXiv e-prints*, May 2014.

F. Dong, E. Pierpaoli, J. E. Gunn, and R. H. Wechsler. Optical Cluster Finding with an Adaptive Matched-Filter Technique: Algorithm and Comparison with Simulations. *Astrophysical Journal*, 676:868–879, April 2008. doi: 10.1086/522490.

F. Dydak et al. A search for ν_μ oscillations in the δm^2 range $0.3 - 90\,\mathrm{eV}^2$. *Phys. Lett.*, B134:281, 1984.

H. Ebeling, A. C. Edge, H. Bohringer, S. W. Allen, C. S. Crawford, A. C. Fabian, W. Voges, and J. P. Huchra. The ROSAT Brightest Cluster Sample - I. The compilation of the sample and the cluster log N-log S distribution. *Montly Notices of the Royal Astronomical Society*, 301:881–914, December 1998. doi: 10.1046/j.1365-8711.1998.01949.x.

H. Ebeling, A. C. Edge, A. Mantz, E. Barrett, J. P. Henry, C. J. Ma, and L. van Speybroeck. The X-ray brightest clusters of galaxies from the Massive Cluster Survey. *Montly Notices of the Royal Astronomical Society*, 407:83–93, September 2010. doi: 10.1111/j.1365-2966.2010.16920.x.

A. C. Edge, G. C. Stewart, A. C. Fabian, and K. A. Arnaud. An X-Ray Flux-Limited Sample of Clusters of Galaxies - Evidence for Evolution of the Luminosity Function. *Montly Notices of the Royal Astronomical Society*, 245:559, July 1990.

G. Efstathiou, N. Kaiser, W. Saunders, A. Lawrence, M. Rowan-Robinson, R. S. Ellis, and C. S. Frenk. Largescale Clustering of IRAS Galaxies. *Montly Notices of the Royal Astronomical Society*, 247:10P, November 1990.

P. R. M. Eisenhardt, M. Brodwin, A. H. Gonzalez, S. A. Stanford, D. Stern, P. Barmby, M. J. I. Brown, K. Dawson, A. Dey, M. Doi, A. Galametz, B. T. Jannuzi, C. S. Kochanek, J. Meyers, T. Morokuma, and L. A. Moustakas. Clusters of Galaxies in the First Half of the Universe from the IRAC Shallow Survey. *Astrophysical Journal*, 684:905–932, September 2008. doi: 10.1086/590105.

D. J. Eisenstein, I. Zehavi, D. W. Hogg, R. Scoccimarro, M. R. Blanton, R. C. Nichol, R. Scranton, H.-J. Seo, M. Tegmark, Z. Zheng, S. F. Anderson, J. Annis, N. Bahcall, J. Brinkmann, S. Burles, F. J. Castander, A. Connolly, I. Csabai, M. Doi, M. Fukugita, J. A. Frieman, K. Glazebrook, J. E. Gunn, J. S. Hendry, G. Hennessy, Z. Ivezić, S. Kent, G. R. Knapp, H. Lin, Y.-S. Loh, R. H. Lupton, B. Margon, T. A. McKay, A. Meiksin, J. A. Munn, A. Pope, M. W. Richmond, D. Schlegel, D. P. Schneider, K. Shimasaku, C. Stoughton, M. A. Strauss, M. SubbaRao, A. S. Szalay, I. Szapudi, D. L. Tucker, B. Yanny, and D. G. York. Detection of the Baryon Acoustic Peak in the Large-Scale Correlation Function of SDSS Luminous Red Galaxies. *Astrophysical Journal*, 633:560–574, November 2005. doi: 10.1086/466512.

D. J. Eisenstein, H.-J. Seo, E. Sirko, and D. N. Spergel. Improving Cosmological Distance Measurements by Reconstruction of the Baryon Acoustic Peak. *Astrophysical Journal*, 664:675–679, August 2007. doi: 10.1086/518712.

A. E. Evrard, T. J. MacFarland, H. M. P. Couchman, J. M. Colberg, N. Yoshida, S. D. M. White, A. Jenkins, C. S. Frenk, F. R. Pearce, J. A. Peacock, and P. A. Thomas. Galaxy Clusters in Hubble Volume Simulations: Cosmological Constraints from Sky Survey Populations. *Astrophysical Journal*, 573:7–36, July 2002. doi: 10.1086/340551.

D. Fabjan, S. Borgani, E. Rasia, A. Bonafede, K. Dolag, G. Murante, and L. Tornatore. X-ray mass proxies from hydrodynamic simulations of galaxy clusters - I. *Montly Notices of the Royal Astronomical Society*, 416:801–816, September 2011. doi: 10.1111/j.1365-2966.2011.18497.x.

W. Fang and Z. Haiman. Constraining dark energy by combining cluster counts and shear-shear correlations in a weak lensing survey. *Physical Review D*, 75(4): 043010, February 2007. doi: 10.1103/PhysRevD.75.043010.

S. Farrens, F. B. Abdalla, E. S. Cypriano, C. Sabiu, and C. Blake. Friends-of-friends groups and clusters in the 2SLAQ catalogue. *Montly Notices of the Royal Astronomical Society*, 417:1402–1416, October 2011. doi: 10.1111/j.1365-2966.2011.19356.x.

R. Fassbender. *Studying Cosmic Evolution with the XMM-Newton Distant Cluster Project: X-ray Luminous Galaxy Clusters at z¿1 and their Galaxy Populations*. PhD thesis, PhD Thesis, 2008, 2008.

S. M. Feeney, H. V. Peiris, and L. Verde. Is there evidence for additional neutrino species from cosmology? *Journal of Cosmology and Astroparticle Physics*, 4:036, April 2013. doi: 10.1088/1475-7516/2013/04/036.

H. A. Feldman, N. Kaiser, and J. A. Peacock. Power-spectrum analysis of three-dimensional redshift surveys. *Astrophysical Journal*, 426:23–37, May 1994. doi: 10.1086/174036.

A. Ferrara and S. Pandolfi. Reionization of the Intergalactic Medium. *ArXiv e-prints*, September 2014.

A. Finoguenov, M. G. Watson, M. Tanaka, C. Simpson, M. Cirasuolo, J. S. Dunlop, J. A. Peacock, D. Farrah, M. Akiyama, Y. Ueda, V. Smolčić, G. Stewart, S. Rawlings, C. van Breukelen, O. Almaini, L. Clewley, D. G. Bonfield, M. J. Jarvis, J. M. Barr, S. Foucaud, R. J. McLure, K. Sekiguchi, and E. Egami. X-ray groups and clusters of galaxies in the Subaru-XMM Deep Field. *Montly Notices of the Royal Astronomical Society*, 403:2063–2076, April 2010. doi: 10.1111/j.1365-2966.2010.16256.x.

G. L. Fogli, E. Lisi, A. Marrone, D. Montanino, A. Palazzo, and *et al.* Global analysis of neutrino masses, mixings, and phases: Entering the era of leptonic CP violation searches. *Physical Review D*, 86(1):013012, July 2012. doi: 10.1103/PhysRevD.86.013012.

A. Font-Ribera, D. Kirkby, N. Busca, J. Miralda-Escudé, N. P. Ross, A. Slosar, J. Rich, É. Aubourg, S. Bailey, V. Bhardwaj, J. Bautista, F. Beutler, D. Bizyaev, M. Blomqvist, H. Brewington, J. Brinkmann, J. R. Brownstein, B. Carithers, K. S. Dawson, T. Delubac, G. Ebelke, D. J. Eisenstein, J. Ge, K. Kinemuchi, K.-G. Lee, V. Malanushenko, E. Malanushenko, M. Marchante, D. Margala, D. Muna, A. D. Myers, P. Noterdaeme, D. Oravetz, N. Palanque-Delabrouille, I. Pâris, P. Petitjean, M. M. Pieri, G. Rossi, D. P. Schneider, A. Simmons, M. Viel, C. Yeche, and D. G. York. Quasar-Lyman α forest cross-correlation from BOSS DR11: Baryon Acoustic Oscillations. *Journal of Cosmology and Astroparticle Physics*, 5:027, May 2014. doi: 10.1088/1475-7516/2014/05/027.

D. V. Forero, M. Tórtola, and J. W. F. Valle. Global status of neutrino oscillation parameters after Neutrino-2012. *Physical Review D*, 86(7):073012, October 2012. doi: 10.1103/PhysRevD.86.073012.

L. Fu, E. Semboloni, H. Hoekstra, M. Kilbinger, L. van Waerbeke, I. Tereno, Y. Mellier, C. Heymans, J. Coupon, K. Benabed, J. Benjamin, E. Bertin, O. Doré, M. J. Hudson, O. Ilbert, R. Maoli, C. Marmo, H. J. McCracken, and B. Ménard. Very weak lensing in the CFHTLS wide: cosmology from cosmic shear in the linear regime. *Astronomy and Astrophysics*, 479:9–25, February 2008. doi: 10.1051/0004-6361:20078522.

G. Gamow. Expanding Universe and the Origin of Elements. *Physical Review*, 70: 572–573, October 1946. doi: 10.1103/PhysRev.70.572.2.

A. Gelman and D. B. Rubin. Inference from iterative simulation using multiple sequences. *Statistical Science*, 7(4):457–472, November 1992.

I. M. Gioia, J. P. Henry, T. Maccacaro, S. L. Morris, J. T. Stocke, and A. Wolter. The Extended Medium Sensitivity Survey distant cluster sample - X-ray cosmological evolution. *Astrophysical Journal Letters*, 356:L35–L38, June 1990. doi: 10.1086/185744.

C. Giunti, M. Laveder, Y. F. Li, Q. Y. Liu, and H. W. Long. Update of short-baseline electron neutrino and antineutrino disappearance. *Physical Review D*, 86(11):113014, December 2012. doi: 10.1103/PhysRevD.86.113014.

E. Giusarma, E. Di Valentino, M. Lattanzi, A. Melchiorri, and O. Mena. Relic Neutrinos, thermal axions and cosmology in early 2014. *ArXiv e-prints*, March 2014.

M. D. Gladders and H. K. C. Yee. A New Method For Galaxy Cluster Detection. I. The Algorithm. *The Astronomical Journal*, 120:2148–2162, October 2000. doi: 10.1086/301557.

M. D. Gladders and H. K. C. Yee. The Red-Sequence Cluster Survey. I. The Survey and Cluster Catalogs for Patches RCS 0926+37 and RCS 1327+29. *Astrophysical Journal Supplement*, 157:1–29, March 2005. doi: 10.1086/427327.

M. Grossi, K. Dolag, E. Branchini, S. Matarrese, and L. Moscardini. Evolution of massive haloes in non-Gaussian scenarios. *Montly Notices of the Royal Astronomical Society*, 382:1261–1267, December 2007. doi: 10.1111/j.1365-2966.2007.12458.x.

L. Guzzo, M. Pierleoni, B. Meneux, E. Branchini, O. Le Fèvre, C. Marinoni, B. Garilli, J. Blaizot, G. De Lucia, A. Pollo, H. J. McCracken, D. Bottini, V. Le Brun, D. Maccagni, J. P. Picat, R. Scaramella, M. Scodeggio, L. Tresse, G. Vettolani, A. Zanichelli, C. Adami, S. Arnouts, S. Bardelli, M. Bolzonella, A. Bongiorno, A. Cappi, S. Charlot, P. Ciliegi, T. Contini, O. Cucciati, S. de la Torre, K. Dolag, S. Foucaud, P. Franzetti, I. Gavignaud, O. Ilbert, A. Iovino, F. Lamareille, B. Marano, A. Mazure, P. Memeo, R. Merighi, L. Moscardini, S. Paltani, R. Pellò, E. Perez-Montero, L. Pozzetti, M. Radovich, D. Vergani, G. Zamorani, and E. Zucca. A test of the nature of cosmic acceleration using galaxy redshift distortions. *Nature*, 451:541–544, January 2008. doi: 10.1038/nature06555.

T. Hamana, S. Miyazaki, K. Shimasaku, H. Furusawa, M. Doi, M. Hamabe, K. Imi, M. Kimura, Y. Komiyama, F. Nakata, N. Okada, S. Okamura, M. Ouchi, M. Sekiguchi, M. Yagi, and N. Yasuda. Cosmic Shear Statistics in the Suprime-Cam 2.1 Square Degree Field: Constraints on Ω_m and σ_8. *Astrophysical Journal*, 597:98–110, November 2003. doi: 10.1086/378348.

J. Hamann and J. Hasenkamp. A new life for sterile neutrinos: resolving inconsistencies using hot dark matter. *ArXiv e-prints*, August 2013.

J. Hamann, S. Hannestad, and Y. Y. Y. Wong. Measuring neutrino masses with a future galaxy survey. *Journal of Cosmology and Astroparticle Physics*, 11:052, November 2012. doi: 10.1088/1475-7516/2012/11/052.

A. J. S. Hamilton. Linear Redshift Distortions: a Review. In D. Hamilton, editor, *The Evolving Universe*, volume 231 of *Astrophysics and Space Science Library*, page 185, 1998.

S. Hannestad, I. Tamborra, and T. Tram. Thermalisation of light sterile neutrinos in the early universe. *Journal of Cosmology and Astroparticle Physics*, 7:025, July 2012. doi: 10.1088/1475-7516/2012/07/025.

D. Hanson, S. Hoover, A. Crites, and et al. Detection of B-Mode Polarization in the Cosmic Microwave Background with Data from the South Pole Telescope. *Physical Review Letters*, 111(14):141301, October 2013. doi: 10.1103/PhysRevLett.111.141301.

Jiangang Hao et al. A GMBCG Galaxy Cluster Catalog of 55,437 Rich Clusters from SDSS DR7. *Astrophys.J.Suppl.*, 191:254–274, 2010. doi: 10.1088/0067-0049/191/2/254.

J. Harnois-Déraps, S. Vafaei, and L. Van Waerbeke. Gravitational lensing simulations - I. Covariance matrices and halo catalogues. *Montly Notices of the Royal Astronomical Society*, 426:1262–1279, October 2012. doi: 10.1111/j.1365-2966.2012.21624.x.

M. Hasselfield, M. Hilton, T. A. Marriage, G. E. Addison, L. F. Barrientos, N. Battaglia, E. S. Battistelli, J. R. Bond, D. Crichton, S. Das, M. J. Devlin, S. R. Dicker, J. Dunkley, R. Dünner, J. W. Fowler, M. B. Gralla, A. Hajian, M. Halpern, A. D. Hincks, R. Hlozek, J. P. Hughes, L. Infante, K. D. Irwin, A. Kosowsky, D. Marsden, F. Menanteau, K. Moodley, M. D. Niemack, M. R. Nolta, L. A. Page, B. Partridge, E. D. Reese, B. L. Schmitt, N. Sehgal, B. D. Sherwin, J. Sievers, C. Sifón, D. N. Spergel, S. T. Staggs, D. S. Swetz, E. R. Switzer, R. Thornton, H. Trac, and E. J. Wollack. The Atacama Cosmology Telescope: Sunyaev-Zel'dovich selected galaxy clusters at 148 GHz from three seasons of data. *Journal of Cosmology and Astroparticle Physics*, 7:008, July 2013. doi: 10.1088/1475-7516/2013/07/008.

E. Hawkins, S. Maddox, S. Cole, O. Lahav, D. S. Madgwick, P. Norberg, J. A. Peacock, I. K. Baldry, C. M. Baugh, J. Bland-Hawthorn, T. Bridges, R. Cannon, M. Colless, C. Collins, W. Couch, G. Dalton, R. De Propris, S. P. Driver, G. Efstathiou, R. S. Ellis, C. S. Frenk, K. Glazebrook, C. Jackson, B. Jones, I. Lewis, S. Lumsden, W. Percival, B. A. Peterson, W. Sutherland, and K. Taylor. The 2dF Galaxy Redshift Survey: correlation functions, peculiar velocities and the matter density of the Universe. *Montly Notices of the Royal Astronomical Society*, 346: 78–96, November 2003. doi: 10.1046/j.1365-2966.2003.07063.x.

J. P. Henry, A. E. Evrard, H. Hoekstra, A. Babul, and A. Mahdavi. The X-Ray Cluster Normalization of the Matter Power Spectrum. *Astrophysical Journal*, 691: 1307–1321, February 2009. doi: 10.1088/0004-637X/691/2/1307.

C. Heymans and A. Heavens. Weak gravitational lensing: reducing the contamination by intrinsic alignments. *Montly Notices of the Royal Astronomical Society*, 339: 711–720, March 2003. doi: 10.1046/j.1365-8711.2003.06213.x.

C. Heymans, M. L. Brown, M. Barden, J. A. R. Caldwell, K. Jahnke, C. Y. Peng, H.-W. Rix, A. Taylor, S. V. W. Beckwith, E. F. Bell, A. Borch, B. Häußler, S. Jogee, D. H. McIntosh, K. Meisenheimer, S. F. Sánchez, R. Somerville, L. Wisotzki, and C. Wolf. Cosmological weak lensing with the HST GEMS survey. *Montly Notices of the Royal Astronomical Society*, 361:160–176, July 2005. doi: 10.1111/j.1365-2966.2005.09152.x.

C. Heymans, E. Grocutt, A. Heavens, and et al. CFHTLenS tomographic weak lensing cosmological parameter constraints: Mitigating the impact of intrinsic galaxy alignments. *Montly Notices of the Royal Astronomical Society*, 432:2433–2453, July 2013. doi: 10.1093/mnras/stt601.

G. Hinshaw, D. Larson, E. Komatsu, and et al. Nine-Year Wilkinson Microwave Anisotropy Probe (WMAP) Observations: Cosmological Parameter Results. *Astrophysical Journal Supplement*, 208:19, October 2013. doi: 10.1088/0067-0049/208/2/19.

C. M. Hirata and U. Seljak. Intrinsic alignment-lensing interference as a contaminant of cosmic shear. *Physical Review D*, 70(6):063526, September 2004. doi: 10.1103/PhysRevD.70.063526.

R. W. Hockney and J. W. Eastwood. *Computer Simulation Using Particles*. 1981.

H. Hoekstra. A comparison of weak-lensing masses and X-ray properties of galaxy clusters. *Montly Notices of the Royal Astronomical Society*, 379:317–330, July 2007. doi: 10.1111/j.1365-2966.2007.11951.x.

H. Hoekstra and B. Jain. Weak Gravitational Lensing and Its Cosmological Applications. *Annual Review of Nuclear and Particle Science*, 58:99–123, November 2008. doi: 10.1146/annurev.nucl.58.110707.171151.

H. Hoekstra, H. K. C. Yee, and M. D. Gladders. Constraints on Ω_m and σ_8 from Weak Lensing in Red-Sequence Cluster Survey Fields. *Astrophysical Journal*, 577:595–603, October 2002. doi: 10.1086/342120.

H. Hoekstra, M. Bartelmann, H. Dahle, H. Israel, M. Limousin, and M. Meneghetti. Masses of Galaxy Clusters from Gravitational Lensing. *Space Science Reviews*, 177:75–118, August 2013. doi: 10.1007/s11214-013-9978-5.

D. Hooper, F. S. Queiroz, and N. Y. Gnedin. Nonthermal dark matter mimicking an additional neutrino species in the early universe. *Physical Review D*, 85(6):063513, March 2012. doi: 10.1103/PhysRevD.85.063513.

Z. Hou, R. Keisler, L. Knox, M. Millea, and C. Reichardt. How Additional Massless Neutrinos Affect the Cosmic Microwave Background Damping Tail. *ArXiv e-prints*, April 2011.

W. Hu. Wandering in the Background: A CMB Explorer. *ArXiv Astrophysics e-prints*, August 1995.

W. Hu and A. V. Kravtsov. Sample Variance Considerations for Cluster Surveys. *Astrophysical Journal*, 584:702–715, February 2003. doi: 10.1086/345846.

W. Hu, D. J. Eisenstein, and M. Tegmark. Weighing Neutrinos with Galaxy Surveys. *Physical Review Letters*, 80:5255–5258, June 1998. doi: 10.1103/PhysRevLett.80.5255.

J. P. Huchra and M. J. Geller. Groups of galaxies. I - Nearby groups. *Astrophysical Journal*, 257:423–437, June 1982. doi: 10.1086/160000.

E. M. Huff. *Seeing in the Dark: Weak Lensing from the Sloan Digital Sky Survey*. PhD thesis, University of California, Berkeley, 2012.

G. Hütsi. Power spectrum of the SDSS luminous red galaxies: constraints on cosmological parameters. *Astronomy and Astrophysics*, 459:375–389, November 2006. doi: 10.1051/0004-6361:20065377.

G. Hütsi. Power spectrum of the maxBCG sample: detection of acoustic oscillations using galaxy clusters. *Montly Notices of the Royal Astronomical Society*, 401:2477–2489, February 2010. doi: 10.1111/j.1365-2966.2009.15824.x.

K. Ichiki and M. Takada. Impact of massive neutrinos on the abundance of massive clusters. *Physical Review D*, 85(6):063521, March 2012. doi: 10.1103/PhysRevD.85.063521.

H. Israel, T. H. Reiprich, T. Erben, R. J. Massey, C. L. Sarazin, P. Schneider, and A. Vikhlinin. The 400d Galaxy Cluster Survey weak lensing programme. III. Evidence for consistent WL and X-ray masses at $z \approx 0.5$. *Astronomy and Astrophysics*, 564:A129, April 2014. doi: 10.1051/0004-6361/201322870.

Y. I. Izotov, G. Stasińska, and N. G. Guseva. Primordial ^{4}He abundance: a determination based on the largest sample of H II regions with a methodology tested on model H II regions. *Astronomy and Astrophysics*, 558:A57, October 2013. doi: 10.1051/0004-6361/201220782.

M. Jarvis, G. M. Bernstein, P. Fischer, D. Smith, B. Jain, J. A. Tyson, and D. Wittman. Weak-Lensing Results from the 75 Square Degree Cerro Tololo Inter-American Observatory Survey. *The Astronomical Journal*, 125:1014–1032, March 2003. doi: 10.1086/367799.

M. Jauzac, E. Jullo, J.-P. Kneib, H. Ebeling, A. Leauthaud, C.-J. Ma, M. Limousin, R. Massey, and J. Richard. A weak lensing mass reconstruction of the large-scale filament feeding the massive galaxy cluster MACS J0717.5+3745. *Montly Notices of the Royal Astronomical Society*, 426:3369–3384, November 2012. doi: 10.1111/j.1365-2966.2012.21966.x.

M. J. Jee, J. A. Tyson, M. D. Schneider, D. Wittman, S. Schmidt, and S. Hilbert. Cosmic Shear Results from the Deep Lens Survey. I. Joint Constraints on Ω_M and σ_8 with a Two-dimensional Analysis. *Astrophysical Journal*, 765:74, March 2013. doi: 10.1088/0004-637X/765/1/74.

A. Jenkins, C. S. Frenk, S. D. M. White, J. M. Colberg, S. Cole, A. E. Evrard, H. M. P. Couchman, and N. Yoshida. The mass function of dark matter haloes. *Montly Notices of the Royal Astronomical Society*, 321:372–384, February 2001. doi: 10.1046/j.1365-8711.2001.04029.x.

R. Jimenez, T. Kitching, C. Peña-Garay, and L. Verde. Can we measure the neutrino mass hierarchy in the sky? *Journal of Cosmology and Astroparticle Physics*, 5:035, May 2010. doi: 10.1088/1475-7516/2010/05/035.

Y. P. Jing. Accurate Fitting Formula for the Two-Point Correlation Function of Dark Matter Halos. *Astrophysical Journal Letters*, 503:L9–L13, August 1998. doi: 10.1086/311530.

B. Joachimi and P. Schneider. The removal of shear-ellipticity correlations from the cosmic shear signal via nulling techniques. *Astronomy and Astrophysics*, 488:829–843, September 2008. doi: 10.1051/0004-6361:200809971.

David E. Johnston et al. Cross-correlation Weak Lensing of SDSS galaxy Clusters II: Cluster Density Profiles and the Mass–Richness Relation. 2007.

S. Joudaki. Constraints on Neutrino Mass and Light Degrees of Freedom in Extended Cosmological Parameter Spaces. *ArXiv e-prints*, January 2012.

N. Kaiser, G. Wilson, and G. A. Luppino. Large-Scale Cosmic Shear Measurements. *ArXiv Astrophysics e-prints*, March 2000.

J. Kaplan. Polarisation du CMB comme information complémentaire aux anisotropies. *Comptes Rendus Physique*, 4:917–924, October 2003. doi: 10.1016/j.crhy.2003.10.006.

S. T. Kay, M. W. Peel, C. J. Short, P. A. Thomas, O. E. Young, R. A. Battye, A. R. Liddle, and F. R. Pearce. Sunyaev-Zel'dovich clusters in Millennium gas simulations. *Montly Notices of the Royal Astronomical Society*, 422:1999–2023, May 2012. doi: 10.1111/j.1365-2966.2012.20623.x.

E. A. Kazin, J. Koda, C. Blake, N. Padmanabhan, S. Brough, M. Colless, C. Contreras, W. Couch, S. Croom, D. J. Croton, T. M. Davis, M. J. Drinkwater, K. Forster, D. Gilbank, M. Gladders, K. Glazebrook, B. Jelliffe, R. J. Jurek, I.-h. Li, B. Madore, D. C. Martin, K. Pimbblet, G. B. Poole, M. Pracy, R. Sharp, E. Wisnioski, D. Woods, T. K. Wyder, and H. K. C. Yee. The WiggleZ Dark Energy Survey: improved distance measurements to z = 1 with reconstruction of the baryonic acoustic feature. *Montly Notices of the Royal Astronomical Society*, 441:3524–3542, July 2014. doi: 10.1093/mnras/stu778.

C. Kelso, C. A. d. S. Pires, S. Profumo, F. S. Queiroz, and P. S. Rodrigues da Silva. A 331 WIMPy dark radiation model. *European Physical Journal C*, 74:2797, March 2014. doi: 10.1140/epjc/s10052-014-2797-3.

S. Khedekar and S. Majumdar. Cosmology with the largest galaxy cluster surveys: going beyond Fisher matrix forecasts. *Journal of Cosmology and Astroparticle Physics*, 2:030, February 2013. doi: 10.1088/1475-7516/2013/02/030.

M. Kilbinger, L. Fu, C. Heymans, F. Simpson, J. Benjamin, T. Erben, J. Harnois-Déraps, H. Hoekstra, H. Hildebrandt, T. D. Kitching, Y. Mellier, L. Miller, L. Van Waerbeke, K. Benabed, C. Bonnett, J. Coupon, M. J. Hudson, K. Kuijken, B. Rowe, T. Schrabback, E. Semboloni, S. Vafaei, and M. Velander. CFHTLenS: combined probe cosmological model comparison using 2D weak gravitational lensing. *Montly Notices of the Royal Astronomical Society*, 430:2200–2220, April 2013. doi: 10.1093/mnras/stt041.

L. King and P. Schneider. Suppressing the contribution of intrinsic galaxy alignments to the shear two-point correlation function. *Astronomy and Astrophysics*, 396:411–418, December 2002. doi: 10.1051/0004-6361:20021372.

D. Kirkman, D. Tytler, N. Suzuki, J. M. O'Meara, and D. Lubin. The Cosmological Baryon Density from the Deuterium-to-Hydrogen Ratio in QSO Absorption Systems: D/H toward Q1243+3047. *Astrophysical Journal Supplement*, 149:1–28, November 2003. doi: 10.1086/378152.

T. D. Kitching, A. F. Heavens, J. Alsing, T. Erben, C. Heymans, H. Hildebrandt, H. Hoekstra, A. Jaffe, A. Kiessling, Y. Mellier, L. Miller, L. van Waerbeke, J. Benjamin, J. Coupon, L. Fu, M. J. Hudson, M. Kilbinger, K. Kuijken, B. T. P. Rowe, T. Schrabback, E. Semboloni, and M. Velander. 3D cosmic shear: cosmology from CFHTLenS. *Montly Notices of the Royal Astronomical Society*, 442:1326–1349, August 2014. doi: 10.1093/mnras/stu934.

A. A. Klypin and S. F. Shandarin. Three-dimensional numerical model of the formation of large-scale structure in the Universe. *Montly Notices of the Royal Astronomical Society*, 204:891–907, September 1983.

J.-P. Kneib, R. S. Ellis, I. Smail, W. J. Couch, and R. M. Sharples. Hubble Space Telescope Observations of the Lensing Cluster Abell 2218. *Astrophysical Journal*, 471:643, November 1996. doi: 10.1086/177995.

C. S. Kochanek, M. White, J. Huchra, L. Macri, T. H. Jarrett, S. E. Schneider, and J. Mader. Clusters of Galaxies in the Local Universe. *Astrophysical Journal*, 585: 161–181, March 2003. doi: 10.1086/345896.

B. P. Koester, T. A. McKay, J. Annis, R. H. Wechsler, A. Evrard, L. Bleem, M. Becker, D. Johnston, E. Sheldon, R. Nichol, C. Miller, R. Scranton, N. Bahcall, J. Barentine, H. Brewington, J. Brinkmann, M. Harvanek, S. Kleinman, J. Krzesinski, D. Long, A. Nitta, D. P. Schneider, S. Sneddin, W. Voges, and D. York. A MaxBCG Catalog of 13,823 Galaxy Clusters from the Sloan Digital Sky Survey. *Astrophysical Journal*, 660:239–255, May 2007. doi: 10.1086/509599.

E. Komatsu and U. Seljak. The Sunyaev-Zel'dovich angular power spectrum as a probe of cosmological parameters. *Montly Notices of the Royal Astronomical Society*, 336:1256–1270, November 2002. doi: 10.1046/j.1365-8711.2002.05889.x.

E. Komatsu, T. Kitayama, Y. Suto, M. Hattori, R. Kawabe, H. Matsuo, S. Schindler, and K. Yoshikawa. Submillimeter Detection of the Sunyaev-Zeldovich Effect toward the Most Luminous X-Ray Cluster at Z = 0.45. *Astrophysical Journal Letters*, 516:L1–L4, May 1999. doi: 10.1086/311983.

E. Komatsu et al. Seven-year Wilkinson Microwave Anisotropy Probe (WMAP) Observations: Cosmological Interpretation. *Astrophysical Journal Supplement*, 192: 18–+, February 2011. doi: 10.1088/0067-0049/192/2/18.

C. Kraus, B. Bornschein, L. Bornschein, J. Bonn, B. Flatt, A. Kovalik, B. Ostrick, E. W. Otten, J. P. Schall, T. Thümmler, and C. Weinheimer. Final results from phase II

of the Mainz neutrino mass searchin tritium $\{\beta\}$ decay. *European Physical Journal C*, 40:447–468, April 2005. doi: 10.1140/epjc/s2005-02139-7.

A. V. Kravtsov and S. Borgani. Formation of Galaxy Clusters. *Annual Review of Astronomy & Astrophysics*, 50:353–409, September 2012. doi: 10.1146/annurev-astro-081811-125502.

A. V. Kravtsov, A. Vikhlinin, and D. Nagai. A New Robust Low-Scatter X-Ray Mass Indicator for Clusters of Galaxies. *Astrophysical Journal*, 650:128–136, October 2006. doi: 10.1086/506319.

T. F. Laganá, R. S. de Souza, and G. R. Keller. On the influence of non-thermal pressure on the mass determination of galaxy clusters. *Astronomy and Astrophysics*, 510:A76, February 2010. doi: 10.1051/0004-6361/200911855.

Paul Langacker. ON THE COSMOLOGICAL PRODUCTION OF LIGHT STERILE-NEUTRINOS. *University of Pennsylvania*, 1989.

R. Laureijs, J. Amiaux, S. Arduini, J. . Augueres, J. Brinchmann, R. Cole, M. Cropper, C. Dabin, L. Duvet, A. Ealet, and et al. et al. Euclid Definition Study Report. *ArXiv e-prints*, October 2011.

D. Lazzati, S. Campana, P. Rosati, M. R. Panzera, and G. Tagliaferri. The Brera Multiscale Wavelet ROSAT HRI Source Catalog. I. The Algorithm. *Astrophysical Journal*, 524:414–422, October 1999. doi: 10.1086/307788.

B. Leistedt, H. V. Peiris, and L. Verde. No new cosmological concordance with massive sterile neutrinos. *ArXiv e-prints*, April 2014.

J. Lesgourgues and S. Pastor. Massive neutrinos and cosmology. *Physics Reports*, 429:307–379, July 2006. doi: 10.1016/j.physrep.2006.04.001.

J. Lesgourgues and T. Tram. The Cosmic Linear Anisotropy Solving System (CLASS) IV: efficient implementation of non-cold relics. *Journal of Cosmology and Astroparticle Physics*, 9:032, September 2011. doi: 10.1088/1475-7516/2011/09/032.

J. Lesgourgues, S. Pastor, and L. Perotto. Probing neutrino masses with future galaxy redshift surveys. *Physical Review D*, 70(4):045016–+, August 2004. doi: 10.1103/PhysRevD.70.045016.

J. Lesgourgues, M. Viel, M. G. Haehnelt, and R. Massey. A combined analysis of 3D weak lensing, Lyman-α forest and WMAP year three data. *Journal of Cosmology and Astroparticle Physics*, 11:008, November 2007. doi: 10.1088/1475-7516/2007/11/008.

A. Lewis and S. Bridle. Cosmological parameters from CMB and other data: A Monte Carlo approach. *Physical Review D*, 66(10):103511, November 2002. doi: 10.1103/PhysRevD.66.103511.

A. Lewis, A. Challinor, and A. Lasenby. Efficient Computation of Cosmic Microwave Background Anisotropies in Closed Friedmann-Robertson-Walker Models. *Astrophysical Journal*, 538:473–476, August 2000. doi: 10.1086/309179.

I. H. Li and H. K. C. Yee. Finding Galaxy Groups in Photometric-Redshift Space: The Probability Friends-of-Friends Algorithm. *The Astronomical Journal*, 135:809–822, March 2008. doi: 10.1088/0004-6256/135/3/809.

A. Lidz, K. Heitmann, L. Hui, S. Habib, M. Rauch, and W. L. W. Sargent. Tightening Constraints from the Lyα Forest with the Flux Probability Distribution Function. *Astrophysical Journal*, 638:27–44, February 2006. doi: 10.1086/498699.

M. Lima and W. Hu. Self-calibration of cluster dark energy studies: Observable-mass distribution. *Physical Review D*, 72(4):043006–+, August 2005. doi: 10.1103/PhysRevD.72.043006.

M. Limousin, H. Ebeling, J. Richard, A. M. Swinbank, G. P. Smith, M. Jauzac, S. Rodionov, C.-J. Ma, I. Smail, A. C. Edge, E. Jullo, and J.-P. Kneib. Strong lensing by a node of the cosmic web. The core of MACS J0717.5+3745 at z = 0.55. *Astronomy and Astrophysics*, 544:A71, August 2012. doi: 10.1051/0004-6361/201117921.

H. Lin, S. Dodelson, H.-J. Seo, M. Soares-Santos, J. Annis, J. Hao, D. Johnston, J. M. Kubo, R. R. R. Reis, and M. Simet. The SDSS Co-add: Cosmic Shear Measurement. *Astrophysical Journal*, 761:15, December 2012. doi: 10.1088/0004-637X/761/1/15.

Y.-T. Lin, J. J. Mohr, and S. A. Stanford. Near-infrared properties of galaxy clusters: Luminosity as a binding mass predictor and the state of cluster baryons. *Astrophysical Journal*, 591:749–763, July 2003.

Y.-T. Lin, J. J. Mohr, A. H. Gonzalez, and S. A. Stanford. Evolution of the K-Band Galaxy Cluster Luminosity Function and Scaling Relations. *Astrophysical Journal Letters*, 650:L99–L102, October 2006. doi: 10.1086/508940.

C. Lobo, A. Iovino, D. Lazzati, and G. Chincarini. EISily looking for distant clusters of galaxies - a new algorithm and its application to the EIS-wide data. *Astronomy and Astrophysics*, 360:896–910, August 2000.

E. L. Łokas and G. A. Mamon. Dark matter distribution in the Coma cluster from galaxy kinematics: breaking the mass-anisotropy degeneracy. *Montly Notices of the Royal Astronomical Society*, 343:401–412, August 2003. doi: 10.1046/j.1365-8711.2003.06684.x.

Z. Lukić, K. Heitmann, S. Habib, S. Bashinsky, and P. M. Ricker. The Halo Mass Function: High-Redshift Evolution and Universality. *Astrophysical Journal*, 671:1160–1181, December 2007. doi: 10.1086/523083.

S. J. Maddox, G. Efstathiou, W. J. Sutherland, and J. Loveday. Galaxy correlations on large scales. *Montly Notices of the Royal Astronomical Society*, 242:43P–47P, January 1990.

A. Mahdavi, H. Hoekstra, A. Babul, and J. P. Henry. Evidence for non-hydrostatic gas from the cluster X-ray to lensing mass ratio. *Montly Notices of the Royal Astronomical Society*, 384:1567–1574, March 2008. doi: 10.1111/j.1365-2966.2007.12796.x.

A. Mahdavi, H. Hoekstra, A. Babul, C. Bildfell, T. Jeltema, and J. P. Henry. Joint Analysis of Cluster Observations. II. Chandra/XMM-Newton X-Ray and Weak Lensing Scaling Relations for a Sample of 50 Rich Clusters of Galaxies. *Astrophysical Journal*, 767:116, April 2013. doi: 10.1088/0004-637X/767/2/116.

S. Majumdar and J. J. Mohr. Self-Calibration in Cluster Studies of Dark Energy: Combining the Cluster Redshift Distribution, the Power Spectrum, and Mass Measurements. *Astrophysical Journal*, 613:41–50, September 2004. doi: 10.1086/422829.

A. Mana, T. Giannantonio, J. Weller, B. Hoyle, G. Hütsi, and B. Sartoris. Combining clustering and abundances of galaxy clusters to test cosmology and primordial non-Gaussianity. *Montly Notices of the Royal Astronomical Society*, 434:684–695, September 2013. doi: 10.1093/mnras/stt1062.

R. Mandelbaum, A. Slosar, T. Baldauf, U. Seljak, C. M. Hirata, R. Nakajima, R. Reyes, and R. E. Smith. Cosmological parameter constraints from galaxy-galaxy lensing and galaxy clustering with the SDSS DR7. *Montly Notices of the Royal Astronomical Society*, 432:1544–1575, June 2013. doi: 10.1093/mnras/stt572.

G. Mangano, G. Miele, S. Pastor, T. Pinto, O. Pisanti, and *et al.* Relic neutrino decoupling including flavour oscillations. *Nuclear Physics B*, 729:221–234, November 2005. doi: 10.1016/j.nuclphysb.2005.09.041.

A. Mantz, S. W. Allen, H. Ebeling, and D. Rapetti. New constraints on dark energy from the observed growth of the most X-ray luminous galaxy clusters. *Montly Notices of the Royal Astronomical Society*, 387:1179–1192, July 2008. doi: 10.1111/j.1365-2966.2008.13311.x.

A. Mantz, S. W. Allen, D. Rapetti, and H. Ebeling. The observed growth of massive galaxy clusters - I. Statistical methods and cosmological constraints. *Montly Notices of the Royal Astronomical Society*, 406:1759–1772, August 2010. doi: 10.1111/j.1365-2966.2010.16992.x.

A. B. Mantz, A. von der Linden, S. W. Allen, D. E. Applegate, P. L. Kelly, R. G. Morris, D. A. Rapetti, R. W. Schmidt, S. Adhikari, M. T. Allen, P. R. Burchat, D. L. Burke, M. Cataneo, D. Donovon, H. Ebeling, and S. Shandera. Weighing the Giants IV: Cosmology and Neutrino Mass. *ArXiv e-prints*, July 2014.

M. Markevitch. The L_X-T Relation and Temperature Function for Nearby Clusters Revisited. *Astrophysical Journal*, 504:27–34, September 1998. doi: 10.1086/306080.

D. P. Marrone, G. P. Smith, N. Okabe, M. Bonamente, J. E. Carlstrom, T. L. Culverhouse, M. Gralla, C. H. Greer, N. Hasler, D. Hawkins, R. Hennessy, M. Joy, J. W. Lamb, E. M. Leitch, R. Martino, P. Mazzotta, A. Miller, T. Mroczkowski, S. Muchovej, T. Plagge, C. Pryke, A. J. R. Sanderson, M. Takada, D. Woody, and Y. Zhang. LoCuSS: The Sunyaev-Zel'dovich Effect and Weak-lensing Mass Scaling Relation. *Astrophysical Journal*, 754:119, August 2012. doi: 10.1088/0004-637X/754/2/119.

D. Martizzi, I. Mohammed, R. Teyssier, and B. Moore. The biasing of baryons on the cluster mass function and cosmological parameter estimation. *Montly Notices of the Royal Astronomical Society*, 440:2290–2299, May 2014. doi: 10.1093/mnras/stu440.

F. Marulli, C. Carbone, M. Viel, L. Moscardini, and A. Cimatti. Effects of massive neutrinos on the large-scale structure of the Universe. *Montly Notices of the Royal Astronomical Society*, 418:346–356, November 2011. doi: 10.1111/j.1365-2966.2011.19488.x.

R. Massey, A. Refregier, D. J. Bacon, R. Ellis, and M. L. Brown. An enlarged cosmic shear survey with the William Herschel Telescope. *Montly Notices of the Royal Astronomical Society*, 359:1277–1286, June 2005. doi: 10.1111/j.1365-2966.2005.09011.x.

R. Massey, C. Heymans, J. Bergé, G. Bernstein, S. Bridle, D. Clowe, H. Dahle, R. Ellis, T. Erben, M. Hetterscheidt, F. W. High, C. Hirata, H. Hoekstra, P. Hudelot, M. Jarvis, D. Johnston, K. Kuijken, V. Margoniner, R. Mandelbaum, Y. Mellier, R. Nakajima, S. Paulin-Henriksson, M. Peeples, C. Roat, A. Refregier, J. Rhodes, T. Schrabback, M. Schirmer, U. Seljak, E. Semboloni, and L. van Waerbeke. The Shear Testing Programme 2: Factors affecting high-precision weak-lensing analyses. *Montly Notices of the Royal Astronomical Society*, 376:13–38, March 2007a. doi: 10.1111/j.1365-2966.2006.11315.x.

R. Massey, J. Rhodes, A. Leauthaud, P. Capak, R. Ellis, A. Koekemoer, A. Réfrégier, N. Scoville, J. E. Taylor, J. Albert, J. Bergé, C. Heymans, D. Johnston, J.-P. Kneib, Y. Mellier, B. Mobasher, E. Semboloni, P. Shopbell, L. Tasca, and L. Van Waerbeke. COSMOS: Three-dimensional Weak Lensing and the Growth of Structure. *Astrophysical Journal Supplement*, 172:239–253, September 2007b. doi: 10.1086/516599.

B. J. Maughan, L. R. Jones, H. Ebeling, and C. Scharf. The evolution of the cluster X-ray scaling relations in the Wide Angle ROSAT Pointed Survey sample at 0.6 ¡ z ¡ 1.0. *Montly Notices of the Royal Astronomical Society*, 365:509–529, January 2006. doi: 10.1111/j.1365-2966.2005.09717.x.

B. J. Maughan, P. A. Giles, S. W. Randall, C. Jones, and W. R. Forman. Self-similar scaling and evolution in the galaxy cluster X-ray luminosity-temperature relation. *Montly Notices of the Royal Astronomical Society*, 421:1583–1602, April 2012. doi: 10.1111/j.1365-2966.2012.20419.x.

P. McDonald and D. J. Eisenstein. Dark energy and curvature from a future baryonic acoustic oscillation survey using the Lyman-α forest. *Physical Review D*, 76 (6):063009, September 2007. doi: 10.1103/PhysRevD.76.063009.

P. McDonald, U. Seljak, R. Cen, D. Shih, D. H. Weinberg, S. Burles, D. P. Schneider, D. J. Schlegel, N. A. Bahcall, J. W. Briggs, J. Brinkmann, M. Fukugita, Ž. Ivezić, S. Kent, and D. E. Vanden Berk. The Linear Theory Power Spectrum from the Lyα Forest in the Sloan Digital Sky Survey. *Astrophysical Journal*, 635:761–783, December 2005. doi: 10.1086/497563.

N. Mehrtens, A. K. Romer, M. Hilton, E. J. Lloyd-Davies, C. J. Miller, S. A. Stanford, M. Hosmer, B. Hoyle, C. A. Collins, A. R. Liddle, P. T. P. Viana, R. C. Nichol, J. P. Stott, E. N. Dubois, S. T. Kay, M. Sahlén, O. Young, C. J. Short, L. Christodoulou, W. A. Watson, M. Davidson, C. D. Harrison, L. Baruah, M. Smith, C. Burke, J. A. Mayers, P.-J. Deadman, P. J. Rooney, E. M. Edmondson, M. West, H. C. Campbell, A. C. Edge, R. G. Mann, K. Sabirli, D. Wake, C. Benoist, L. da Costa, M. A. G. Maia, and R. Ogando. The XMM Cluster Survey: optical analysis methodology and the first data release. *Montly Notices of the Royal Astronomical Society*, 423: 1024–1052, June 2012. doi: 10.1111/j.1365-2966.2012.20931.x.

A. Melchiorri, O. Mena, S. Palomares-Ruiz, S. Pascoli, A. Slosar, and *et al.* Sterile neutrinos in light of recent cosmological and oscillation data: a multi-flavor scheme approach. *Journal of Cosmology and Astroparticle Physics*, 1:036, January 2009. doi: 10.1088/1475-7516/2009/01/036.

J.-B. Melin, J. G. Bartlett, and J. Delabrouille. Catalog extraction in SZ cluster surveys: a matched filter approach. *Astronomy and Astrophysics*, 459:341–352, November 2006. doi: 10.1051/0004-6361:20065034.

M. Meneghetti, E. Rasia, J. Merten, F. Bellagamba, S. Ettori, P. Mazzotta, K. Dolag, and S. Marri. Weighing simulated galaxy clusters using lensing and X-ray. *Astronomy and Astrophysics*, 514:A93+, May 2010. doi: 10.1051/0004-6361/200913222.

G. Mention, M. Fechner, T. Lasserre, T. A. Mueller, D. Lhuillier, M. Cribier, and A. Letourneau. Reactor antineutrino anomaly. *Physical Review D*, 83(7):073006, April 2011. doi: 10.1103/PhysRevD.83.073006.

D. Merritt. The distribution of dark matter in the coma cluster. *Astrophysical Journal*, 313:121–135, February 1987. doi: 10.1086/164953.

P. Meszaros. The behaviour of point masses in an expanding cosmological substratum. *Astronomy and Astrophysics*, 37:225–228, December 1974.

L. Miller, T. D. Kitching, C. Heymans, A. F. Heavens, and L. van Waerbeke. Bayesian galaxy shape measurement for weak lensing surveys - I. Methodology and a fast-fitting algorithm. *Montly Notices of the Royal Astronomical Society*, 382:315–324, November 2007. doi: 10.1111/j.1365-2966.2007.12363.x.

H. J. Mo and S. D. M. White. An analytic model for the spatial clustering of dark matter haloes. *Montly Notices of the Royal Astronomical Society*, 282:347–361, September 1996.

Houjun Mo, Frank Van den Bosch, and Simon White. *Galaxy Formation and Evolution*. Cambridge University Press, The Edinburgh Building, Cambridge CB2 8RU, UK, May 2010. ISBN 9780521857932.

S. G. Murray, C. Power, and A. S. G. Robotham. HMFcalc: An online tool for calculating dark matter halo mass functions. *Astronomy and Computing*, 3:23–34, November 2013. doi: 10.1016/j.ascom.2013.11.001.

S. Naess, M. Hasselfield, J. McMahon, and et al. The Atacama Cosmology Telescope: CMB Polarization at $200 < \ell < 9000$. *ArXiv e-prints*, May 2014.

D. Nagai, A. V. Kravtsov, and A. Vikhlinin. Effects of Galaxy Formation on Thermodynamics of the Intracluster Medium. *Astrophysical Journal*, 668:1–14, October 2007. doi: 10.1086/521328.

P. Natarajan and J.-P. Kneib. Probing the dynamics of cluster-lenses. *Montly Notices of the Royal Astronomical Society*, 283:1031–1046, December 1996.

J. F. Navarro, C. S. Frenk, and S. D. M. White. A Universal Density Profile from Hierarchical Clustering. *Astrophysical Journal*, 490:493, December 1997. doi: 10.1086/304888.

J. Nevalainen, L. David, and M. Guainazzi. Cross-calibrating X-ray detectors with clusters of galaxies: an IACHEC study. *Astronomy and Astrophysics*, 523:A22, November 2010. doi: 10.1051/0004-6361/201015176.

A. Nusser and M. Haehnelt. The amplitude of mass density fluctuations at z˜3.25 from the Lyα forest of Q1422+231. *Montly Notices of the Royal Astronomical Society*, 313:364–376, April 2000. doi: 10.1046/j.1365-8711.2000.03263.x.

L. F. Olsen, M. Scodeggio, L. da Costa, C. Benoist, E. Bertin, E. Deul, T. Erben, M. D. Guarnieri, R. Hook, M. Nonino, I. Prandoni, R. Slijkhuis, A. Wicenec, and

R. Wichmann. ESO imaging survey. II. Searching for distant clusters of galaxies. *Astronomy and Astrophysics*, 345:681–690, May 1999.

J. M. O'Meara, D. Tytler, D. Kirkman, N. Suzuki, J. X. Prochaska, D. Lubin, and A. M. Wolfe. The Deuterium to Hydrogen Abundance Ratio toward a Fourth QSO: HS 0105+1619. *Astrophysical Journal*, 552:718–730, May 2001. doi: 10.1086/320579.

N. Padmanabhan, X. Xu, D. J. Eisenstein, R. Scalzo, A. J. Cuesta, K. T. Mehta, and E. Kazin. A 2 per cent distance to z = 0.35 by reconstructing baryon acoustic oscillations - I. Methods and application to the Sloan Digital Sky Survey. *Montly Notices of the Royal Astronomical Society*, 427:2132–2145, December 2012. doi: 10.1111/j.1365-2966.2012.21888.x.

N. Palanque-Delabrouille, C. Yèche, A. Borde, and et al. The one-dimensional Lyα forest power spectrum from BOSS. *Astronomy and Astrophysics*, 559:A85, November 2013. doi: 10.1051/0004-6361/201322130.

S. Palomares-Ruiz, S. Pascoli, and T. Schwetz. Explaining LSND by a decaying sterile neutrino. *Journal of High Energy Physics*, 9:048, September 2005. doi: 10.1088/1126-6708/2005/09/048.

J. A. Peacock. *Cosmological Physics*. January 1999.

J. A. Peacock, S. Cole, P. Norberg, C. M. Baugh, J. Bland-Hawthorn, T. Bridges, R. D. Cannon, M. Colless, C. Collins, W. Couch, G. Dalton, K. Deeley, R. De Propris, S. P. Driver, G. Efstathiou, R. S. Ellis, C. S. Frenk, K. Glazebrook, C. Jackson, O. Lahav, I. Lewis, S. Lumsden, S. Maddox, W. J. Percival, B. A. Peterson, I. Price, W. Sutherland, and K. Taylor. A measurement of the cosmological mass density from clustering in the 2dF Galaxy Redshift Survey. *Nature*, 410:169–173, March 2001.

P. J. E. Peebles. *Principles of Physical Cosmology*. 1993.

A. A. Penzias and R. W. Wilson. A Measurement of Excess Antenna Temperature at 4080 Mc/s. *Astrophysical Journal*, 142:419–421, July 1965. doi: 10.1086/148307.

W. J. Percival and M. White. Testing cosmological structure formation using redshift-space distortions. *Montly Notices of the Royal Astronomical Society*, 393:297–308, February 2009. doi: 10.1111/j.1365-2966.2008.14211.x.

W. J. Percival, B. A. Reid, D. J. Eisenstein, N. A. Bahcall, T. Budavari, J. A. Frieman, M. Fukugita, J. E. Gunn, Ž. Ivezić, G. R. Knapp, R. G. Kron, J. Loveday, R. H. Lupton, T. A. McKay, A. Meiksin, R. C. Nichol, A. C. Pope, D. J. Schlegel, D. P. Schneider, D. N. Spergel, C. Stoughton, M. A. Strauss, A. S. Szalay, M. Tegmark, M. S. Vogeley, D. H. Weinberg, D. G. York, and I. Zehavi. Baryon acoustic oscillations in the Sloan Digital Sky Survey Data Release 7 galaxy sample. *Montly Notices of the Royal Astronomical Society*, 401:2148–2168, February 2010. doi: 10.1111/j.1365-2966.2009.15812.x.

S. Perlmutter, G. Aldering, G. Goldhaber, R. A. Knop, P. Nugent, P. G. Castro, S. Deustua, S. Fabbro, A. Goobar, D. E. Groom, I. M. Hook, A. G. Kim, M. Y. Kim, J. C. Lee, N. J. Nunes, R. Pain, C. R. Pennypacker, R. Quimby, C. Lidman, R. S. Ellis, M. Irwin, R. G. McMahon, P. Ruiz-Lapuente, N. Walton, B. Schaefer, B. J. Boyle, A. V. Filippenko, T. Matheson, A. S. Fruchter, N. Panagia, H. J. M. Newberg, W. J. Couch, and T. S. C. Project. Measurements of Ω and Λ from 42 High-Redshift Supernovae. *Astrophysical Journal*, 517:565–586, June 1999. doi: 10.1086/307221.

L. Perotto, J. Lesgourgues, S. Hannestad, H. Tu, and Y. Y Y Wong. Probing cosmological parameters with the CMB: forecasts from Monte Carlo simulations. *Journal of Cosmology and Astroparticle Physics*, 10:13, October 2006. doi: 10.1088/1475-7516/2006/10/013.

J. R. Peterson, J. G. Jernigan, R. R. Gupta, J. Bankert, and S. M. Kahn. Evidence for Nonlinear Growth of Structure from an X-Ray-Selected Cluster Survey using a Novel Joint Analysis of the Chandra and XMM-Newton Archives. *Astrophysical Journal*, 707:878–889, December 2009. doi: 10.1088/0004-637X/707/2/878.

C. Pichon, J. L. Vergely, E. Rollinde, S. Colombi, and P. Petitjean. Inversion of the Lyman α forest: three-dimensional investigation of the intergalactic medium. *Montly Notices of the Royal Astronomical Society*, 326:597–620, September 2001. doi: 10.1046/j.1365-8711.2001.04595.x.

M. Pierre, F. Pacaud, P.-A. Duc, J. P. Willis, S. Andreon, I. Valtchanov, B. Altieri, G. Galaz, A. Gueguen, J.-P. Le Fèvre, O. L. Fèvre, T. Ponman, P.-G. Sprimont, J. Surdej, C. Adami, A. Alshino, M. Bremer, L. Chiappetti, A. Detal, O. Garcet, E. Gosset, C. Jean, D. Maccagni, C. Marinoni, A. Mazure, H. Quintana, and A. Read. The XMM Large-Scale Structure survey: a well-controlled X-ray cluster sample over the D1 CFHTLS area. *Montly Notices of the Royal Astronomical Society*, 372:591–608, October 2006. doi: 10.1111/j.1365-2966.2006.10886.x.

R. Piffaretti, M. Arnaud, G. W. Pratt, E. Pointecouteau, and J.-B. Melin. The MCXC: a meta-catalogue of x-ray detected clusters of galaxies. *Astronomy and Astrophysics*, 534:A109, October 2011. doi: 10.1051/0004-6361/201015377.

Planck Collaboration. The Scientific Programme of Planck. *ArXiv Astrophysics e-prints*, April 2006.

Planck Collaboration. Planck 2013 results. XX. Cosmology from Sunyaev-Zeldovich cluster counts. *ArXiv e-prints*, March 2013a.

Planck Collaboration. Planck 2013 results. XXIX. Planck catalogue of Sunyaev-Zeldovich sources. *ArXiv e-prints*, March 2013b.

Planck Collaboration. Planck 2013 results. XV. CMB power spectra and likelihood. *ArXiv e-prints*, March 2013c.

Planck Collaboration. Planck 2013 results. XVI. Cosmological parameters. *ArXiv e-prints*, March 2013d.

Planck Collaboration. Planck 2013 results. XVII. Gravitational lensing by large-scale structure. *ArXiv e-prints*, March 2013e.

Planck Collaboration. Planck intermediate results. XXX. The angular power spectrum of polarized dust emission at intermediate and high Galactic latitudes. *ArXiv e-prints*, September 2014.

E. Pointecouteau, M. Giard, A. Benoit, F. X. Désert, N. Aghanim, N. Coron, J. M. Lamarre, and J. Delabrouille. A Sunyaev-Zel'dovich map of the massive core in the luminous X-ray cluster RXJ1347-1145. *ArXiv Astrophysics e-prints*, May 1999.

POLARBEAR Collaboration. Measurement of the Cosmic Microwave Background Polarization Lensing Power Spectrum with the POLARBEAR experiment. *ArXiv e-prints*, December 2013.

Polarbear Collaboration. Evidence for Gravitational Lensing of the Cosmic Microwave Background Polarization from Cross-Correlation with the Cosmic Infrared Background. *Physical Review Letters*, 112(13):131302, April 2014. doi: 10.1103/PhysRevLett.112.131302.

P. Popesso, A. Biviano, H. Böhringer, M. Romaniello, and W. Voges. RASS-SDSS galaxy cluster survey. III. Scaling relations of galaxy clusters. *Astronomy and Astrophysics*, 433:431–445, April 2005. doi: 10.1051/0004-6361:20041915.

M. Postman, L. M. Lubin, J. E. Gunn, J. B. Oke, J. G. Hoessel, D. P. Schneider, and J. A. Christensen. The Palomar Distant Clusters Survey. I. The Cluster Catalog. *The Astronomical Journal*, 111:615, February 1996. doi: 10.1086/117811.

G. W. Pratt, J. H. Croston, M. Arnaud, and H. Böhringer. Galaxy cluster X-ray luminosity scaling relations from a representative local sample (REXCESS). *Astronomy and Astrophysics*, 498:361–378, May 2009. doi: 10.1051/0004-6361/200810994.

G. W. Pratt, M. Arnaud, R. Piffaretti, H. Böhringer, T. J. Ponman, J. H. Croston, G. M. Voit, S. Borgani, and R. G. Bower. Gas entropy in a representative sample of nearby X-ray galaxy clusters (REXCESS): relationship to gas mass fraction. *Astronomy and Astrophysics*, 511:A85, February 2010. doi: 10.1051/0004-6361/200913309.

W. H. Press and P. Schechter. Formation of Galaxies and Clusters of Galaxies by Self-Similar Gravitational Condensation. *Astrophysical Journal*, 187:425–438, February 1974. doi: 10.1086/152650.

J. R. Pritchard and E. Pierpaoli. Constraining massive neutrinos using cosmological 21cm observations. *Physical Review D*, 78(6):065009, September 2008. doi: 10.1103/PhysRevD.78.065009.

QUIET Collaboration. Second Season QUIET Observations: Measurements of the Cosmic Microwave Background Polarization Power Spectrum at 95 GHz. *Astrophysical Journal*, 760:145, December 2012. doi: 10.1088/0004-637X/760/2/145.

E. Rasia, M. Meneghetti, R. Martino, S. Borgani, A. Bonafede, K. Dolag, S. Ettori, D. Fabjan, C. Giocoli, P. Mazzotta, J. Merten, M. Radovich, and L. Tornatore. Lensing and x-ray mass estimates of clusters (simulations). *New Journal of Physics*, 14(5):055018, May 2012. doi: 10.1088/1367-2630/14/5/055018.

D. Reed, J. Gardner, T. Quinn, J. Stadel, M. Fardal, G. Lake, and F. Governato. Evolution of the mass function of dark matter haloes. *Montly Notices of the Royal Astronomical Society*, 346:565–572, December 2003. doi: 10.1046/j.1365-2966.2003.07113.x.

D. S. Reed, R. Bower, C. S. Frenk, A. Jenkins, and T. Theuns. The halo mass function from the dark ages through the present day. *Montly Notices of the Royal Astronomical Society*, 374:2–15, January 2007. doi: 10.1111/j.1365-2966.2006.11204.x.

A. Refregier. Shapelets - I. A method for image analysis. *Montly Notices of the Royal Astronomical Society*, 338:35–47, January 2003. doi: 10.1046/j.1365-8711.2003.05901.x.

C. L. Reichardt, L. Shaw, O. Zahn, K. A. Aird, B. A. Benson, L. E. Bleem, J. E. Carlstrom, C. L. Chang, H. M. Cho, T. M. Crawford, A. T. Crites, T. de Haan, M. A. Dobbs, J. Dudley, E. M. George, N. W. Halverson, G. P. Holder, W. L. Holzapfel, S. Hoover, Z. Hou, J. D. Hrubes, M. Joy, R. Keisler, L. Knox, A. T. Lee, E. M. Leitch, M. Lueker, D. Luong-Van, J. J. McMahon, J. Mehl, S. S. Meyer, M. Millea, J. J. Mohr, T. E. Montroy, T. Natoli, S. Padin, T. Plagge, C. Pryke, J. E. Ruhl, K. K. Schaffer, E. Shirokoff, H. G. Spieler, Z. Staniszewski, A. A. Stark, K. Story, A. van Engelen, K. Vanderlinde, J. D. Vieira, and R. Williamson. A Measurement of Secondary Cosmic Microwave Background Anisotropies with Two Years of South Pole Telescope Observations. *Astrophysical Journal*, 755:70, August 2012. doi: 10.1088/0004-637X/755/1/70.

B. A. Reid, L. Samushia, M. White, W. J. Percival, M. Manera, N. Padmanabhan, A. J. Ross, A. G. Sánchez, S. Bailey, D. Bizyaev, A. S. Bolton, H. Brewington, J. Brinkmann, J. R. Brownstein, A. J. Cuesta, D. J. Eisenstein, J. E. Gunn, K. Honscheid, E. Malanushenko, V. Malanushenko, C. Maraston, C. K. McBride, D. Muna, R. C. Nichol, D. Oravetz, K. Pan, R. de Putter, N. A. Roe, N. P. Ross, D. J. Schlegel, D. P. Schneider, H.-J. Seo, A. Shelden, E. S. Sheldon, A. Simmons, R. A. Skibba, S. Snedden, M. E. C. Swanson, D. Thomas, J. Tinker, R. Tojeiro, L. Verde, D. A. Wake, B. A. Weaver, D. H. Weinberg, I. Zehavi, and G.-B. Zhao. The clustering of galaxies in the SDSS-III Baryon Oscillation Spectroscopic Survey: measurements of the growth of structure and expansion rate at z = 0.57 from anisotropic clustering. *Montly Notices of the Royal Astronomical Society*, 426: 2719–2737, November 2012. doi: 10.1111/j.1365-2966.2012.21779.x.

T. H. Reiprich and H. Böhringer. The Mass Function of an X-Ray Flux-limited Sample of Galaxy Clusters. *Astrophysical Journal*, 567:716–740, March 2002. doi: 10.1086/338753.

J. Rhodes, A. Refregier, and E. J. Groth. Detection of Cosmic Shear with the Hubble Space Telescope Survey Strip. *Astrophysical Journal Letters*, 552:L85–L88, May 2001. doi: 10.1086/320336.

S. Riemer-Sørensen, D. Parkinson, T. M. Davis, and C. Blake. Simultaneous Constraints on the Number and Mass of Relativistic Species. *Astrophysical Journal*, 763:89, February 2013. doi: 10.1088/0004-637X/763/2/89.

A. G. Riess, A. V. Filippenko, P. Challis, A. Clocchiatti, A. Diercks, P. M. Garnavich, R. L. Gilliland, C. J. Hogan, S. Jha, R. P. Kirshner, B. Leibundgut, M. M. Phillips, D. Reiss, B. P. Schmidt, R. A. Schommer, R. C. Smith, J. Spyromilio, C. Stubbs, N. B. Suntzeff, and J. Tonry. Observational Evidence from Supernovae for an Accelerating Universe and a Cosmological Constant. *The Astronomical Journal*, 116:1009–1038, September 1998. doi: 10.1086/300499.

A. G. Riess, L. Macri, S. Casertano, H. Lampeitl, H. C. Ferguson, A. V. Filippenko, S. W. Jha, W. Li, and R. Chornock. A 3% Solution: Determination of the Hubble Constant with the Hubble Space Telescope and Wide Field Camera 3. *Astrophysical Journal*, 730:119, April 2011. doi: 10.1088/0004-637X/730/2/119.

K. Rines and A. Diaferio. CIRS: Cluster Infall Regions in the Sloan Digital Sky Survey. I. Infall Patterns and Mass Profiles. *The Astronomical Journal*, 132:1275–1297, September 2006. doi: 10.1086/506017.

K. Rines, M. J. Geller, M. J. Kurtz, and A. Diaferio. CAIRNS: The Cluster and Infall Region Nearby Survey. I. Redshifts and Mass Profiles. *The Astronomical Journal*, 126:2152–2170, November 2003. doi: 10.1086/378599.

A. Ringwald and Y. Y. Y. Wong. Gravitational clustering of relic neutrinos and implications for their detection. *Journal of Cosmology and Astroparticle Physics*, 12: 005, December 2004. doi: 10.1088/1475-7516/2004/12/005.

A. K. Romer, P. T. P. Viana, A. R. Liddle, and R. G. Mann. A Serendipitous Galaxy Cluster Survey with XMM: Expected Catalog Properties and Scientific Applications. *Astrophysical Journal*, 547:594–608, February 2001. doi: 10.1086/318382.

P. Rosati, R. Della Ceca, R. Burg, C. Norman, and R. Giacconi. A first determination of the surface density of galaxy clusters at very low x-ray fluxes. *Astrophysical Journal Letters*, 445:L11–L14, May 1995. doi: 10.1086/187877.

P. Rosati, R. Della Ceca, C. Norman, and R. Giacconi. The ROSAT Deep Cluster Survey: The X-Ray Luminosity Function out to z = 0.8. *Astrophysical Journal Letters*, 492:L21–L24, January 1998. doi: 10.1086/311085.

P. Rosati, S. Borgani, and C. Norman. The Evolution of X-ray Clusters of Galaxies. *Annual Review of Astronomy & Astrophysics*, 40:539–577, 2002. doi: 10.1146/annurev.astro.40.120401.150547.

G. Rossi, N. Palanque-Delabrouille, A. Borde, M. Viel, C. Yèche, J. S. Bolton, J. Rich, and J.-M. Le Goff. Suite of hydrodynamical simulations for the Lyman-α forest with massive neutrinos. *Astronomy and Astrophysics*, 567:A79, July 2014. doi: 10.1051/0004-6361/201423507.

E. Rozo, E. S. Rykoff, A. Evrard, M. Becker, T. McKay, R. H. Wechsler, B. P. Koester, J. Hao, S. Hansen, E. Sheldon, D. Johnston, J. Annis, and J. Frieman. Constraining the Scatter in the Mass-richness Relation of maxBCG Clusters with Weak Lensing and X-ray Data. *Astrophysical Journal*, 699:768–781, July 2009. doi: 10.1088/0004-637X/699/1/768.

E. Rozo, R. H. Wechsler, E. S. Rykoff, J. T. Annis, M. R. Becker, A. E. Evrard, J. A. Frieman, S. M. Hansen, J. Hao, D. E. Johnston, B. P. Koester, T. A. McKay, E. S. Sheldon, and D. H. Weinberg. Cosmological Constraints from the Sloan Digital Sky Survey maxBCG Cluster Catalog. *Astrophysical Journal*, 708:645–660, January 2010. doi: 10.1088/0004-637X/708/1/645.

E. Rozo, E. S. Rykoff, J. G. Bartlett, and A. E. Evrard. Cluster Cosmology at a Crossroads: Neutrino Masses. *ArXiv e-prints*, February 2013.

D. H. Rudd, A. R. Zentner, and A. V. Kravtsov. Effects of Baryons and Dissipation on the Matter Power Spectrum. *Astrophysical Journal*, 672:19–32, January 2008. doi: 10.1086/523836.

E. S. Rykoff, A. E. Evrard, T. A. McKay, M. R. Becker, D. E. Johnston, B. P. Koester, B. Nord, E. Rozo, E. S. Sheldon, R. Stanek, and R. H. Wechsler. The L_X-M relation of clusters of galaxies. *Montly Notices of the Royal Astronomical Society*, 387:L28–L32, June 2008. doi: 10.1111/j.1745-3933.2008.00476.x.

E. S. Rykoff, E. Rozo, M. T. Busha, C. E. Cunha, A. Finoguenov, A. Evrard, J. Hao, B. P. Koester, A. Leauthaud, B. Nord, M. Pierre, R. Reddick, T. Sadibekova, E. S. Sheldon, and R. H. Wechsler. redMaPPer. I. Algorithm and SDSS DR8 Catalog. *Astrophysical Journal*, 785:104, April 2014. doi: 10.1088/0004-637X/785/2/104.

R. K. Sachs and A. M. Wolfe. Perturbations of a Cosmological Model and Angular Variations of the Microwave Background. *Astrophysical Journal*, 147:73, January 1967. doi: 10.1086/148982.

L. Samushia, W. J. Percival, and A. Raccanelli. Interpreting large-scale redshift-space distortion measurements. *Montly Notices of the Royal Astronomical Society*, 420:2102–2119, March 2012. doi: 10.1111/j.1365-2966.2011.20169.x.

B. Sartoris. *Study of structure formation and evolution in non-standard cosmological models*. PhD thesis, Universitá degli Studi di Trieste, 2012.

B. Sartoris, S. Borgani, C. Fedeli, S. Matarrese, L. Moscardini, and *et al.* The potential of X-ray cluster surveys to constrain primordial non-Gaussianity. *Montly Notices of the Royal Astronomical Society*, 407:2339–2354, October 2010. doi: 10.1111/j.1365-2966.2010.17050.x.

B. Sartoris, S. Borgani, P. Rosati, and J. Weller. Probing dark energy with the next generation X-ray surveys of galaxy clusters. *Montly Notices of the Royal Astronomical Society*, 423:2503–2517, July 2012. doi: 10.1111/j.1365-2966.2012.21064.x.

B. Sartoris, A. Biviano, C. Fedeli, and et al. Euclid – Forecast on Cosmological Constraints from Clusters of Galaxies. *Montly Notices of the Royal Astronomical Society*, 10:081, October 2014. doi: 10.1088/1475-7516/2014/10/081.

G. Schellenberger, T. H. Reiprich, L. Lovisari, J. Nevalainen, and L. David. XMM-Newton and Chandra Cross Calibration Using HIFLUGCS Galaxy Clusters. *ArXiv e-prints*, April 2014.

T. Schrabback, J. Hartlap, B. Joachimi, M. Kilbinger, P. Simon, K. Benabed, M. Bradač, T. Eifler, T. Erben, C. D. Fassnacht, F. W. High, S. Hilbert, H. Hildebrandt, H. Hoekstra, K. Kuijken, P. J. Marshall, Y. Mellier, E. Morganson, P. Schneider, E. Semboloni, L. van Waerbeke, and M. Velander. Evidence of the accelerated expansion of the Universe from weak lensing tomography with COSMOS. *Astronomy and Astrophysics*, 516:A63, June 2010. doi: 10.1051/0004-6361/200913577.

N. Sehgal, P. Bode, S. Das, C. Hernandez-Monteagudo, K. Huffenberger, Y.-T. Lin, J. P. Ostriker, and H. Trac. Simulations of the Microwave Sky. *Astrophysical Journal*, 709:920–936, February 2010. doi: 10.1088/0004-637X/709/2/920.

U. Seljak, A. Slosar, and P. McDonald. Cosmological parameters from combining the Lyman-α forest with CMB, galaxy clustering and SN constraints. *Journal of Cosmology and Astroparticle Physics*, 10:14, October 2006. doi: 10.1088/1475-7516/2006/10/014.

E. Semboloni, Y. Mellier, L. van Waerbeke, H. Hoekstra, I. Tereno, K. Benabed, S. D. J. Gwyn, L. Fu, M. J. Hudson, R. Maoli, and L. C. Parker. Cosmic shear analysis with CFHTLS deep data. *Astronomy and Astrophysics*, 452:51–61, June 2006. doi: 10.1051/0004-6361:20054479.

R. K. Sheth and G. Tormen. Large-scale bias and the peak background split. *Montly Notices of the Royal Astronomical Society*, 308:119–126, September 1999. doi: 10.1046/j.1365-8711.1999.02692.x.

R. K. Sheth, H. J. Mo, and G. Tormen. Ellipsoidal collapse and an improved model for the number and spatial distribution of dark matter haloes. *Montly Notices of the Royal Astronomical Society*, 323:1–12, May 2001. doi: 10.1046/j.1365-8711.2001.04006.x.

X. Shi and E. Komatsu. Analytical model for non-thermal pressure in galaxy clusters. *ArXiv e-prints*, January 2014.

M. Shoji and E. Komatsu. Erratum: Massive neutrinos in cosmology: Analytic solutions and fluid approximation [Phys. Rev. D 81, 123516 (2010)]. *Physical Review D*, 82(8):089901–+, October 2010. doi: 10.1103/PhysRevD.82.089901.

J. Silk. Fluctuations in the Primordial Fireball. *Nature*, 215:1155–1156, September 1967. doi: 10.1038/2151155a0.

F. Simpson, C. Heymans, D. Parkinson, C. Blake, M. Kilbinger, J. Benjamin, T. Erben, H. Hildebrandt, H. Hoekstra, T. D. Kitching, Y. Mellier, L. Miller, L. Van Waerbeke, J. Coupon, L. Fu, J. Harnois-Déraps, M. J. Hudson, K. Kuijken, B. Rowe, T. Schrabback, E. Semboloni, S. Vafaei, and M. Velander. CFHTLenS: testing the laws of gravity with tomographic weak lensing and redshift-space distortions. *Montly Notices of the Royal Astronomical Society*, 429:2249–2263, March 2013. doi: 10.1093/mnras/sts493.

A. Slosar, A. Font-Ribera, M. M. Pieri, J. Rich, J.-M. Le Goff, É. Aubourg, J. Brinkmann, N. Busca, B. Carithers, R. Charlassier, M. Cortês, R. Croft, K. S. Dawson, D. Eisenstein, J.-C. Hamilton, S. Ho, K.-G. Lee, R. Lupton, P. McDonald, B. Medolin, D. Muna, J. Miralda-Escudé, A. D. Myers, R. C. Nichol, N. Palanque-Delabrouille, I. Pâris, P. Petitjean, Y. Piškur, E. Rollinde, N. P. Ross, D. J. Schlegel, D. P. Schneider, E. Sheldon, B. A. Weaver, D. H. Weinberg, C. Yeche, and D. G. York. The Lyman-α forest in three dimensions: measurements of large scale flux correlations from BOSS 1st-year data. *Journal of Cosmology and Astroparticle Physics*, 9:001, September 2011. doi: 10.1088/1475-7516/2011/09/001.

A. Slosar, V. Iršič, D. Kirkby, S. Bailey, N. G. Busca, T. Delubac, J. Rich, É. Aubourg, J. E. Bautista, V. Bhardwaj, M. Blomqvist, A. S. Bolton, J. Bovy, J. Brownstein, B. Carithers, R. A. C. Croft, K. S. Dawson, A. Font-Ribera, J.-M. Le Goff, S. Ho,

K. Honscheid, K.-G. Lee, D. Margala, P. McDonald, B. Medolin, J. Miralda-Escudé, A. D. Myers, R. C. Nichol, P. Noterdaeme, N. Palanque-Delabrouille, I. Pâris, P. Petitjean, M. M. Pieri, Y. Piškur, N. A. Roe, N. P. Ross, G. Rossi, D. J. Schlegel, D. P. Schneider, N. Suzuki, E. S. Sheldon, U. Seljak, M. Viel, D. H. Weinberg, and C. Yèche. Measurement of baryon acoustic oscillations in the Lyman-α forest fluctuations in BOSS data release 9. *Journal of Cosmology and Astroparticle Physics*, 4:026, April 2013. doi: 10.1088/1475-7516/2013/04/026.

T. L. Smith, E. Pierpaoli, and M. Kamionkowski. New Cosmic Microwave Background Constraint to Primordial Gravitational Waves. *Physical Review Letters*, 97 (2):021301, July 2006. doi: 10.1103/PhysRevLett.97.021301.

G. F. Smoot, M. V. Gorenstein, and R. A. Muller. Detection of anisotropy in the cosmic blackbody radiation. *Physical Review Letters*, 39:898–901, October 1977. doi: 10.1103/PhysRevLett.39.898.

D. Spergel, R. Flauger, and R. Hlozek. Planck Data Reconsidered. *ArXiv e-prints*, December 2013.

V. Springel. The cosmological simulation code GADGET-2. *Montly Notices of the Royal Astronomical Society*, 364:1105–1134, December 2005. doi: 10.1111/j.1365-2966.2005.09655.x.

V. Springel, S. D. M. White, G. Tormen, and G. Kauffmann. Populating a cluster of galaxies - I. Results at [formmu2]z=0. *Montly Notices of the Royal Astronomical Society*, 328:726–750, December 2001. doi: 10.1046/j.1365-8711.2001.04912.x.

V. Springel, S. D. M. White, A. Jenkins, C. S. Frenk, N. Yoshida, L. Gao, J. Navarro, R. Thacker, D. Croton, J. Helly, J. A. Peacock, S. Cole, P. Thomas, H. Couchman, A. Evrard, J. Colberg, and F. Pearce. Simulations of the formation, evolution and clustering of galaxies and quasars. *Nature*, 435:629–636, June 2005. doi: 10.1038/nature03597.

R. Stanek, D. Rudd, and A. E. Evrard. The effect of gas physics on the halo mass function. *Montly Notices of the Royal Astronomical Society*, 394:L11–L15, March 2009. doi: 10.1111/j.1745-3933.2008.00597.x.

Z. Staniszewski, P. A. R. Ade, K. A. Aird, B. A. Benson, L. E. Bleem, J. E. Carlstrom, C. L. Chang, H.-M. Cho, T. M. Crawford, A. T. Crites, T. de Haan, M. A. Dobbs, N. W. Halverson, G. P. Holder, W. L. Holzapfel, J. D. Hrubes, M. Joy, R. Keisler,

T. M. Lanting, A. T. Lee, E. M. Leitch, A. Loehr, M. Lueker, J. J. McMahon, J. Mehl, S. S. Meyer, J. J. Mohr, T. E. Montroy, C.-C. Ngeow, S. Padin, T. Plagge, C. Pryke, C. L. Reichardt, J. E. Ruhl, K. K. Schaffer, L. Shaw, E. Shirokoff, H. G. Spieler, B. Stalder, A. A. Stark, K. Vanderlinde, J. D. Vieira, O. Zahn, and A. Zenteno. Galaxy Clusters Discovered with a Sunyaev-Zel'dovich Effect Survey. *Astrophysical Journal*, 701:32–41, August 2009. doi: 10.1088/0004-637X/701/1/32.

G. Steigman. Equivalent Neutrinos, Light WIMPs, and the Chimera of Dark Radiation. *ArXiv e-prints*, February 2013.

A. Stril, R. N. Cahn, and E. V. Linder. Testing standard cosmology with large-scale structure. *Montly Notices of the Royal Astronomical Society*, 404:239–246, May 2010. doi: 10.1111/j.1365-2966.2010.16193.x.

R. A. Sunyaev and Y. B. Zeldovich. The Observations of Relic Radiation as a Test of the Nature of X-Ray Radiation from the Clusters of Galaxies. *Comments on Astrophysics and Space Physics*, 4:173–+, November 1972.

T. Szabo, E. Pierpaoli, F. Dong, A. Pipino, and J. Gunn. An Optical Catalog of Galaxy Clusters Obtained from an Adaptive Matched Filter Finder Applied to Sloan Digital Sky Survey Data Release 6. *Astrophysical Journal*, 736:21, July 2011. doi: 10.1088/0004-637X/736/1/21.

The ALEPH Collaboration, the DELPHI Collaboration, the L3 Collaboration, the OPAL Collaboration, the SLD Collaboration, and the LEP Electroweak Working Group. Precision Electroweak Measurements on the Z Resonance. *ArXiv High Energy Physics - Experiment e-prints*, September 2005.

J. Tinker, A. V. Kravtsov, A. Klypin, K. Abazajian, M. Warren, G. Yepes, S. Gottlöber, and D. E. Holz. Toward a Halo Mass Function for Precision Cosmology: The Limits of Universality. *Astrophysical Journal*, 688:709–728, December 2008. doi: 10.1086/591439.

J. L. Tinker, B. E. Robertson, A. V. Kravtsov, A. Klypin, M. S. Warren, G. Yepes, and S. Gottlöber. The Large-scale Bias of Dark Matter Halos: Numerical Calibration and Model Tests. *Astrophysical Journal*, 724:878–886, December 2010. doi: 10.1088/0004-637X/724/2/878.

E. Tundo, A. Moretti, P. Tozzi, L. Teng, P. Rosati, G. Tagliaferri, and S. Campana. The Swift X-ray Telescope Cluster Survey: data reduction and cluster catalog

for the GRB fields. *Astronomy and Astrophysics*, 547:A57, November 2012. doi: 10.1051/0004-6361/201219038.

C. van Breukelen, L. Clewley, D. G. Bonfield, S. Rawlings, M. J. Jarvis, J. M. Barr, S. Foucaud, O. Almaini, M. Cirasuolo, G. Dalton, J. S. Dunlop, A. C. Edge, P. Hirst, R. J. McLure, M. J. Page, K. Sekiguchi, C. Simpson, I. Smail, and M. G. Watson. Galaxy clusters at 0.6 ¡ z ¡ 1.4 in the UKIDSS Ultra Deep Survey Early Data Release. *Montly Notices of the Royal Astronomical Society*, 373:L26–L30, November 2006. doi: 10.1111/j.1745-3933.2006.00236.x.

R. P. van der Marel, J. Magorrian, R. G. Carlberg, H. K. C. Yee, and E. Ellingson. The Velocity and Mass Distribution of Clusters of Galaxies from the CNOC1 Cluster Redshift Survey. *The Astronomical Journal*, 119:2038–2052, May 2000. doi: 10.1086/301351.

L. Van Waerbeke, Y. Mellier, T. Erben, J. C. Cuillandre, F. Bernardeau, R. Maoli, E. Bertin, H. J. McCracken, O. Le Fèvre, B. Fort, M. Dantel-Fort, B. Jain, and P. Schneider. Detection of correlated galaxy ellipticities from CFHT data: first evidence for gravitational lensing by large-scale structures. *Astronomy and Astrophysics*, 358:30–44, June 2000.

M. Velliscig, M. P. van Daalen, J. Schaye, I. G. McCarthy, M. Cacciato, A. M. C. Le Brun, and C. D. Vecchia. The impact of galaxy formation on the total mass, mass profile and abundance of haloes. *Montly Notices of the Royal Astronomical Society*, 442:2641–2658, August 2014. doi: 10.1093/mnras/stu1044.

L. Verde, S. M. Feeney, D. J. Mortlock, and H. V. Peiris. (Lack of) Cosmological evidence for dark radiation after Planck. *Journal of Cosmology and Astroparticle Physics*, 9:013, September 2013. doi: 10.1088/1475-7516/2013/09/013.

A. Veropalumbo, F. Marulli, L. Moscardini, M. Moresco, and A. Cimatti. An improved measurement of baryon acoustic oscillations from the correlation function of galaxy clusters at z 0.3. *Montly Notices of the Royal Astronomical Society*, 442: 3275–3283, August 2014. doi: 10.1093/mnras/stu1050.

M. Viel, M. G. Haehnelt, and V. Springel. Inferring the dark matter power spectrum from the Lyman α forest in high-resolution QSO absorption spectra. *Montly Notices of the Royal Astronomical Society*, 354:684–694, November 2004a. doi: 10.1111/j.1365-2966.2004.08224.x.

M. Viel, S. Matarrese, A. Heavens, M. G. Haehnelt, T.-S. Kim, V. Springel, and L. Hernquist. The bispectrum of the Lyman α forest at $z\tilde{}$ 2-2.4 from a large sample of UVES QSO absorption spectra (LUQAS). *Montly Notices of the Royal Astronomical Society*, 347:L26–L30, January 2004b. doi: 10.1111/j.1365-2966.2004.07404.x.

M. Viel, M. G. Haehnelt, and V. Springel. The effect of neutrinos on the matter distribution as probed by the intergalactic medium. *Journal of Cosmology and Astroparticle Physics*, 6:15–+, June 2010. doi: 10.1088/1475-7516/2010/06/015.

A. Vikhlinin, B. R. McNamara, W. Forman, C. Jones, H. Quintana, and A. Hornstrup. A Catalog of 200 Galaxy Clusters Serendipitously Detected in the ROSAT PSPC Pointed Observations. *Astrophysical Journal*, 502:558–581, August 1998. doi: 10.1086/305951.

A. Vikhlinin, R. A. Burenin, H. Ebeling, W. R. Forman, A. Hornstrup, C. Jones, A. V. Kravtsov, S. S. Murray, D. Nagai, H. Quintana, and A. Voevodkin. Chandra Cluster Cosmology Project. II. Samples and X-Ray Data Reduction. *Astrophysical Journal*, 692:1033–1059, February 2009a. doi: 10.1088/0004-637X/692/2/1033.

A. Vikhlinin, A. V. Kravtsov, R. A. Burenin, H. Ebeling, W. R. Forman, and *et al.* Chandra Cluster Cosmology Project III: Cosmological Parameter Constraints. *Astrophysical Journal*, 692:1060–1074, February 2009b. doi: 10.1088/0004-637X/692/2/1060.

F. Villaescusa-Navarro, J. Miralda-Escudé, C. Peña-Garay, and V. Quilis. Neutrino halos in clusters of galaxies and their weak lensing signature. *Journal of Cosmology and Astroparticle Physics*, 6:027, June 2011. doi: 10.1088/1475-7516/2011/06/027.

F. Villaescusa-Navarro, S. Bird, C. Peña-Garay, and M. Viel. Non-linear evolution of the cosmic neutrino background. *Journal of Cosmology and Astroparticle Physics*, 3:019, March 2013. doi: 10.1088/1475-7516/2013/03/019.

F. Villaescusa-Navarro, F. Marulli, M. Viel, E. Branchini, E. Castorina, E. Sefusatti, and S. Saito. Cosmology with massive neutrinos I: towards a realistic modeling of the relation between matter, haloes and galaxies. *Journal of Cosmology and Astroparticle Physics*, 3:011, March 2014. doi: 10.1088/1475-7516/2014/03/011.

M. Vogelsberger, S. Genel, V. Springel, P. Torrey, D. Sijacki, D. Xu, G. F. Snyder, D. Nelson, and L. Hernquist. Introducing the Illustris Project: Simulating the coevolution of dark and visible matter in the Universe. *ArXiv e-prints*, May 2014.

W. Voges, B. Aschenbach, T. Boller, H. Bräuninger, U. Briel, W. Burkert, K. Dennerl, J. Englhauser, R. Gruber, F. Haberl, G. Hartner, G. Hasinger, M. Kürster, E. Pfeffermann, W. Pietsch, P. Predehl, C. Rosso, J. H. M. M. Schmitt, J. Trümper, and H. U. Zimmermann. The ROSAT all-sky survey bright source catalogue. *Astronomy and Astrophysics*, 349:389–405, September 1999.

A. von der Linden, A. Mantz, S. W. Allen, D. E. Applegate, P. L. Kelly, R. G. Morris, A. Wright, M. T. Allen, P. R. Burchat, D. L. Burke, D. Donovan, and H. Ebeling. Robust weak-lensing mass calibration of Planck galaxy clusters. *Montly Notices of the Royal Astronomical Society*, 443:1973–1978, September 2014. doi: 10.1093/mnras/stu1423.

M. S. Warren, K. Abazajian, D. E. Holz, and L. Teodoro. Precision Determination of the Mass Function of Dark Matter Halos. *Astrophysical Journal*, 646:881–885, August 2006. doi: 10.1086/504962.

W. A. Watson, I. T. Iliev, A. D'Aloisio, A. Knebe, P. R. Shapiro, and G. Yepes. The halo mass function through the cosmic ages. *Montly Notices of the Royal Astronomical Society*, 433:1230–1245, August 2013. doi: 10.1093/mnras/stt791.

D. H. Weinberg, M. J. Mortonson, D. J. Eisenstein, C. Hirata, A. G. Riess, and E. Rozo. Observational probes of cosmic acceleration. *Physics Reports*, 530:87–255, September 2013. doi: 10.1016/j.physrep.2013.05.001.

Z. L. Wen, J. L. Han, and F. S. Liu. A Catalog of 132,684 Clusters of Galaxies Identified from Sloan Digital Sky Survey III. *Astrophysical Journal Supplement*, 199:34, April 2012. doi: 10.1088/0067-0049/199/2/34.

M. White. The Mass Function. *Astrophysical Journal Supplement*, 143:241–255, December 2002. doi: 10.1086/342752.

M. White. The Ly-a forest. In *The Davis Meeting On Cosmic Inflation*, March 2003.

S. D. M. White, C. S. Frenk, and M. Davis. Clustering in a neutrino-dominated universe. *Astrophysical Journal Letters*, 274:L1–L5, November 1983. doi: 10.1086/184139.

S. D. M. White, G. Efstathiou, and C. S. Frenk. The amplitude of mass fluctuations in the universe. *Montly Notices of the Royal Astronomical Society*, 262:1023–1028, June 1993a.

S. D. M. White, J. F. Navarro, A. E. Evrard, and C. S. Frenk. The baryon content of galaxy clusters: a challenge to cosmological orthodoxy. *Nature*, 366:429–433, December 1993b. doi: 10.1038/366429a0.

D. M. Wittman, J. A. Tyson, D. Kirkman, I. Dell'Antonio, and G. Bernstein. Detection of weak gravitational lensing distortions of distant galaxies by cosmic dark matter at large scales. *Nature*, 405:143–148, May 2000.

R. Wojtak, E. L. Łokas, S. Gottlöber, and G. A. Mamon. Radial velocity moments of dark matter haloes. *Montly Notices of the Royal Astronomical Society*, 361:L1–L5, July 2005. doi: 10.1111/j.1745-3933.2005.00054.x.

L. Wolz, M. Kilbinger, J. Weller, and T. Giannantonio. On the validity of cosmological Fisher matrix forecasts. *Journal of Cosmology and Astroparticle Physics*, 9:009, September 2012. doi: 10.1088/1475-7516/2012/09/009.

M. Wyman, D. H. Rudd, R. A. Vanderveld, and W. Hu. nu-LCDM: Neutrinos reconcile Planck with the Local Universe. *ArXiv e-prints*, July 2013.

J.-Q. Xia, G.-B. Zhao, and X. Zhang. Cosmological neutrino mass limit and the dynamics of dark energy. *Physical Review D*, 75(10):103505, May 2007. doi: 10.1103/PhysRevD.75.103505.

J.-Q. Xia, B. R. Granett, M. Viel, S. Bird, L. Guzzo, M. G. Haehnelt, J. Coupon, H. J. McCracken, and Y. Mellier. Constraints on massive neutrinos from the CFHTLS angular power spectrum. *Journal of Cosmology and Astroparticle Physics*, 6:010, June 2012. doi: 10.1088/1475-7516/2012/06/010.

G. Xu. A New Parallel N-Body Gravity Solver: TPM. *Astrophysical Journal Supplement*, 98:355, May 1995. doi: 10.1086/192166.

X. Xu, A. J. Cuesta, N. Padmanabhan, D. J. Eisenstein, and C. K. McBride. Measuring D_A and H at z=0.35 from the SDSS DR7 LRGs using baryon acoustic oscillations. *Montly Notices of the Royal Astronomical Society*, 431:2834–2860, May 2013. doi: 10.1093/mnras/stt379.

M. Zaldarriaga, D. N. Spergel, and U. Seljak. Microwave Background Constraints on Cosmological Parameters. *Astrophysical Journal*, 488:1, October 1997. doi: 10.1086/304692.

M. Zaldarriaga, L. Hui, and M. Tegmark. Constraints from the Lyα Forest Power Spectrum. *Astrophysical Journal*, 557:519–526, August 2001. doi: 10.1086/321652.

Y. B. Zel'dovich. Fragmentation of a homogeneous medium under the action of gravitation. *Astrophysics*, 6:164–174, April 1970. doi: 10.1007/BF01007263.

G.-B. Zhao, S. Saito, W. J. Percival, A. J. Ross, F. Montesano, and *et al.* The clustering of galaxies in the SDSS-III Baryon Oscillation Spectroscopic Survey: weighing the neutrino mass using the galaxy power spectrum of the CMASS sample. *ArXiv e-prints*, November 2012.

G.-B. Zhao, S. Saito, W. J. Percival, A. J. Ross, F. Montesano, M. Viel, D. P. Schneider, M. Manera, J. Miralda-Escudé, N. Palanque-Delabrouille, N. P. Ross, L. Samushia, A. G. Sánchez, M. E. C. Swanson, D. Thomas, R. Tojeiro, C. Yèche, and D. G. York. The clustering of galaxies in the SDSS-III Baryon Oscillation Spectroscopic Survey: weighing the neutrino mass using the galaxy power spectrum of the CMASS sample. *Montly Notices of the Royal Astronomical Society*, 436: 2038–2053, December 2013. doi: 10.1093/mnras/stt1710.

F. Zwicky. Die Rotverschiebung von extragalaktischen Nebeln. *Helvetica Physica Acta*, 6:110–127, 1933.

.

.